Implementation, validation and evaluation of a Quasi-3D model in Delft3D

Johan Henrotte

Implementation, validation and evaluation of a Quasi-3D model in Delft3D

M.Sc. thesis
Johan Henrotte

Graduation Committee
Prof. dr. ir. M.J.F. Stive
Ir. A.P. Luijendijk
Ir. D.J.R. Walstra
Ir. R.J. Labeur

Report

July 2008

Preface

The M.Sc. thesis is the final step of my study at Delft, University of Technology, faculty Civil Engineering and Geosciences, section Hydraulic Engineering.

This thesis describes the implementation, validation and evaluation of a Quasi-3D model in Delft3D.

I am grateful to all the people who were involved in my master thesis. First, I would like to thank my graduation committee, Prof. dr. ir. M.J.F. Stive (Delft University of Technology), Ir. R.J. Labeur (Delft University of Technology) and especially Ir. D.J.R. Walstra (Deltares / Delft University of Technology) and Ir. A.P. Luijendijk (Deltares) for their enthusiastic support. Furthermore, I would like to thank Deltares for the opportunity and facilities they offered me.

During my stay at Deltares, I had the privilege to sit at one of the 'student-islands'. I would like to thank my fellow graduate students: John, Robert, Noud, Thomas, Laura, Sam & Moos, Thijs, Carola, Arend, Marten and Claire for the very pleasant time we had at Deltares. Furthermore, I want to specify my special thanks to Anton, Mr Gao, Renske and Claartje with whom I had a great time on the island at the Hydraulic Engineering section.

Finally, I would like to thank my friends and family for their support during the last six years.

Johan Henrotte,

Delft, July 2008

Summary

In almost every coastal engineering problem, morphological changes play an important role. To understand and predict morphological changes, numerical models such as Delft3D are often used. In the last couple of years the time scale of interest has increased considerably. Due to the large calibration effort and especially the large computational time a full three-dimensional (3D) simulation is generally not very practical. Therefore most of these morphological studies are carried out in the depth-averaged (2DH) mode. Several projects showed that especially in depth-averaged mode the present possibilities to adjust the cross-shore transport in the nearshore area, and the associated cross-shore profile developments, are inadequate.

Based on these drawbacks it was decided to implement, validate and evaluate a new approach in Delft3D which represents the 3D results in the nearshore zone, but with less computational time.

When considering the depth-averaged current field to be representative of the entire flow pattern, one makes the implicit assumption of vertical similarity of the velocity profile, i.e. the velocity profile in every point in the horizontal has the same shape (e.g. logarithmic). In reality, however, the velocity field is more complex than this. Such as in nearshore areas where breaking waves cause (secondary) return flow currents. To reproduce these secondary currents a quasi-three dimensional (Q3D) model based on the concepts of Reniers et al. (2004) was implemented into the Delft3D model. This model computes the vertical velocity distribution at every grid point accounting for tidal forcing, wave breaking, wind and dissipation due to bottom friction.

Validation of the Q3D approach was carried out on four validation cases: three flume experiments (LIP, Boers and Reniers) and one field case (Egmond). Because of the complexity of morphological modelling, this validation process was divided in three parts: hydrodynamic, sediment concentration and transport, and morphological validation, with the following findings:

- *Hydrodynamics:* Q3D cross-shore velocity profiles show high agreement with 3D velocity profiles in both shape and magnitude. Longshore velocity profiles show the same logarithmic shaped profile for both Q3D and 3D model results.

- *Sediment transport:* Q3D equilibrium concentrations are higher than 2DH concentrations. In combination with an increased reference velocity, the suspended transport rates are increased. This results in higher total sediment transport rates.

- *Morphology:* The profile model shows an increase in an offshore bar migration for Q3D modelling compared with 2DH and 3D. Q3D erosion and sedimentation patterns show high similarity with 3D model results.

Implementation of the Q3D model introduced two additional calibration parameters:

- A multiplication factor for the wave boundary layer thickness (*facdel*), and

- A multiplication parameter to scale the wave-induced eddy viscosity (*fcvisc*)

Sensitivity analysis for five important calibration parameters was performed (including the two new Q3D additional parameters) which shows the importance of the roller process and the calibration parameter *fcvisc*.

The four validation cases show the time efficiency of the Q3D model clearly. With only an increase between the 14-20% (Q3D) against an increase of 236-608% for fully 3D computations, the Q3D model can be competitive with depth-averaged models.

To investigate the applicability of the model, four evaluation cases were performed. A uniform coast was modelled with no obstacles, including a long groyne and including a short groyne. Finally a stretch of coast with a submerged breakwater is modelled. Q3D model results show again agreement with 3D model results with only a small increase in computational time.

Contents

List of Tables

List of Figures

List of Symbols

Symbol	Unit	Description
θ	degree	wave angle
c	m/s	wave celerity
c_g	m/s	wave group velocity
$c_{g,0}$	m/s	wave group velocity in deep water
k_s	-	shoaling factor
s_d	-	wave steepness
k	1/m	wave number
h	m	water depth
h'	m	average water level in point x
S_{xx}	N/m	Radiation stress in landward direction
S_{yx}	N/m	Radiation stress parallel to the coast
$u(z)$	m/s	velocity at height z
$c(z)$	kg/m^3	sediment concentration at height z
$\vec{S}$	m^3/m/s	sediment transport flux
u, v, w	m/s	velocity in x, y and z direction
x	m	coordinate normal to the shore
y	m	coordinate parallel to the shore
z	m	level above reference height
f_c	-	Coriolis factor
ν_t	m^2/s	turbulent eddy viscosity
$\tilde{u}, \tilde{v}, \tilde{w}$	m/s	wave orbital velocities in x, y and z direction
f_p	-	vertical distribution function
z_b	m	bed level
$\overline{u}, \overline{v}$	m/s	depth-averaged velocity in x and y direction
p_n	Pa	hydrostatic pressure
z_s	m	surface level
z_t	m	wave trough level
z_b	m	level top bottom boundary layer
u_p, v_p, w_p	m/s	primary velocity in x, y and z-direction
u_s, v_s, w_s	m/s	secondary velocity in x, y and z-direction
τ_{bpx}, τ_{bsx}	N/m^2	bottom shear stress in x-direction related to primary and secondary currents
W_x	N/m^2	the x-component of the wind shear stress
ρ	kg/m^3	water density
E	J/m^2	wave energy
H	m	wave height
g	m/s^2	gravitational acceleration

η	m	water surface level
$\tilde{u}, \tilde{v}, \tilde{w}$	m/s	wave orbital velocity components in x, y and z direction
C_τ	-	constant which establishes the relation between the primary bottom shear stress and the depth-averaged velocity
F_x	N/m^2	depth-averaged wave induced force in x-direction
σ	-	non-dimensional vertical coordinate
δ	-	non-dimensional thickness bottom boundary layer
f_δ	-	bottom boundary layer factor
k_s	m	roughness height
A	m	orbital excursion
z_0	m	zero velocity level
ω	s^{-1}	wave frequency
D_f	N/m/s	Dissipation due to bottom friction
f_w	-	friction coefficient
u_{orb}	m/s	wave orbital velocity
τ_i	N/m^2	shear stress in i-direction
$\tau_{t,i}$	N/m^2	shear stress at wave trough level
ρ_a	kg/m^3	air density
C_d	-	wind drag coefficient
U_{10}	m/s	wind speed at 10 m above the free surface
$\tau_{s,wind}$	N/m^2	wind induced shear stress at surface level
$\tau_{s,wave}$	N/m^2	wave-induced shear stress at surface level
D_r	N/m/s	dissipation of roller energy
ϕ_s	-	scale factor viscosity profile middle layer
ϕ_b	-	scale factor viscosity profile bottom boundary layer
$\overline{\nu}_t$	m^2/s	depth-averaged eddy viscosity
ν_t	m^2/s	eddy viscosity
$\overline{\nu}_{tb}$	m^2/s	eddy viscosity in bottom boundary layer
$\overline{\nu}_{t,current}$	m^2/s	flow induced viscosity
κ	-	von Karman constant
s	-	gradient of the water level
f_v	-	multiplication factor wave-induced viscosity
H_{rms}	m	root-mean-square wave height
$\overline{\nu}_{t,wave}$	m^2/s	wave-induced viscosity
$\overline{\nu}_{t,wind}$	m^2/s	wind-induced viscosity
c_f	-	friction coefficient
σ_s	-	non dimensional surface level

σ_b	-	non-dimensional wave boundary level
σ_0	-	non-dimensional zero velocity level
$u_{\delta,i}$	m/s	velocity at top bottom boundary layer
$\overline{c}$	kg/m^3	depth-averaged sediment concentration
D_H	m^2/s	horizontal dispersion coefficient
$\overline{c}_{eq}$	kg/m^3	depth-average equilibrium concentration
T_s	s	adaptation time scale
S_x S_y	m^3/s/m	sediment transport in x- and y- direction
ε_{por}	-	bed porosity
u_{q3d}	m/s	Q3D velocity
c_{q3d}	kg/m^3	Q3D concentration
S_{q3d}	m^3/s/m	Q3D sediment transport

1 Introduction

In almost every coastal engineering problem, morphological changes play an important role. To understand and predict morphological changes, numerical models such as Delft3D are often used.

Figure 1.1 Breaking waves at the Dutch coast (Egmond) [source: www.kustfoto.nl/]

Morphological modelling with Delft3D these days is more often done in studies that focus at the combined cross-shore and longshore behaviour (Figure 1.1). In the last couple of years the time scale of interest has increased considerably. In the past, morphological simulations were done for initial changes in the order of 5 years, whereas a time span of decades is used more frequently these days.

Due to the large calibration effort and computational time a full three-dimensional (3D) simulation is generally not very practical. Therefore most of these morphological studies are done in depth-averaged (2DH) mode.

Several projects done by WL | Delft Hydraulics as well as by external users of Delft3D, showed that especially in 2DH or 1DH (profile mode) the present possibilities to adjust the cross-shore transport in the nearshore area, and the associated cross-shore profile developments, are inadequate.

Based on these drawbacks it was decided to upgrade the Delft3D model with a new approach.

1.1 Problem description

Cross-shore profile evolution is induced by a combination of longshore and cross-shore sediment transports. In the nearshore zone, the cross-shore velocity profile can exhibit a strong vertical shear. Where in the top layer the flow is directed most of the time onshore because of wave breaking, the middle layer shows a circulation flow which is directed offshore (Figure 1.2).

When considering the depth-averaged current field to be representative of the entire flow pattern, one makes the implicit assumption of vertical similarity of the velocity profile, i.e. the velocity profile in every point in the horizontal has the same shape (e.g.

logarithmic). In reality, however, the velocity field is more complex. Such as in nearshore areas where breaking waves cause (secondary) return flow currents.

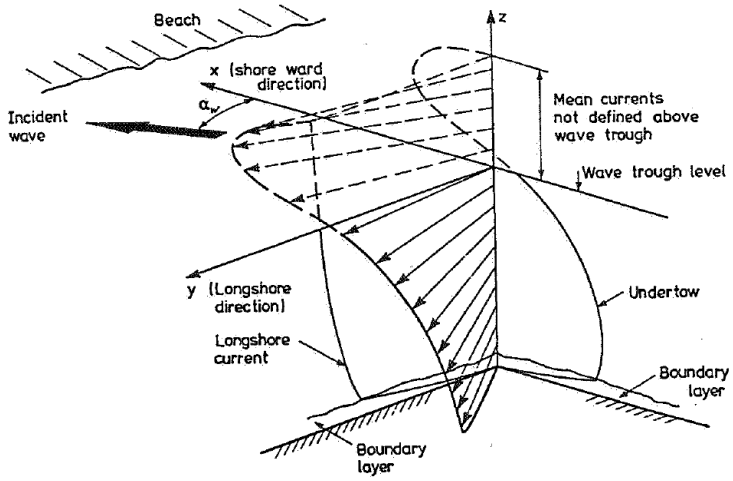

Figure 1.2 Longshore and cross-shore velocity profile in nearshore zone (van Dongeren et al,1995)

This secondary flow, though rather weak compared to the maximum tidal current, can have a significant residual effect in the current, but also on the sediment transport and the bed topography. For an accurate description of the cross-shore sediment transport, current-, wind- and wave-related components have to be taken into account.

To represent this process in the depth-averaged model, without increasing the computational time to a high extent it was decided to implement a new approach in Delft3D: the Quasi-3D (Q3D) model. The Q3D model is an analytical point model (Reniers et al., 2004), which computes the vertical velocity distribution at each grid point. The model has already been used in the profile model UNIBEST-TC[1] (Ruessink et al., 2007).

1.2 Objective

The objective of this thesis was to analyse the implementation, validate and evaluate a new approach (Q3D) in morphological modelling which represents the 3D results in the nearshore zone, but with less computational time.

1.3 Approach

To achieve the objective, this study was divided into three phases:

- Phase 1: Analysis of the implementation of the Q3D approach in the Delft3D code
- Phase 2: Validation of the Q3D approach with the use of four cases
- Phase 3: Evaluation of the Q3D approach based on project cases

After the literature study, the first phase was to analyse the implementation of the new approach in the Delft3D source code.

1. *UNIBEST-TC model (Bosboom et al. 1997), UNiform BEach Sediment Transport – Time dependent Cross-shore developed by Deltares is a process-based model that incorporates models for hydrodynamic processes.*

The second phase covered the validation process. This phase was divided in three main steps: validation on hydrodynamics, sediment transport and morphology. Because the morphology is a direct consequence of the hydrodynamics, it was chosen to first finish the validation process for the hydrodynamics before starting with the sediment transports and morphological changes. Validation was done with the use of four different validation cases; LIP, Boers, Reniers, and Egmond field case. The Q3D model results were compared with measured data, Delft3D fully 3D and depth-averaged (2DH) model results and UNIBEST-TC model results.

After finishing the validation process for the hydrodynamics, the sediment transport and the morphology, the model was evaluated with several case studies in phase 3, to check the performance and limitations of the new approach.

1.4 Reader

Chapter 2 contains a short description of the physical processes in the nearshore area and an extensive theoretical description of the Q3D approach. The implementation of the model into Delft3D is also discussed. The validation of the model is described in Chapter 3 by using four different validation cases. In this validation chapter the Q3D approach was compared with Delft3D (2DH and 3D) model results. Besides that, the sensitivity of the most important parameters was discussed for the hydrodynamics, sediment transport and morphology. Finally the calculation times of the different models was compared in this chapter. In Chapter 4 the Q3D-approach was evaluated with a number of practical cases to investigate the applicability of the model. Finally in Chapter 5 the conclusions and recommendations were given.

The appendices give background information about the different models used and about Delft3D.

To improve the readability of the report, large figures are shown in Appendix F. Reference to these figures is made with e.g. Figure F3.4.1, in which F denotes the Appendix number, the first two numbers the section where the figure belongs to, and the last number represents the figure number.

2 Theoretical Description of the Q3D Model

2.1 Introduction

At the moment two dimensional depth-averaged (2DH) models are often used to model coastal areas. Because of the complexity of the flow patterns, a 2DH model is not always accurate enough to model nearshore morphological developments. In these cases a full three-dimensional (3D) approach is desired. However, from a computation time point of view, a 3D model is not always feasible.

A Quasi-3D (Q3D) model of nearshore currents is developed, on the basis of existing concepts of 2DH (horizontal plane) and 1DV (vertical plane) current models. The result is a combination of a depth-integrated model and a vertical profile technique.

Several studies have been done using this technique, e.g.:

- Stive and de Vriend (1987)
- Reniers and Roelvink (1994, 2004)
- Zitman (1993)
- Van Dongeren (1995)

They are all based on the concepts described by Stive and de Vriend (1987). The Q3D-model which is described in this study is the same which is implemented in the profile model UNIBEST-TC (Appendix G) and is mainly based on the concepts described by Reniers et al (2004).

The Q3D model (Reniers et al, 2004) solves the vertical velocity distribution in the cross-shore and alongshore direction accounting for tidal forcing, wind, breaking waves and dissipation due to bottom friction.

Before starting describing the Q3D model in section 2.4 the physical processes are discussed in section 2.2. In section 2.3 the momentum equations are derived. Section 2.5 and 2.6 shortly described the sediment transport and morphology formulations. Finally, the implementation into Delft3D is mentioned in section 2.7.

2.2 Physical processes in nearshore zone

The nearshore zone (i.e. the surf zone) is defined as the area where the bottom affects the wave and flow characteristics. In the surf zone, complex hydrodynamic processes take place. These processes are described in this section.

2.2.1 Wave field

In shallow nearshore areas the characteristic of waves change strongly due to the decreasing water depth and the interaction with the sea bed. A short description of three important processes, refraction, shoaling and wave breaking is given in this section.

Refraction

When waves travel from deep water into shallow water, significant changes do occur. The wave speed decreases with depth. This means that the wave celerity is lower in shallow water compared to deep water. When a wave approaches depth contours at an angle, it is evident that the sections of the crest in the deeper parts travel faster than those in the shallower sections. This causes the wave crest to turn towards the depth contour (Figure 2.1). This bending effect is called refraction.

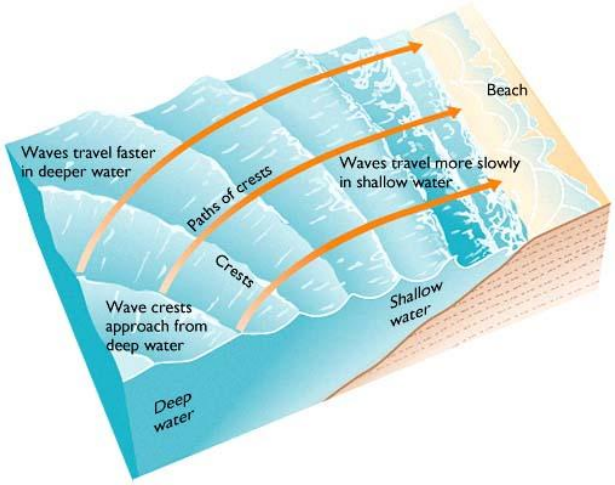

Figure 2.1 Definition sketch of refraction [source: http://piru.alexandria.ucsb.edu/]

When assuming that no wave energy moves laterally along the wave crest (i.e. energy remains constant between orthogonals normal to the wave crest), the local value of the wave direction can be computed with Snell's law:

$$\frac{\sin(\theta)}{c} = \text{constant along a ray} \qquad (2.1)$$

In which θ is the wave angle and c the celerity of the wave.

Shoaling

If waves approach water which is gradually becoming shallower, the wave will be affected by the bottom when the water depth becomes less than about half the wavelength. Nearing the breaker line, shoaling occurs. This means that the wave celerity and therefore the wave length decrease because of the decreasing water depth. Because no energy is dissipated the wave height increases (Figure 2.2). The shoaling factor k_s (equation (2.2)) is defined as the root of the ratio of wave celerity in deep water (c_{g0}) and wave group celerity at a certain point (c_g).

$$k_s = \left(\frac{c_{g0}}{c_g} \right)^{0.5} \qquad (2.2)$$

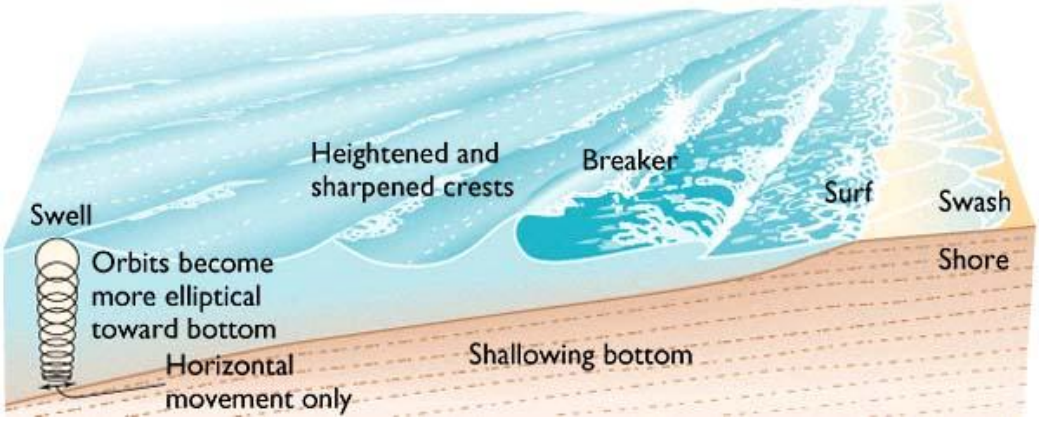

Figure 2.2 Shoaling [source: http://piru.alexandria.ucsb.edu/]

Wave Breaking

At a certain point, the wave height (or in some cases the steepness of the wave) becomes too high and the waves will break. In the surf zone of coastal areas and on beaches wave energy is finally dissipated during the wave breaking processes. Several formulations are available to compute the depth where waves tend to break. The ratio between the depth and the wave height is called the breaker parameter ($\gamma = \frac{H_{\max}}{h}$). Besides a constant ratio, several formulations to compute the breaker parameter are derived e.g. Battjes and Stive (1985) who determined that γ depends weakly on the deep-water steepness s_d as:

$$\gamma = 0.5 + 0.4\tanh(33 s_d) \tag{2.3}$$

And Ruessink et al (2003):

$$\gamma = 0.76kh + 0.29 \tag{2.4}$$

In which k represents the wave number and h the water depth.

2.2.2 Radiation stress

Propagating waves exert a net horizontal force. Additionally to the hydrostatic force, this force, called radiation stress, is always present when waves migrate through a body of water. However, its effect is most eminent in the nearshore zone, where relatively strong longshore currents can be generated by radiation stresses.

In deep water, it can be argued that this net effect will be very small (pressure fluctuations occur over a relatively small portion of the water column). Therefore, in deep water the pressure contribution to the radiation stress is often neglected (Figure 2.3).

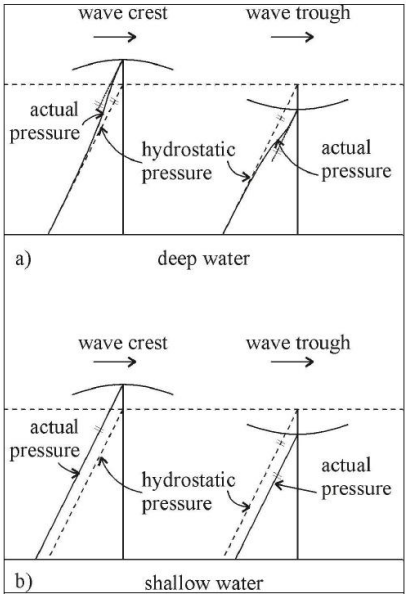

Figure 2.3 Radiation stress [source: lecture notes coastal morphology]

In shallow water the pressure fluctuations due to wave action are felt over the entire water column and are even felt at the bottom, both under a wave crest and under a wave trough, hydrostatic pressures can be assumed to occur (Figure 2.3b). Under these conditions it is quite clear that the net effect over a wave period (formal integration) results in a net force (contribution to the radiation stress) in wave propagation direction equation (2.5).

$$S_{xx} = \int \left(p + \rho u^2 \right) dz - \int p_0 dz \qquad (2.5)$$

The magnitude of the radiation stress depends mainly on the wave height, via the wave energy (Longuet-Higgins and Stewart, 1964).

$$S_{xx} = \left[\frac{1}{2} + \frac{2kh}{\sinh 2kh} \right] E \qquad (2.6)$$

In which S_{xx} is defined as the radiation stress normal to the coast, k the wave number, h the water depth and E the wave energy

$$E = 1/8 \, \rho g H^2 \qquad (2.7)$$

With ρ defined as the water density and H the wave height.

2.2.3 Wave set-up and set-down

The magnitude of the radiation stress depends on the water depth, the wave number and the wave height equation (2.6). If dissipation of wave energy can be neglected outside the breaker zone, then in this area the energy flux (Ec_g)is constant. With linear wave theory it can be shown that the radiation stress increases with decreasing depth in the region outside the breaker zone.

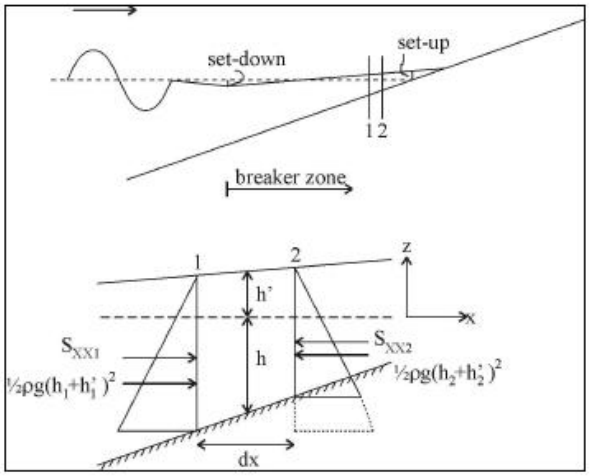

Figure 2.4 Wave set-up and set-down [source: lecture notes coastal morphology]

An increasing radiation stress S_{xx} in landward direction, means that at a water column a resulting force is acting in seaward direction equation (2.8). By a (small) difference in water level at both sides of the water column, equilibrium of forces can be achieved again (Figure 2.4). This is called wave *set-down*, which means that outside the breaker zone in intermediate depths, the water level at the landward side of a water column is a little bit lower at the seaward side.

$$\frac{dS_{xx}}{dx} = -\rho g\left(h + h'\right)\frac{dh'}{dx} \qquad (2.8)$$

In which h' is the average water level change at point x.

Inside the surf zone the magnitude of the radiation stress S_{xx} decreases rapidly due to wave breaking while moving towards the coast. A resulting force is now acting in shoreward direction. To achieve equilibrium again, the water level at the landward side of the column should be higher than the water level at the seaward side (*wave set-up*).

2.2.4 Longshore current

Inside the breaker zone a gradient in the radiation stress S_{yx} occurs due to changes in wave height because of wave breaking. This results in a force in longshore direction (Figure 2.5) dependent on the cross-shore gradient of S_{yx}.This longshore current leads to a bottom shear stress, which counter-acts the driving force. Equilibrium is reached once, via the longshore current, the bottom shear stress equals the cross-shore gradient in S_{yx}. The longshore current depends on the angle between the wave direction and the shore. By increasing the angle, the longshore currents increases until a maximum at an angle of 45 degrees (e.g. Ashton et al, 2001).

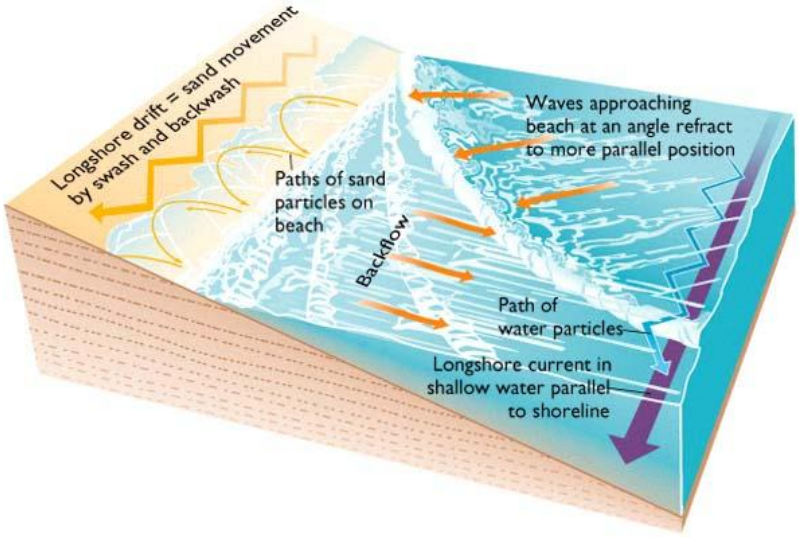

Figure 2.5 Nearshore currents [source: http://piru.alexandria.ucsb.edu/]

2.2.5 Cross-shore current

Breaking waves cause a net shoreward mass (water) transport which results in a wave set-up shoreward of the breaker zone (Section 2.2.3). Looking at a vertical plane a mass of water transport towards the coast occurs in the part between wave crest and wave trough. In the lower part of the water column, in a two dimensional case, the same mass of water has to return towards the sea again. This results in a so-called undertow or return flow (Figure 2.6). In case of non-breaking waves the undertow is rather small, in breaking waves the mass transport towards the coast may become quite large, resulting in significant undertow velocities.

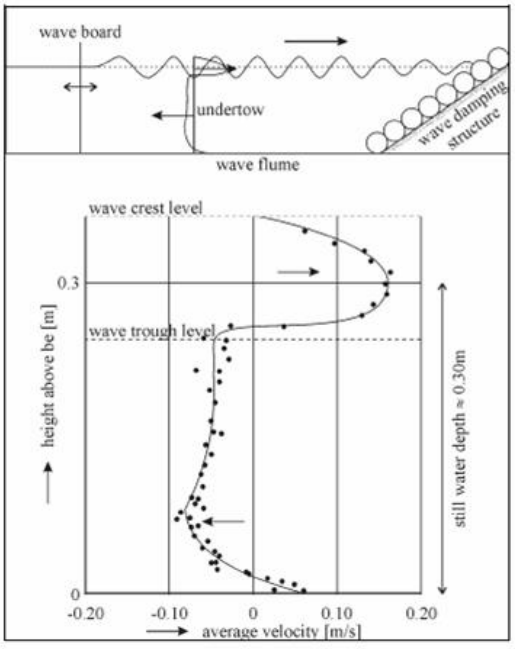

Figure 2.6 Velocities under a propagating wave [source: lecture notes coastal morphology]

2.2.6 Sediment transport

Sediment transport can be defined as the movement of sediment particles through a well defined plane over a certain period of time. The transport rate depends on the characteristics of the transported material and on the forces which induce such a transport. The primary force behind sediment transport is the bed shear stress exerted by the water motion at the bed. Sediment particles will tend to move when a certain critical bed shear stress is exceeded. The local bed shear stress can be induced by wind, wave, tide and density driven currents, by the oscillatory water motion itself (wave-related transport) or by a combination of currents and waves.

Sediment transport is generally split into two modes of transport: bed load and suspended load. To compute sediment transport it is first necessary to determine the velocity distribution $u(z)$ and the sediment concentration distribution $c(z)$ Figure 2.7.

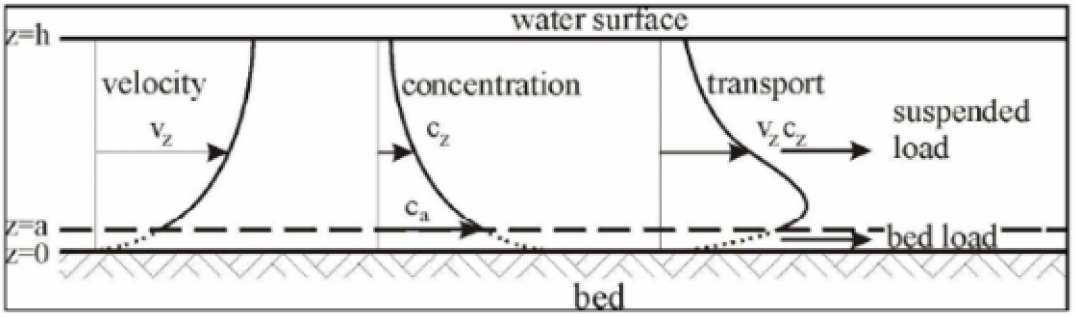

Figure 2.7 Principle of (suspended) sediment transport computation [source: lecture notes coastal morphology]

Basically, sediment transport can be defined as a quantity of sediment that is moving with a specific velocity through a well-defined plane. The total depth-integrated transport (from bottom till surface level) at a point is defined as:

$$\vec{S} = \int_{z=-d}^{z=\eta} c(z) \cdot \vec{u}(z)\, dz \tag{2.9}$$

When considering sediment transport in the coastal zone, it is convenient to distinguish sediment transport normal to the coast (cross-shore transport) and sediment transport parallel to the coast (longshore transport). Cross-shore transport is generally caused by a combined effect of the orbital velocities in case of wave asymmetry and in case of breaking waves by the undertow. Gravity along the slope also plays a role. Longshore transport is usually caused by the longshore current that is driven by radiation stress of waves approaching under an angle.

2.2.7 Morphology

Sediment transport itself does not cause any changes in the topography of the coastline. Only when there are gradients in the transport rate, there will be erosion or sedimentation. Gradients in the cross-shore direction lead to a realignment of the profile. Gradients in the longshore direction will lead to systematic erosion or sedimentation along the coastline.

2.3 Hydrodynamics: flow field

To compute the flow field, balance equations are considered. The full three-dimensional momentum equations can be divided in primary and secondary flow according to Stive and de Vriend (1987). The primary flow can be considered as the depth-averaged (2DH) flow field, and the secondary flow as the vertical distribution of the horizontal velocities (Figure 2.8).

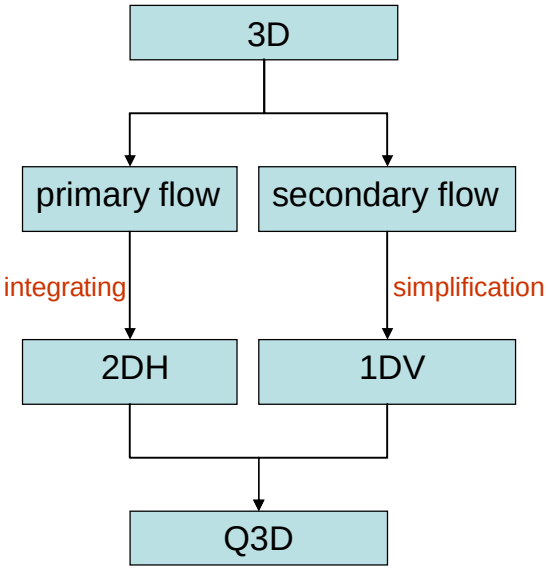

Figure 2.8 Process scheme equations

The vertical distribution of the velocity field can be estimated by neglecting parts in the secondary flow equation. By using both the depth-averaged (2DH) equations and a 1DV equation a Q3D flow field is computed.

The velocities, u and v in the x and y direction respectively, includes the wave-induced drift velocity (Stokes, 1847):

$$u = u^E + u^S \tag{2.10}$$

Where the superscripts E and S stand for Eulerian and Stokes, respectively, and a similar expression is used for the v component. This allows differentiating between the onshore velocity near the surface owing the waves and flow beneath that can include the offshore undertow. Separating the velocities in this manner can be important in specifying the mass flux and the bottom shear stress (e.g. Reniers et al. 2004).

In this section, first the full three-dimensional (3D) balance equations are considered. Subsequently, the division in primary and secondary flows is discussed and finally, both the 2DH and the 1DV momentum equations are derived.

2.3.1 Reynolds equations for turbulence averaged flow

The starting point of the Q3D current model is the Reynolds equations for turbulence-averaged flow. The Reynolds-averaged equations represent transport equations for the mean flow momentum only, with all the scales of the turbulence being modeled. If, in addition, the Boussinesq-hypothesis is adopted to model the Reynolds stress terms (i.e.

relate the Reynolds stresses to the mean velocity gradient), the wave- and turbulence-averaged horizontal momentum equations in the x - direction can be written as:

$$\underbrace{\frac{\partial u}{\partial t}}_{1} + \underbrace{u\frac{\partial u}{\partial x} + v\frac{\partial u}{\partial y} + w\frac{\partial u}{\partial z}}_{2} - \underbrace{f_c v}_{3} = \underbrace{-\frac{1}{\rho}\frac{\partial p_n}{\partial x}}_{4} + \underbrace{\frac{\partial}{\partial x}\left(\nu_t \frac{\partial u}{\partial x}\right) + \frac{\partial}{\partial y}\left(\nu_t \frac{\partial u}{\partial y}\right) + \frac{\partial}{\partial z}\left(\nu_t \frac{\partial u}{\partial z}\right)}_{5} - \underbrace{\frac{\partial}{\partial x}\left(\left\langle \tilde{u}^2 \right\rangle - \left\langle \tilde{w}^2 \right\rangle\right) - \frac{\partial}{\partial y}\left(\left\langle \tilde{u}\tilde{v} \right\rangle\right) - \frac{\partial}{\partial z}\left(\left\langle \tilde{u}\tilde{w} \right\rangle\right)}_{6} \quad (2.11)$$

In which:

1: inertia
2: advective terms
3: coriolis
4: pressure gradient
5: viscous (diffusive) terms
6: waves

with u, v and w defined as the velocity components, f_c the coriolis factor, p_n the total hydrostatic pressure, ν_t the turbulent eddy viscosity and $\tilde{u}, \tilde{v}$ and $\tilde{w}$ the wave orbital velocity components.

To solve the eddy viscosity a turbulence closure model is needed.

2.3.2 Similarity approach

The basic idea of the flow model is similarity approach (equation (2.12)). Assuming that each dependent variable can be written in the form:

$$u = \sum_i \overline{u}_i \left(x, y, t\right) f_i \left(\frac{z - z_b}{h}\right) \quad (2.12)$$

With f_i the vertical distribution function, z_b the bottom level and $\overline{u}_i$ is the depth-independent velocity.

The independent variables in the model are:

- The total hydrostatic pressure p_n (or the mean water surface elevation $\left\langle z_s \right\rangle$)
- The velocity components u, v and w.

2.3.3 Division in primary and secondary currents

According to Stive and de Vriend (1987) the momentum equation is divided into primary and secondary currents. Which are defined as:

$$u = u_p + u_s \quad \text{with} \quad u_p = \overline{u}(x,y,t)\, f_p\left(\frac{z - z_b}{h}\right) \quad \text{and} \quad \overline{u}_s = 0 \tag{2.13}$$

$$v = v_p + v_s \quad \text{with} \quad v_p = \overline{v}(x,y,t)\, f_p\left(\frac{z - z_b}{h}\right) \quad \text{and} \quad \overline{v}_s = 0 \tag{2.14}$$

in which the subscript p denotes the primary current, the subscript s the secondary current, the overbar the depth-averaged value and f_p the vertical distribution function (see Stive and de Vriend, 1987). The vertical distribution function is assumed to be constant in x- and y- direction (e.g. a logarithmic shape function). This means that the depth-averaged flow is determined entirely by the primary current.

To obtain expressions for the primary and secondary currents, the velocities u and v in the momentum equation (2.11) are first replaced by the primary and secondary velocities from equation (2.13) and (2.14). This result in the following momentum equation for the x-direction:

$$\begin{aligned}
&\frac{\partial u_p}{\partial t} + u_p \frac{\partial u_p}{\partial x} + v_p \frac{\partial u_p}{\partial y} + w_p \frac{\partial u_p}{\partial z} - f_c v_p \\
&+ \frac{\partial u_s}{\partial t} + u_s \frac{\partial u_s}{\partial x} + v_s \frac{\partial u_s}{\partial y} + w_s \frac{\partial u_s}{\partial z} - f_c v_s \\
&+ u_s \frac{\partial u_p}{\partial x} + v_s \frac{\partial u_p}{\partial y} + w_s \frac{\partial u_p}{\partial z} + u_p \frac{\partial u_s}{\partial x} + v_p \frac{\partial u_s}{\partial y} + w_p \frac{\partial u_s}{\partial z} = \\
&-\frac{1}{\rho}\frac{\partial p_n}{\partial x} + \frac{\partial}{\partial x}\left(\nu_t \frac{\partial u_p}{\partial x}\right) + \frac{\partial}{\partial y}\left(\nu_t \frac{\partial u_p}{\partial y}\right) + \frac{\partial}{\partial z}\left(\nu_t \frac{\partial u_p}{\partial z}\right) \\
&+ \frac{\partial}{\partial x}\left(\nu_t \frac{\partial u_s}{\partial x}\right) + \frac{\partial}{\partial y}\left(\nu_t \frac{\partial u_s}{\partial y}\right) + \frac{\partial}{\partial z}\left(\nu_t \frac{\partial u_s}{\partial z}\right) \\
&- \frac{\partial}{\partial x}\left(\langle \tilde{u}^2 \rangle - \langle \tilde{w}^2 \rangle\right) - \frac{\partial}{\partial y}\left(\langle \tilde{u}\tilde{v} \rangle\right)
\end{aligned} \tag{2.15}$$

With u_p, u_s, v_p, v_s, w_p and w_s the primary and secondary currents in x-, y- and z-direction.

After integration from the bottom to a point above the highest water surface elevation the momentum equation (2.15) in the x-direction becomes:

$$
\begin{aligned}
&\frac{\partial \overline{u}}{\partial t} + \overline{f}_p^2 \left(\overline{u} \frac{\partial \overline{u}}{\partial x} + \overline{v} \frac{\partial \overline{u}}{\partial y} \right) - f_c \overline{v} \\
&+ \frac{1}{h}\left[\frac{\partial}{\partial x} \right] \left(h \overline{u}_s^2 \right) + \frac{1}{h} \frac{\partial}{\partial y} \left[h \overline{u_s v_s} \right] + \frac{1}{h} \left[\frac{\partial}{\partial x} \right] \left(h \overline{u_p u_s} \right) + \\
&\frac{1}{h} \frac{\partial}{\partial y} \left[h \overline{u_p v_s} \right] + \frac{1}{h}\left[\frac{\partial}{\partial x} \right] \left(h \overline{u_s u_p} \right) + \frac{1}{h} \frac{\partial}{\partial y} \left[h \overline{u_s v_p} \right] = \\
&- \frac{1}{\rho} \frac{\partial p_n}{\partial x} \\
&+ \overline{\frac{\partial}{\partial x} \left(\nu_t \frac{\partial u_p}{\partial x} \right)} + \overline{\frac{\partial}{\partial y} \left(\nu_t \frac{\partial u_p}{\partial y} \right)} + \overline{\frac{\partial}{\partial x} \left(\nu_t \frac{\partial u_s}{\partial x} \right)} + \overline{\frac{\partial}{\partial y} \left(\nu_t \frac{\partial u_s}{\partial y} \right)} \\
&- \frac{\tau_{bpx}}{\rho h} - \frac{\tau_{bsx}}{\rho h} \\
&- \frac{1}{\rho h} \left(\frac{\partial S_{xx}}{\partial x} + \frac{\partial S_{xy}}{\partial y} \right) + \frac{W_x}{\rho h}
\end{aligned}
\tag{2.16}
$$

In here τ_{bpx} and τ_{bsx} represents the bottom shear stress related to the primary and secondary flow, W_x the x-component of the wind shear stress at the water surface and S_{xx} and S_{xy} are components of the radiation stress, defined as (Battjes, 1974):

$$
S_{xx} = \int_{z_b}^{\langle z_s \rangle} \rho \left(\left\langle \tilde{u}^2 \right\rangle - \left\langle \tilde{w}^2 \right\rangle \right) dz + \frac{1}{2} \left\langle \left(z_s - \langle z_s \rangle \right)^2 \right\rangle \tag{2.17}
$$

$$
S_{xy} = \int_{z_b}^{\langle z_s \rangle} \left\langle \rho \tilde{u} \tilde{v} \right\rangle dz \tag{2.18}
$$

After elimination of the pressure gradient term (independent variable) by combining equations (2.16) and (2.15) (see Appendix E), the momentum equation can be rewritten into an equation with only the velocity components as independent variables:

$$
\begin{aligned}
&\frac{\partial}{\partial z} \left(\nu_t \frac{\partial u_p}{\partial z} \right) + \frac{\tau_{bpx}}{\rho h} + \frac{\partial}{\partial z} \left(\nu_t \frac{\partial u_s}{\partial z} \right) + \frac{\tau_{bsx}}{\rho h} + f_c v_s = \\
&\frac{W_x}{\rho h} + \frac{\partial}{\partial x} \left(\left\langle \tilde{u}^2 \right\rangle - \left\langle \tilde{w}^2 \right\rangle \right) - \frac{1}{\rho h} \frac{\partial S_{xx}}{\partial x} + \frac{\partial}{\partial y} \left(\left\langle \tilde{u} \tilde{v} \right\rangle \right) - \frac{1}{\rho h} \frac{\partial S_{xy}}{\partial y} \\
&+ \left(f_p - 1 \right) \left(\frac{\partial \overline{u}}{\partial t} - f_c \overline{v} \right) + \left(f_p^2 - \overline{f}_p^2 \right) \left(\overline{u} \frac{\partial \overline{u}}{\partial x} + \overline{v} \frac{\partial \overline{u}}{\partial y} \right)
\end{aligned}
\tag{2.19}
$$

This equation (2.19) is used to derive de secondary flow equations described in section 2.3.5.

2.3.4 Depth-averaged flow field (primary currents)

To derive the depth-averaged momentum equations, all terms concerning the secondary flow are left out of consideration (i.e. all terms with subscript s). Applying this in equation (2.16), the depth-averaged momentum equation for the x-direction becomes:

$$\frac{\partial \overline{u}}{\partial t} + \overline{f}_p^2 \left(\overline{u}\frac{\partial \overline{u}}{\partial x} + \overline{v}\frac{\partial \overline{u}}{\partial y} \right) - f_c \overline{v} = -\frac{1}{\rho}\frac{\partial p'_n}{\partial x} + \frac{1}{h}\frac{\partial}{\partial x}\left(\overline{\nu}_t h \frac{\partial \overline{u}}{\partial x} \right) + \frac{1}{h}\frac{\partial}{\partial y}\left(\overline{\nu}_t h \frac{\partial \overline{u}}{\partial y} \right) - \frac{C_\tau \overline{v}_t}{h^2}\overline{u} + \frac{F_x}{\rho h} + \frac{W_x}{\rho h} \qquad (2.20)$$

In here $p_n^{'}$ is an approximation of the total hydrostatic pressure, the (dimensionless) constant C_τ which establishes the relation between the primary bottom shear stress and the depth-averaged velocity, and F_x denotes the x-component of the depth-averaged wave-induced force per unit area.

Together with the corresponding equation in the y-direction:

$$\frac{\partial \overline{v}}{\partial t} + \overline{f}_p^2 \left(\overline{u}\frac{\partial \overline{v}}{\partial x} + \overline{v}\frac{\partial \overline{v}}{\partial y} \right) + f_c \overline{u} = -\frac{1}{\rho}\frac{\partial p'_n}{\partial y} + \frac{1}{h}\frac{\partial}{\partial x}\left(\overline{\nu}_t h \frac{\partial \overline{v}}{\partial x} \right) + \frac{1}{h}\frac{\partial}{\partial y}\left(\overline{\nu}_t h \frac{\partial \overline{v}}{\partial y} \right) - \frac{C_\tau \overline{v}_t}{h^2}\overline{v} + \frac{F_y}{\rho h} + \frac{W_y}{\rho h} \qquad (2.21)$$

And the depth-averaged continuity equation:

$$\frac{\partial h}{\partial t} + \frac{\partial (\overline{u}h)}{\partial x} + \frac{\partial (\overline{v}h)}{\partial y} = 0 \qquad (2.22)$$

This combination of equations forms the well-known depth-averaged (2DH) shallow water equations.

2.3.5 Vertical velocity distribution (secondary currents)

The secondary currents are defined as the vertical distribution of the flow. To derive the momentum equation for the secondary currents, the primary currents are left out of consideration in equation (2.19). The primary current is defined such, that:

$$\frac{\partial}{\partial z}\left(\nu_t \frac{\partial u_p}{\partial z} \right) + \frac{\tau_{bpx}}{\rho h} = 0 \qquad (2.23)$$

This implies that it is driven by the depth-invariant part of the forces. Subtract this part from equation (2.19) gives the momentum equation in x-direction for the secondary flow:

$$\begin{aligned}
&\frac{\partial}{\partial z}\left(\nu_t \frac{\partial u_s}{\partial z}\right) + \frac{\tau_{bsx}}{\rho h} + f_c v_s = \underbrace{\frac{W_x}{\rho h}}_{1} \\
&\underbrace{+\frac{\partial}{\partial x}\left(\left\langle \tilde{u}^2 \right\rangle - \left\langle \tilde{w}^2 \right\rangle\right) - \frac{1}{\rho h}\frac{\partial S_{xx}}{\partial x} + \frac{\partial}{\partial y}\left(\left\langle \tilde{u}\tilde{v} \right\rangle\right) - \frac{1}{\rho h}\frac{\partial S_{xy}}{\partial y}}_{2} \\
&\underbrace{+\left(f_p - 1\right)\left(\frac{\partial \overline{u}}{\partial t} - f_c \overline{v}\right)}_{3} + \underbrace{\left(f_p^2 - \overline{f}_p^2\right)\left(\overline{u}\frac{\partial \overline{u}}{\partial x} + \overline{v}\frac{\partial \overline{u}}{\partial y}\right)}_{4}
\end{aligned} \tag{2.24}$$

According to this equation (2.24), the secondary flow is described by four terms namely:

1 The wind shear stress at the water surface, which gives rise to a current velocity with a vertical distribution that deviates from the primary current distribution and, if the coriolis-effect is important, even to a velocity direction that varies along the vertical (Ekman, 1905); in the present concept, the deviations from the fictitious velocity obtained by multiplying the depth-averaged wind-induced current velocity with the primary velocity distribution function f_p are considered as secondary flow;

2 The vertical non uniformity of the wave-induced forces, related to the mass flux above the wave through level and the return flow or undertow below this level (Stive and Wind, 1986);

3 The vertical non-uniformity of the main flow acceleration, in time and due to coriolis effect;

4 The vertical non uniformity of the advective accelerations of the main flow, including the curvature-induced secondary flow (Boussinesq, 1868), but also the deformation of the current profile due to downstream accelerations (de Vriend, 1977).

2.3.6 Simplified secondary currents

To describe the vertical velocity distribution, the vertical is divided into three layers (Figure 2.9), according to de Vriend and Stive (1987):

- the surface layer (wave crest till wave trough);
- the middle layer (top bottom boundary layer, till wave trough level);
- and the bottom boundary layer (bottom till top wave boundary layer).

The *surface layer* is bounded by the moving free surface, which makes a continuum description of the water motion here particularly difficult. On the other hand, this description, itself, is not of primary interest to the present model, if only the effects of

the top layer on the layers below can be identified. Svendsen (1985) and Stive and de Wind (1986) suggested considering only the area below wave trough level and account for the surface layer via:

- An effective shear stress at the trough level to compensate the momentum decay in the top layer
- the condition that the net mean flow in the middle layer balances the mass flux at the top layer

By only considering wave-induced currents the x-momentum equation for the middle layer becomes:

$$\begin{aligned}&\frac{\partial}{\partial z}\left(\nu_t \frac{\partial u_s}{\partial z}\right)-\frac{\tau_{tsx}-\tau_{bsx}}{\rho\left(z_t-z_b\right)}+f_c\left(v_s-\overline{v}_{s,r}\right)=\frac{\partial}{\partial x}\left(\left\langle\tilde{u}^2\right\rangle-\left\langle\tilde{w}^2\right\rangle\right)\\&-\frac{1}{z_t-z_b}\int_{z_b}^{z_t}\frac{\partial}{\partial x}\left(\left\langle\tilde{u}^2\right\rangle-\left\langle\tilde{w}^2\right\rangle\right)dz+\frac{\partial}{\partial y}\left(\left\langle\tilde{u}\tilde{v}\right\rangle\right)-\frac{1}{z_t-z_b}\int_{z_b}^{z_t}\frac{\partial}{\partial y}\left(\left\langle\tilde{u}\tilde{v}\right\rangle\right)dz\end{aligned} \tag{2.25}$$

In the case of an irrotational wave field on a horizontal bottom, the right hand part of this equation is equal to zero. In a practical situation, with random waves, breaking and non-breaking, in combination with a turbulent net current on uneven bottom topography, this is not exactly the case. Still the right-hand side of equation (2.25) is assumed to be negligibly small for the non-breaking fraction of the waves (Craik, 1982). Stive and Wind (1986) show that the effective stress terms in equation (2.25), as far as they are due to breaking waves, are hardly varying with z. This means, that for the breaking fraction of the waves, the right-hand part of equation (2.25) can be assumed zero.

The velocity in the bottom boundary layer due to non-breaking waves is assumed to be similar to Longuet-Higgins (1953).

The coriolis-term in equation (2.25) and its y-equivalent are usually small compared to the other terms. Their principal effect is a tendency of the velocity vector to rotate with z (Ekman, 1905). In general this effect is negligible (e.g. Neuman and Pierson, 1966):

$$h \ll \left(\frac{2\overline{\nu}_t}{f_c}\right)^{1/2} \tag{2.26}$$

Especially in the relatively shallow breaker zone, this will mostly be the case. Then the reduced version of the equation (for the middle layer) becomes:

$$\frac{\partial}{\partial z}\left(\nu_t \frac{\partial u_s}{\partial z}\right)=\frac{\tau_{tsx}-\tau_{bsx}}{\rho\left(z_t-z_b\right)} \tag{2.27}$$

This reduced momentum equation is the starting point of the 1DV model which computes the velocity distribution (section 2.4).

2.4 Description of the mean velocity distribution (Q3D model)

The Q3D model is based on the concepts described by Reniers et al (2004). This model solves the momentum equations for secondary currents (equation (2.27)). In this section the model is described. Only variables which are computed in the Q3D module are discussed. Other values like wave characteristics are assumed to be known (e.g. from a wave model like SWAN) and are not derived in this study.

2.4.1 Vertical layers

Stive and de Vriend (1987) divided the water column in three layers (section 2.3.6):

- the surface layer (wave crest till wave trough);
- the middle layer (top bottom boundary layer, till wave trough level);
- and the bottom boundary layer (bottom till top wave boundary layer).

The *middle layer* is defined as the layer from the top of the wave boundary layer till the trough level (Figure 2.9). For simplicity, the non-dimensional vertical coordinates σ are used which are positive upwards from the bed.

$$\sigma = \frac{z}{h} \tag{2.28}$$

In here h is the mean water depth and z the vertical position positive upwards from the bed level. Sigma is defined such a way, that it equals one at the surface level (mean water level) and zero at the bottom.

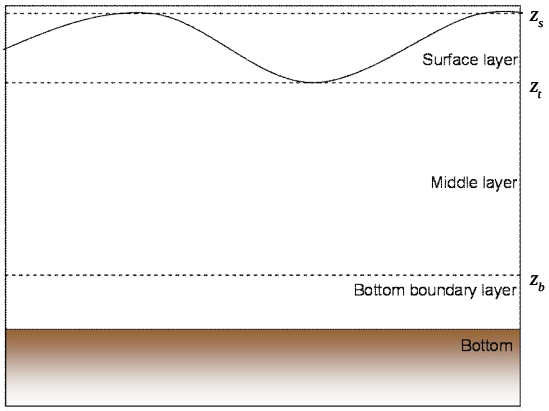

Figure 2.9 Definition of the vertical layers

The *bottom boundary* layer (Figure 2.9) represents the transition layer between the bed and the layer of 'normal' oscillating flow. The thickness of this layer depends on the roughness of the bed and the orbital excursion of the waves. The larger the waves, the larger the orbital excursion, A, and the larger the thickness of the bottom boundary layer. An increase of the roughness height k_s also results in an increase of the bottom boundary layer thickness. A smooth bottom produces less friction, and less turbulence, so the wave boundary layer remains small.

The non-dimensional thickness δ of the bottom boundary layer is given by (Fredsoe and Deigaard, 1992):

$$\delta = 0.09 f_\delta \left(\frac{A}{k_s} \right)^{0.82} \frac{k_s}{h} \tag{2.29}$$

With a minimum and maximum of:

$$\begin{aligned} \delta_{\max} &= 0.5 \\ \delta_{\min} &= f_\delta \frac{ez_0}{h} \end{aligned} \tag{2.30}$$

In here the multiplication factor f_δ represents the increase of the thickness of the bottom boundary layer for irregular waves as compared to regular waves. For monochromatic waves this factor equals one. The zero velocity level z_0 for a hydraulically rough bottom depends on the bed roughness height k_s and is given by:

$$z_0 = \frac{k_s}{33} \tag{2.31}$$

For both the middle and the wave boundary layer the momentum equation needs to be solved to get the vertical distribution of the mean flow. This is described in the next section.

2.4.2 Momentum equation (secondary currents)

The rewritten horizontal momentum equation for secondary currents (equation (2.27)) becomes:

$$\frac{\partial \tau_i}{\partial \sigma} = F_i \qquad \sigma > \delta \quad \text{(middle layer)} \tag{2.32}$$

$$\frac{\partial \tau_i}{\partial \sigma} = F_i + \frac{\partial}{\partial \sigma}\left(\rho \widetilde{u_i} \widetilde{w} \right) \qquad \sigma < \delta \quad \text{(bottom boundary layer)} \tag{2.33}$$

Where the subscript i denotes either the cross-shore direction x or the longshore direction y.

The assumption that the forcing F_i is dominated by a pressure gradient and that the depth-variation of F_i can be neglected is made.

In the bottom boundary layer, an additional forcing is added due to the dissipation of short wave energy caused by bottom friction (streaming).

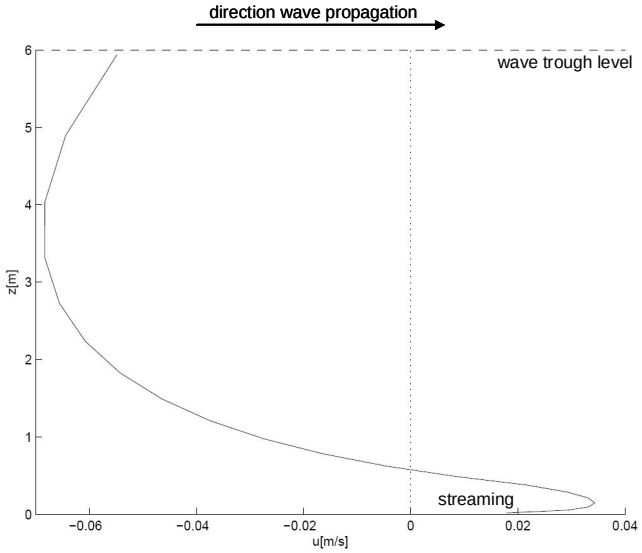

Figure 2.10 Cross-shore velocity profile including streaming

Streaming is defined as a wave-induced current in the direction of wave propagation in the wave boundary layer (Figure 2.10). This is modelled as a time-averaged shear stress which results from the fact that the horizontal and vertical orbital velocities are not exactly 90° out of phase. It is based on the wave bottom dissipation and is assumed to be zero at the bed and reaches linearly an asymptotic value at the top of the wave boundary layer (Fredsoe and Deigaard,1992).

$$\frac{\partial}{\partial\sigma}\left(\rho\widetilde{u_i}\widetilde{w}\right) = -\frac{1}{\delta}\frac{D_f k_i}{\omega} \tag{2.34}$$

In which k is the wave number, ω the wave frequency and the dissipation due to bottom friction D_f is given by:

$$D_f = \frac{1}{2\sqrt{\pi}}\rho f_w u_{orb}^3 \tag{2.35}$$

In here u_{orb} is the wave orbital velocity, and f_w the friction coefficient which is computed by (Soulsby, 1994):

$$f_w = 1.39\left(\frac{A}{z_0}\right)^{0.53} \tag{2.36}$$

To compute the shear stress distribution along the vertical, equation (2.32) and (2.33) needs to be integrated along the sigma-axis. With the assumption of the depth invariant forcing, integration from the surface downwards yields:

$$\tau_i = \tau_{t,i} - F_i\left(1-\sigma\right) \qquad \sigma < \delta \tag{2.37}$$

$$\tau_i = \tau_{t,i} - F_i\left(1-\sigma\right) + \frac{D_f k_i}{\omega}\frac{\left(\delta-\sigma\right)}{\delta} \qquad \sigma > \delta \tag{2.38}$$

In here $\tau_{t,i}$ represents the shear stress at the trough level, which accounts for wave breaking and wind (section 2.4.3).
The shear stress τ_i is related to the velocity gradient through the eddy viscosity:

$$\tau_i = \frac{\rho \nu_t}{h} \frac{\partial u_i}{\partial \sigma} \tag{2.39}$$

To solve these equations (2.37), (2.38) and (2.39), the surface shear stress, the distribution of the eddy viscosity, and the forcing needs to be known. This is described in the next paragraphs.

2.4.3 Surface layer effective shear stress

The effective shear stress at the top of the middle layer (trough level) has to be computed before you can solve equation (2.37) and (2.38). At the trough level the effective shear stress consists of the two components:

- The wind shear stress
- The wave-induced shear stress (momentum decay of surface layer due to wave breaking)

The wind-induced shear stress in the wind direction ($\tau_{s,wind}$) is calculated according to the following equation (Delft3D manual)

$$\left|\vec{\tau}_{s,wind}\right| = \rho_a C_d U_{10}^2 \tag{2.40}$$

In which ρ_a id the air density, C_d the wind drag coefficient (depending on U_{10}) and U_{10} the wind speed at 10 meter above the free surface.

The wave-induced shear stress ($\tau_{s,wave}$), in the wave propagation direction (Deigaard, 1993) becomes:

$$\tau_{s,wave} = \frac{D_r k_i}{\omega} = \frac{D_r}{c} \tag{2.41}$$

In which D_r is the dissipation of roller energy (Appendix B) And c the wave propagation speed. This wave induced shear stress can be seen as an additional term, caused by wave breaking in the surface layer.

The total effective shear stress at the top of the middle layer is the summation of these two shear stress components:

$$\tau_{t,i} = \tau_{s,wind} + \tau_{s,wave} \tag{2.42}$$

2.4.4 Eddy viscosity distribution

As described in section 2.4.2 the shear stress τ_i is related to the velocity gradient through the eddy viscosity.

The eddy viscosity represents the coefficient for vertical diffusion of horizontal momentum. The turbulence fluctuations tend to smooth the gradient analogous to a diffusion process. The higher the eddy viscosity, the more diffusion of momentum and the more gentle the vertical shear of the velocity profile. It can be regarded as a measure that indicates how 'easily' a certain horizontally moving package of water can move through the water column.

To solve the eddy viscosity distribution an eddy viscosity model (in this case a zero equation turbulence model) is used. The vertical distribution of the eddy viscosity for both the middle and bottom boundary layer is written as a product of a parabolic shape function and a scale factor ϕ_s (middle layer) and ϕ_b (bottom boundary layer).The scale factor may vary with time and location along the profile.

$$\nu_t = \phi_s \bar{\nu}_t \sigma \left(\sigma_s - \sigma\right) \qquad \sigma > \delta \qquad (2.43)$$

$$\nu_t = \left(\phi_s \bar{\nu}_t + \phi_b \bar{\nu}_{tb}\right)\left(\sigma_b - \sigma\right)\sigma \qquad \sigma < \delta \qquad (2.44)$$

In here $\bar{\nu}_t$ is the depth-averaged eddy viscosity and σ_s and σ_b is the upper limit at which the eddy viscosity is zero for respectively the middle layer and the bottom boundary layer (Figure 2.11). In absence of wave breaking and wind, this upper limit of the middle layer equals one. This means that the turbulence at the surface level is zero because no additional turbulence is induced. Both the shape and the scale factor are described in (Appendix C).

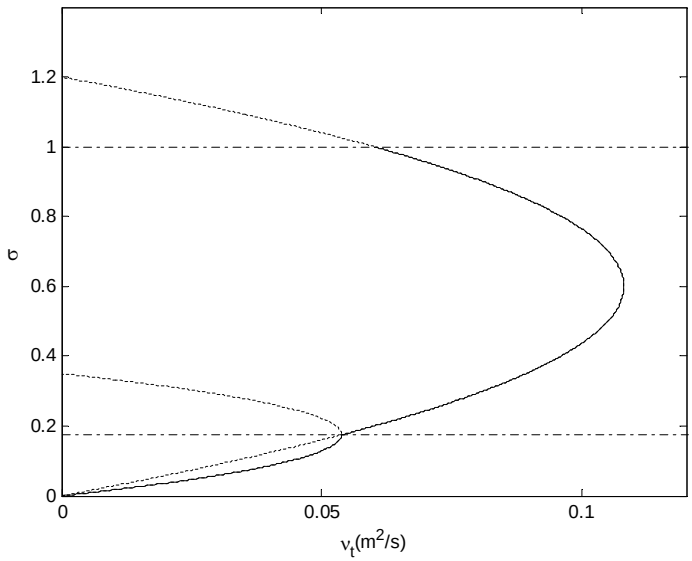

Figure 2.11 Definition of sigma parameters

Depth-averaged eddy viscosity

The depth-averaged turbulent viscosity accounts for three terms:

- flow generated turbulence,
- wind-induced turbulence,
- wave-induced turbulence.

For purely slope-driven stationary currents, the eddy viscosity distribution becomes parabolic, with zero turbulence at the surface and at the bottom. The flow generated depth-averaged eddy viscosity becomes:

$$\bar{\nu}_{t,current} = \frac{1}{6}\kappa h\sqrt{gh|s|} \tag{2.45}$$

In here s is the gradient of the water level $\sqrt{\left(\frac{dh}{dx}\right)^2 + \left(\frac{dh}{dy}\right)^2}$ and κ the von Kármáns constant which is usually set to $\kappa = 0.41$.

The wave-induced depth-averaged eddy viscosity depends on the root-mean-square wave height and the amount of dissipation of roller energy (Battjes, 1975). The more roller dissipation takes place, the more turbulence is generated.

$$\bar{\nu}_{t,wave} = f_v H_{rms}\left(\frac{D_r}{\rho}\right)^{\frac{1}{3}} \tag{2.46}$$

In which D_r is the amount of roller dissipation, H_{rms} the root-mean-square wave height, and f_v the calibration coefficient which increases the turbulent eddy viscosity account for roller energy dissipation.

The amount of wind-induced turbulence depends on the wind induced shear stress. Higher wind speed leads to a higher shear stress value at the water level. Due to this more turbulence is generated in the upper layer. The depth-averaged wind induced turbulence:

$$\bar{\nu}_{t,wind} = \frac{1}{3}\kappa h\sqrt{\frac{|\tau_{s,wind}|}{\rho}} \tag{2.47}$$

In which the wind-induced shear stress at the water level $\tau_{s,wind}$ is computed with equation (2.40).

The total depth-averaged eddy viscosity is calculated in the following way (Stive and de Vriend, 1987):

$$\bar{\nu}_t = \sqrt{\bar{\nu}^2_{t,current} + \bar{\nu}^2_{t,wind} + \bar{\nu}^2_{t,breaking}} \tag{2.48}$$

The depth-averaged eddy viscosity for the wave boundary layer is obtained by including additional bed friction induced turbulence.

$$\bar{\nu}_{tb} = \frac{c_f^2 u_{orb}^2}{\omega} \qquad \text{with} \qquad c_f = \frac{f_w}{2} \tag{2.49}$$

The orbital velocity is based on the root mean square wave height.

2.4.5 Velocity distribution

The velocity gradient can be calculated by combining equations (2.37) and (2.38) with (2.39) and becomes for the middle layer:

$$\frac{\partial u_i}{\partial \sigma} = \frac{h}{\rho \phi_s \bar{\nu}_t}\left(\frac{\tau_{t,i} - F_i(1-\sigma)}{\sigma(\sigma_s - \sigma)}\right) \tag{2.50}$$

And for the bottom boundary layer:

$$\frac{\partial u_i}{\partial \sigma} = \frac{h}{\rho\left(\phi_s \bar{\nu}_t + \phi_b \bar{\nu}_{tb}\right)} \cdot \left(\frac{\left(\tau_{t,i} - F_i + \frac{D_f k_i}{\omega}\right) + \left(F_i - \frac{D_f k_i}{\omega}\right)\sigma}{\sigma(\sigma_b - \sigma)}\right) \tag{2.51}$$

Vertical integration of both equations yields the vertical distribution of the velocity. For the wave boundary layer a no slip condition at the bed ($u = 0$) is utilized, whereas the velocity at the top of the wave boundary layer is needed for the middle layer. After integration and simplification the velocity distribution becomes:

$$u_i = u_{\delta,i} + A\left(\frac{B_i}{\sigma_s}\ln\frac{\sigma}{\delta} - \left(\frac{B_i}{\sigma_s} + C_i\right)\ln\frac{\sigma_s - \sigma}{\sigma_s - \delta}\right) \qquad \sigma > \delta \tag{2.52}$$

$$u_i = A_b\left(\frac{B_{b,i}}{\sigma_b}\ln\frac{\sigma}{\sigma_0} - \left(\frac{B_{b,i}}{\sigma_b} + C_{b,i}\right)\ln\frac{\sigma_b - \sigma}{\sigma_b - \sigma_0}\right) \qquad \sigma < \delta \tag{2.53}$$

In here the coefficients A, B and C are described in Appendix C. Integrating once more results in a direct relationship between the depth-mean velocity, the depth independent forcing, the known surface stress and known streaming term

$$\bar{u}_i = \underbrace{\left(H_b + H - G_b - G\right)F_i}_{\text{depth independent forcing}} + \underbrace{\left(G_b + G\right)\tau_{s,i}}_{\text{surface shear stress}} + \underbrace{\left(G_b - \frac{H_b}{\delta}\right)\left(\frac{D_f k_i}{\omega}\right)}_{\text{streaming}} \tag{2.54}$$

The coefficients G, G_b, H and H_b are described in Appendix C.

2.5 Sediment transport

The sediment transport is determined with access to a variety of semi-empirical formulae and a depth integrated advection-diffusion solver for suspended sediment. The transport computation is based on time-dependent current fields.

For depth-averaged applications the 3D advection-diffusion equation is approximated by the depth-integrated advection-diffusion equation (Gallappatti, 1983) equation (2.55). The depth-averaged concentrations $\overline{c}$ are computed by dividing the total sediment transport by the depth-averaged velocity and the depth.

$$\frac{\partial h\overline{c}}{\partial t}+u\frac{-\partial h\overline{c}}{\partial x}+v\frac{-\partial h\overline{c}}{\partial y}-D_H\frac{\partial^2 h\overline{c}}{\partial x^2}-D_H\frac{\partial^2 h\overline{c}}{\partial y^2}=\frac{\overline{c}_{eq}-\overline{c}}{T_s} \qquad (2.55)$$

In here h is the water depth, $\overline{u}$ and $\overline{v}$ are the depth-averaged velocities in x- and y-direction, D_H is the horizontal dispersion coefficient, $\overline{c}$ is the depth-averaged sediment concentration, $\overline{c}_{eq}$ the depth-averaged equilibrium sediment concentration and T_s is an adaptation time-scale.

2.6 Morphology

The bed level changes due to gradients in the sediment transport fields. The determination of bed evolution is based on the conservation of sediment mass. Bed level changes due to bed-load are computed by:

$$\frac{\partial hc}{\partial t}+\left(1-\varepsilon_{por}\right)\frac{\partial z_a}{\partial t}+\left(\frac{\partial S_x}{\partial x}+\frac{\partial S_y}{\partial y}\right)=0 \qquad (2.56)$$

In which z_a is the bed level, S_x and S_y the sediment transport in x- and y-directions and ε_{por} the bed porosity.

2.7 Implementation of the Q3D model into Delft3D

To solve this set of equations, numerical two-dimensional depth-averaged (2DH) and full three-dimensional (3D) morphological models are used. Delft3D provides different modules which computes e.g. the hydrodynamics (Delft3D-Flow), the wave field (Delft3D-Wave).

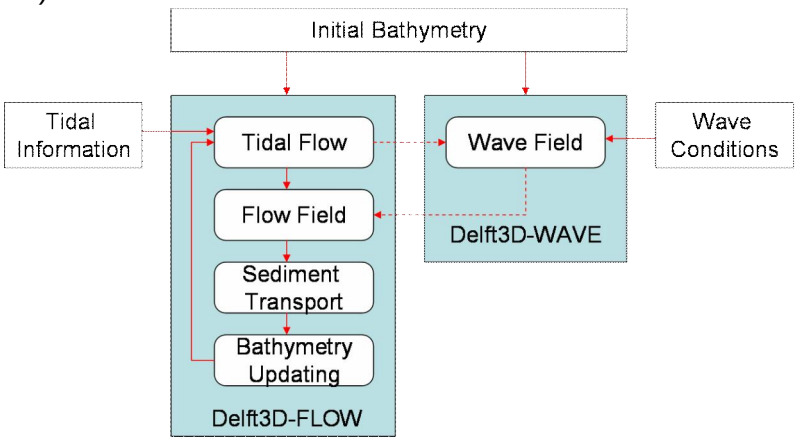

Figure 2.12 Computational procedure Delft3D model [Sun 2004]

Before calculating the morphological changes, the wave field is computed with a wave model (e.g. SWAN). With this wave field and the tidal information the flow field is computed. This flow field induces sediment transport, which finally results in bed level changes (Figure 2.12). This cycle is done for each time step.

2.7.1 Hydrodynamic implementation (secondary currents)

The computation of the vertical velocity profile is added to the two-dimensional depth-averaged module of Delft3D-FLOW (Figure 2.13). After the computation of the depth-averaged flow field, the vertical distribution of the mean current is computed with the use of the Q3D method described in section 2.4.

It is important to notice that only the vertical velocity distribution is changed by the Q3D model. The forcing is calculated according the 2DH method. The bed shear stress formulations are not coupled.

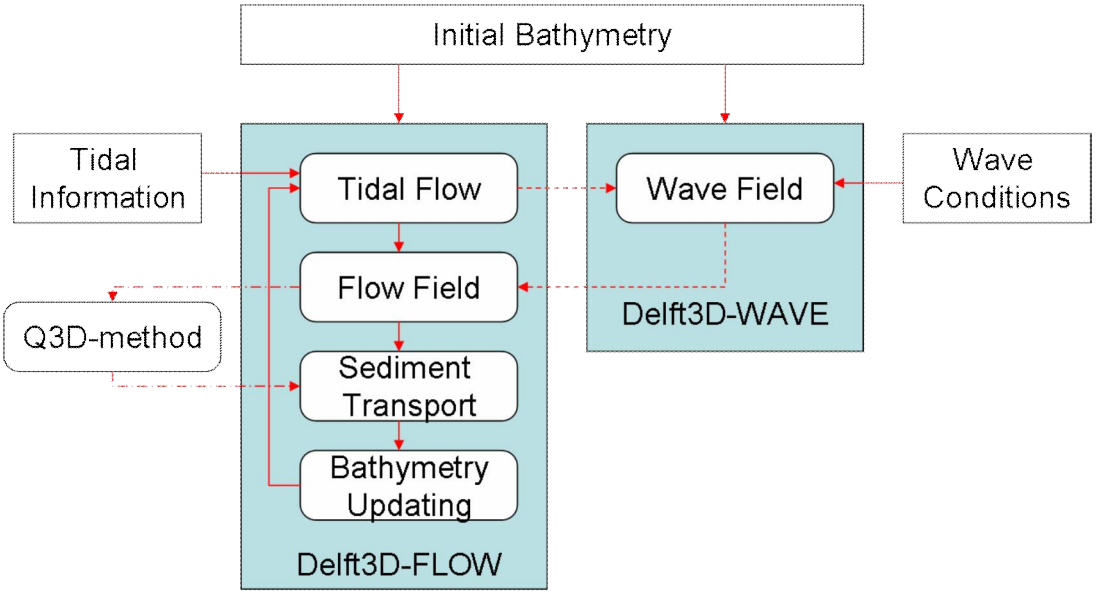

Figure 2.13 Computational procedure Delft3D with implemented Q3D mode

The Q3D routine, computes the viscosity and velocity distribution at each grid point. The vertical is divided into 20 sigma-layers (Figure 2.14). The thickness of these layers is based on the distribution used for 2DH sediment computations. Because more accuracy is required in the lower region of the water column (sediment transport mainly takes place in this region) the accuracy of the layers is increased.

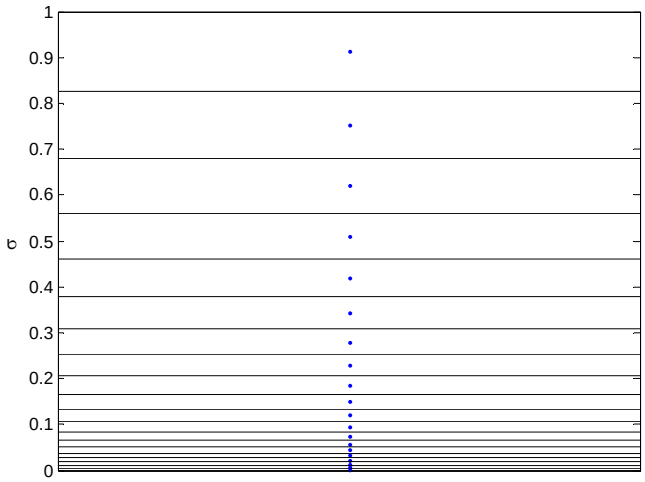

Figure 2.14 Vertical sigma-layer distribution

To solve the vertical distribution an iterative procedure is adopted in which the double vertical integration of equation (2.54) has to equal the depth-averaged velocity computed with the 2DH model in both longshore and cross-shore directions.

2.7.2 Sediment transport and morphology implementation

The Q3D method is applied for the Van Rijn 2004 transport formulations. With the new computed reference height (consistent with the 3D computations) and the velocity at that level, the reference concentration is calculated.

Instead of using the logarithmic velocity distribution in case of 2DH modelling, the Q3D velocity distribution is used to compute the sediment transport:

$$\int_{z=a}^{z=z_t} u_{q3d}(z)c_{q3d}(z)dz = S_{q3d} \qquad (2.57)$$

In which the Q3D velocity u_{q3d} times the Q3D concentration rates c_{q3d} is integrated from the Van Rijn reference height a till the wave trough level z_t.

Suspended load transport is computed by solving the depth-integrated advection-diffusion equation. This means that a reference concentration is needed. The computed Q3D transport is divided by the depth-averaged velocity and the depth to obtain the Q3D reference concentration for suspended load computations (equation (2.58)).

$$\frac{S_{q3d}}{\overline{u}h} = c_{rep,q3d} \qquad (2.58)$$

Bed load transport is computed with the Q3D velocity and concentration at the Van Rijn reference height.

In short the only differences compared with 2DH are the reference concentration and the bed-load transports. All the other values are 2DH values and are not influenced by the Q3D implementation.

2.7.3 Assumptions and restrictions of the Q3D model

When implementing a new approach, assumptions have to be made. This leads to restrictions of the model. Restrictions can be divided into conceptual and implementation restrictions. These two are described in this section.

Conceptual restrictions

- As the suspended sediment transports are calculated by using a depth-averaged advection-diffusion equation in which the depth-averaged velocities have to be applied to ensure mass conservation it is imperative that the difference between the depth-integrated suspended Q3D and 2DH transports is accounted for in the concentration. This implies that diffusion processes might be affected. However it is thought that in coastal environments this is does not influence the results.

- Wave-induced streaming is not included yet in the model.

- Density currents are not included in the Q3D model.

Implementation restrictions

In contradiction with the conceptual restrictions, the restrictions of the model caused by implementation are easily to solve. The main implementation restrictions are shortly described in this section.

- Bed shear stress formulations are not coupled. 2DH computed bed shear stress is used.

- The Q3D model can only be used in combination with the Van Rijn 2004 transport formula

- The bed-roughness predictor for the current-related and wave-related bed roughness parameters of Van Rijn needs to be used.

- At present the Q3D model can only be solved with the use of Eulerian velocities.

- Wind is not yet included in the model.

3 Validation of the Q3D approach

3.1 Introduction

The first step after the implementation phase is the validation of the Q3D model. Because of the complexity of morphological modelling, this validation process is divided into several parts. The main driving forces behind sediment transport are flow currents. Due to this phenomenon it is decided to first validate the hydrodynamics (Section 3.3). Subsequently, the sediment concentration profiles and sediment transports are considered in Section 3.4. Finally, in Section 3.5 the morphological changes are discussed.

3.2 Validation cases for the Q3D approach

Four different cases are used to validate the hydrodynamics, sediment transport and morphology of the Q3D approach. A short description of these validation cases are given in this section. For an extensive description and numerical parameters, one is referred to Appendix D.

LIP (Large Installation Plan) experiment (1993)

The LIP11D flume experiments were conducted in the 240 m long Delta flume of WL | Delft Hydraulics (Figure 3.1). Different wave conditions (erosive and accretive) were generated perpendicular to a barred beach and, meanwhile, wave height, water level, flow velocity profiles and concentration profiles were measured.

Figure 3.1 Delta Flume at Deltares(left) and measurements during Boers experiment (right) [Boers,1995]

Boers experiment (1995)

As a part of the Phd. research of Marien Boers, the LIP experiments were done on a smaller scale in the TU-Delft flume. Several detailed measurements were performed including wave height (Figure 3.1), water level, velocity profiles, concentration profiles, turbulence measurements and shear stresses. The main objective of these measurements was to obtain detailed data of turbulence in the surfzone.

Reniers experiment (1994)
Several measurements were performed in a large basin with a pump recirculation system to create spatially homogeneous longshore currents (Figure 3.2). Unidirectional oblique incident waves (regular and random) were used on barred and non-barred beaches to get information on wave transformation, set-up of the mean water level and the cross-shore distribution of wave-driven longshore current velocity.

Figure 3.2 Measurements during Reniers experiment (Reniers, 1994)

Egmond field case (1998)
As a part of the Coast3D program, several measurements were carried out near the coast of Egmond, The Netherlands (Figure 3.3). The coast of Egmond is characterised by an alongshore uniform beach with no obstacles. Two breaker bars are located parallel to the coast. Several measurements were performed and also detailed boundary conditions like wind field, deep water wave height and water levels were obtained.

Figure 3.3 Coast of Egmond (www.kustfoto.nl)

3.3 Hydrodynamic validation

3.3.1 Introduction
The hydrodynamic Delft3D-FLOW module computes the non-steady flow resulting from tidal and meteorological forcing (Appendix A).

In this section, the hydrodynamics of the Q3D approach is validated by comparing the wave height, water level, viscosity and velocity profiles with measurements and the results of the 2DH and 3D (Delft3D) models. This hydrodynamic validation process is divided in three parts. In the first part, the LIP and Boers experiments are used to validate the cross-shore hydrodynamics. Secondly, the combined longshore and cross-shore hydrodynamics is validated with the use of the Reniers experiment. Finally the field case of Egmond is used to validate the field model.

3.3.2 Cross-shore hydrodynamics
The flume experiments LIP11D-1b and Boers-1b were done for irregular waves approaching perpendicular to the coast (Figure 3.4), so only cross-shore circulation currents occurs. Stationary model results computed with the Q3D model are compared with the results computed with the profile model UNIBEST-TC (Appendix G), Delft3D

(3D and 2DH) and the results from measurements. Morphological changes are not taken into account yet; these will be discussed in Section 3.5.

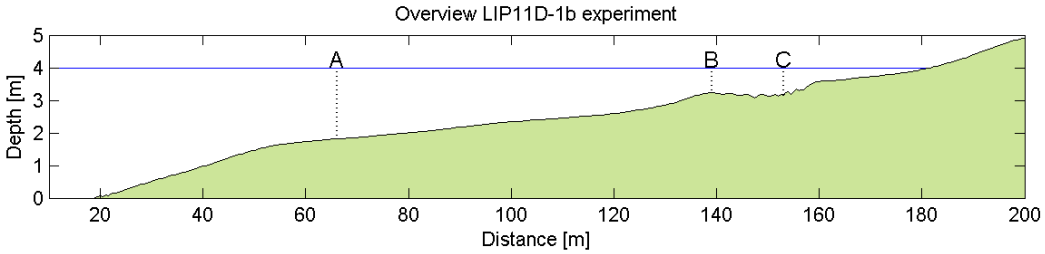

Figure 3.4 Initial bed level LIP11D-1b experiment including locations of vertical profiles

Model results

Wave height and water level

Concerning waves approaching perpendicular to the shore, wave breaking leads to a slight decrease of the mean water level outside the surf zone due to shoaling (Section 2.2.1). However, inside the surf zone it leads to a rise in the mean water level close to the shore (wave set-up). The measurements for the LIP experiment show a decrease in wave height when approaching the coast (Figure 3.5 and Figure F3.3.1). Around the bar (at x=140), wave breaking occurs, and the water level increases (Figure 3.5).

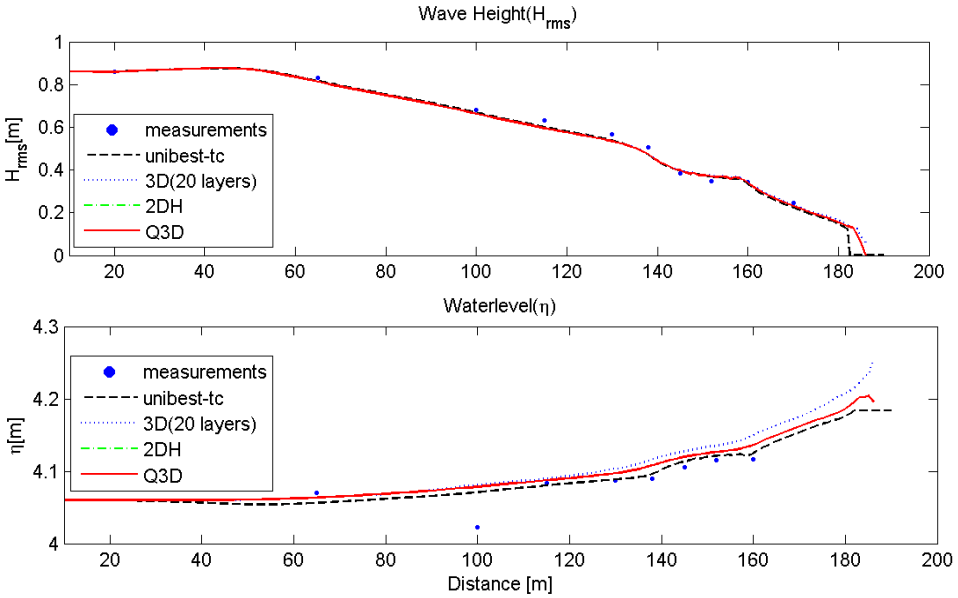

Figure 3.5 Wave height and water level 3D, 2DH and Q3D model results

Only small deviations between measured data and model results are observed. The different model approaches (2DH, 3D and Q3D) show almost no deviation for the wave heights results. The results of the water levels are slightly higher in case of the 3D model, compared to the 2DH/Q3D and UNIBEST-TC model results. This dissimilarity is mainly caused by the differences in bed shear stress between the 2DH and 3D model.

The implementation of the Q3D method only affects the vertical velocity distribution (secondary currents), the sediment transport rates and the resulted bed level changes.

This indicates when morphological changes are not taken into account the Q3D and 2DH results will be equal with respect to water level and wave height.

Depth-averaged velocity
Equal to the wave height and water level, the 2DH and Q3D results for the depth-averaged velocity are identical (Figure F3.3.1). 3D results show only a small difference (slightly lower depth-averaged velocities) with the 2DH/Q3D model results.

Viscosity profiles
Fully 3D computations are performed with the use of the k-ε turbulence closure model while the Q3D and UNIBEST-TC approaches computes the viscosity profile by a scale and parabolic shape function (Section 2.4.4).

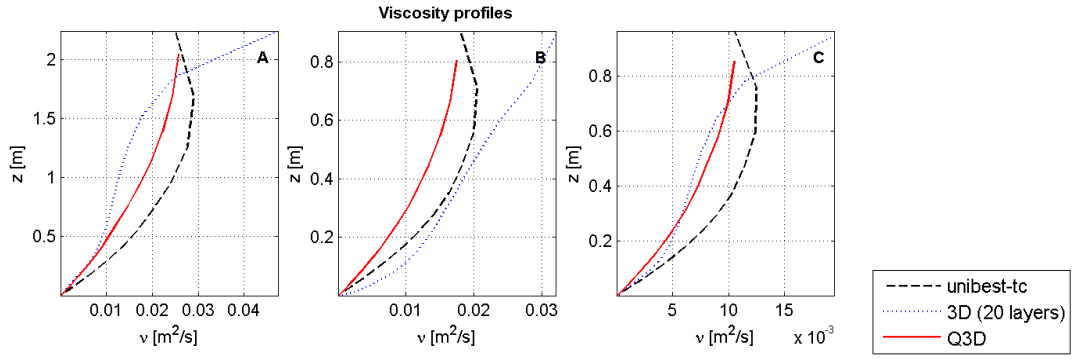

Figure 3.6 Viscosity profiles of 3D, Q3D and Unibest-TC model results.

The Q3D model results correspond very well with 3D model results (Figure 3.6 and Figure F3.3.2)). Especially the magnitude of the viscosity profiles is comparable. However, the shape of both profiles show differences. These differences can be prescribed to the aforementioned different turbulence closure models used to compute the viscosity profiles. The UNIBEST-TC and Q3D results show good correspondence in shape which is explainable by the fact that UNIBEST-TC uses the same computation procedure as the Q3D model (Appendix G and Section 2.4.4).

Velocity profiles
By means of the viscosity profiles the velocity distributions are computed.

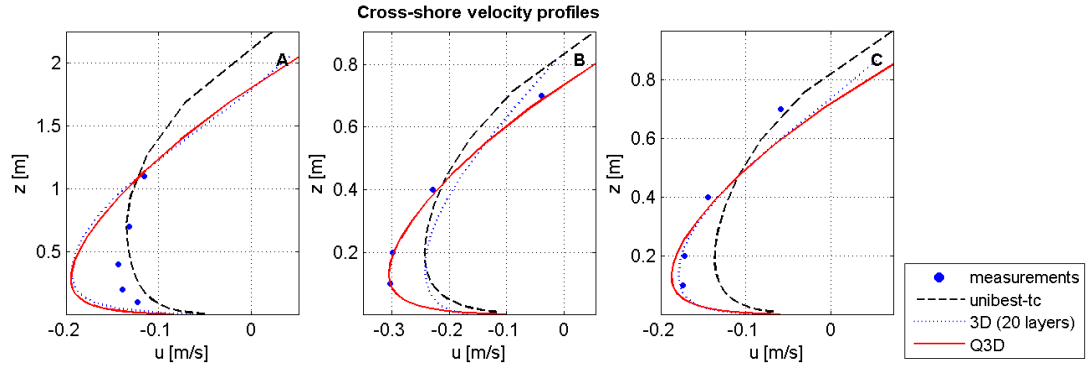

Figure 3.7 Velocity profiles of 3D, Q3D and Unibest-TC model results

The shape of the Q3D profiles show more vertical shear compared with UNIBEST-TC model results. The lower magnitudes of the viscosity lead to less momentum transport over the vertical and results in higher velocity gradients and thus more vertical shear.
Results of Q3D and 3D model correspond fairly well. Only in the region of the breaker bar (profile B in Figure 3.7), the Q3D results are over-predicted. This can be explained by the lower magnitude of viscosity of Q3D compared with 3D in this region. However, comparison with measured data shows a good fit of the model results for profile B and C.

Parameter sensitivity

Besides the comparison between the different models, the sensitivity of the most important calibration parameters is discussed. In the Q3D model two additional parameters are introduced (Section 2.4):

- The multiplication factor for the bottom layer thickness *facdel* (f_δ in equation (2.29)) and
- The multiplication factor for the wave-induced viscosity *fcvisc* (f_ν in equation (2.46))

In addition, roller dissipation is an important process for the vertical velocity distribution (section 2.4.3). Therefore, the sensitivity of two roller calibration parameters, the angle of the wave front and the breaker parameter are discussed. Finally, the sensitivity of the roughness height is investigated.

Bottom layer thickness (facdel)

The first additional parameter f_δ (*facdel*) represents a multiplication factor which increases the thickness of the bottom boundary layer caused by irregular waves (section 2.2.3). The amount of shear stress in this layer remains constant, only the thickness differs. If the thickness of the boundary layer is increased, the shear stress is distributed along a larger area. This results in lower viscosity values and therefore lower velocity gradients which, in its turn, increases the vertical shear of the velocity profile.

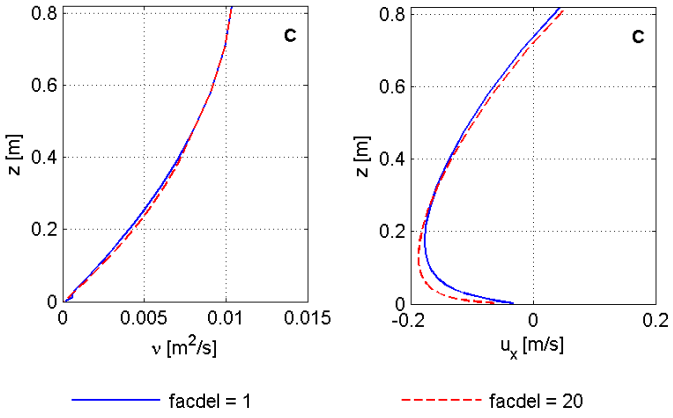

Figure 3.8 Sensitivity of parameter facdel on viscosity profile (left) and cross-shore velocity profile (right)

A decrease of the multiplication factor *facdel* leads directly to a decrease of the thickness of the wave boundary layer (Figure 3.8). The effects on the viscosity and velocity distributions though are almost negligible. A higher value of *facdel* seems to

shift the maximum of the velocity profile in downwards direction (Figure F3.3.3). More vertical shear due to decreased viscosity is generated in the lower region of the water column (bottom boundary layer). From these results, it can be concluded that the effect of changing the value of *facdel* does not lead to significant differences in the viscosity and velocity profiles.

Vertical viscosity (fcvisc)

The second additional parameter f_v (*fcvisc*) is a multiplication parameter to scale the viscosity distribution. By increasing *fcvisc*, the wave-induced turbulence increases (equation (2.46)). This leads to an increase of the total amount of eddy viscosity. As a result of the increased eddy viscosity profile, more momentum is transported in the vertical direction which decreases the gradient of the return flow profiles and results in more uniform velocity profiles (red line in Figure 3.9).

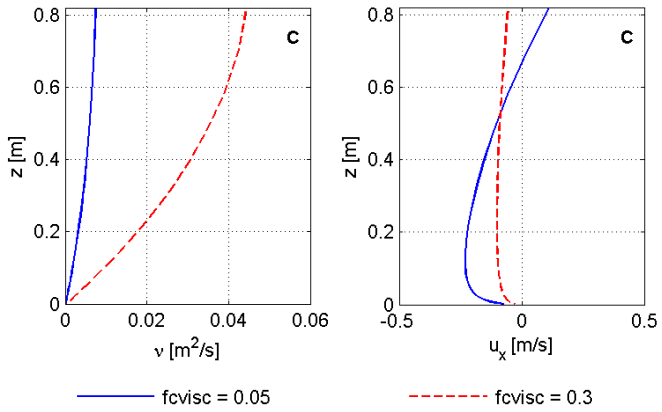

Figure 3.9 Sensitivity of parameter fcvisc on viscosity profile (left) and cross-shore velocity profile (right)

The model results (Figure 3.9 and Figure F3.3.4) for the viscosity distribution show a relatively large increase of turbulence when increasing the multiplication factor in every profile along the cross-section. The velocity profiles show the aforementioned decrease of the velocity gradient which results in more uniform velocity profiles, whereas low values of *fcvisc* show more vertical shear in the profile.

Regarding the measurements, the velocity profiles located offshore of the breaker bar are vertically more uniform distributed, because no wave breaking occurs. In other words, the velocity is more evenly distributed along the vertical whereas in the area close to the breaker bar, more vertical shear is observed due to wave breaking. From these observations it can be concluded that a lower value of *fcvisc* is necessary in the vicinity of the breaker bar whereas the other areas require a higher value. A value of 0.1 is used as default. This multiplication factor can be considered as a very important calibration parameter, since it directly affects the vertical velocity distribution whereas the forcing remains unchanged.

Besides the two new introduced parameters, *fcvisc* and *facdel*, a number of other parameters also have a direct influence on the vertical velocity profiles. Roller dissipation is an important process in the computation of the vertical velocity distribution. It is applied to calculate the wave-induced shear stress and the wave-induced depth-averaged eddy viscosity (Section 2.4.3 and 2.4.4). Increasing the amount of roller dissipation leads to a higher forcing and higher viscosity. Roller energy

dissipation is determined by the roller model (Appendix B) and depends mainly on the values of *betaro* and *gamdis*, which are described below.

Angle of roller front (betaro)
Betaro is a parameter used in the roller model and represents the angle of the front of the roller relative to the waterline (Figure 3.10). Increasing this angle, the roller energy is stored shorter in the roller and as a result the energy is transported faster into turbulence.

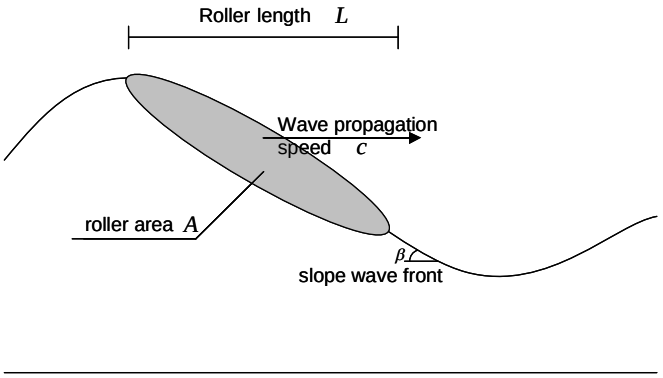

Figure 3.10 Definition sketch of parameters used in the roller model

An increase of the angle *betaro* leads to an increase in the roller energy dissipation. When the angle is increased, the wave energy dissipation is shifted in the onshore direction (Figure 3.11). In addition this result in a wave set-up level also moved in the onshore direction. By lower values of *betaro* wave energy is transferred faster into turbulence. More wave-induced turbulence is generated near the shore for lower values of *betaro*, which leads to an increase of the total viscosity.

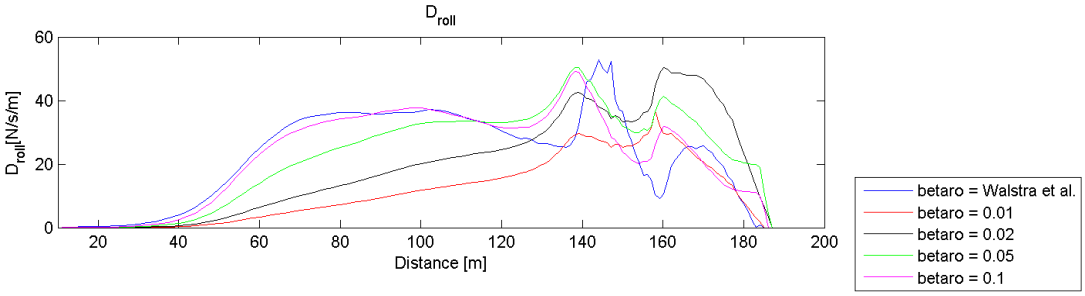

Figure 3.11 Q3D model results of dissipation of roller energy for different values of angle of wave front (betaro)

Model results (Figure F3.3.5) show an increase in cross-shore velocities by a decrease of the wave front angle for the onshore located (profile B and C in Figure F3.3.5) velocity profiles. The offshore located velocity profiles shows a decrease of maximum velocities and a more uniform profile for lower values of *betaro*. This can be explained by the decrease of roller dissipation in the offshore region. The value of *betaro* ranges from 0.01 till 0.1. It is also possible to use an optimized value of *betaro* [-1] (Walstra et al, 1996).

Breaker parameter (gamdis)

The amount of roller dissipation depends also on the wave breaking (Figure 3.12). The point of wave breaking is determined by the breaker parameter, which is the ratio between the wave height and the water depth (section 2.2.1). By increasing the wave breaker parameter, waves break in shallower waters which results in an increase of turbulence in the nearshore region. Besides a constant ratio, two formulations which compute the breaker parameter are available. The first one defined by Battjes and Stive (1985) and the second one by Ruessink et al. (2003) (Section 2.2.1).

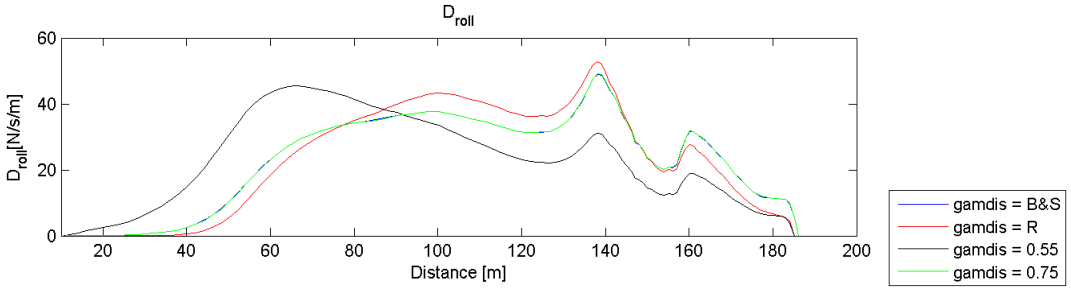

Figure 3.12 Q3D model results dissipation of roller energy for different values of the breaker parameter (gamdis)

Model results (Figure F3.3.6) show that the cross-shore velocity profiles are sensitive to changes in the breaker parameter. Higher values of *gamdis* lead to higher values of roller dissipation in the onshore region, because waves break in shallower areas. This results in an increase of viscosity at the onshore located profiles and a decrease in viscosity at offshore located profiles.

Roughness height (ks)

Changing the Nikuradse roughness coefficient (*ks*) does not only affect the forcing, it has also a direct influence on the vertical viscosity and velocity distributions. Increasing the roughness height leads to an increase of the bottom boundary layer (section 2.4.1) and the amount of turbulence induced by bottom friction (section 2.4.4). As mentioned before a higher viscosity leads to lower gradients in the velocity profiles, and therefore in more uniform velocity profiles. With increasing roughness height, the amount of turbulence (eddy viscosity) in the bottom boundary layer is increased. This result, in its turn, in somewhat more uniform velocity profiles in the lower regions of the water column. To compensate for the decreased velocity in the bottom boundary layer, the velocities in the middle layer become higher. Overall, the velocity profile for lower roughness heights becomes more uniform distributed over the vertical and results in lower maximum velocities (Figure 3.13 and Figure F3.3.7).

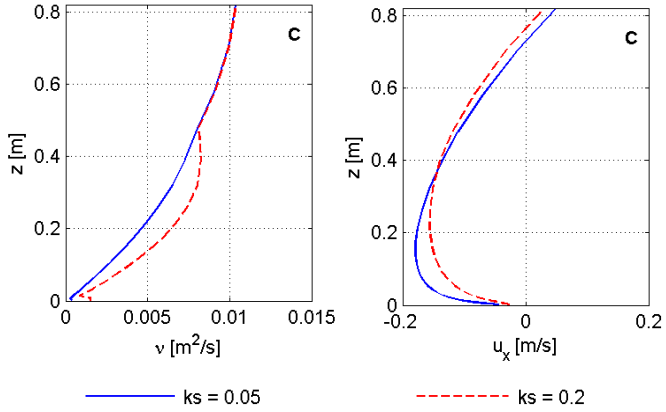

Figure 3.13 Sensitivity of parameter ks on viscosity profile (left) and cross-shore velocity profile (right)

The roughness can be considered as an important calibration parameter for the velocity profiles in shape.

Conclusions

Comparison between Q3D and 3D model results shows high agreement. Only in the vicinity of the breaker bar, the Q3D velocities are higher compared with 3D velocity profiles. This can be attributed to the differences in viscosities computed with Q3D and 3D models. The roughness height (*ks)* and multiplication parameter for wave-induced turbulence (*fcvisc*) both have a significant influence on the vertical distribution of the cross-shore flow profiles. The model does not seem very sensitive to changes in the wave boundary multiplication factor *facdel*.

3.3.3 Longshore hydrodynamics (including cross-shore)

After validation of the cross-shore hydrodynamics, the combined cross-shore and longshore hydrodynamics have been validated. The Reniers-experiments were conducted with irregular waves approaching a barred beach (Figure 3.14) with an oblique wave angle (Appendix D). Due to this angle, cross-shore and longshore currents occur. Comparisons are made similar to the LIP and Boers cases described in the previous section.

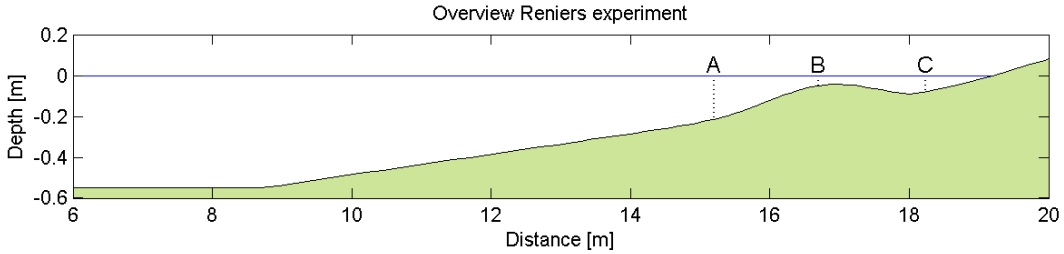

Figure 3.14 Initial bed level Reniers experiment including locations of vertical profiles

Model results

Wave height and water level

Measurements show a strong decay in wave height (Figure F3.3.8) around the breaker bar (x=16), which means that almost all wave energy is dissipated in this region. The wave heights of the three different approaches show high agreement. The Q3D and 2DH model show again exactly the same results. Differences with the 3D model are also insignificantly small.

Model results show significant differences in water levels in relation to measurements. These are not observed using the default version of Delft3D, and can be ascribed by differences of the wave breaking formulation. This is not within the scope of this study, and therefore the comparison with the measurements is not discussed.

The water level in the case of the 3D model is higher nearshore compared to the Q3D model. This is in line with the results from the LIP and Boers cases and can be attributed to the difference in the bottom shear stress between the 3D and 2DH/Q3D approach.

Depth-averaged velocity

The depth-averaged velocities in cross-shore direction show good agreement between the 3D and Q3D model results (Figure F3.3.8). However, regarding the longshore currents, a significant difference is observed. The longshore velocities in case of the full 3D model are lower compared to the Q3D/2DH model results and measurements (Figure 3.15).

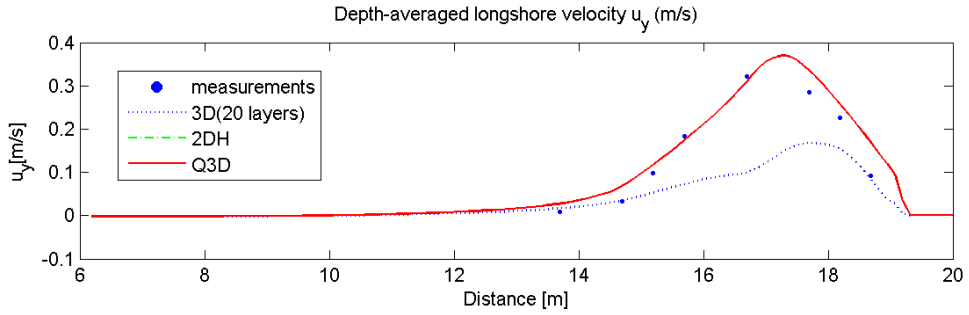

Figure 3.15 Model results depth-averaged longshore velocity Reniers experiment

This difference can be ascribed to the difference in bottom shear stress and the modelling of the undertow in the 3D model. The undertow leads to a higher offshore component of the cross-shore currents. This results in lower values of the longshore current. These differences have already been observed at Deltares and are investigated at this moment. These differences in longshore currents between 2DH and 3D model are not in the scope of this study and are therefore not discussed further on.

Viscosity profiles

The Q3D results concerning viscosity profiles show high agreement in relation to the 3D profiles. Especially the magnitude is again similar for the two different approaches (Figure F3.3.9). This is consistent with results from the two previous cases LIP and Boers which also showed similarity in magnitude.

Velocity profiles

Due to the fact that the magnitude of the viscosity profiles are more or less equal for the Q3D and 3D model results, velocity profiles show good agreement in the cross-shore direction. Especially after wave breaking the results are both in shape and in magnitude comparable. The offshore velocity profiles (Figure F3.3.9, profile A) show differences in the higher region of the water column. This is caused by the Stokes drift, which induces a bend in the 3D cross-shore velocity profiles. Longshore currents are generated by shear stress induced by oblique incident waves. These currents are not dominated by wave breaking, so the shape of these longshore velocity profiles is more or less logarithmic.

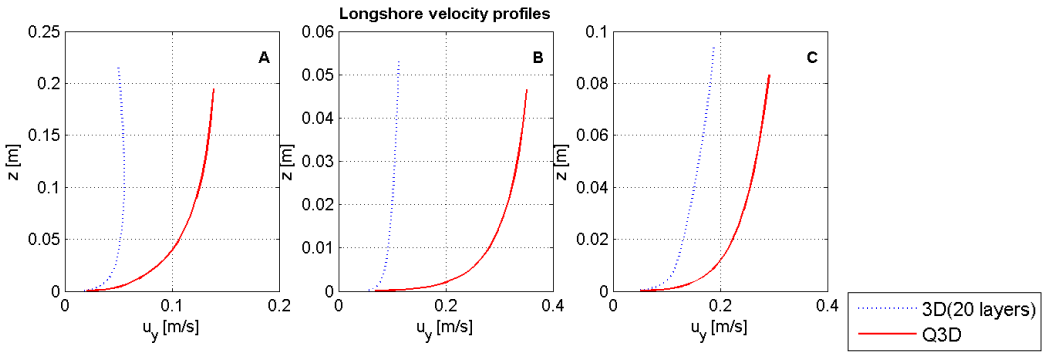

Figure 3.16 Model results for longshore velocity profiles

Due to the fact that the longshore depth-averaged velocities for the 3D model are much lower than those computed with the 2DH (and Q3D) results, the magnitude of the 3D velocity profiles are also lower (Figure 3.16). However, the Q3D results show in longshore direction almost the same logarithmic velocity profiles as computed with the full 3D approach, just the magnitude differs.

Parameter sensitivity

Bottom layer thickness (facdel)

The LIP and Boers experiments showed very minor influence of the multiplication factor on the velocity profiles. Considering combined cross-shore and longshore currents a similar sensitivity of *facdel* is expected. This can indeed be observed in model results (Figure 3.17). Increasing the thickness of the bottom boundary layer has almost no influence on the velocity profiles in both cross-shore and longshore direction (Figure F3.3.10).

Similar with the cross-shore velocity profiles, an increase of *facdel* leads to an increase in vertical shear in the lower region of the water column (bottom boundary layer) for the longshore velocity profiles.

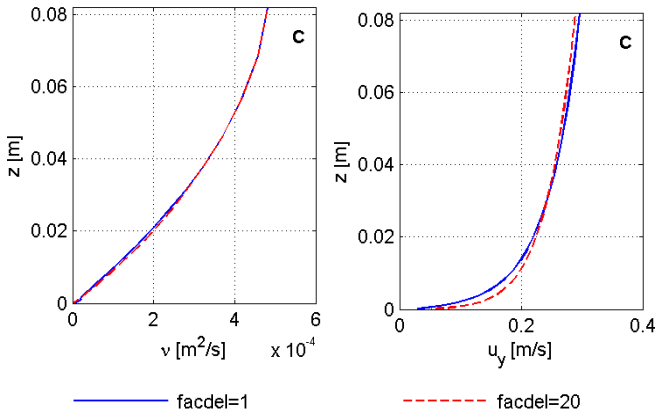

Figure 3.17 Sensitivity of parameter facdel on viscosity profile (left) and longshore velocity profile (right)

Vertical viscosity (fcvisc)

Instead of cross-shore velocity profiles, the shape of the longshore velocity profiles is not dominated by wave breaking. Therefore an increase in the wave breaking induced turbulence does not significantly affect the longshore velocity profiles (Figure 3.18). An increase of *fcvisc* leads to a more uniform longshore velocity profile.

The effects of variation of the *fcvisc*-value on the cross-shore velocity profiles are comparable with LIP and Boers model results (Figure F3.3.11). It results in more uniform distributed velocity profile as *fcvisc* increases, whereas the vertical shear increases in the case of lower values.

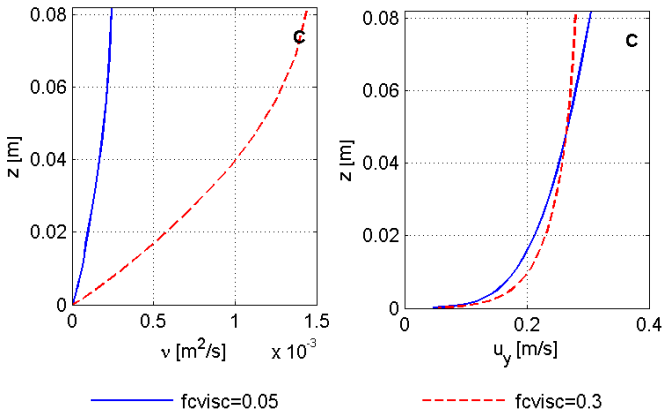

Figure 3.18 Sensitivity of parameter fcvisc on viscosity profile (left) and longshore velocity profile (right)

Angle of roller front (betaro)

On both the longshore and the cross-shore velocity profiles variation of *betaro* has a significant influence (Figure F3.3.12). Changing the value of *betaro* has a direct influence on the amount of roller energy dissipation and therefore not only the magnitude of the cross-shore velocity profile is changed (because the depth-averaged velocity has increased/decreased) but the shape of the profile transforms as well. The longshore velocity profiles only vary in magnitude.

Breaker Parameter (gamdis)

Model results show again the same influence of varying the breaker parameter on the cross-shore profiles as observed at LIP and Boers. When varying *gamdis* both the magnitude and the vertical shear of the profiles are changed (Figure F3.3.13). In the case of the longshore current profiles, only the magnitude is changed. The shape of the profiles remains more or less logarithmic.

Roughness height (ks)

Consistent with the results of the two previous models, an increase of the bed roughness height leads to more uniform cross-shore velocity profiles (Figure F3.3.14). Although, the longshore velocity profiles seems to become more uniform by decreasing the value of *ks* (Figure 3.19). The velocity profiles become more uniform as values of the roughness height decreases.

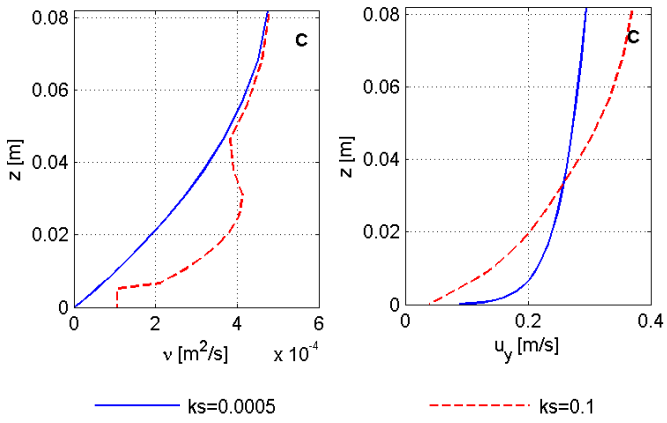

Figure 3.19 Sensitivity of parameter ks on viscosity profile (left) and longshore velocity profile (right)

Conclusions

Model results show consistent results with the two previous validation cases (LIP and Boers) with respect to the cross-shore viscosity and velocity profiles. The Q3D longshore velocity profiles show the same logarithmic shaped distribution as the 3D profiles. The influence of the different calibration parameters is less significant on the longhore profiles. While *fcvisc* influences the cross-shore velocity profiles significantly, the longshore velocity profiles do not seem to be affected by varying this multiplication factor. In both the cross-shore and longshore direction, *facdel* has no significant influence on the velocity distribution as well. Increasing the amount of roller dissipation (by increasing *betaro* or *gamdis*) only influences the magnitude of the longshore velocity profiles. Finally changing the roughness height influences both the cross-shore and the longshore velocity profiles.

3.3.4 Hydrodynamics Egmond field case

After the validation of the combined cross-shore and longshore currents for a profile model, the hydrodynamics of a more complex situation is done. A field model combined with varying waves, tides and currents is performed. The Egmond model is performed in combination with the Delft3D-WAVE module. Also here, bed level changes are not yet taken into account.

Model results

Several measurements were carried out in the Egmond area. The observation locations 18a, 1a, 1b, 1c and 1d were chosen to compare the Q3D model results with both measurements and 3D model results (Figure F3.3.15). These observations points (Figure 3.20) are respectively located just in front of the outer breaker bar (18a) and around the inner breaker bar (1a-1d).

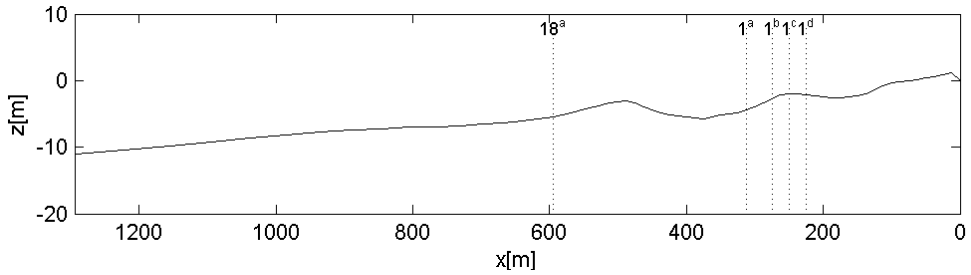

Figure 3.20 Depth along cross-section (N = 35) Egmond model

Wave height and water level

The coast of Egmond is characterized by two breaker bars which are located parallel to the coast. Almost all the wave energy is dissipated at these two bars. Especially at low tide the influence of the offshore bar dominates the wave energy dissipation and the wave set-up becomes more important (Figure F3.3.16).

Comparison between 2DH and Q3D model results show again no differences with respect to the wave heights, water levels and depth-averaged velocities. The comparison between the Q3D and 3D model show, just like the previous validation cases almost no deviation for both the wave height and the water levels.

Depth-averaged flow patterns

During high tide the flow velocities show a uniform distribution of longshore velocities in both the 3D and the Q3D/2DH model. As a result of the high tide and the increased water levels, less wave breaking occurs on the two breaker bars. This means that the

currents are not dominated by wave breaking but by alongshore directed tide and wind forcing (Figure 3.21).

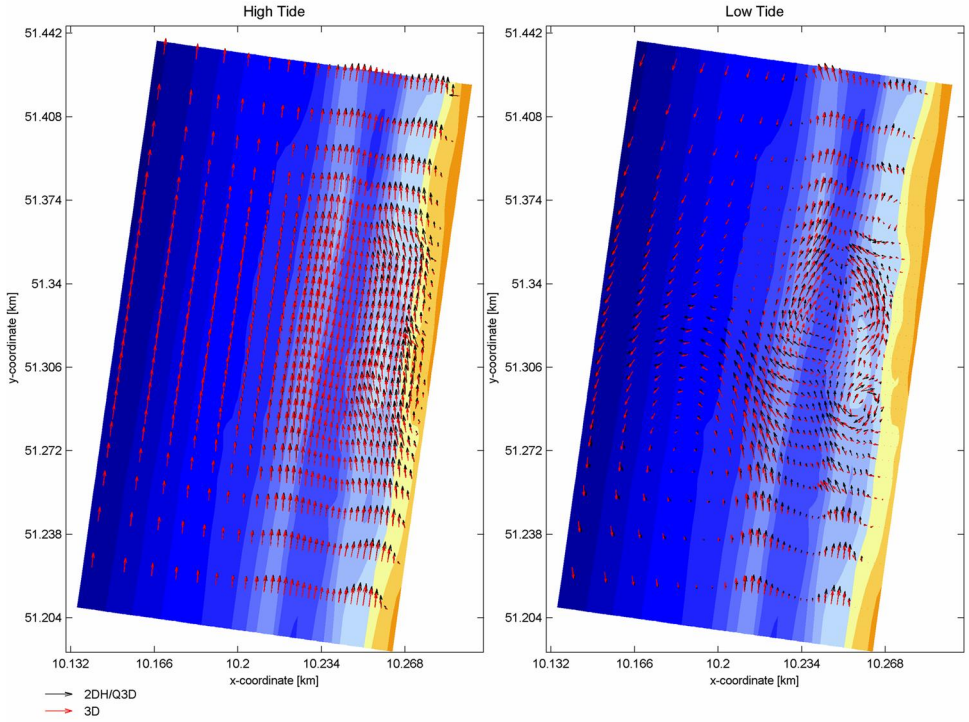

Figure 3.21 Flow patterns during high tide (left) and low tide (right) for 3D (red arrows) and Q3D (black arrows) model results

During low tide however, the water level is significant lower. Now waves start breaking on top of the breaker bars. Wave breaking and an increase in wave set-up allow rip-currents to develop at the tip of the breaker bar (Figure 3.21, large version Figure F3.3.17). Model results show small differences between 2DH and 3D flow patterns. During high tide 3D velocities are slightly lower compared to 2DH velocities. During low tide, both the direction and magnitude between 2DH and 3D models deviates.

Because the currents differ at each time step, the time series are compared at several locations. These points correspond with the locations where measurements were taken in 1998.

Longshore currents

The measured longshore velocities show tidal variation with peak flood velocities of approximately 0.4 m/s (toward north) and peak ebb velocities of approximately -0.3 m/s (south). Increased wave activity induces a reduction of the north going flood velocities, while ebb velocities increase up to -0.5 m/s as a result of increased wind and wave driven longshore currents. During high tide the currents are longshore dominated. The model results correspond very well with measurements (Figure 3.22).

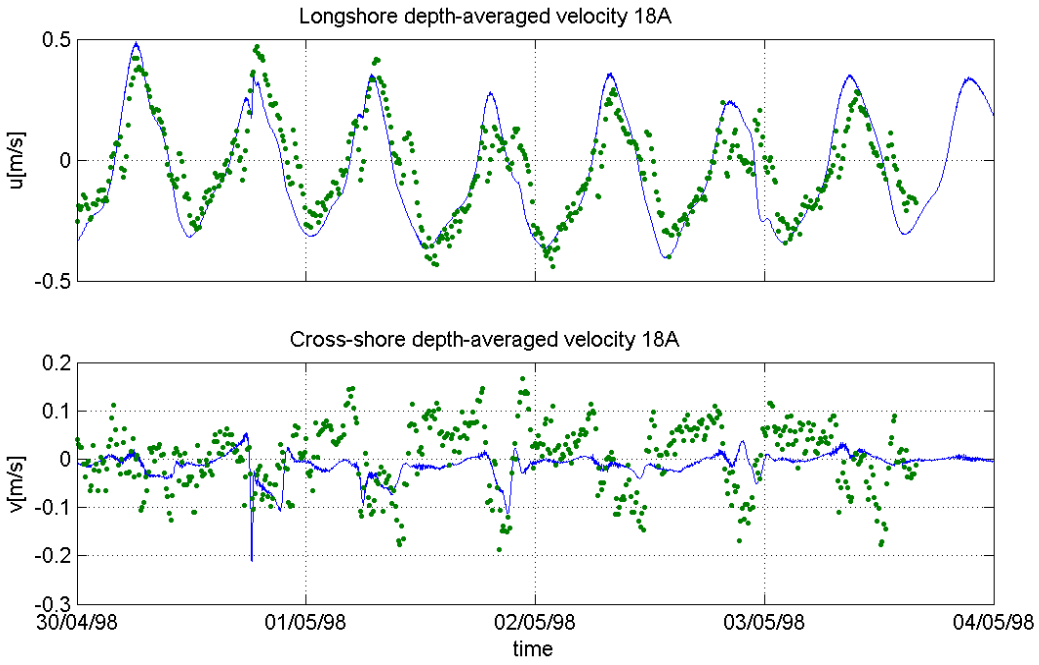

Figure 3.22 2DH model results (line) and measurements (dots) observation point 18a for depth-averaged longshore (upper) and cross-shore (lower) velocity

Cross-shore currents
Besides the longshore currents, also a comparison between the measured and different calculated cross-shore currents is made. The measurements (Figure 3.22) show a clear tidal variation with values between 0.05 m/s (onshore directed) and -0.30 m/s (offshore directed). During high tide, the cross-shore velocities are very low, 0.05 m/s while at low tide as more breaking occurs, the cross-shore current becomes more dominant and reaches a maximum of almost 0.3 m/s.

Viscosity profiles
At some characteristic time steps (high tide, low tide, maximum and minimum velocities), the vertical distribution of viscosity and velocity are compared at the observation points. Because no measured data is available for vertical velocity profiles: only a comparison in flow profiles between Q3D and 3D can be made.

The viscosity profiles of the Q3D and 3D model show at each time step high agreement at each profile along the cross-section. The viscosity profiles obtained with the k-ε model differs in shape, but the magnitude show high agreement with the profiles computed by the Q3D model (Figure 3.23 left and Figure F3.3.18).

Velocity profiles
The alongshore profiles show a logarithmic shaped profile for both the 3D and the Q3D model (Figure 3.23 and Figure F3.3.19). The magnitude of both models shows a small deviation. This is caused by the differences in depth-averaged velocities which are also higher for the 2DH model compared to the 3D model (Figure F3.3.16).

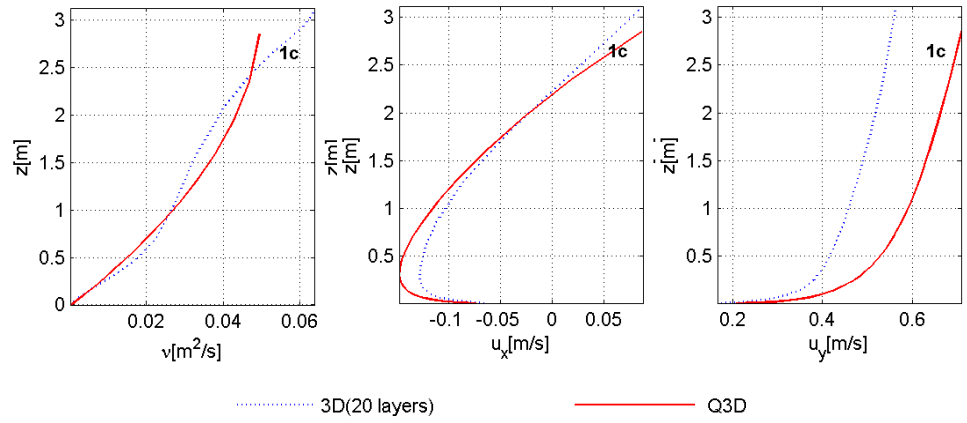

Figure 3.23 Viscosity profile (left), velocity profiles cross-shore (middle) and longshore (right) in observation point 1c during high tide

During high tide, the 3D and Q3D cross-shore profiles show a lot of similarity in both shape and magnitude. (Figure 3.23 and F3.3.20).

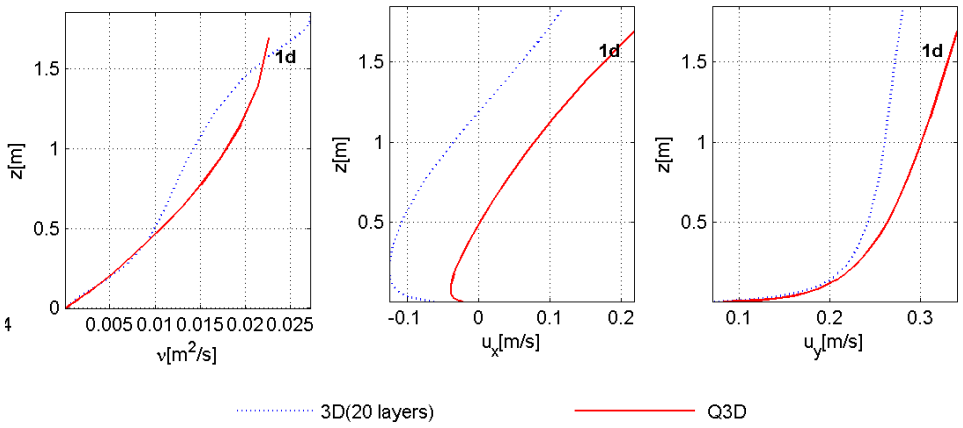

Figure 3.24 Viscosity profiles (left), velocity profiles cross-shore (middle) and longshore (right) in observation point 1d during low tide

During low tide the cross-shore currents increase due to the increased wave energy dissipation due to wave breaking. The longshore velocity profiles (Figure F3.3.23) show again similarity in shape and a small deviation in magnitude between the Q3D and 3D model results. The cross-shore velocity profiles (Figure F3.3.24) show again correspondence in shape, but in magnitude also some deviations occurs (Figure 3.24). These differences are mainly caused by the differences in depth-averaged velocities, caused by the differences in bed shear stresses between the different models (2DH and 3D).

Conclusions

Model results show high agreement in magnitude of the viscosity profiles between 3D and Q3D. The Q3D cross-shore velocity profiles show a high agreement in relation to the 3D cross-shore velocity profiles. Longshore velocity profiles show again similarity in shape. Due to the differences in depth-averaged velocities between the 3D and Q3D models, differences in magnitudes of the velocity profiles occur.

3.3.5 Conclusions hydrodynamics for all cases

Four different validation cases were performed to validate the hydrodynamics of the Q3D approach. Comparison between 3D and Q3D model results show overall high similarity in cross-shore velocity profiles. The longshore velocity profiles show good correspondence in shape (logarithmic) only the magnitude differs between 3D and Q3D. This difference can be ascribed to the differences in depth-averaged velocities.

The Q3D method introduced two additional parameter, *fcvisc* and *facdel*. Besides these two parameters, *betaro* and *gamdis* (roller model) and the roughness height *ks* are also important parameters for the velocity profiles. The sensitivity of these five different parameters is investigated. This sensitivity analysis showed that:

- The model is not very sensitive to changes in the multiplication factor for the bottom boundary layer thickness *facdel* for both the longshore and the cross-shore velocity profiles. Increase of *facdel* leads to a slight increase of vertical shear of both the longshore and the cross-shore velocity profiles.

- Model results show significant changes in the cross-shore velocity profiles by varying *fcvisc.* Increasing the value of *fcvisc* leads to an increase in viscosity and results in a more uniform cross-shore velocity profile. However, the longshore velocity profiles are not very sensitive in varying *fcvisc.*

- By increasing the value of *betaro* and increasing *gamdis*, the dissipation of roller energy is shifted in the onshore direction. The cross-shore velocity profiles changes both in magnitude and vertical shear, while the longshore profiles only changes in magnitude.

- The roughness height *ks* influences both the longshore and the cross-shore velocity profiles. It not only increases the boundary layer thickness, but also the magnitude of viscosity. Lower values of the roughness height *ks* result in more uniform velocity profiles.

3.4 Sediment concentrations and transport validation

3.4.1 Introduction

The previous section described the hydrodynamics (i.e. velocity profiles) of the model. This section will focus on the sediment concentration profiles and the resulting sediment transports. Sediment transport can be defined as the total amount of transport integrated from bed to surface. This can be calculated by multiplying the velocity profiles with the concentration profiles.

Delft3D gives the opportunity to choose between different transport formulae. In this study the Van Rijn 2004 formulation is used (Appendix A). In this approach bed-load and suspended load transport are computed separately.

To validate the Q3D model, the same validation cases as the previous section (Section 3.3) are used. First only cross-shore transport for the LIP and Boers cases are considered. Subsequently the combined cross-shore and alongshore sediment transport are discussed with the use of the Reniers case. The Egmond field case is used to validate a prototype field model. Finally the conclusions with respect to the sediment transport are drawn for this section.

3.4.2 Cross-shore sediment transport

To calibrate the cross-shore transport of the Q3D model, two validation cases are performed: the LIP and the Boers experiment. The previous section described the hydrodynamics of these two cases. In this section the resulting sediment concentration and sediment transport rates are discussed.

Model results

Sediment concentration

The *near-bed reference concentration* is defined as the sediment concentration at the Van Rijn reference height (Appendix A). Q3D model results show a significant larger reference concentration in the breaker zone compared to 2DH and 3D results (Figure 3.25). This is caused by the increased velocity at the reference height.

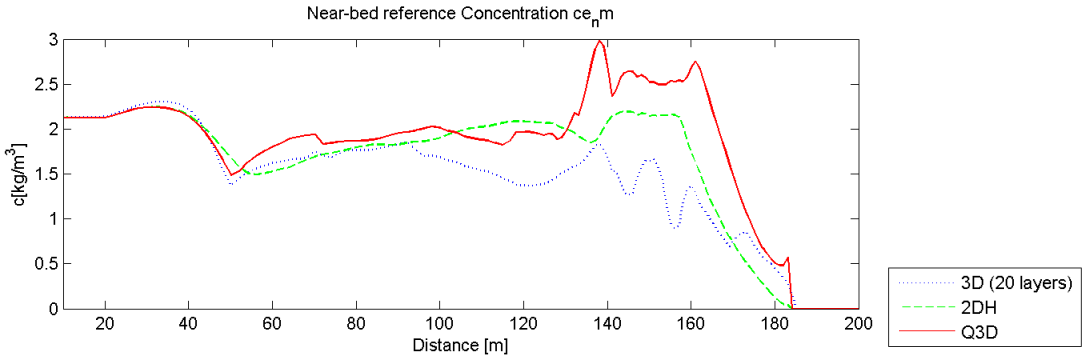

Figure 3.25 Near-bed reference concentration LIP11D experiment for 3D (blue), 2DH (green) and Q3D (red) model results.

The depth-integrated concentration profiles (e.g. equilibrium concentration) are directly related with the near-bed reference concentrations and are used in the advection-diffusion solver (Gallappatti). Therefore the depth-integrated concentration is only

relevant for 2DH and Q3D computations. Model results show a higher equilibrium concentration for the Q3D model compared to the 2DH model (Figure 3.26).

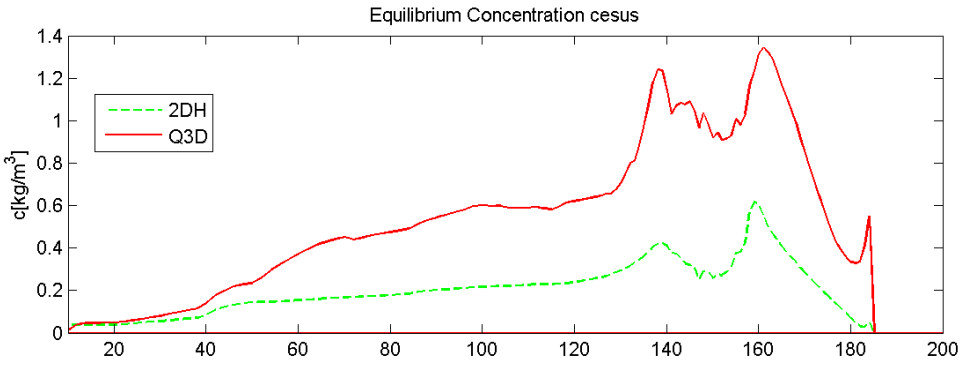

Figure 3.26 Depth-integrated concentration for Q3D(red) and 2DH(green) model results

The offshore located concentration profiles for both 3D and Q3D model results corresponds very well, both in shape and magnitude. This is expected when looking at the reference concentration and the velocity profiles offshore. In onshore direction the deviation between 3D and Q3D model results increases.

Sediment transport

Sediment transport is divided into bed load and suspended load transport. As described in Appendix A, b*ed Load Transport* is divided in three components. Both the suspended and the bed load transport due to waves show similarity between the three models (Figure F3.4.1).

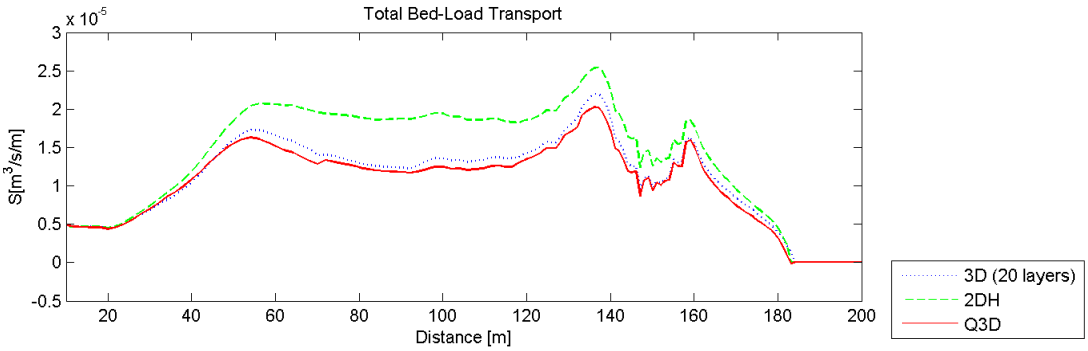

Figure 3.27 Total Bed-Load Transport model 3D (blue), 2DH (green) and Q3D (red) model results

Besides the magnitude, also the direction of the three different components of bed load differs. The bed load transport due to currents is directed in offshore direction, while the wave-induced components are onshore directed. The waves create an onshore directed mass-flux, which is also observed in the area under the wave trough. To compensate for this shore directed mass-flux (and reach equilibrium) a return flow current is offshore directed. This is seen in the current induced transport. Q3D and 3D model results shows high agreement in total bed load transport rates (Figure 3.27).

The suspended sediment transport rates consist of the sediment transport induced by currents. When not taking streaming into account, these currents are offshore directed (undertow). This induces an offshore directed sediment transport. Suspended load

transport is computed by solving the advection diffusion equation. In case of Q3D and 2DH computations the Gallappatti method is used (Section 2.5).

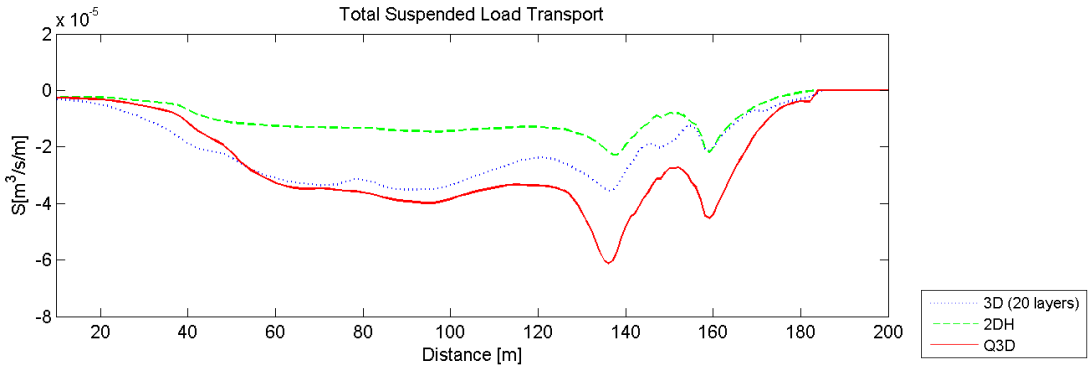

Figure 3.28 Model results suspended load transport. 3D (blue), Q3D (red) and 2DH (green)

Q3D model results show a significant increase in suspended load transport compared to 2DH model results. In the vicinity of the breaker bar, the Q3D model shows even higher suspended transport rates compared to the 3D model (Figure 3.28). As seen in the hydrodynamic validation, the velocity profiles around the breaker bar are also higher for Q3D compared to 3D model results. This results in higher concentration profiles, and finally higher suspended sediment transport rates.

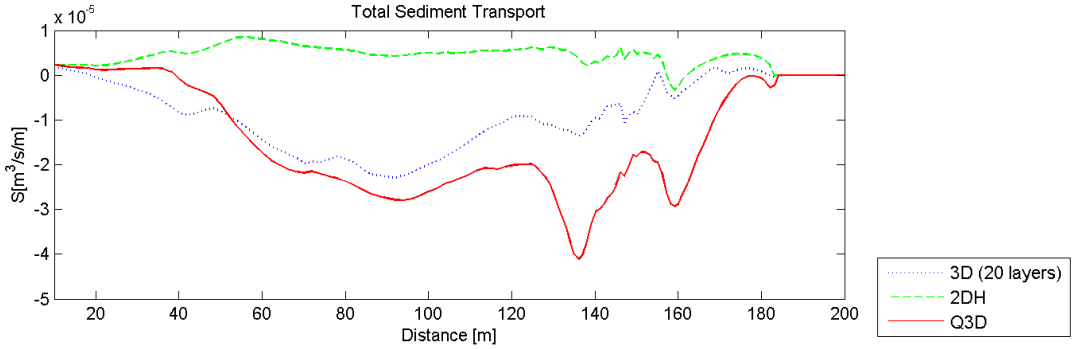

Figure 3.29 Total Sediment Transport model results. 3D (blue), Q3D (red) and 2DH (green)

Summation of the bed load and suspended load results in the total sediment transport. Model results show especially around the breaker bar significant differences between 2DH, 3D and Q3D models (Figure 3.29). This is mainly caused by the difference in the suspended load due to currents.

Parameter sensitivity

The hydrodynamic validation section (3.3) discussed the influence of the most important (Q3D) calibration parameters on the viscosity and velocity profile. These changes in hydrodynamics also influence the concentration profiles. Generally it can be expected that an increase in the velocity leads to an increase in the concentrations. A higher velocity and a higher concentration value finally results in a higher sediment transport value. The sensitivity of 5 parameters on the sediment concentration and sediment transport is discussed in this section.

Bottom layer thickness (facdel)
Increase of the multiplication factor *facdel* leads to a slight increase of the concentration rates. Both the bed load and suspended load transport are increased due to this increase amount of sediment concentration (Figure F3.4.2a). The total amount of sediment transport is finally also increased slightly (Figure F3.4.2b). However, the sensitivity of the parameter *facdel* seems not to be significant.

Vertical viscosity (fcvisc)
A decrease of the value of *fcvisc* leads to an increase in concentration profiles (Figure F3.4.3a). This is caused by the increased maximum velocities near the bottom which is discussed in section 3.3.2. The increased concentration rates, leads to an increase of bed load and suspended load transport (Figure F3.4.3b). This finally results in an increase in total sediment transport rates.

Angle of roller front (betaro)
A decrease in the parameter *betaro* leads to a significant increase in the nearshore concentration rates (Figure F3.4.4a). Concentration profile B and C shows a significant increase by a decrease of betaro, while the offshore located profile A almost shows no deviation. This increase in concentration rates, results in a strong increase in current induced bed-load and suspended load transport in the area after wave breaking. Due to this increase the total amount of sediment transport is also increased in the nearshore area (Figure F3.4.4).

Breaker Parameter (gamdis)
Decrease of the breaker parameter *gamdis* leads to an increase in sediment concentration rates offshore and a decrease after wave breaking. This result also in an increase in sediment transport rates offshore and a slight decrease onshore (Figure F3.4.5).

Roughness height (ks)
A decrease of the roughness height leads to an increase in reference concentration rates (Figure F3.4.6). All the sediment transport components increases by an increase of *ks.* This results in an increased total sediment transport.

Conclusions
Q3D model results show a significant increase of the reference concentration profiles compared to 2DH concentration rates. This results in an increase of suspended sediment transport rates. The total sediment transport rates show agreement with 3D model results. It seems that the Q3D model over-predicts the transport rates in vicinity of the breaker bar which is induced by higher velocities near the bottom. As seen in the hydrodynamic validation section, the influence of the parameter *fcvisc* is significant on the velocity profiles. Due to the increased velocity the concentration rates are increased. This results in higher suspended load transport.

3.4.3 Longshore sediment transport (including cross-shore)
The Reniers-experiment is again used to validate the sediment transport rates for the combined cross-shore and longshore sediment transport. The hydrodynamic validation already showed a significant deviation in longshore depth-averaged velocities between the 2DH/Q3D and 3D model (section 3.3.3). These differences may also result in significant differences in sediment transport rates.

Model results

Sediment concentration
The hydrodynamic section showed a significant under estimated (depth-averaged) longshore current in case of 3D modelling. This underestimation of the longshore current will also induce a lower reference concentration. Comparison between 2DH and Q3D results shows higher concentration rates for the Q3D model. This is consistent with results from the LIP and Boers cases.

Q3D equilibrium concentration rates are again significantly higher compared to 2DH model results. It seems that the velocity at the reference height is increased considerably.

Sediment transport
Consistent with the LIP validation case, the higher Q3D concentration rates compared with 2DH sediment concentration result in higher sediment transport (both bed load and suspended load) rates for the Q3D model. Due to the significant lower longshore velocities and the resulting lower concentration rates, the 3D sediment transport rates are again much lower compared to 2DH and Q3D model results (Figure F3.47c).

Parameter sensitivity

Model results show the same changes in cross-shore transport by varying the values of the different parameters. Variation in longshore transport rates are discussed in this section.

Bottom layer thickness (facdel)
Hydrodynamic validation already showed the low influence of varying facdel on the velocity profiles. Just like the cross-shore sediment transport rates, the longshore sediment transport is hardly influenced by varying *facdel*. Although, an increase of *facdel* leads to a slightly increase in longshore sediment transport rates (Figure F3.4.8).

Vertical viscosity (fcvisc)
Consistent with model results from the LIP and Boers case, the concentration rates are increased by a decrease of *fcvisc*. This leads in both the longshore and cross-shore direction to an increase in sediment transport rates for lower values of *fcvisc* (Figure F3.4.9).

Angle of roller front (betaro)
An increase of the value of *betaro* leads to higher longshore bed-load and suspended load transport rates. This results in higher total sediment transport rates by an increase of *betaro.* Model results show clearly the influence of the roller process. As shown before a decrease of *betaro* leads to an onshore shift of the maximum roller dissipation. This leads to a shift of the maximum longshore sediment transport in the onshore direction. Besides a shift onshore, the magnitude of the longshore sediment transport decreases by a decrease of *betaro* (Figure F3.4.10).

Breaker Parameter (gamdis)
An increase of the value of *gamdis* leads to a shift of maximum velocities in onshore direction. This is also observed in the longshore sediment transport rates. Higher values of *gamdis* lead to an increase of the maximum longshore sediment transport and a shift of this peak in the onshore direction (Figure F3.4.11).

Roughness height (ks)
A decrease of the roughness height leads to more uniform longshore velocity profiles, with higher values near the bottom. This results in higher longshore sediment transport rates for lower values of *ks* (Figure F3.4.12).

Conclusions
Model results show an increase in longshore sediment transport rates in case of Q3D modelling compared with 2DH modelling. 3D model results show significantly lower values of longshore sediment transport rates, which is mainly induced by the lower depth-averaged longshore velocity values. Sensitivity analysis showed an increase in longshore sediment transport rates by an increase of *facdel* and by a decrease of *fcvisc.* Also the influence of roller process is clearly observed in model results. Increase of *gamdis* and an increase of *betaro* leads to an onshore shift of the maximum longshore sediment transport. Finally, decreasing the roughness height *ks* result in higher longshore sediment transport rates.

3.4.4 Sediment transport Egmond field case
After the validation of the sediment transport rates in cross-shore and longshore direction, this section describes the sediment transport rates of the Egmond field case.

Model results

Sediment concentration
Consistent with previous validation cases, the Egmond model results (2DH, 3D and Q3D) show clearly an increase in concentration rates during high tide (Figure F3.4.13) around the two breaker bars. Again the value of the near bed reference concentration is increased in case of Q3D modelling. During low tide, the near-bed reference concentration in the vicinity of the outer breaker bar is higher for 3D model results compared to Q3D model results. This is caused by the differences in depth-averaged velocities (Figure F3.3.21). During low tide, waves break at the outer breaker bar and induce a return flow current. This results in different values of depth-averaged velocity (longshore and cross-shore) for 3D model results and 2DH. The higher 3D depth-averaged velocities result in significantly higher velocity profiles (Figure F3.3.23 and F3.3.24), which finally results in higher concentration rates for 3D model results.

Sediment transport
The differences in concentration rates, also results in differences in sediment transport values. Q3D longshore sediment transport rates corresponds very well with 3D sediment transport rates during high tide (Figure F3.4.14). However, during low tide (Figure F3.4.17) 3D model results show significantly higher values of longshore sediment transport in vicinity of the outer breaker bar. This is caused by the increased concentration rates and higher depth-averaged velocity values for 3D model results. Q3D cross-shore sediment transport rates show an increase in sediment transport compared with 2DH modelling. However, 3D model results show significant differences with Q3D model results during high and especially during low tide. Again these differences can be prescribed mainly to the differences in depth-averaged velocities.

Conclusions
Q3D longshore sediment transport rates show similarity with 3D longshore sediment transport rates during high tide. During low tide, these values differ in the vicinity of the outer breaker bar. This difference is mainly caused by the differences between 2DH/Q3D and 3D depth-averaged velocities.

Cross-shore sediment transport rates show both during low tide and high tide an increase compared with 2DH sediment transport rates. However, 3D model results differ significantly with the Q3D model results. Again this is mainly induced by the differences in depth-averaged velocities of 2DH and 3D model results.

3.4.5 Conclusions sediment transport for all cases

Q3D model results show an increase in equilibrium concentration compared with 2DH model results. This results in higher sediment transport rates. The bed-load transport rates show similarity between the three (2DH, 3D and Q3D) different model approaches. Suspended load transport shows similarity in the longshore direction. However, cross-shore suspended load transport rates show significant differences in the Egmond field case. This is mainly induced by differences in depth-averaged velocity values.

The Q3D method introduced two additional parameter, *fcvisc* and *facdel*. The sensitivity of five different parameters is investigated. This sensitivity analysis showed that:

- By increasing the value of *facdel* the sediment concentration rates are increased. This results in higher sediment transport rates in both longshore and cross-shore direction. However, the model seems not very sensitive to changing *facdel.*

- A decrease of *fcvisc* leads to higher velocities near the bottom. This leads to an increase in sediment concentration and thus sediment transport rates. Varying *fcvisc* mainly influences the cross-shore sediment transport rates.

- By increasing the value of *betaro* and increasing *gamdis*, the dissipation of roller energy is shifted in the onshore direction. Both the longshore and cross-shore sediment transport is increased and in its maximum is shifted in the onshore direction.

- The roughness height *ks* influences both the longshore and cross-shore sediment transport rates. Lower values of the roughness height *ks* result in more uniform and lower maximum velocities near the bottom, which results in lower transport rates and therefore lower longshore and cross-shore sediment transport rates.

3.5 Morphology validation

3.5.1 Introduction

The final phase in the validation process of the Q3D approach is the validation of the morphological changes. Differences in the rate of sediment transports lead to erosion or deposition of sediment in certain regions. This causes changes in the bed level or morphology. In this section bed level changes of the Q3D model are compared with both the 2DH and 3D model results.

3.5.2 Cross-shore morphology

In absence of longshore transport only cross-shore profile development occurs for the LIP and Boers experiment.

Model results

Model results show similarity between the three different models in the offshore region (Figure F3.5.1). When looking at the total sediment transport rates discussed in section 3.4.2, no large differences are expected in bed level changes. However, in the breaker zone large differences are observed. Especially around the 150m line 3D model results show large erosion volumes (Figure 3.30), while both 2DH and Q3D results show less.

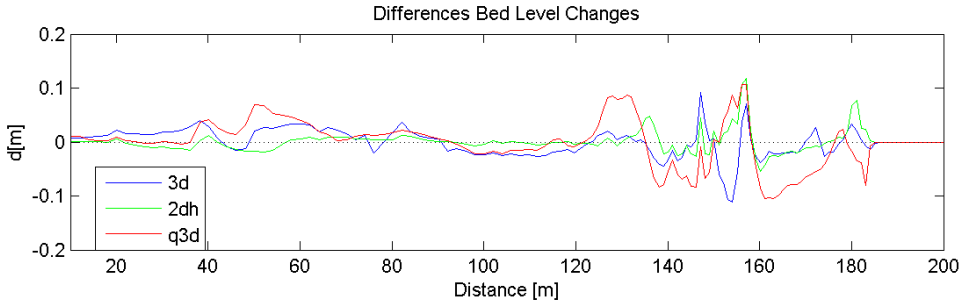

Figure 3.30 Differences Bed Level Changes 2DH (black) 3D (red) and Q3D (blue)

Q3D modelling show a strong offshore migration of the breaker bar, compared with 2DH and 3D model results.

Parameter sensitivity

It is expected that the parameters which influenced the sediment transport the most, also will have the most effect on the bed level changes. In this section, the sensitivity of *facdel, fcvisc, betaro, gamdis* and *ks* on the morphology are discussed.

Bottom layer thickness (facdel)

Again model results show hardly any deviation by varying the value of *facdel.* The previous section already showed hardly any variation in sediment transport rates by increasing the value of *facdel* (Figure F3.5.2). It can be observed that a small variation in sediment transport rates only affects the bed level changes minor. An increase of the bottom layer thickness, leads to a slightly higher erosion deposition pattern, which result in an increase in offshore bar development.

Vertical viscosity (fcvisc)

Increasing the value of *fcvisc* decreases the amount erosion and deposition over the entire area (Figure F3.5.2). From these results it can be clearly seen that decreasing the value of *fcvisc* has the most effect in vicinity of the breaker bar. Due to the

increased near bed velocities for lower values of *fcvisc,* an increase in offshore migration of the breaker bar is induced.

Angle of roller front (betaro)
Model results already showed an increase of sediment transport by decreasing the value of *betaro*. This results in a significant change in bed level (Figure F3.5.3). Lower values of *betaro* increases the sedimentation in front of the breaker bar, and erosion has taken place behind the breaker bar. Sediment is transported from the coast in offshore direction.

Breaker Parameter (gamdis)
Section 3.4.3 shows that higher values of the breaker parameter lead to increase sediment transport rates around the breaker bar. This result in higher sedimentation and deposition rates for higher values of *gamdis* (Figure F3.5.3).

Roughness height (ks)
By increasing the roughness height, the amount of turbulence in the bottom boundary layer is increased (section 3.3.2). Due to this increased turbulence the total sediment transport is increased which results in an increase of the realignment of the cross-shore profile (Figure F3.5.4). Increasing *ks* leads to more erosion in the offshore part of the cross-section and deposition after wave breaking.

Conclusions

Q3D modelling shows a strong offshore migration of the breaker bar, compared with 2DH and 3D model results. Parameter sensitivity showed an increase in sedimentation/erosion for a decrease of *fcvisc.* Differences in the value of *betaro* influence the bed level changes significantly. Decrease of *betaro* leads to a significant increase of erosion and deposition. Finally an increase of the roughness height leads to more erosion offshore and deposition after wave breaking.

3.5.3 Longshore morphology (including cross-shore)

Bed level changes induced by cross-shore and longshore sediment transport will be different compared with only cross-shore transport rates. Instead of only profile development, sediment is exported or imported into the profile.

Model results

Because of the differences in depth-averaged longshore velocities with the Reniers model, which already started in the hydrodynamics, the sediment transport rates were not very accurate. This is also observed in the bed-level changes (Figure F3.3.5).

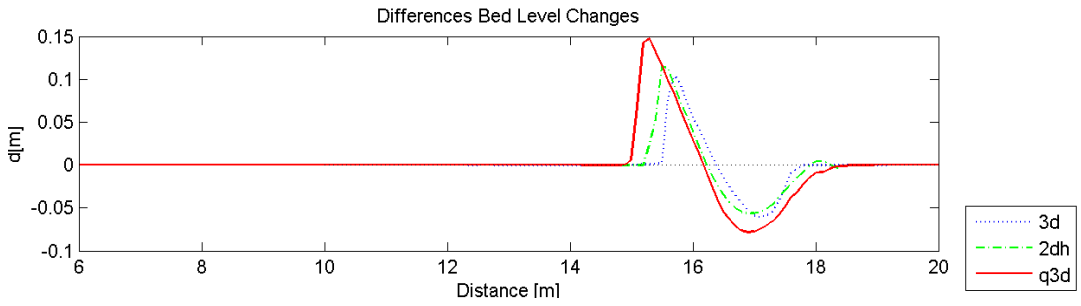

Figure 3.31 Differences Bed Level Changes Reniers Experiment 2DH (green) 3D (red) and Q3D (blue)

The three different models show the same erosion and sedimentation pattern. The magnitudes are different though. The Q3D solution shows the highest erosion and deposition rates (Figure 3.31), while the 2DH and 3D solutions seem quite similar. This can be explained by the under estimation of the longshore current in 3D modelling. Lower velocities will induce less sediment transport (section 3.4.3) and this will finally result in lower erosion and sedimentation values.

Parameter sensitivity

Bottom layer thickness (facdel)
Increase of the parameter facdel increases the amount of sediment transport only a little. This results in a small increase in offshore migration of the breaker bar.

Vertical viscosity (fcvisc)
A decrease of the *fcvisc* value increases the offshore migration of the breaker bar. Again it is clear that the model is quite sensitive to changes in the value of *fcvisc.*

Angle of roller front (betaro)
Model results show an increase in sediment transport rates (section 3.4.3) in the area after wave breaking by increasing the value of *betaro.* This increase in sediment transport rates results in an offshore migration of the breaker bar by an increase of *betaro.* The amount of erosion after wave breaking also increases. Sediment is moved in offshore direction.

Breaker Parameter (gamdis)
The LIP and Boers cases already showed that higher values of the breaker parameter leads to an increase sediment transport rates around the breaker bar. This result in higher sedimentation and deposition rates for higher values of *gamdis .*The Reniers experiment shows the same pattern. An increase of *gamdis* leads to an increase in erosion and sedimentation and therefore an increase of bar migration.

Roughness height (ks)
Increasing the roughness height, the amount of turbulence in the bottom boundary layer is increased (section 3.3.2). Due to this increased turbulence the total sediment transport is increased which results in an increase of the realignment of the cross-shore profile

Conclusions
Model results show consistency with the LIP case: an increase in erosion/sedimentation pattern in the case of Q3D modelling compared with 2DH. However, 3D model results show a significant lower migration of the breaker bar, which is induced by the low longshore currents. Sensitivity analysis shows again an increase of erosion and sedimentation by a decrease of *fcvisc* and an increase of *facdel.*

3.5.4 Morphology Egmond field case
Morphological changes are taken into account after 12 hours of simulation time. With a morphological scale factor of one, the bed level changes over one tidal cycle are computed and compared for 3D, 2DH, and Q3D model results.

Model results
3D model results show a band of sedimentation at the offshore side of the outer breaker bar. An offshore migration of the outer breaker bar is observed in the 3D model. Q3D model results show partly the same pattern. Especially the Q3D migration of the inner

breaker bar corresponds very well with the result of the 3D model. The same patterns are observed. 2DH modelling shows mainly a migration of the bar in onshore direction.

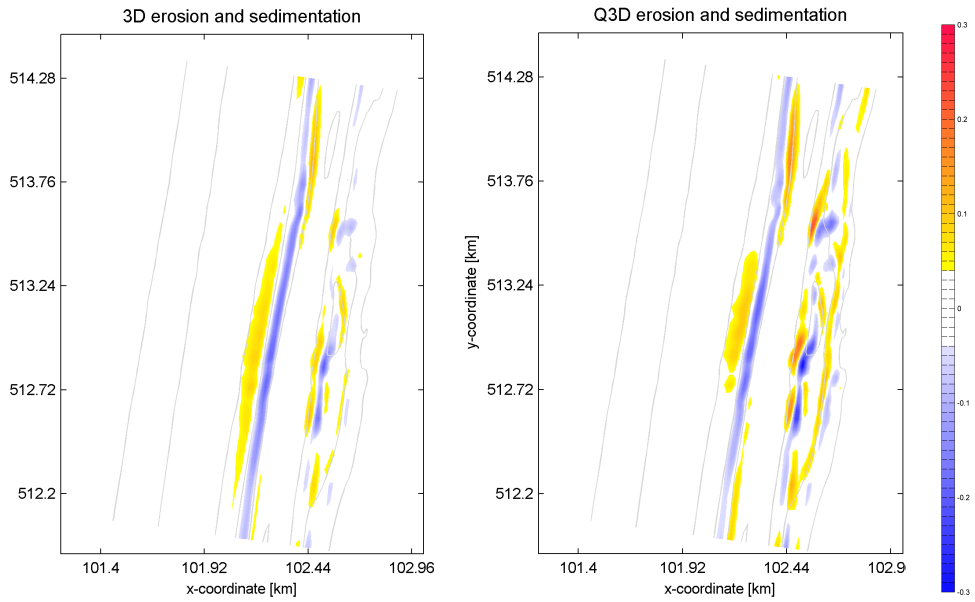

Figure 3.32 3D (left) and Q3D (right) model result erosion sedimentation patterns Egmond field case

Erosion and sedimentation patterns show differences between 3D and 2DH computations (Figure F3.5.9). 3D computations show an offshore migration of the outer breaker bar, which is hardly visible in the 2DH model results. In vicinity wave breaking is increased which give rise to secondary (return flow) currents. This is not represented in the 2DH model which gives the differences in bed level changes. The Q3D erosion and sedimentation patterns show high agreement with the 3D results (Figure 3.32). However, it seems that the amount of erosion and sedimentation in case of Q3D modelling is higher in relation to 3D. The outer bar is also migrated in offshore direction. Furthermore it is obvious that the Q3D model shows more detail in the nearshore region compared with 2DH and 3D model results.

Conclusions

Q3D model results show agreement with 3D model results. The erosion and sedimentation patterns are represented fairly well. Especially in the region of the outer breaker bar, 3D and Q3D models show an offshore migration of the outer breaker bar, whereas 2DH model results shows hardly any.

3.5.5 Conclusions morphology for all cases

Four different validation cases were performed to validate the morphodynamics of the Q3D approach. Comparison with 2DH and 3D model results shows an increase in breaker migration for the Q3D model. The Q3D erosion/sedimentation results for the Egmond field case shows similarity with both 2DH and 3D model results. The Q3D model results seem to be a combination of 2DH and 3D effects.

The Q3D method introduced two additional parameter, *fcvisc* and *facdel*. The sensitivity of five different parameters is investigated. This sensitivity analysis showed that:

- The model is not sensitive to changes in the multiplication factor for the bottom boundary layer thickness *facdel*. Increase of the bottom layer thickness, leads to a slightly higher erosion deposition pattern. This result in an increase in bar developments.

- The bed level changes are sensitive in changing the value of *fcvisc.* Erosion and sedimentation rates increase by decreasing the value of *fcvisc.* This lead to an increase of offshore bar migration by lower values of *fcvisc.*

- By increasing the value of *betaro* and increasing *gamdis*, the dissipation of roller energy is shifted in the onshore direction. Especially *betaro* influences the bed level changes significantly. A decrease of *betaro* leads to an increase of erosion and sedimentation.

- By increasing the value of *ks* the amount of erosion and deposition increases. The bar migrates in offshore direction for higher values of *ks.*

3.6 Computational time

3.6.1 Introduction

One of the main reasons to implement the Q3D method in Delft3D is to reduce the computational time. This section compares the calculation time of the different approaches (2DH, 3D and Q3D). To compare the calculation times, the CPU-time of the different models are discussed. The times are divided in several parts to check the overhead time for each part of the model. The best value to make a comparison between the three different modes of Delft3D is the simulation time, which is defined as the calculation time from the first time step till the last time step.

3.6.2 Cross-shore case

The 2DH simulation time is taken as a reference time. It is seen in Table 3.1 that for the 3D mode with 20 layers the simulation time is increased with almost 237%, while the Q3D method has an additional time of less than 15%. This additional time in the Q3D model is mainly generated in the 3D morphology and transport computation part of the code.

CPU Time (LIP11D-1b validation case)						
	2DH		3D (20 layers)		Q3D	
name	**sec**	**%**	**sec**	**%**	**sec**	**%**
Initialization	0,58	100	0,73	125,86	0,52	89,66
Simulation	**67,47**	**100**	**227**	**336,45**	**77,05**	**114,20**
Close and stop	0,11	100	0,16	145,45	0,12	109,09
Total	68,16	100	227,89	334,35	77,69	113,98
Momentum equation	0,91	100	32,08	3525,27	0,97	106,59
Continuity	0,73	100	12,73	1743,84	0,88	120,55
Transport	3,31	100	39,62	1196,98	3,42	103,32
Turbulence	0,05	100	31,34	62680,00	0,05	100,00
3D Morphology	30,88	100	46,75	151,39	40,34	130,63
Wait (dd module)	0	100	0	100,00	0,00	100,00
Wait (ext. modules)	0,19	100	0,27	142,11	0,16	84,21

Table 3.1 Overview calculation time LIP11D-1b experiment

3.6.3 Longshore case (including cross-shore)

Compared to the case with only cross-shore currents, the combined cross- and longshore case did not need more calculation time. Apparently no additional iteration steps are needed in the case of combined long and cross-shore currents compared to only cross-shore currents. Again the differences between 2DH and Q3D are less than 15%, while the 3D model needs almost 265% more computational time (Table 3.2).

CPU Time (Reniers validation case)						
	2DH		3D (20 layers)		Q3D	
name	**sec**	**%**	**sec**	**%**	**sec**	**%**
Initialization	0,62	100	0,7	112,90	0,59	95,16
Simulation	**359,19**	**100**	**1305,77**	**363,53**	**410,77**	**114,36**
Close and stop	0,14	100	0,17	121,43	0,14	100,00
Total	359,95	100	1306,64	363,01	411,50	114,32
Momentum equation	7,02	100	229,64	3271,23	6,44	91,74
Continuity	5,73	100	70,79	1235,43	5,25	91,62
Transport	22,59	100	219,34	970,96	23,67	104,78
Turbulence	0,23	100	172,53	75013,04	0,27	117,39
3D Morphology	76,05	100	153,31	201,59	127,56	167,73
Wait (dd module)	0	100	0	100,00	0,00	100,00
Wait (ext. modules)	0,23	100	0,25	108,70	0,19	82,61

Table 3.2 Overview calculation time Reniers experiment

3.6.4 Egmond field case

The Egmond field case differs in two ways with the previous experiments. In the first place it is a field model, which means that the computations are done in two directions. In the second place the Egmond model has an online coupling with the Delft3D-WAVE module. This takes a lot of additional computation time. Still a comparison can be made between the different models. The CPU-times only takes the flow computations into account. When comparing the simulation CPU-times it can be seen that the Q3D has an overhead time of less than 20% (Table 3.3). This is slightly more than the test done before. This can be explained by the fact that more iteration steps have to be done, because the gradient has to be solved in two directions. Besides the overhead time of the Q3D model which increases, also those of the fully 3D calculations. Due to this the Q3D approach is still more time efficient.

CPU Time (Egmond validation case)						
	2DH		3D (20 layers)		Q3D	
name	**sec**	**%**	**sec**	**%**	**sec**	**%**
Initialization	0,27	100	0,58	214,81	0,28	103,70
Simulation	**1810,58**	**100**	**12831,06**	**708,67**	**2157,53**	**119,16**
Close and stop	0,05	100	0,11	220,00	0,06	120,00
Total	1810,9	100	12831,75	708,58	2157,87	119,16
Momentum equation	45,64	100	2646,69	5799,06	45,50	99,69
Continuity	42,81	100	1244,09	2906,07	43,97	102,71
Transport	200,38	100	3082,53	1538,34	201,80	100,71
Turbulence	1,31	100	2186,3	166893,13	1,52	116,03
3D Morphology	1239,27	100	2079,7	167,82	1582,88	127,73
Wait (dd module)	0	100	0	100,00	0,00	100,00
Wait (ext. modules)	0,08	100	0,12	150,00	0,09	112,50

Table 3.3 Overview calculation time Egmond field case

3.6.5 Conclusion calculation time

In case of the profile models (LIP, Boers and Reniers), the Q3D model only needs an overhead calculation time of less then 15%, while the 3D approach needs more than 235% compared to 2DH models (Table 3.4).

Percentage simulation time			
Experiment	**2DH**	**3D (20 layers)**	**Q3D**
LIP11D-1b	100	336.45	114.20
Boers-1b	100	314.56	123.52
Reniers SO014	100	363.53	114.36
Egmond	100	708.67	119.16

Table 3.4 Overview percentage calculation time different models (percentage relative to 2DH calculation time)

For the field model, the overhead time becomes almost 20% for the Q3D approach against almost 610% for 3D calculations.

From a computational time point of view, the Q3D approach seems very effective compared to 3D models. The Q3D model generally leads to an increase in calculation time of less than 20% against up to 610% of fully 3D models.

3.7 Conclusions validation Q3D approach

After implementation of the Q3D approach four different cases were used to validate the model. This process was divided into three parts.

- *Hydrodynamic* validation showed high agreement between Q3D and 3D cross-shore velocity profiles. However, some differences do occur in the Egmond field case. These are mainly induced by differences in depth-averaged velocities.

- Q3D model results show overall an increase of *sediment concentration* compared with 2DH modelling. This results in higher sediment transport rates for the Q3D model. 3D model results still show higher transport rates in the Egmond field case. This is again induced by the higher values of depth-averaged velocities.

- These differences in sediment transport finally results also in differences in *bed level changes*. Q3D model results show a more offshore migration of the breaker bar compared to 2DH model results. Q3D field model results showed partly similarity with 2DH and 3D model results.

From a computation time point of view the Q3D model show some great results. For the profile models only an overhead time of 15% is reached, while 3D models almost need 250% more computation time. Although the Egmond case needs 20% more computation time for the Q3D approach, the 3D model needs almost 610% overhead time.

These results shows that the Q3D computation is significantly more time efficient compared with 3D computation with comparable model results.

4 Application on Practical Cases

4.1 Introduction

The previous sections described the theory about the Q3D model and the validation cases. In this section, the Q3D model is evaluated for a number of practical cases. First a uniform straight coast (based on Egmond model) is subjected to a single wave condition. Subsequently, a short and a long groyne are added to this model. Finally, a perched beach including a submerged breakwater is investigated.

In this chapter, the Q3D model results are compared with 2DH and 3D model results for hydrodynamics, sediment transport and morphological impact. Besides the model results, the computational time is described shortly. Large figures are shown in Appendix F.

4.2 Uniform straight coast

The area is characterised by two breaker bars orientated parallel to the shore (Figure 4.1 and Figure F4.1.1). A Delft3D model is constructed with an alongshore uniform depth profile and zero Neumann lateral and water level boundaries, forced with a single wave condition (Hs = 2.1 m, Tp = 8s) and an incident wave angle of 30 degrees normal to the shore.

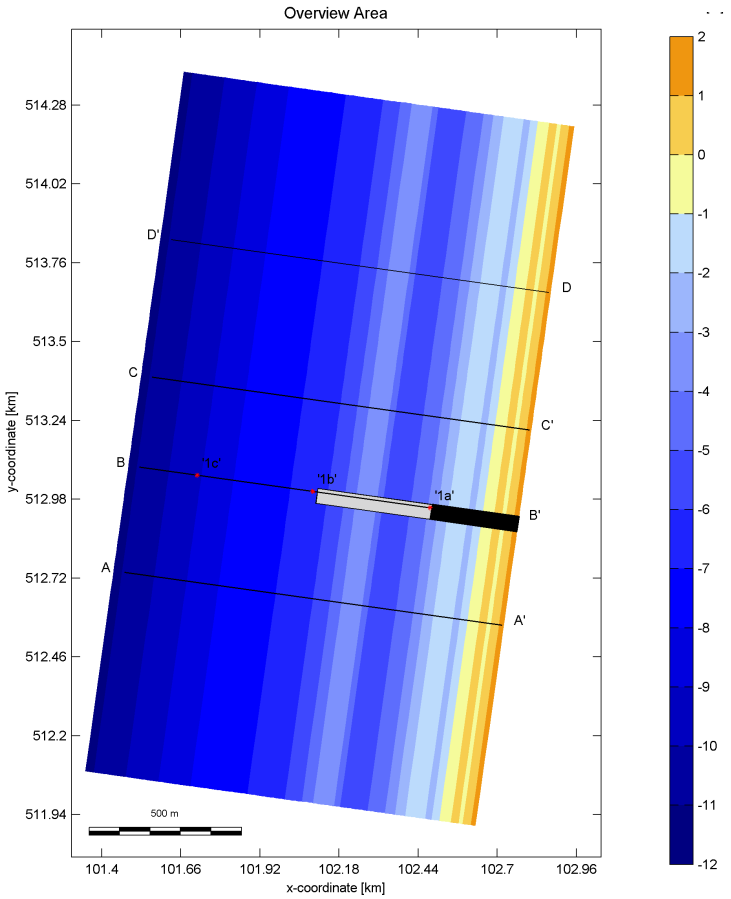

Figure 4.1 Overview area uniform coast (including long groyne and short groyne)

4.2.1 Hydrodynamics

Due to the obliquely angle of the waves, both a longshore and cross-shore current is generated. A northward directed flow pattern is recognizable in which the longshore component is dominant. In the vicinity of both breaker bars the wave driven current is increased due the wave breaking process. The depth-averaged flow field shows differences between the 2DH and 3D model (Figure F4.2.1).

Figure 4.2 shows the depth-averaged longshore and cross-shore velocities over a cross-section perpendicular to the shore. The longshore depth-averaged velocities show a significant deviation between the 2DH and 3D model results. Especially in vicinity of the breaker bar the 2DH (and Q3D) depth-averaged longshore velocity is significantly higher in relation to the 3D longshore depth-averaged velocity (up to 30%). The cross-shore depth-averaged velocities show high agreement in both models.

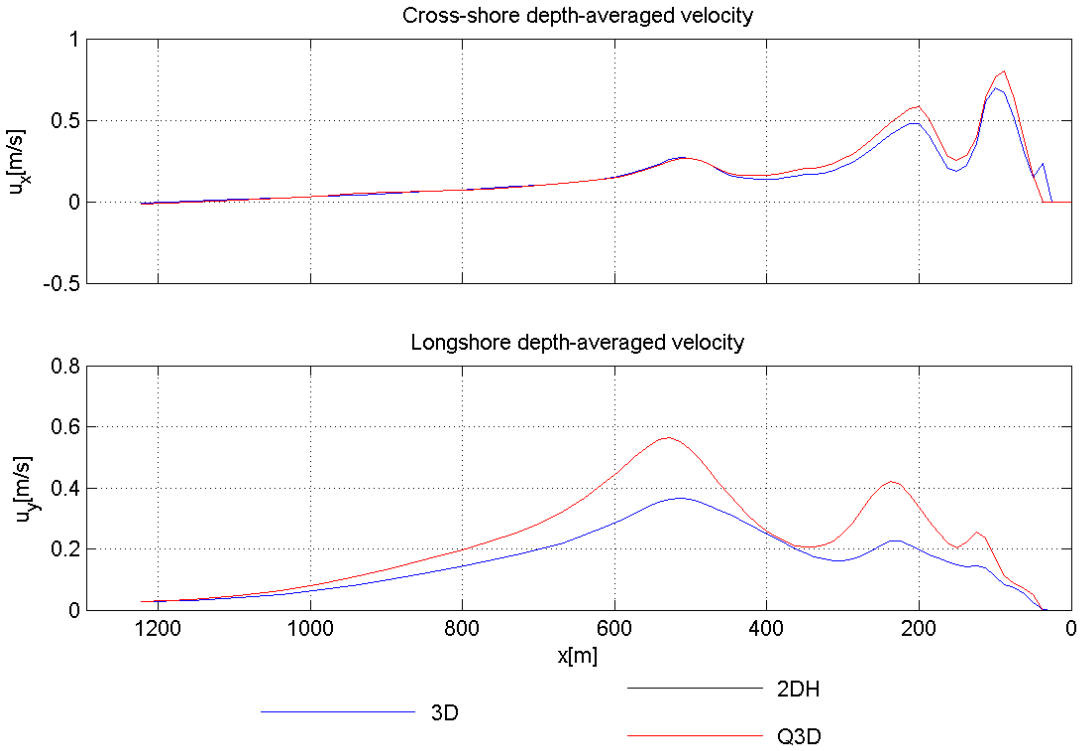

Figure 4.2 depth-averaged cross-shore and longshore velocities at cross-section BB'

These differences in depth-averaged velocities, also lead to differences in the velocity profiles (Figure 4.3 and Figure F4.2.3). Model results show good agreement between the Q3D and 3D (Eulerian) velocity profiles in shape. The magnitude of the Q3D model in both the cross-shore and longshore direction are higher in relation to the 3D velocity profiles.

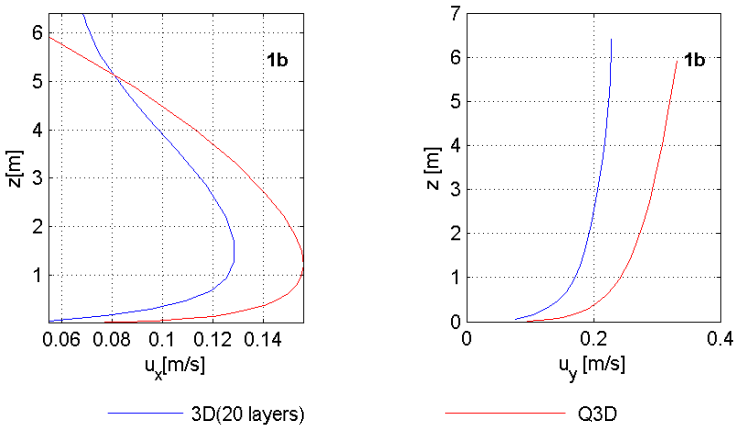

Figure 4.3 Cross-shore (left) and longshore (right) velocity profiles at point 1b

4.2.2 Sediment transport

Model results show differences between 2DH and 3D model results in both magnitude and direction. Longshore sediment transport rates show a uniform northwards directed pattern (Figure 4.4). Cross-shore sediment transport rates show differences both in magnitude and direction. The 3D model shows only offshore directed sediment transport rates, while the 2DH model also shows a shoreward directed component (Figure F4.2.4). These differences are mainly caused by the modelling of the undertow.

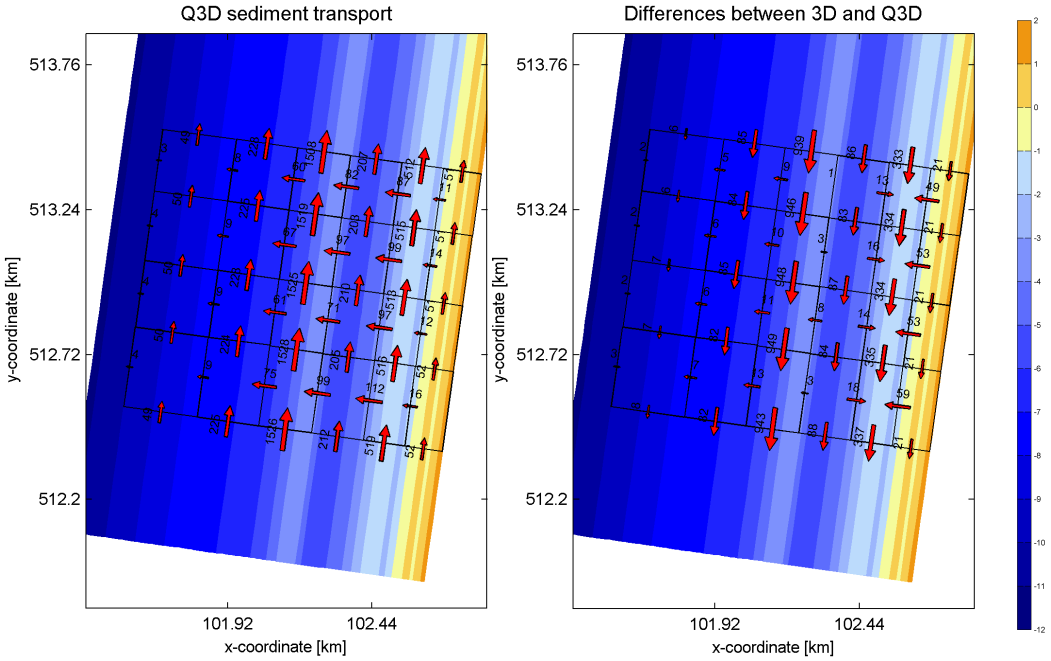

Figure 4.4 Q3D and differences (3D-Q3D) of sediment transport rates through transect [10^3 m^3/year]

Q3D model results show an increase of sediment transport rates in relation to 2DH sediment transport. The northwards directed longshore sediment transport is increased significantly in relation to both 2DH and 3D model results. Q3D cross-shore sediment transport rates show high agreement with 3D sediment transport. A similar offshore directed transport is recognisable. This implies that the improvement in velocity profiles indeed leads to a better approximation of the 3D model results.

4.2.3 Morphology

Figure 4.5 shows the erosion and sedimentation of the 2DH and 3D model after 30 days of morphological modelling (large figure is shown in Appendix F). These figures show clearly the differences between both models. Due to the modelling of the undertow, the 3D model shows an offshore migration of the breaker bar which is not observed in 2DH model results. The Q3D model results correspond fairly well with 3D model results. Similar patterns are recognisable. However, the magnitude of the erosion and sedimentation of the Q3D model seems higher in relation to the 3D model.

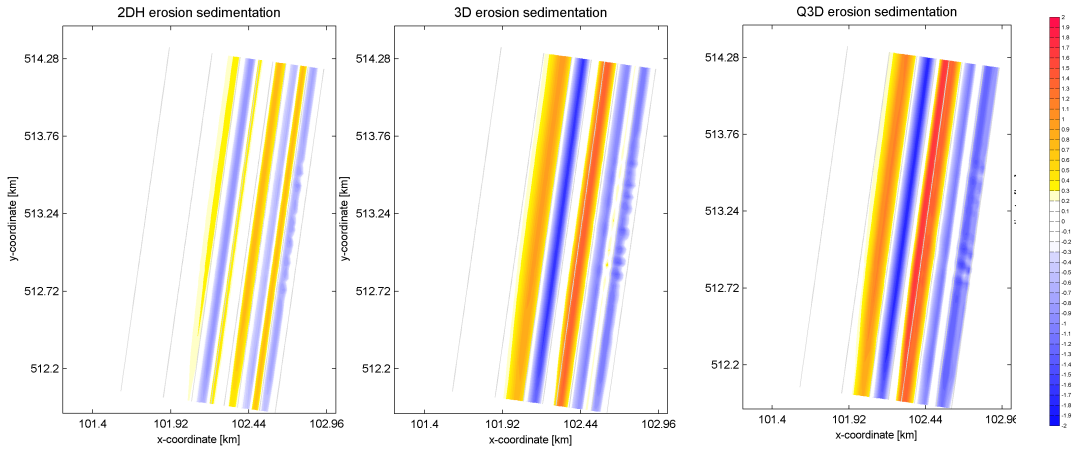

Figure 4.5 2DH (left) and 3D (middle) and Q3D (right) erosion and sedimentation after 30 days

Figure F4.2.8 shows the bed level of the different models after 30 days of morphological time. Q3D and 3D bed level show high agreement in vicinity of the outer breaker bar. Both models show an offshore migration of the breaker bar, while the 2DH model only shows a decrease in height (Figure 4.6 and Figure F4.2.7).

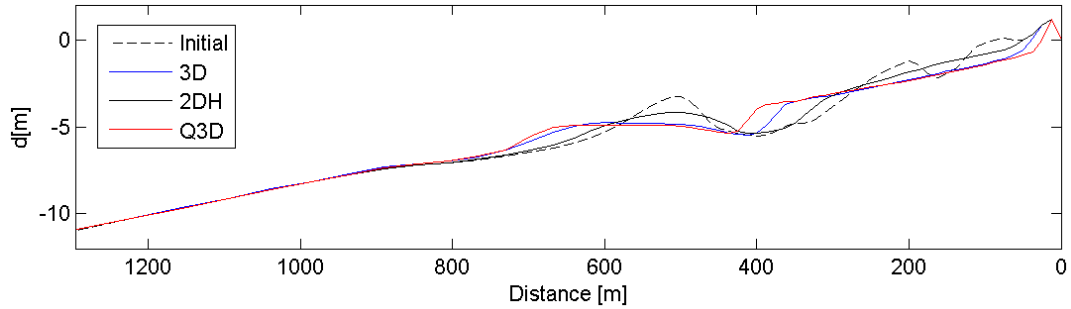

Figure 4.6 Initial, 2DH, 3D and Q3D bed level at cross-section BB'

The inner breaker bar is smoothed in all cases. As already observed in the erosion sedimentation patterns, the magnitudes differ. The Q3D model shows the biggest changes in bed profile. Sediment is transported from the beach in offshore direction.

4.3 Uniform straight coast including long groyne

The second practical case to evaluate the Q3D model is a stretch of coast interrupted by a long groyne. Similar bathymetry and wave condition were used as described in the previous section.

4.3.1 Hydrodynamics

The previous section showed a uniform northwards directed flow pattern. In this section the current is interrupted by a long groyne. On the south side of the groyne the current is forced in offshore direction and leads to an increase of the depth-averaged velocities in vicinity of the tip of the groyne.

Figure 4.7 Depth-averaged cross-shore and longshore velocities at cross-section BB'

Significant differences between 3D and 2DH depth-averaged velocities occur (Figure 4.7). These differences are present in both the longshore and the cross-shore components of the current.

These differences in depth-averaged velocity also lead in differences in the velocity profiles (Figure F4.3.3). Q3D and 3D model results show large deviation in especially magnitude of the cross-shore velocity profiles. At the tip of the groyne, the cross-shore velocity near the bottom is significantly higher for Q3D model results compared with 3D. The longshore velocity profiles seem to correspond to a great extent.

4.3.2 Sediment transport

Besides the flow current, also the northwards directed sediment transport is interrupted by the groyne. This results in an increased offshore directed sediment transport pattern in vicinity of the groyne in relation to the previous case (case without groyne).

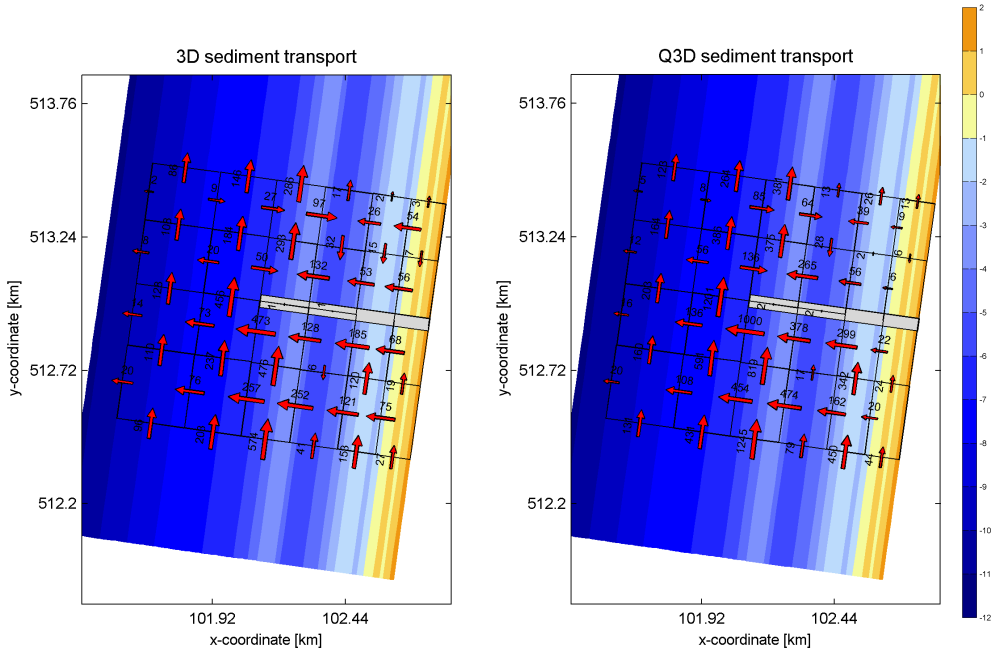

Figure 4.8 3D and Q3D total sediment transport through transect [10^3 m^3/year]

Q3D sediment transport patterns show again similarity in relation to 3D computed sediment transport patterns (Figure 4.8). Still the 3D results are mostly higher. Q3D longshore sediment transport rates are again increased significantly in relation to both 3D and 2DH computations (Figure F4.3.4).

The sediment transport at cross-section BB' shows significantly higher cross-shore bed load rates in case of Q3D modelling. This is caused by the higher velocity near the bed, which induced higher near-bed references concentration rates (Figure F4.3.5)

4.3.3 Morphology

3D and Q3D model results show high similarity in erosion and sedimentation patterns. The outer breaker bar which migrates in offshore direction is again observable in both models, whereas the 2DH model did not show this pattern at all (Figure F4.3.7).

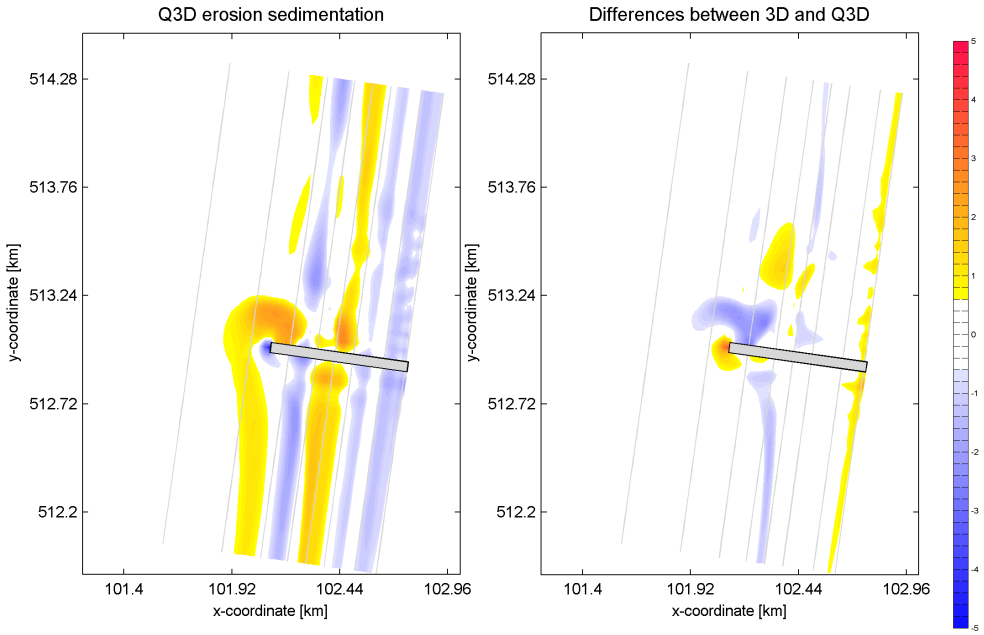

Figure 4.9 Q3D and differences (3D-Q3D) erosion and sedimentation model results

The right plane of Figure 4.9 shows the differences between the 3D and Q3D model results. The main differences are in the vicinity of the tip of the groyne. The Q3D model shows a significantly higher scour hole (Figure 4.10), which results in a higher deposition of sediment northwards of the groyne.

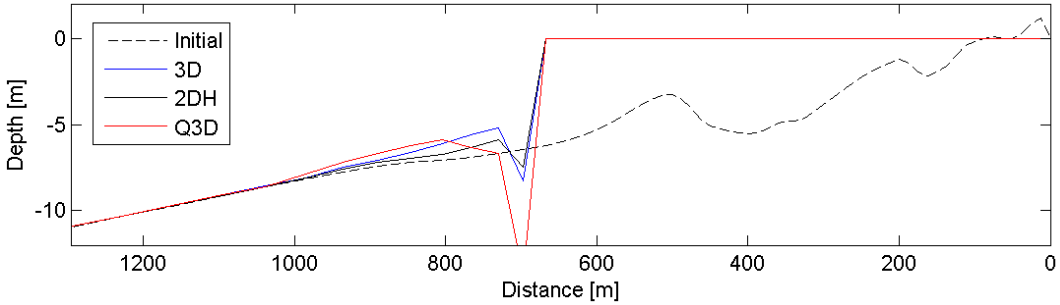

Figure 4.10 bed level at cross-section BB'

4.4 Uniform straight coast including short groyne

In this section again a stretch of coast including a groyne is used to evaluate the Q3D model. The length of the groyne is shortened and extends to the end of the inner breaker bar.

4.4.1 Hydrodynamics

The northwards directed flow field is interrupted by a short groyne. Again the longshore current is forced in offshore direction. However, it's only for a relatively small part. The flow field in vicinity of the outer breaker bar is not influenced to a great extent by the short groyne. This means that the longshore current is still dominant in that region.

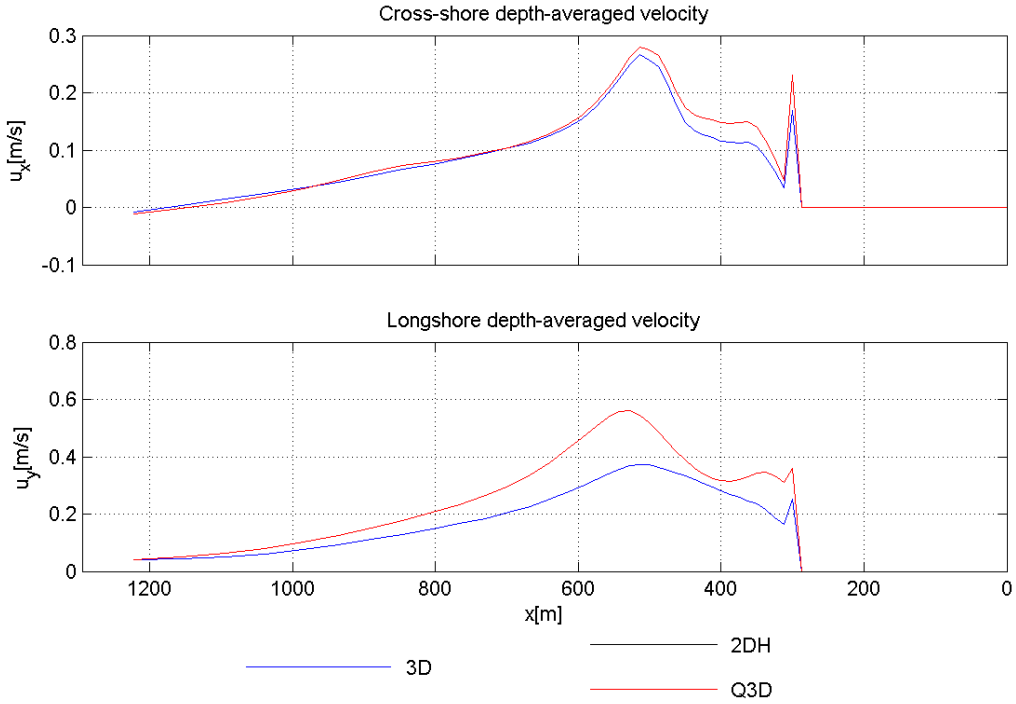

Figure 4.11 longshore and cross-shore depth-averaged velocities at cross-section BB'

Figure 4.11 shows the cross-shore and longshore depth-averaged velocities of the three different models at cross-section BB'. The cross-shore velocities show only a small deviation in vicinity of the groyne. Longshore depth-averaged velocity shows a larger deviation between the 2DH and 3D model results. This is already observed in the first evaluation case.

Q3D velocity profiles show again high agreement with 3D velocity profiles in both longshore and cross-shore direction (Figure F4.4.3).

4.4.2 Sediment transport

Comparison between the 2DH and 3D sediment transport (Figure F4.4.4) shows again differences in magnitudes and direction. The 3D model results show mainly an offshore directed cross-shore sediment transport, which is higher compared to 2DH. The Q3D model results show a similar pattern of sediment transport in relation to 3D (Figure 4.12). Magnitudes of cross-shore transport show a significant deviation in vicinity of the groyne (i.e. the Q3D offshore directed transport rates are higher).

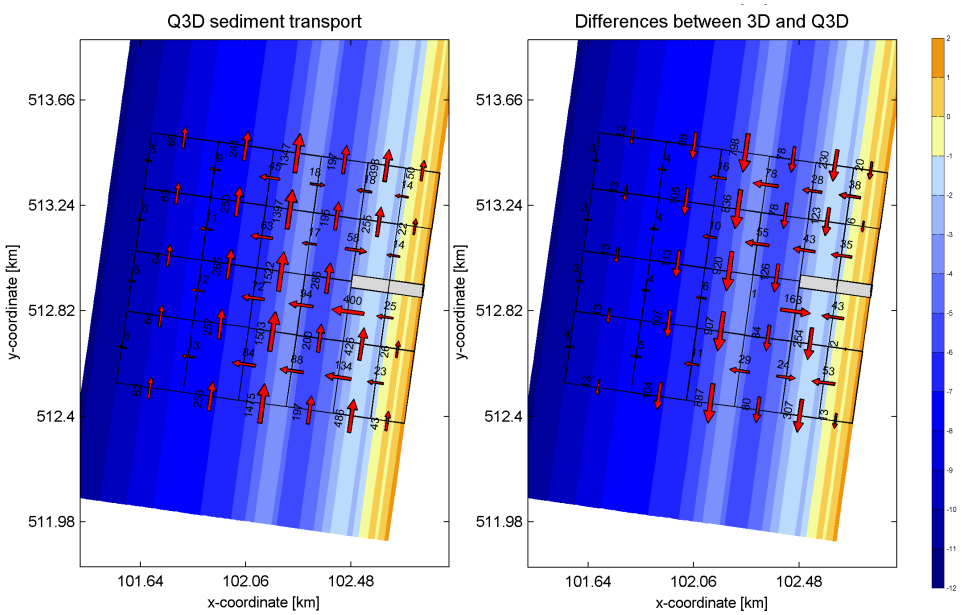

Figure 4.12 Q3D and differences (3D-Q3D) of sediment transport rates through transect [10^3 m^3/year]

The Q3D longshore sediment transport is again significantly higher compared to 2DH and 3D (Figure F4.4.5).

4.4.3 Morphology

2DH erosion and sedimentation results show similar differences with 3D model results like in section 4.2.3 (Figure F4.4.7). The agreement in sediment transport between 3D and Q3D result in bed level changes which show high similarity between 3D and Q3D. The offshore migration of the outer breaker bar shows the same patterns as in the case without a groyne. This implies that the short groyne has hardly any influence in this region. The erosion and sedimentation pattern show high agreement between Q3D and 3D (Figure 4.13). However, the magnitude of the Q3D model is higher compared to the 3D solution.

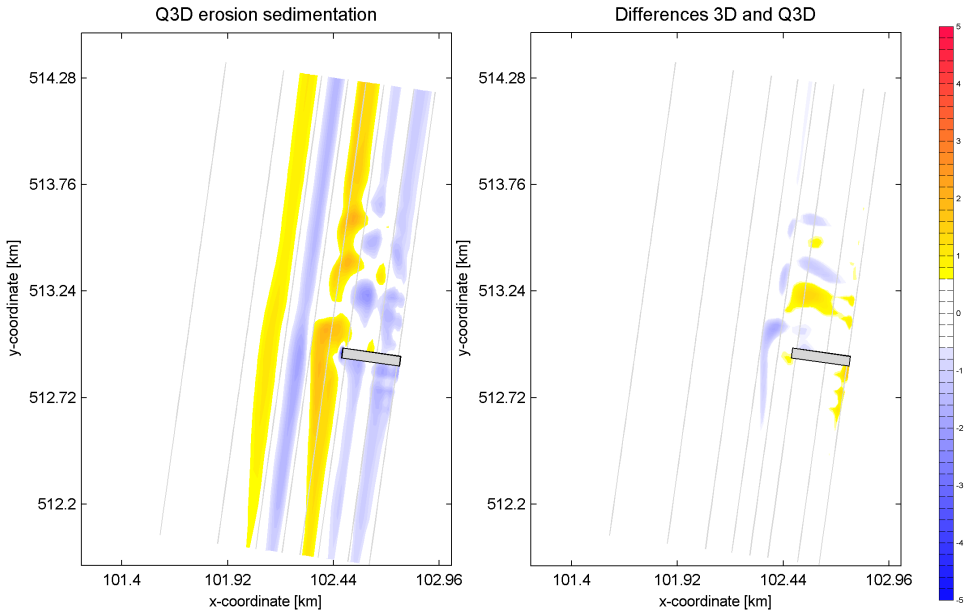

Figure 4.13 Q3D and differences (3D-Q3D) erosion and sedimentation model results

At the tip of the groyne, a scour hole is generated (Figure 4.14). The three models show good agreement at this point, in contradiction with the previous case (the case including a long groyne).

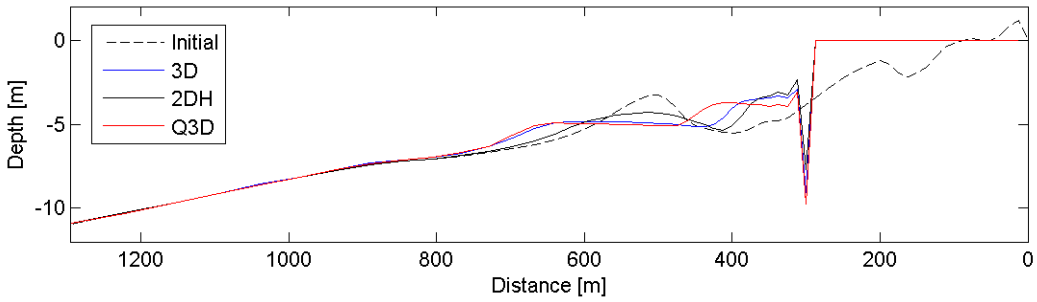

Figure 4.14 bed level at cross-section BB'

4.4.4 Computational time

Besides the model results, also the computational time of the three different models are compared. To compare the computational times of the different models, the CPU simulation times are considered. The simulation time is defined as the calculation time from the first time step till the last time step.

Averaged percentage simulation time relative to 2DH		
2DH	**3D (20 layers)**	**Q3D**
100%	481%	123 %

Table 4.1 Averaged percentage 3D and Q3D computational time relative to 2DH

Table 4.1 shows the averaged computation times of the three previous practical cases (Section 4.2, 4.3 and 4.4). Table 4.1 shows an increase in computational time with a factor 4.8 for the 3D model compared with the 2DH model. The Q3D model only needs 1.23 times more computational time in relation to the 2DH model

4.5 Pocket beach including submerged breakwater

4.5.1 Introduction

The final practical case which is used to evaluate the Q3D model is the morphology of a pocket beach including a submerged breakwater (Figure F.4.5.1). The area consists of two pocket beaches. At the sea side the beach is enclosed by alternating submerged breakwaters. The centrelines of these structures are located about 260 meters from the shoreline. Waves approach under a large angle from the north.

Hydrodynamic and morphological model results of the 2DH, 3D and Q3D model are compared.

4.5.2 Hydrodynamics

Due to the large angle of the wave, a complex flow field occurs. Hydrodynamic model results show a longshore current inside the scheme near the shoreline, which is generally directed to the South-east in the northern bay, and directed to the north-west in the southern bay.

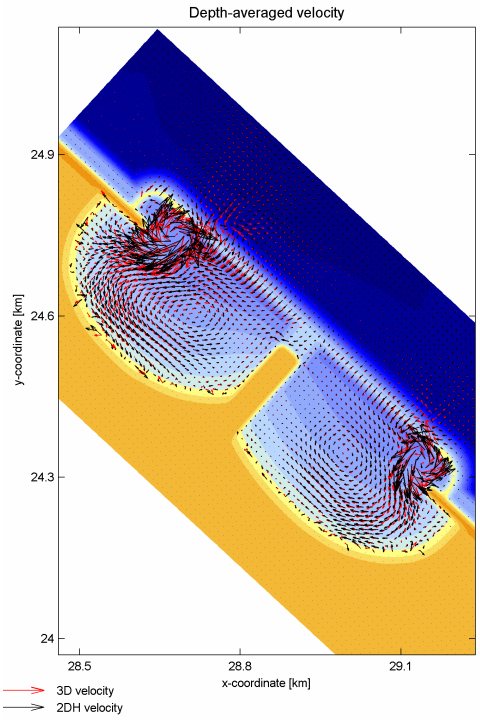

Figure 4.15 3D and 2DH depth-averaged velocity field pocket beach after 2 hours of simulation time

Hydrodynamic model results show again differences between the 2DH and 3D computed depth-averaged velocities in both direction and magnitude (Figure 4.15).

4.5.3 Morphology

After 20 days of morphological modelling differences in bed level are observed between 2DH and 3D model results (Figure F4.5.3). 3D model results show more sediment transport from the beach in offshore direction.

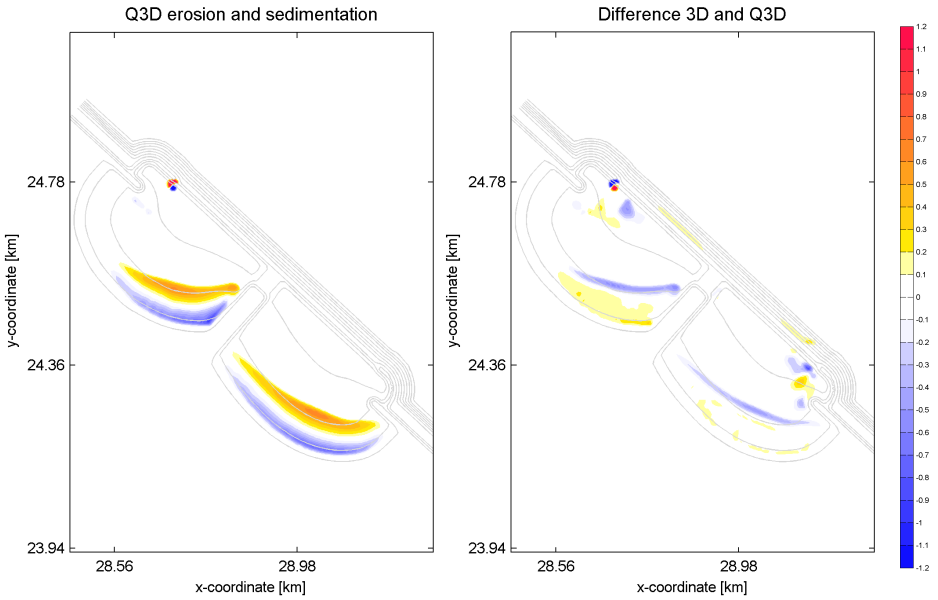

Figure 4.16 Q3D and differences (3D-Q3D) erosion and sedimentation model results pocket beach

Q3D and 3D model results show agreement. Similar erosion and sedimentation patterns are recognisable (Figure 4.16). However, the magnitude of the sediment movement is higher in case of Q3D modelling, which is already seen in previous tests.

4.6 Conclusions evaluation

The applicability of the Q3D model is tested with the use of four different practical cases.

- Hydrodynamic evaluation shows agreement between 3D and Q3D cross-shore and longshore velocity profiles in shape. Still differences occur in magnitude, which is mainly caused by the differences in depth-averaged longshore velocities of the 2DH and 3D model

- Sediment transport results shows high similarity in sediment transport patterns. The offshore directed sediment transport rates are represented fairly well with the Q3D model. Longshore sediment transport is increased significantly. This can partly be ascribed to the differences in depth-averaged velocities.

- Q3D morphological changes show high similarity with 3D model results. The outer breaker bar

- Finally the computational time of the Q3D is still increased with a maximum factor of 1.27 whereas the 3D computational time is increased up to a factor 5.88.

5 Conclusions and Recommendations

This final chapter describes the conclusion and recommendations of the implementation, validation and evaluation of a quasi-three-dimensional (Q3D) model. First, conclusions according to the hydrodynamics, sediment transport, morphology and calculation time are described. Subsequently, recommendations are given.

5.1 Conclusions

A quasi-three-dimensional (Q3D) model based on the concepts of Reniers et al. (2004) has been implemented into the Delft3D modelling software to calculate the vertical velocity distribution account for tidal forcing, wave breaking, wind and dissipation due to bottom friction.

Validation with the use of four validation cases showed high agreement between Q3D model results and fully 3D model results, with the following findings:

- *Hydrodynamics:* Q3D cross-shore velocity profiles show high agreement with 3D velocity profiles in both shape and magnitude. Longshore velocity profiles show the same logarithmic shaped profile for both Q3D and 3D model results.

- *Sediment transport:* Q3D equilibrium concentrations are higher compared with depth-averaged (2DH) concentrations. In combination with an increased reference velocity, the suspended transport rates are increased. This results in higher total sediment transport rates.

- *Morphology:* Profile models shows an increase in the migration of an offshore bar for Q3D modelling compared with 2DH and 3D. Q3D erosion and sedimentation patterns show both 2DH and 3D effects.

Implementation of the Q3D model introduced two additional calibration parameters:

- A multiplication factor for the wave boundary layer thickness (*facdel*): increase of *facdel* leads to an increase of the bottom boundary layer. This results in a downwards shift of the maximum velocity due to the decreased viscosity in this region.

- A multiplication parameter to increase the wave-induced viscosity (*fcvisc*): decrease of *fcvisc* leads to an increase of the amount of viscosity. This results in more uniform velocity profiles.

The four validation cases show the time efficiency of the Q3D model clearly. With only an increase between the 14-20% (Q3D) against an increase of 236-608% for fully 3D computations, the Q3D model can be competitive with 2DH.

Percentage simulation time			
Experiment	**2DH**	**3D (20 layers)**	**Q3D**
LIP11D-1b	100	336.45	114.20
Boers-1b	100	314.56	123.52
Reniers SO014	100	363.53	114.36
Egmond	100	708.67	119.16

Table 5.1 Overview calculation time 2DH, 3D and Q3D validation cases

Evaluation of the Q3D model is done with four practical cases. Morphological model results show high agreement with 3D model results. Especially, the offshore migration of the outer breaker bar of the Q3D model show high agreement in relation to 3D results. The 2DH computational time is only increased with a factor of 1.27 for Q3D computations, whereas the 3D computational time is increased up to a factor 5.88.

The Q3D model reproduces the 3D model results very well with significant more time efficiency and seems therefore a good additional mode to the Delft3D modelling software.

5.2 Recommendations

In spite of the good results of the Q3D model, still several improvements can be made.

- At the moment, only the vertical velocity distribution to compute sediment transport rates is implemented in Delft3D. The 2DH bed shear stress is used in the computation of the forcing. It would be better to use the Q3D velocity instead of 2DH velocities for bottom shear stress calculations.

- Streaming is not included in the Q3D model. It is recommended to implement this in the bed load transport.

- Model results show the significant influence of the calibration factor *fcvisc.* In vicinity of the breaker bar lower values of the fcvisc parameter seems desired compared to regions where wave breaking is less important. Therefore an optimized value of *fcvisc* could improve the results significantly.

- Wind-induced turbulence is not yet included in the model. It is recommended to implement and validate this part.

- Several cases show large deviation in depth-averaged longshore velocities between 2DH and 3D model results. This dissimilarity is investigated at this moment at Deltares. It is recommended when these problems are solved to validate the longshore Q3D velocity profiles again with 3D model results.

6 References

Arcilla, A. S., J. A. Roelvink, B. A. O'Connor, A. Reniers, and J. A. Jimenez, 1994. The Delta flume '93 experiment, in Coastal Dynamics '94, edited by A. S. Arcilla, N. C. Kraus, and S. J. F. Marcel, pp. 488–502, Am. Soc. of Civ. Eng., Reston, Va.

Ashton et al., 2001, Formation of coastline features by large-scale instabilities induced by high-angle waves, Nature 414, 296-300.

Battjes, J.A., 1974. Computation of set-up, longshore currents, run-up and overtopping due to wind-generated waves. Doct.Thesis, Delft Univ. of Technol., 244pp.

Battjes, J.A., 1975. Modelling of turbulence in the surfzone. Proceedings Symposium on Modeling Techniques. ASCE, New York, pp. 1050– 1061

Battjes, J.A. and Janssen, J.P.F.M., 1978. Energy loss and set-up due to breaking of random waves. Proc. 16th ICCE, Hamburg, pp. 569-587

Battjes, J.A. and Stive, M.J.F., 1985. Calibration and verification of a dissipation model for random breaking waves. J. Geophys. Res., 90 (C5): 9159-9167

Boers, M., 2005. Surf zone turbulence, Doct.Thesis, Delft University of Technology

D'Angremond, K., Pluim- van der Velden, 2001. Introduction to coastal engineering, lecture notes Delft University of Technology.

Deigaard, R., 1993. A note on the three dimensional shear stress distribution in a surf zone. Coast. Eng. 20, 157– 171.

Dean, R. G., 1977. Equilibrium beach profiles: US Atlantic and Gulf Coasts, Univ. of Del. Rep. 12, Dep. of Civ. Eng., Ocean Eng., Newark, N. J.

Van Dongeren van, A.R., Svendsen, I.A., 2000. Nonlinear 3D effects in leaky infragravity waves. Coast. Eng. 41, 467– 496.

Van Dongeren, A.R. et al. 1995, SHORECIRC: a quasi 3-D nearshore model, In: Coastal engineering 1994 : proceedings of the 24th international conference (October 23-28, 1994, Kobe, Japan), vol. 3 ; p. 2741-2754

Elias, E.P.L., Walstra, D.J.R., Roelvink, J.A., Stive, M.J.F., and Klein, M.D. Hydrodynamic validation of Delft3D with field measurements at Egmond. COAST3D program project number Z2394.20.

Fredsoe, J., Deigaard, R., 1992. Mechanics of Coastal Sediment Transport. World Scientific, Singapore.

Galappatti, R.,1983. A depth integrated model for suspended transport, Delft Univ. Rep. 83-7, Dep. of Civ. Eng., Delft Univ. of Technol., Delft, Netherlands.

Van der Graaff, J., 2004. Coastal Morphology & Coastal Protection, lecture notes Delft University of Technology

Longuet-Higgins, M.S., 1953. Mass transport in water waves. Philos. Trans. R. Soc. Lond., A, 535– 581.

Longuet-Higgins, M. S., and R. W. Stewart, 1964. Radiation stress in water waves, a physical discussion with applications, Deep Sea Res., 11, 529–563.

Mocke, G., Reniers, A.J.H.M., Smith, G., 1994. A surfzone parameter sensitivity analysis on LIP11D suspended sediment and return flow measurements. In: Coastal dynamics 1994: the role of large scale experiments in coastal engineering: international conference proceedings (Barcelona, Spain, February 21-25, 1994); p. 571-585

Nairn, R. B., J. A. Roelvink, and H. N. Southgate, 1990. Transition zone width and implications for modelling surfzone hydrodynamics, in Coastal Engineering Conference, 1990: Proceedings of the International Conference, edited by B. L. Edge, pp. 68 – 81, Am. Soc. of Civ. Eng., Reston, Va.

Reniers, A.J.H.M. and Battjes, J.A., 1996. A laboratory study of longshore currents over barred and non-barred beaches. Coastal Engineering, 30, 1-22.

Reniers, A.J.H.M., Thornton, E.B.,Stanton, T.P., and Roelvink, J.A., 2004. Vertical flow structure during Sandy Duck: observations and modeling. Coastal Engineering 51, pp. 237-260.

Van Rijn L.C., Walstra D.J.R., Ormondt van M., Description of TRANSPOR2004 and Implementation in Delft3D-ONLINE. WL|Delft Hydraulics report Z3748

Roelvink, J.A., 1993. Surf beat and its effect on cross-shore profiles. Ph. D. Thesis, Delft University of Technology.

Ruessink et al., 2003. Calibration and verification of a parametric wave model on barred beaches. Coastal Engineering. - Vol. 48 (2003) ; p. 139-149

Soulsby, R. L., L. Hamm, G. Klopman, D. Myrhaug, R. R. Simons, and G. P. Thomas, 1993. Wave-current interaction within and outside the bottom boundary layer, Coastal Eng., 21, 41–69.

Stelling, G. S., 1984. On the construction of computational methods for shallow water flow

Stive, M.J.F., Wind, H.G., 1986. Cross-shore mean flow in the surf zone. Coast. Eng. 10, 325–340.

Stokes, G. G., 1847. On the theory of oscillatory waves, Trans. Cambridge Philos. Soc., 8, 441–455.

Sun B. ,2004. Verification of Hydrodynamic and Morphodynamic Modelling on a Shoreface Nourishment at Egmond, The Netherlands. WL-report Z3624

Svendsen, I.A., 1984. Mass flux and undertow in a surf zone. Coast. Eng. 8, 347– 365.

Uijttewaal, W., 2006. Turbulence in hydraulics, lecture notes Delft University of Technology

De Vriend, H.J. and Stive, M.J.F., 1987. Quasi-3D Modelling of Nearshore Currents. In: P.P.G. Dyke (editor), JONSMOD ’86, Coastal Engineering, 11, pp. 565-601.

Walstra, D.J.R., G.P. Mocke, and F.Smit, Roller contributions as inferred from inverse modeling techniques, in Proceedings 25th International Coastal Engineering Conference, pp. 1205-1218, Am. Soc. of Civ. Eng., New York, 1996.

WL | Delft Hydraulics, 2005. Delft3D FLOW Manual

WL | Delft Hydraulics, 2005. Delft3D WAVE Manual

Zitman, T.J., 1993. Formulation of a quasi-3 dimensional flow model. Delft Hydraulics progress report H 840.10 part IV. Dongeren, A.R. van, Sancho, F.E., Svendsen, I.A. and Putrevu, U., 1994. SHORECIRC: a quasi 3-D Nearshore model. In: Coastal engineering 1994 : proceedings of the 24th international conference (October 23-28, 1994, Kobe, Japan), vol. 3 ; p. 2741-2754

A Description Delft3D

A.1 Introduction

The numerical model Delft3D is under continuous development. Different modes are available within Delft3D: 3D, 2DH, 2DV and 1D (Figure A.1)

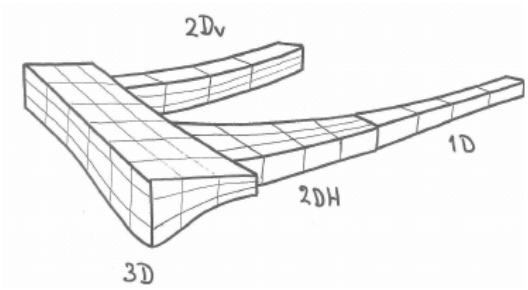

Figure A.1 Different modes of Delft3D

A.2 Hydrodynamics (Delft3D-Flow)

In Delft3D-FLOW a staggered grid is applied [FLOW-manual; *WL|Delft Hydraulics*, 2006]. This means that not all quantities are defined at the same location in the numerical grid. (Figure A.2) shows the locations on the grid where the different quantities are computed in the model; the water level points are defined in the middle of each cell and the current components are defined on the cell boundaries.

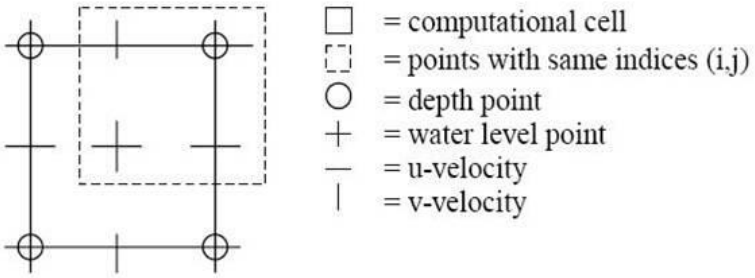

Figure A.2 Staggered grid used in Delft3D (source: Stelling, 1984)

Delft3D FLOW contains the shallow water equations, under the condition of some assumptions, like a hydrostatic pressure profile over the depth. The depth averaged equations (2DH) are developed from a combination between the momentum and continuity equation.

Continuity equation in two dimensions:

$$\frac{\partial \zeta}{\partial t} + \frac{\partial}{\partial x}(HU) + \frac{\partial}{\partial y}(HV) = 0 \qquad \text{(A.1)}$$

Momentum equation in two dimensions:

$$\frac{\partial U}{\partial t}+U\frac{\partial U}{\partial x}+V\frac{\partial U}{\partial y}=-g\frac{\partial \zeta}{\partial x}+fV+\nu_H\left[\frac{\partial^2 U}{\partial x^2}+\frac{\partial^2 U}{\partial y^2}\right]-\frac{gU\sqrt{U^2+V^2}}{HC^2}+\frac{\rho_{lucht}C_d W_x\sqrt{W_x^2+W_y^2}}{\rho_0 H} \quad \text{(A.2)}$$

$$\frac{\partial V}{\partial t}+U\frac{\partial V}{\partial x}+V\frac{\partial V}{\partial y}=-g\frac{\partial \zeta}{\partial y}-fU+\nu_H\left[\frac{\partial^2 V}{\partial x^2}+\frac{\partial^2 V}{\partial y^2}\right]-\frac{gV\sqrt{U^2+V^2}}{HC^2}+\frac{\rho_{lucht}C_d W_y\sqrt{W_x^2+W_y^2}}{\rho_0 H} \quad \text{(A.3)}$$

Wherein:

ζ	Water level according to some reference level
d	Depth towards some reference level (downwards is positive)
H	Total water depth ($H = d + \zeta$)
U, V	Depth averaged velocity in respectively x and y-direction
W_x, W_y	Wind speed in respectively x and y-direction
f	Coriolis parameter
g	Gravitational acceleration
C	Chezy-coefficient
C_d	Wind shear stress coefficient
ρ_0	Density of water
ρ_{air}	Density of air
ν_H	Horizontal eddy viscosity

A.2.1 Numerical stability

The Courant number gives an indication of the numerical stability and accuracy. In models that have large differences in the geometry or coastline, the Courant number should not exceed a value of 10. The Courant number for two-dimensional models is defined as (Stelling, 1984):

$$Cr = 2\Delta t\sqrt{gh\left(\frac{1}{\Delta x^2}+\frac{1}{\Delta y^2}\right)} \quad \text{(A.4)}$$

Wherein:

C_r	Courant number [-]
Δt	Time step [s]
g	Gravitational acceleration [m/s^2]
h	Local water depth [m]
$\Delta x, \Delta y$	Grid mesh size in respectively x and y direction [m]

By means of adjusting the time step the Courant number can be set. The Courant number reduces as the time step is decreased. However, the required computational time is increased when the time step is decreased. A time step of $\Delta t = 15s$ is sufficiently small not to violate the criterion C≤10, and it keeps the computational time to an allowable value.

A.3 Waves (Delft3D-Wave)

The wave module in Delft3D is based on the 3rd generation numerical model called SWAN (Simulating WAves Nearshore) (www.swan.tudelft.nl; Booy and Holthuijsen) to

simulate the evolution of random, short-crested wind-generated waves in coastal water, estuaries, tidal inlets and lakes [WAVE-manual; *WL|Delft Hydraulics*, 2006].

In SWAN the waves are described using the two-dimensional wave action density spectrum $N(\sigma,\theta)$ rather than the energy density spectrum $E(\sigma,\theta)$ since in the presence with currents, action density is conserved whereas energy density is not.
The action density function reads:

$$N(\sigma,\theta) = \frac{E(\sigma,\theta)}{\sigma} \tag{A.5}$$

N Action density
E Energy density
σ Relative radian frequency (as observed in a frame of reference moving with the current velocity)
θ direction (the direction normal to the wave crest of each spectral component)

In SWAN the evolution of the wave spectrum is described by the spectral action balance equation which for Cartesian co-ordinates is (e.g., Hasselmann et al., 1973):

$$\frac{\partial N}{\partial t} + \frac{\partial c_{g,x} N}{\partial x} + \frac{\partial c_{g,y} N}{\partial y} + \frac{\partial c_{\sigma} N}{\partial \sigma} + \frac{\partial c_{\theta} N}{\partial \theta} = \frac{\partial S_{tot}}{\partial \sigma} \tag{A.6}$$

In which:
$N = N(\sigma,\theta,x,y,t)$ Action density
$S = S(\sigma,\theta,x,y,t)$ Source term

The source term $S(f,\theta)$ can be divided into terms representing generation, wave-wave interaction and dissipation:

$$S(f,\theta) = S_{in}(f,\theta) + S_{nl}(f,\theta) + S_{diss}(f,\theta) \tag{A.7}$$

In which:
S_{in} Generation by wind
S_{nl} Non-linear wave-wave interactions representing triad wave-wave interaction S_{nl3} (shallow water) and quadruplet wave-wave interaction S_{nl4} (deep water).
S_{diss} Dissipation by white-capping S_{wc} bottom friction S_{bfr} and depth-induced (surf)breaking S_{surf}

A.4 Sediment Transport

Delft3D makes a distinction between bed load and suspended load transport. Bed load transport accounts for three components (Figure A.3):

- Bed-load due to currents S_{bc}
- Bed-load due to waves S_{bw}

Suspended load due to waves S_{sw}

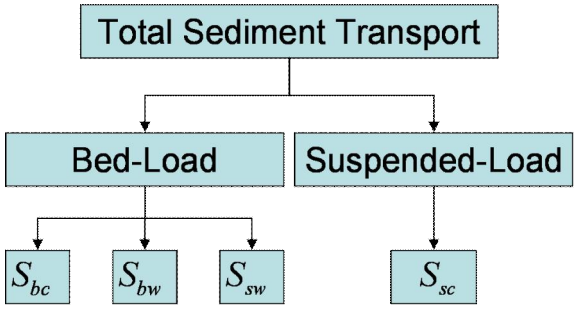

Figure A.3 Sediment transport components in Delft3D

A.4.1 Mathematical description

Sediment transport is computed by solving the transport (advection-diffusion) equation. The advection diffusion equation reads:

$$\frac{\partial[hc]}{\partial t}+\frac{\partial[hUc]}{\partial x}+\frac{\partial[hVc]}{\partial y}+\frac{\partial[wc]}{\partial \sigma}=h\left[\frac{\partial}{\partial x}\left(D_H\frac{\partial c}{\partial x}\right)+\frac{\partial}{\partial y}\left(D_H\frac{\partial c}{\partial y}\right)\right]+\frac{1}{h}\frac{\partial}{\partial \sigma}\left[D_V\frac{\partial c}{\partial \sigma}\right]+hS \qquad \text{(A.8)}$$

With h represents the water depth (m), U and V the flow components (m/s) consisting of the Eulerian flow velocities and stokes drift components if waves are included (Walstra et al., 2000), c is the mass concentration of sediment (kg/m^3), w is the vertical velocity component, S represents the contributions per unit area due to e.g. discharge or evaporation of water and D_H and D_V are the eddy diffusivities.

The Online Morphology version of Delft3D supplements the flow results with sediment transports. Different transport formulations are available.

Sediment exchange with the bed is implemented through source (D) and sink (E) relations following the Van Rijn (1993) approach.

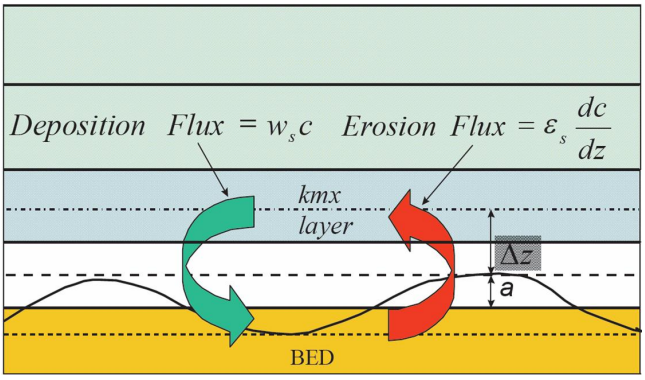

Figure A.4 Schematic arrangement of flux bottom boundary condition

This approach is based on the calculation of a reference sediment concentration at a reference height determined by bed roughness (based on Van Rijn 1984):

$$D = c_a \left(\frac{D_V}{\Delta z} \right) \tag{A.9}$$

And

$$E = c_{kmx} \left(\frac{D_V}{\Delta z} + w_s \right) \tag{A.10}$$

Where D_V is the vertical diffusion coefficient at the bottom of the reference cell (first cell above the reference height), Δz the vertical distance from the reference cell a to the centre of the reference cell (Van Rijn, 1993), and c_{kmx} the mass concentration in the reference cell (see Lesser, 2000 for implementation), w_s is the sediment settling velocity.

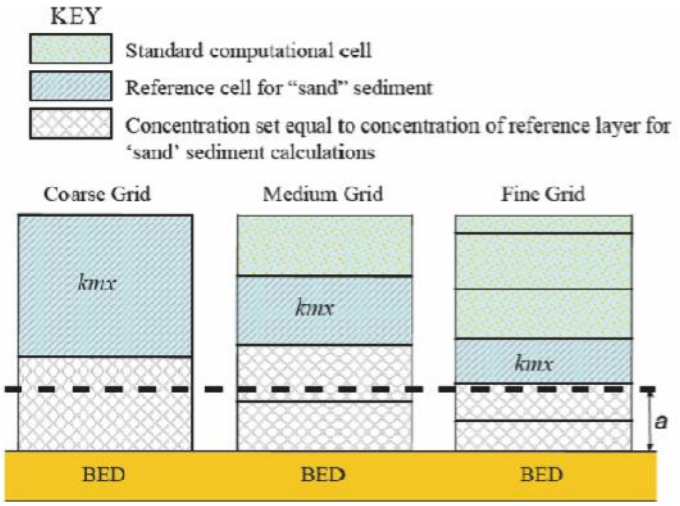

Figure A.5 Selection of kmx layer (a is the reference height according to Van Rijn 1993)

The sediment concentration at the reference height (c_a) is specified as:

$$c_a = f_{sus} \eta 0.015 \rho_s \frac{d_{50}}{a} \frac{T_a^{1.5}}{D_*^{0.3}} \tag{A.11}$$

In here f_{sus} is a calibration coefficient, η is the relative availability of the sediment fraction at the bed, ρ_s and d_{50} are respectively the mass density and grain size diameter of the soil, a the reference height, and T_a and D_* the dimensionless bed shear stress and particle diameter (Van Rijn, 1993, 2000).

A.4.2 Suspended load transport

For depth-averaged applications, the 3D advection-diffusion equation is approximated by the depth-integrated advection-diffusion equation:

$$\frac{\partial h\overline{c}}{\partial t}+\overline{u}\frac{\partial h\overline{c}}{\partial x}+\overline{v}\frac{\partial h\overline{c}}{\partial y}-D_H\frac{\partial^2 h\overline{c}}{\partial x^2}-D_H\frac{\partial^2 h\overline{c}}{\partial y^2}=h\frac{\overline{c}_{eq}-\overline{c}}{T_s} \tag{A.12}$$

Here h is the water depth, $\overline{u}$ and $\overline{v}$ are the depth-averaged velocity components in x- and y-direction, $\overline{c}$ is the depth-averaged sediment concentration, D_H the horizontal dispersion coefficient, and T_s is an adaptation time scale.

$$\overline{c}_{eq}=\frac{\left|S_{sus,eq}\right|}{\left|\overline{\vec{u}}\right|h} \tag{A.13}$$

Here, $S_{sus,eq}$ is the depth-averaged suspended sediment transport for steady and uniform conditions. There are two ways of specifying this transport rate, depending on the type of formulation used. In using a formulation developed for depth-averaged simulations, the existing algorithms provide $S_{sus,eq}$ directly and no further action is required. For formulations developed for 3D simulations, such as Van Rijn 1993 or 2004, $S_{sus,eq}$ has to be determined by (1DV) numerical integration:

$$S_{sus,eq}=\int_{z_b}^{z_s}u_{eq}\left(z\right)c_{eq}\left(z\right)dz \tag{A.14}$$

The equilibrium velocity profile is assumed to be logarithmic:

$$u_{eq}\left(z\right)=\overline{u}\frac{\ln\left(1+\frac{z}{z_0}\right)}{\ln\left(1+\frac{h}{ez_0}\right)} \tag{A.15}$$

The equilibrium concentration profile is computed by numerically integrating Schmidt's equation:

$$wc_{eq}\left(z\right)+D_v\left(z\right)\frac{\partial c_{eq}\left(z\right)}{\partial z}=0 \tag{A.16}$$

In here, $D_\upsilon(z)$ is the vertical dispersion coefficient as prescribed by Van Rijn (1993); the boundary condition is taken as $c_{eq}(z_{ref})=c_{ref}$, where the reference concentration is a function of the local bed shear stress.

A.4.3 Bed load transport

The Van Rijn (1993) formula distinguishes the following transport components that are all treated like bed or total load, i.e. without relaxation effects of an advection diffusion equation:

- Bed-load due to currents S_{bc}

- Bed-load due to waves S_{bw}
- Suspended load due to waves S_{sw}

Bed-Load transport rate
For simulations including waves the magnitude and direction of the bed-load transport on a horizontal bed are calculated using an approximation method developed by Van Rijn et al. (2003). The method computes the magnitude of the bed-load transport S_b as:

$$|S_b| = 0.006\rho_s w_s d_{50}^{(\ell)} M^{0.5} M_e^{0.7} \tag{A.17}$$

In here M represents the sediment mobility number due to waves and currents and M_e the excess sediment mobility number.

$$M = \frac{v_{eff}^2}{(s-1)gd_{50}} \tag{A.18}$$

$$M_e = \frac{(v_{eff} - v_{cr})^2}{(s-1)gd_{50}} \tag{A.19}$$

$$v_{eff} = \sqrt{v_R^2 + U_{on}^2} \tag{A.20}$$

With v_{cr} the critical depth-averaged velocity for initiation of motion.

The three separate transport modes are imposed separately. The direction of the bed-load due to currents S_{bc} is assumed to be equal to the direction of the current, whereas the two wave related transport components S_{bw} and S_{sw} take on the wave propagation direction. This results in the following transport components:

$$S_{bc,u} = \frac{u_{b,u}}{|u_b|}|S_{bc}|$$
$$S_{bc,v} = \frac{u_{b,v}}{|u_b|}|S_{bc}| \tag{A.21}$$

$$S_{bw,u} = S_{bw}\cos\phi$$
$$S_{bw,u} = S_{bw}\sin\phi \tag{A.22}$$

$$S_{sw,u} = S_{sw}\cos\phi$$
$$S_{sw,u} = S_{sw}\sin\phi \tag{A.23}$$

Where ϕ is the local angle between the direction of the wave propagation and the computational grid. The different components can be calibrated with *BedW, Bedw* and *SusW* keywords in the morphology input file.

A.5 Morphological module

The sediment transport and morphology (sub) module within Delft3D-FLOW supports both bed-load and suspended load transport of non-cohesive sediments and suspended load transport of cohesive sediments. The suspended load transport of non-cohesive and cohesive sediments is calculated by solving the advection-diffusion equation. The bed-load transport is calculated using a transport formula. In this model the advection-diffusion equation is only used to calculate the suspended load transport of non-cohesive sediments. In order to calculate bed load transport the transport formula of Van Rijn [2004] is applied: TRANSPOR2004 [Van Rijn et al., 2004].

B Roller Model

Investigation of model performance learned that model prediction of wave height decay were reasonably well in correspondence with wave height measurement through the surf zone, however, the location of initial set-up was predicted too far seaward. The roller model according to Nairn et al. (1990) has been incorporated in Delft3D-FLOW.

The idea is that the organised wave energy released at breaking, is first transferred to energy of a roller which rides on the wave front with the phase speed of the waves. The difference in velocity between the roller and the water particles at the wave front yields a shear stress between the roller and the underlying wave front. The work done by the shear stress equals the dissipation of roller energy. The time needed for the organised wave energy to dissipate through the roller causes a spatial time lag between the location of wave breaking and the actual dissipation.

Instead of being dissipated immediately after the breakpoint, organized wave energy is converted into turbulent kinetic energy first (which can be seen from the development of a roller at the face of a breaking wave), before being dissipated ultimately via the production of turbulence. In this way, the dissipation process is delayed, hence shifting the region of wave set-up in shoreward direction.

The roller acts on the set-up of the mean water level through the cross-shore momentum balance. This results in three coupled differential equations to model the wave transformation, being the time averaged wave energy balance, the energy balance for rollers in breaking waves and the cross-shore momentum balance to compute the set-up of the mean water level.

The energy balance for organised wave energy reads:

$$\frac{\partial}{\partial x}\left(Ec_g \cos(\alpha)\right) = -D_w - D_f \tag{B.1}$$

Where c_g is the wave group velocity, α the angle of incidence of the wave field, D_f the dissipation due to bottom friction and D_w the dissipation of wave energy due to breaking. Only the energy balance for rollers in breaking waves is discussed in this Appendix and yields:

$$\frac{\partial}{\partial x}\left(2E_r c \cos\alpha\right) = D_w - D_r \tag{B.2}$$

in here, c is the wave propagation speed, D_r the dissipation of roller energy and D_w the dissipation of organized wave energy which acts as a source term for the roller balance equation. The factor ‘2’ originates from additional dissipation of roller energy due to a net transfer of water from the wave to the roller (Stive and De Vriend, 1994).

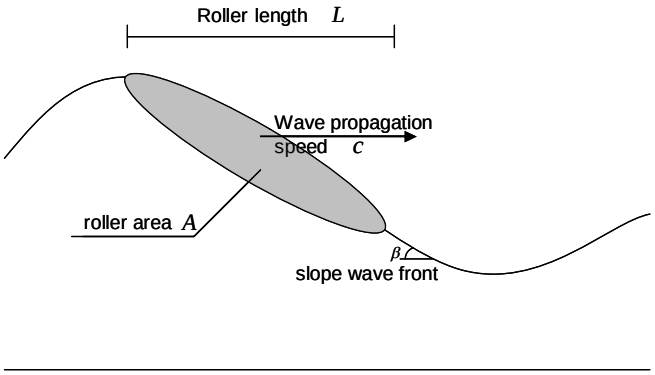

Figure B.1 Definition sketch roller model

The roller energy E_r represents the amount of kinetic energy in a roller with area A and length L , and is defined as:

$$E_r = \frac{\rho A c^2}{2L} \tag{B.3}$$

The roller energy balance is closed by modeling the dissipation of roller energy D_r as the power per unit length performed by the shear stress between roller and water surface:

$$D_r = \beta \rho g c \frac{A}{L} = 2\beta g \frac{E_r}{c} \tag{B.4}$$

In which β represents the slope of the wave front (normally between 0.05-0.10) and A is written in terms of E_r via equation (B.3).

The storage of wave energy and momentum depends on the value of β . Large values correspond to instantaneous dissipation, resulting a small roller area, and vice versa. The wave slope is not known a priori, but the cross-shore momentum equation can be used to obtain a good estimate, given the fact that the roller contributes to the set-up of the mean water level.

C Velocity Distribution

C.1 Eddy viscosity distribution

The vertical eddy viscosity distribution is assumed with a parabolic function.

$$\nu_t = \phi_s \bar{\nu}_t \sigma \left(\sigma_s - \sigma \right) \tag{C.1}$$

The upper vertical position where the eddy viscosity equals zero σ_s is assumed to be one in the case of purely slope driven currents. In other words, the eddy viscosity at the surface level becomes zero. In the presence of purely wind driven turbulence, the eddy viscosity will reach its maximum at the surface. This results in a σ_s of 2.

In the presence of breaking waves and wind, some additional turbulence is added in the upper layer. This means an increasing eddy viscosity at the surface level (which in the absence of wind and waves will be zero).

$$\nu_{t,surface} = \frac{3}{2} \sqrt{\bar{\nu}^2_{t,wind} + \bar{\nu}^2_{t,wave}} \tag{C.2}$$

The value of will range between 1 and 2

$$\sigma_s = \frac{\bar{\nu}_t - \frac{1}{3}\nu_{t,surface}}{\bar{\nu}_t - \frac{1}{2}\nu_{t,surface}} \tag{C.3}$$

Now that the shape of the eddy viscosity is determined, it only has to be scaled. This is done with the scale factor ϕ_s. This scale factor is calculated with the condition that the total depth integrated eddy viscosity must compensate for the total depth-averaged eddy viscosity.

$$\int_0^1 \phi_s \sigma \left(\sigma_s - \sigma \right) d\sigma = 1 \tag{C.4}$$

Hence,

$$\phi_s = \frac{1}{\frac{1}{2}\sigma_s - \frac{1}{3}} \tag{C.5}$$

In the bottom boundary layer an additional turbulence is added due to bed friction compared to the middle layer.

$$\nu_t = \left(\phi_s \bar{\nu}_t + \phi_b \bar{\nu}_{tb} \right) \sigma \left(\sigma_b - \sigma \right) \tag{C.6}$$

In here σ_b represents the upper level at which the eddy viscosity of the wave boundary layer equals zero.

$$\sigma_b = \frac{\phi_s \bar{\nu}_t \sigma_s + \phi_b \bar{\nu}_{tb} \delta}{\phi_s \bar{\nu}_t + \phi_b \bar{\nu}_{tb}} \tag{C.7}$$

The scale function for the wave boundary layer is calculated in the same way as the one for the middle layer:

$$\frac{1}{\delta} \int_0^{\delta} \phi_b \sigma \left(\delta - \sigma \right) d\sigma = 1 \tag{C.8}$$

Which yields:

$$\phi_b = \frac{6}{\delta^2} \tag{C.9}$$

C.2 Velocity profile

From equation (2.39) the velocity gradient can be written as:

$$\frac{\partial u_i}{\partial \sigma} = \frac{h}{\rho \phi_s \bar{\nu}_t} \left(\frac{\left(\tau_{s,i} + F_i \left(\sigma - 1 \right) \right)}{\sigma \left(\sigma_s - \sigma \right)} \right) \qquad \sigma > \delta \tag{C.10}$$

$$\frac{\partial u_i}{\partial \sigma} = \frac{h}{\rho \left(\phi \bar{\nu} \right)_b} \left(\frac{\left(\tau_{s,i} + \left(F_i + \frac{D_f k_i}{\omega} \right) \left(\sigma - 1 \right) \right)}{\sigma \left(\sigma_b - \sigma \right)} \right) \qquad \sigma < \delta \tag{C.11}$$

These equations can be rewritten in the following form:

$$\frac{\partial u_i}{\partial \sigma} = A \left(\frac{\left(B_i + C_i \sigma \right)}{\sigma \left(\sigma_s - \sigma \right)} \right) \qquad \sigma > \delta \tag{C.12}$$

$$\frac{\partial u_i}{\partial \sigma} = A_b \left(\frac{\left(B_{b,i} + C_{b,i} \sigma \right)}{\sigma \left(\sigma_b - \sigma \right)} \right) \qquad \sigma < \delta \tag{C.13}$$

In which the coefficients are given by:

$$A = \frac{h}{\rho \phi_s \bar{\nu}_t} \qquad B_i = \tau_{s,i} - F_i \qquad C_i = F_i$$

$$A_b = \frac{h}{\rho \left(\phi \bar{\nu} \right)_b} \qquad B_{b,i} = \tau_{s,i} - F_i + \frac{D_f k_i}{\omega} \qquad C_{b,i} = F_i - \frac{D_f k_i}{\omega}$$

C.3 Integration wave boundary layer

To obtain the velocity in the bottom boundary layer, equation (C.13) has to be integrated. With the no slip boundary condition $u_i = 0$ at $\sigma = \sigma_0$ the velocity in the wave boundary layer becomes:

$$u_i = A_b \left(\frac{B_{b,i}}{\sigma_b} \ln \frac{\sigma}{\sigma_0} - \left(\frac{B_{b,i}}{\sigma_b} + C_{b,i} \right) \ln \frac{\sigma_b - \sigma}{\sigma_b - \sigma_0} \right) \tag{C.14}$$

This equation is valid for $\sigma > e\sigma_0$ below this level, a linear velocity decay toward the bottom is used.

The velocity at the top of this layer ($\sigma = \delta$)is used as a boundary condition for the middle layer:

$$u_{\delta,i} = A_b \left(\frac{B_{b,i}}{\sigma_b} \ln \frac{\delta}{\sigma_0} - \left(\frac{B_{b,i}}{\sigma_b} + C_{b,i} \right) \ln \frac{\sigma_b - \delta}{\sigma_b - \sigma_0} \right) \tag{C.15}$$

The contribution of the velocity in the bottom boundary layer to the (total)depth-averaged velocity follows from integration of equation (C.14).

$$\int_{\sigma_0}^{\delta} u_i d\sigma = \frac{A_b}{\sigma_b} \left(\delta \ln \frac{\delta}{\sigma_0} + (\sigma_b - \delta) \ln \frac{\sigma_b - \delta}{\sigma_b - \sigma_0} \right) B_{b,i} + A_b \left((\sigma_b - \delta) \ln \frac{\sigma_b - \delta}{\sigma_b - \sigma_0} + (\delta - \sigma_0) \right) C_{b,i} \tag{C.16}$$

C.4 integration middle layer

To obtain the velocity in the middle layer, equation (C.12) has to be integrated with the boundary condition that the velocity at the bottom of the middle layer matches the velocity at the top of the wave boundary layer $u_{\delta,i}$:

$$u_i = u_{\delta,i} + A \left(\frac{B_i}{\sigma_s} \ln \frac{\sigma}{\delta} - \left(\frac{B_i}{\sigma_s} + C_i \right) \ln \frac{\sigma_s - \sigma}{\sigma_s - \delta} \right) \tag{C.17}$$

The contribution of the velocity in the middle layer to the depth-averaged velocity follows after integration of equation (C.17)

$$\int_{\delta}^{1} u_i d\sigma = u_{\delta,i} (1 - \delta) + \frac{A}{\sigma_s} \left(\ln \frac{1}{\delta} + (\sigma_s - 1) \ln \frac{\sigma_s - 1}{\sigma_s - \delta} \right) B_i + A \left((\sigma_s - 1) \ln \frac{\sigma_s - 1}{\sigma_s - \delta} + (1 - \delta) \right) C_i \tag{C.18}$$

C.5 Depth Mean Velocity

The depth mean velocity components are computed by the integral of the velocity components from $\sigma = 0$ to $\sigma = 1$(for simplicity the integration is carried out from $\sigma = \sigma_0$ till mean water level instead of integration from bottom $\sigma = 0$ till wave trough).

$$\begin{aligned}\bar{u}_i &\approx \frac{1}{1-\sigma_0}\int_{\sigma_0}^{1} u_i d\sigma \approx \int_{\sigma_0}^{\delta} u_i d\sigma + \int_{\delta}^{1} u_i d \\ &= \frac{A_b}{\sigma_b}\left(\ln\frac{\delta}{\sigma_0} + (\sigma_b-\delta)\ln\frac{\sigma_b-\delta}{\sigma_b-\sigma_0}\right)B_{b,i} + A_b\left((\sigma_b-\delta)\ln\frac{\sigma_b-\delta}{\sigma_b-\sigma_0} + (\delta-\sigma_0)\right)C_{b,i} \\ &\quad + u_{\delta,i}(1-\delta) + \frac{A}{\sigma_s}\left(\ln\frac{1}{\delta} + (\sigma_s-1)\ln\frac{\sigma_s-1}{\sigma_s-\delta}\right)B_i + A\left((\sigma_s-1)\ln\frac{\sigma_s-1}{\sigma_s-\delta} + (1-\delta)\right)C_i\end{aligned} \tag{C.19}$$

This becomes:

$$\bar{u}_i = G_b B_{b,i} + H_b C_{b,i} + G B_i + H C_i \tag{C.20}$$

With the coefficients given by:

$$G_b = \frac{A_b}{\sigma_b}\left(\ln\frac{\delta}{\sigma_0} + (\sigma_b-\delta)\ln\frac{\sigma_b-\delta}{\sigma_b-\sigma_0}\right) \tag{C.21}$$

$$H_b = A_b\left((\sigma_b-\delta)\ln\frac{\sigma_b-\delta}{\sigma_b-\sigma_0} + (\delta-\sigma_0)\right) \tag{C.22}$$

$$G = \frac{A}{\sigma_s}\left(\ln\frac{1}{\delta} + (\sigma_s-1)\ln\frac{\sigma_s-1}{\sigma_s-\delta}\right) \tag{C.23}$$

$$H = A\left((\sigma_s-1)\ln\frac{\sigma_s-1}{\sigma_s-\delta} + (1-\delta)\right) \tag{C.24}$$

D Description Validation Cases

Four different cases were used to validate the Q3D method of Delft3D. This chapter will give a short description of the different validation cases.

D.1 Description LIP11D Flume Experiment (1993)[2]

Within the framework of the European Large Installation Plan (LIP) a programme of detailed measurements of hydrodynamics and sediment transport in the surf zone has been carried out in Delft Hydraulics delta flume. The aim of this project was to generate hydro- and morpho-dynamic data on a natural 2DV beach under equilibrium, erosive and accretive conditions. Tests were done with different wave conditions, and bed profiles.

D.1.1 Bottom profile

The geometry of the beach consisted of a Dean-type with constant slope near and above the water line. With the grain diameter of 220 μ , a so-called equilibrium parabolic beach profile of bruun-dean-moore was adapted. The initial bottom profile became:

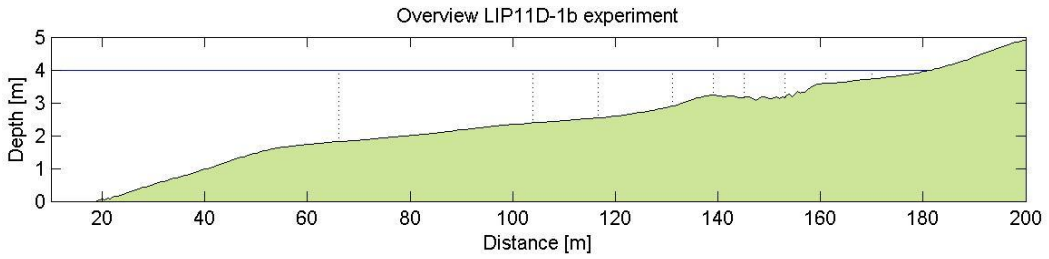

Figure D.1 Bottom Profile LIP11D-1b experiment with initial water level (blue) and velocity measurement locations (dotted lines)

D.1.2 Wave Conditions

Narrow banded, random waves were chosen such that the wave steepness at the peak frequency in combination with the water level were expected to result in a stable, erosive and accretive beach, consecutively.

test code	Initial geometry	H_{m0} [m]	T_p [s]	water level [m]	Duration [h]
1a	Dean-type	0.9	5	4.1	12
1b	result of 1a	1.4	5	4.1	18
1c	result of 1b	0.6	8	4.1	13
2a	Dean-type with dune	0.9	5	4.1	12
2b	result of 2a	1.4	5	4.1	12
2e	result of 2b	1.4	5	4.6	18
2c	result of 2e	0.6	8	4.1	21

Table D.1 Test conditions LIP11D experiments

2. *Source: LIP 11D Delta Flume Experiments, January 1995*

D.1.3 Measurements

At different locations some measurements were done. With an EMF current meter positioned at one third of the water depth, the velocities were measured at 5 different positions.

D.1.4 Model Schematization

Numerical grid

The grid size decreases in onshore direction. The maximum grid size is 2 m (offshore) and the minimum 1m (onshore).

Processes

Waves are modelled by constant conditions.

H_s[m]	T_p[s]	Direction [degree]	Mean sea level [m]
1.2162	5	270	4

Table D.2 Wave conditions

Boundary conditions

Three boundary conditions are needed to model the LIP11D experiment. For both the north and the south boundary, the Neumann conditions are used. A constant water level is imposed at the sea boundary.

Parameter settings

	Parameter	Value	Description
FLOW	Δt	0.02	Flow time step [s]
	g	9.81	Gravitational acceleration [m/s^2]
	ρ_w	1000	Water density [kg/m^3]
	ρ_a	1	Air density [kg/m^3]
	ROUwav	VR04	Stress formulation due to wave forces [Van Rijn 2004]
	Vicouv	0.5	Horizontal eddy viscosity [m^2/s]
	Dicouv	0.01	Horizontal eddy diffusivity [m^2/s]
	Dryflc	0.05	Threshold depth drying and flooding[m]
	Dco	1	Marginal depth in shallow areas [m]
	Trtrou	Y	Flag for roughness predictor
	Trtdef	vrijn2004	Definition of the roughness predictor [Van Rijn 2004]
	Trtu & Trtv	trtuv	Specification of grid characteristics
	TrtDt	2	Time step used in roughness predictor
	TraFrm	vrijn2004	Transport Formula [Van Rijn 2004]
	CSTbnd	yes	Boundary condition: water level offshore and lateral Neumann boundaries
	Roller	yes	turn on Roller model
	F_lam	0	
	fwfac	0	tuning parameter for wave streaming [-]
	Roumet	W	
	Ccofu & Ccofv	0.05	
MOR	MORFAC	10	Morphological scale factor [-]
	EspPar	True	Vertical mixing distribution according to van Rijn
	Dn50	250	Median grain diameter [µm]

MorStt	10	Spin-up interval for morphological changes [min]
Thresh	0.25	Threshold sediment thickness for transport and erosion reduction [m]
EqmBC	TRUE	Equilibrium sediment concentration profile at inflow boundaries
Densin	FALSE	Include effect of sediment on water density
Aksfac	1.0	Van Rijns reference height (Aksfac*k_s) [-]
Rwave	1	Wave related roughness (Rwave*estimated ripple height) [-]
AlphaBs	1	Stream wise bed gradient factor for bed load transport [-]
AlphaBn	1.5	Transverse bed gradient factor for bed load transport [-]
Sus	1.0	Multiplication factor for suspended sediment reference concentration factor [-]
Bed	1.0	Multiplication factor for bed-load transport vector magnitude factor [-]
SusW	1.0	Wave related suspended sediment transport factor [-]
BedW	1.0	Wave related bed load sediment transport factor [-]
SedThr	0.1	Minimum water depth for sediment computations [m]
ThetSD	1.0	Factor for erosion of adjacent dry cells
HMaxTH	0.2	Maximum depth for variable ThetSD [m]
FWFac	0	Tuning parameter for wave streaming [-]
Dzmax	0.05	Maximum bed level change per time step: percentage of the water depth [%]

Table D.3 Model settings

D.2 Description Boers experiment (1995)[3]

Measurements of surf-zone turbulence are very rare, because of technical difficulties and high expenses.
The possibilities for validation of surf zone turbulence models are limited. There are only a few rather inaccurate field data while most of the existing laboratory data come from experiments with regular waves on a plane slope. Therefore, Marien Boers did in 1995 some new experiments in the large wave flume of the fluid mechanics laboratory of the Delft University of Technology.

Measurements were done for three different irregular wave conditions exposed on a bared beach.

test	H_{m0} **[m]**	T_p **[s]**	**measured** H_{m0} **[m]**	**Measured** T_p **[s]**
1a	0.150	2.1	0.157	2.05
1b	0.220	2.1	0.206	2.03
1c	0.107	3.4	0.103	3.33

Table D.4 Test conditions Boers experiment

3. Surf zone turbulence, Marien Boers

The tests were done for the same bottom profile used for the LIP11D-experiments described in section D.1 with a scale factor of 5.6.

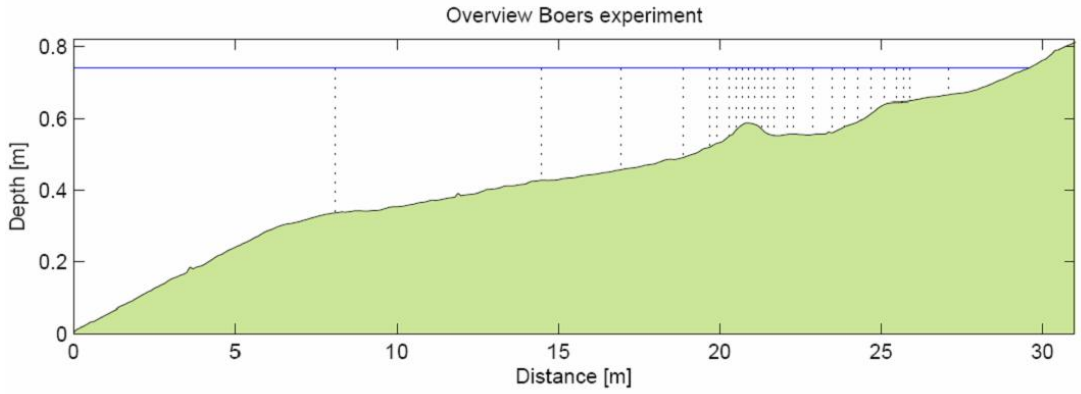

Figure D.2 Bottom profile Boers-1b experiment with water level (blue line) and velocity measurement locations (dotted line)

Measurements were carried out with wave gauges, laser-Doppler velocimeters, an electromagnetic flow meter, a shear stress plate and a video camera. Measuring data comprise wave heights, wave set-up, the phase velocity, the fraction of waves with a roller, the undertow, the orbital velocity, the turbulent velocity, the transport of turbulent kinetic energy, the mass flux, turbulent shear stresses and bed shear stresses.

D.2.1 Model Schematization

Parameter settings

	Parameter	Value	Description
FLOW	Δt	0.02	Flow time step [s]
	g	9.81	Gravitational acceleration [m/s^2]
	ρ_w	1000	Water density [kg/m^3]
	ρ_a	1	Air density [kg/m^3]
	ROUwav	VR04	Stress formulation due to wave forces [Van Rijn 2004]
	Vicouv	0.5	Horizontal eddy viscosity [m^2/s]
	Dicouv	0.01	Horizontal eddy diffusivity [m^2/s]
	Dryflc	0.05	Threshold depth drying and flooding[m]
	Dco	1	Marginal depth in shallow areas [m]
	Trtrou	Y	Flag for roughness predictor
	Trtdef	vrijn2004	Definition of the roughness predictor [Van Rijn 2004]
	Trtu & Trtv	trtuv	Specification of grid characteristics
	TrtDt	2	Time step used in roughness predictor
	TraFrm	vrijn2004	Transport Formula [Van Rijn 2004]
	CSTbnd	yes	Boundary condition: water level offshore and lateral Neumann boundaries
	Roller	yes	turn on Roller model
	F_lam	0	
	fwfac	0	tuning parameter for wave streaming [-]
	Roumet	W	

	Ccofu & Ccofv	0.05	
MOR	MORFAC	10	Morphological scale factor [-]
	EspPar	True	Vertical mixing distribution according to Van Rijn
	Dn50	250	Median grain diameter [µm]
	MorStt	60	Spin-up interval for morphological changes [min]
	Thresh	0.05	Threshold sediment thickness for transport and erosion reduction [m]
	EqmBC	TRUE	Equilibrium sediment concentration profile at inflow boundaries
	Densin	FALSE	Include effect of sediment on water density
	Aksfac	1.0	Van Rijns reference height (Aksfac*k_s) [-]
	Rwave	1	Wave related roughness (Rwave*estimated ripple height) [-]
	AlphaBs	1	Stream wise bed gradient factor for bed load transport [-]
	AlphaBn	1.5	Transverse bed gradient factor for bed load transport [-]
	Sus	1.0	Multiplication factor for suspended sediment reference concentration factor [-]
	Bed	1.0	Multiplication factor for bed-load transport vector magnitude factor [-]
	SusW	0.2	Wave related suspended sediment transport factor [-]
	BedW	0.2	Wave related bed load sediment transport factor [-]
	SedThr	0.1	Minimum water depth for sediment computations [m]
	ThetSD	1.0	Factor for erosion of adjacent dry cells
	HMaxTH	1.5	Maximum depth for variable ThetSD [m]
	FWFac	0	Tuning parameter for wave streaming [-]
	Dzmax	0.05	Maximum bed level change per time step: percentage of the water depth [%]

D.3 Description Reniers Experiment (1994)[4]

Several measurements were performed in a large basin with a pump recirculation system to create spatially homogeneous longshore currents. Unidirectional obliquely incident waves (regular and random) were used on barred and non-barred beaches to get information on wave transformation, set-up of the mean water level and the cross-shore distribution of wave-driven longshore current velocity.

Measurements were done with eight electromagnetic flow meters (EMF) mounted on a mobile carriage. During the experiment, the carriage could be moved along the beach, thus giving the possibility to measure at any transect between inflow and outflow openings. Ten resistant type wave gauges were also mounted on the carriage to monitor the wave transformation and set-up of the mean water level.

4. A laboratory study of longshore currents over barred and non-barred beaches

The measurements were performed on a barred concrete slope (Figure D.3). Lowering the water below the bar crest, to a level where overtopping did not occur, allowed measuring the currents on a non barred beach.

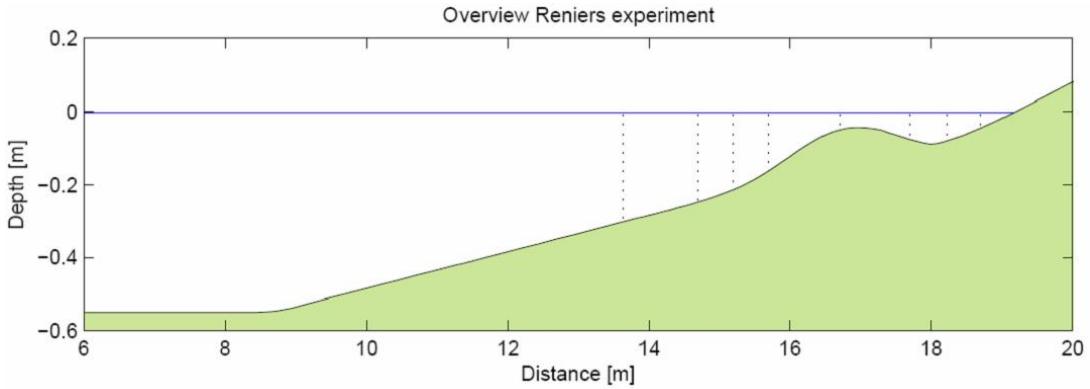

Figure D.3 Bottom profile Reniers SO014 experiment with water level (blue line) and velocity measurement locations (dotted line)

The roughness of the smooth concrete bottom is estimated at ks=0.0005 m.

D.3.1 Test conditions

The Reniers experiment was done for five different test conditions. The angle of wave incidence was 30 for all wave conditions.

test description	test	d(cm)	H(cm)	T(s)
regular waves + barred beach	SA243	55.0	8.0	1.0
regular waves + barred beach	SA537	55.0	8.0	2.0
random waves + barred beach	SO014	55.0	7.0	1.2
regular waves + barred beach	SA337	55.0	10.0	1.0
regular waves + non barred beach	SC219	45.0	8.0	1.0

Table D.5 Test conditions Reniers experiment

The objective of this experiment is to examine the cross-shore distribution of the longshore current velocities for purely wave-driven currents (without an alongshore pressure gradient) with emphasis on the position of maximum current velocity with respect to areas where wave energy is dissipated.

D.3.2 Model schematization

Parameter settings

	Parameter	Value	Description
FLOW	Δt	0.02	Flow time step [s]
	g	9.81	Gravitational acceleration [m/s^2]
	ρ_w	1000	Water density [kg/m^3]
	ρ_a	1	Air density [kg/m^3]
	ROUwav	VR04	Stress formulation due to wave forces [Van Rijn 2004]
	Vicouv	0.0005	Horizontal eddy viscosity [m^2/s]
	Dicouv	0.01	Horizontal eddy diffusivity [m^2/s]
	Dryflc	0.05	Threshold depth drying and flooding[m]

	Dco	1	Marginal depth in shallow areas [m]
	Trtrou	Y	Flag for roughness predictor
	Trtdef	vrijn2004	Definition of the roughness predictor [Van Rijn 2004]
	Trtu & Trtv	trtuv	Specification of grid characteristics
	TrtDt	2	Time step used in roughness predictor
	TraFrm	vrijn2004	Transport Formula [Van Rijn 2004]
	CSTbnd	yes	Boundary condition: water level offshore and lateral Neumann boundaries
	Roller	yes	turn on Roller model
	F_lam	0	
	fwfac	0	tuning parameter for wave streaming [-]
	Roumet	W	
	Ccofu & Ccofv	0.0005	
MOR	MORFAC	10	Morphological scale factor [-]
	EspPar	True	Vertical mixing distribution according to Van Rijn
	Dn50	250	Median grain diameter [µm]
	MorStt	60	Spin-up interval for morphological changes [min]
	Thresh	0.05	Threshold sediment thickness for transport and erosion reduction [m]
	EqmBC	TRUE	Equilibrium sediment concentration profile at inflow boundaries
	Densin	FALSE	Include effect of sediment on water density
	Aksfac	1.0	Van Rijns reference height (Aksfac*k_s) [-]
	Rwave	1	Wave related roughness (Rwave*estimated ripple height) [-]
	AlphaBs	1	Stream wise bed gradient factor for bed load transport [-]
	AlphaBn	1.5	Transverse bed gradient factor for bed load transport [-]
	Sus	1.0	Multiplication factor for suspended sediment reference concentration factor [-]
	Bed	1.0	Multiplication factor for bed-load transport vector magnitude factor [-]
	SusW	0.2	Wave related suspended sediment transport factor [-]
	BedW	0.2	Wave related bed load sediment transport factor [-]
	SedThr	0.1	Minimum water depth for sediment computations [m]
	ThetSD	1.0	Factor for erosion of adjacent dry cells
	HMaxTH	1.5	Maximum depth for variable ThetSD [m]
	FWFac	0	Tuning parameter for wave streaming [-]
	Dzmax	0.05	Maximum bed level change per time step: percentage of the water depth [%]

D.4 Description Egmond field case (1998)[5]

In the framework of the Coast3D project a measurement campaign was conducted at Egmond, the Netherlands, during the spring of 1998. The site has been selected as representative for an alongshore relatively uniform coast. The instrumental lay-out was chosen to allow for validation of numerical models for the nearshore. Not only a dense spatial coverage of the modelling area is available, but also detailed measurements of boundary conditions, like wind filed, deep water wave height and water levels.

Two measurement campaigns were conducted near the town of Egmond in 1998. The pilot campaign is held from 20 April till 5 May, while data is available from 30 April to 5 May. The main experiment is held from 12 October till 20 November, while the majority of the data is available from 15 October to 15 November. The dataset from the pilot campaign is used in this study to evaluate the Q3D model.

D.4.1 Field site

The Egmond site is located in the central part of the Dutch coast, the 120 km long, uninterrupted beach between Den Helder and Hoek van Holland. The Dutch coast faces the North Sea and is exposed to sea waves and swell. The tidal wave which finds its origin on the Atlantic Ocean enters the basin of the North Sea in the north. The coriolis force causes the tidal wave to rotate anti clockwise in the tidal basin. Gradients both in phase and in amplitude occur along the Dutch coast.

The choice of the beach near Egmond as one of the locations in the Coast3D project is justified by the fact that there are no hydraulic structures in the vicinity. Besides, the large-scale bathymetry can be characterised as an uniform, straight coast with parallel depth contours. Detailed description of the system of the Dutch coast can be found in Stive et al. (1990) and Wijnberg (1995).

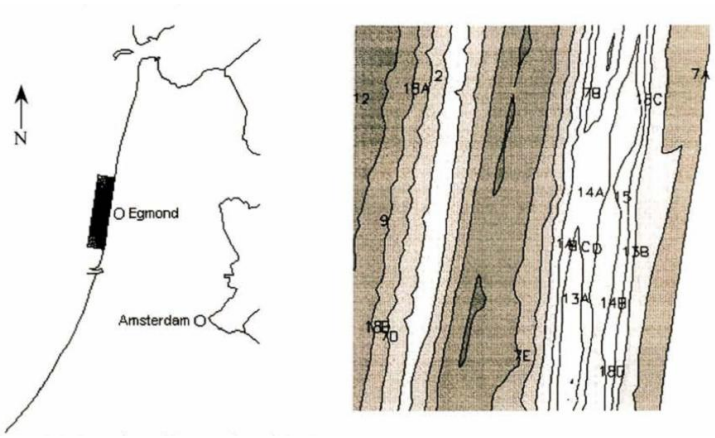

Figure D.4 Overview Egmond area (Netherlands) including observation points

This part of the Dutch coast is typical for the quasi-uniform sandy beaches dominated by breaker bars found on much of the coastlines of Northwest France, Belgium, The Netherlands, Germany, Denmark and England. Two breaker bars run parallel to the wave-dominated, sandy coast. The outer breaker bar is situated 500 m offshore (measured from the intersection between the beach and MSL plane), while the crest level 2.5 m below MSL. The inner breaker bar is located 200 m offshore and has its crest level 1 m below MSL. The cross-shore slope amounts to 1:100 and the median grain size is about 200 µm.

5. *Hydrodynamic validation of Delft3D with field measurements at Egmond*

The small-scale morphology shows irregularities in the large scale uniform pattern. Rip channels interrupt breaker bars and small, local bars are present. The small-scale morphology proved to be highly variable in the main experiment.

The Coast3D field site is an area of 500 m (longshore) by 600 m (cross-shore). In this area a main transect is defined. A large number of instruments are placed in this transect (among other: Stations 1A to 1D and station 18a).

D.4.2 Measurements

The pilot campaign is characterised by calm weather and uni-directional wind with waves from North-North-westerly direction. The first two days of the campaign are calm (maximum, significant, deep water wave height of 1.5 m), the following days are windier (maximum, significant, deep water wave height of 2.75 m) and the last day is calm again.

Hydraulic quantities are measured in and around the field site. Deep water wave height, period and direction are measured with poles located further offshore. Five kilometres in front of the field site, in 15 m deep water, a DIWAR directional wave buoy (Station 8) is placed. Near this buoy an ADCP (station 9) is placed in order to have current velocity information in both horizontal directions at different elevations.

In the main transect, all relevant hydraulic quantities are measured. This main transect consists of 6 stations, which are again surrounded by other instruments. The DIWAR at station 8 is part of this transect. Station 18A, placed just offshore of the outer breaker bar, is the second station. Four maxi-frames, indicated as stations 1A-D, are situated in front of, on top of and behind the inner breaker bar, with a mutual distance of 25 m.

D.4.3 Model schematization

Parameter settings

	Parameter	Value	Description
FLOW	Δt	0.25	Flow time step [s]
	g	9.81	Gravitational acceleration [m/s^2]
	ρ_w	1000	Water density [kg/m^3]
	ρ_a	1	Air density [kg/m^3]
	ROUwav	VR04	Stress formulation due to wave forces [Van Rijn 2004]
	Vicouv	0.5	Horizontal eddy viscosity [m^2/s]
	Dicouv	0.01	Horizontal eddy diffusivity [m^2/s]
	Dryflc	0.05	Threshold depth drying and flooding[m]
	Dco	1	Marginal depth in shallow areas [m]
	Trtrou	Y	Flag for roughness predictor
	Trtdef	vrijn2004	Definition of the roughness predictor [Van Rijn 2004]
	Trtu & Trtv	trtuv	Specification of grid characteristics
	TrtDt	2	Time step used in roughness predictor
	TraFrm	vrijn2004	Transport Formula [Van Rijn 2004]
	CSTbnd	yes	Boundary condition: water level offshore and lateral Neumann boundaries
	Roller	yes	turn on Roller model

	F_lam	0	
	fwfac	0	tuning parameter for wave streaming [-]
	Roumet	C	
	Ccofu & Ccofv	50	
MOR	MORFAC	1	Morphological scale factor [-]
	EspPar	True	Vertical mixing distribution according to Van Rijn
	Dn50	250	Median grain diameter [µm]
	MorStt	720	Spin-up interval for morphological changes [min]
	Thresh	0.05	Threshold sediment thickness for transport and erosion reduction [m]
	EqmBC	TRUE	Equilibrium sediment concentration profile at inflow boundaries
	Densin	FALSE	Include effect of sediment on water density
	Aksfac	1.0	Van Rijns reference height (Aksfac*k_s) [-]
	Rwave	2	Wave related roughness (Rwave*estimated ripple height) [-]
	AlphaBs	1	Stream wise bed gradient factor for bed load transport [-]
	AlphaBn	1.5	Transverse bed gradient factor for bed load transport [-]
	Sus	1.0	Multiplication factor for suspended sediment reference concentration factor [-]
	Bed	1.0	Multiplication factor for bed-load transport vector magnitude factor [-]
	SusW	1.0	Wave related suspended sediment transport factor [-]
	BedW	1.0	Wave related bed load sediment transport factor [-]
	SedThr	0.1	Minimum water depth for sediment computations [m]
	ThetSD	0.0	Factor for erosion of adjacent dry cells
	HMaxTH	1.52	Maximum depth for variable ThetSD [m]
	FWFac	0	Tuning parameter for wave streaming [-]
	Dzmax	0.05	Maximum bed level change per time step: percentage of the water depth [%]

E Derivation of the Momentum Equation for Secondary Currents

Substitution of the primary and secondary currents in the momentum equation in the x-direction leads to the following expression:

$$\begin{aligned}
&\frac{\partial u_p}{\partial t}+u_p\frac{\partial u_p}{\partial x}+v_p\frac{\partial u_p}{\partial y}+w_p\frac{\partial u_p}{\partial z}-f_c v_p\\
&+\frac{\partial u_s}{\partial t}+u_s\frac{\partial u_s}{\partial x}+v_s\frac{\partial u_s}{\partial y}+w_s\frac{\partial u_s}{\partial z}-f_c v_s\\
&+u_s\frac{\partial u_p}{\partial x}+v_s\frac{\partial u_p}{\partial y}+w_s\frac{\partial u_p}{\partial z}+u_p\frac{\partial u_s}{\partial x}+v_p\frac{\partial u_s}{\partial y}+w_p\frac{\partial u_s}{\partial z}=\\
&-\frac{1}{\rho}\frac{\partial p_n}{\partial x}+\frac{\partial}{\partial x}\left(\nu_t\frac{\partial u_p}{\partial x}\right)+\frac{\partial}{\partial y}\left(\nu_t\frac{\partial u_p}{\partial y}\right)+\frac{\partial}{\partial z}\left(\nu_t\frac{\partial u_p}{\partial z}\right)\\
&+\frac{\partial}{\partial x}\left(\nu_t\frac{\partial u_s}{\partial x}\right)+\frac{\partial}{\partial y}\left(\nu_t\frac{\partial u_s}{\partial y}\right)+\frac{\partial}{\partial z}\left(\nu_t\frac{\partial u_s}{\partial z}\right)\\
&-\frac{\partial}{\partial x}\left(\left\langle\tilde{u}^2\right\rangle-\left\langle\tilde{w}^2\right\rangle\right)-\frac{\partial}{\partial y}\left(\left\langle\tilde{u}\tilde{v}\right\rangle\right)
\end{aligned}\qquad \text{(E.1)}$$

integration of equation (E.1) from the bottom to a point above the highest water surface elevation yields, after some elaboration:

$$\begin{aligned}
&\frac{\partial\overline{u}}{\partial t}+\overline{f}_p^2\left(\overline{u}\frac{\partial\overline{u}}{\partial x}+\overline{v}\frac{\partial\overline{u}}{\partial y}\right)-f_c\overline{v}\\
&+\frac{1}{h}\left[\frac{\partial}{\partial x}\right]\left(h\overline{u}_s^2\right)+\frac{1}{h}\frac{\partial}{\partial y}\left[h\overline{u_s v_s}\right]+\frac{1}{h}\left[\frac{\partial}{\partial x}\right]\left(h\overline{u_p u_s}\right)+\\
&\frac{1}{h}\frac{\partial}{\partial y}\left[h\overline{u_p v_s}\right]+\frac{1}{h}\left[\frac{\partial}{\partial x}\right]\left(h\overline{u_s u_p}\right)+\frac{1}{h}\frac{\partial}{\partial y}\left[h\overline{u_s v_p}\right]=\\
&-\frac{1}{\rho}\frac{\partial p_n}{\partial x}\\
&+\overline{\frac{\partial}{\partial x}\left(\nu_t\frac{\partial u_p}{\partial x}\right)}+\overline{\frac{\partial}{\partial y}\left(\nu_t\frac{\partial u_p}{\partial y}\right)}+\overline{\frac{\partial}{\partial x}\left(\nu_t\frac{\partial u_s}{\partial x}\right)}+\overline{\frac{\partial}{\partial y}\left(\nu_t\frac{\partial u_s}{\partial y}\right)}\\
&-\frac{\tau_{bpx}}{\rho h}-\frac{\tau_{bsx}}{\rho h}\\
&-\frac{1}{\rho h}\left(\frac{\partial S_{xx}}{\partial x}+\frac{\partial S_{xy}}{\partial y}\right)+\frac{W_x}{\rho h}
\end{aligned}\qquad \text{(E.2)}$$

To eliminate the pressure gradient from equation (E.1) and (E.2), equation (E.2) has to be rewritten into:

$$\begin{aligned}
&\frac{1}{\rho}\frac{\partial p_n}{\partial x} = -\frac{\partial \overline{u}}{\partial t} - \overline{f}_p^2\left(\overline{u}\frac{\partial \overline{u}}{\partial x} + \overline{v}\frac{\partial \overline{u}}{\partial y}\right) + f_c\overline{v} \\
&-\frac{1}{h}\left[\frac{\partial}{\partial x}\right]\left(h\overline{u}_s^2\right) - \frac{1}{h}\frac{\partial}{\partial y}\left[h\overline{u_s v_s}\right] - \frac{1}{h}\left[\frac{\partial}{\partial x}\right]\left(h\overline{u_p u_s}\right) - \\
&\frac{1}{h}\frac{\partial}{\partial y}\left[h\overline{u_p v_s}\right] - \frac{1}{h}\left[\frac{\partial}{\partial x}\right]\left(h\overline{u_s u_p}\right) - \frac{1}{h}\frac{\partial}{\partial y}\left[h\overline{u_s v_p}\right] \\
&+\overline{\frac{\partial}{\partial x}\left(\nu_t\frac{\partial u_p}{\partial x}\right)} + \overline{\frac{\partial}{\partial y}\left(\nu_t\frac{\partial u_p}{\partial y}\right)} + \overline{\frac{\partial}{\partial x}\left(\nu_t\frac{\partial u_s}{\partial x}\right)} + \overline{\frac{\partial}{\partial y}\left(\nu_t\frac{\partial u_s}{\partial y}\right)} \\
&-\frac{\tau_{bpx}}{\rho h} - \frac{\tau_{bsx}}{\rho h} \\
&-\frac{1}{\rho h}\left(\frac{\partial S_{xx}}{\partial x} + \frac{\partial S_{xy}}{\partial y}\right) + \frac{W_x}{\rho h}
\end{aligned} \tag{E.3}$$

When we substitute this pressure term into equation (E.1) , the equation becomes:

$$\begin{aligned}
&\frac{\partial u_p}{\partial t} + u_p\frac{\partial u_p}{\partial x} + v_p\frac{\partial u_p}{\partial y} + w_p\frac{\partial u_p}{\partial z} - f_c v_p \\
&+\frac{\partial u_s}{\partial t} + u_s\frac{\partial u_s}{\partial x} + v_s\frac{\partial u_s}{\partial y} + w_s\frac{\partial u_s}{\partial z} - f_c v_s \\
&+u_s\frac{\partial u_p}{\partial x} + v_s\frac{\partial u_p}{\partial y} + w_s\frac{\partial u_p}{\partial z} + u_p\frac{\partial u_s}{\partial x} + v_p\frac{\partial u_s}{\partial y} + w_p\frac{\partial u_s}{\partial z} \\
&-\frac{\partial \overline{u}}{\partial t} - \overline{f}_p^2\left(\overline{u}\frac{\partial \overline{u}}{\partial x} + \overline{v}\frac{\partial \overline{u}}{\partial y}\right) + f_c\overline{v} \\
&-\frac{1}{h}\left[\frac{\partial}{\partial x}\right]\left(h\overline{u}_s^2\right) - \frac{1}{h}\frac{\partial}{\partial y}\left[h\overline{u_s v_s}\right] - \frac{1}{h}\left[\frac{\partial}{\partial x}\right]\left(h\overline{u_p u_s}\right) \\
&-\frac{1}{h}\frac{\partial}{\partial y}\left[h\overline{u_p v_s}\right] - \frac{1}{h}\left[\frac{\partial}{\partial x}\right]\left(h\overline{u_s u_p}\right) - \frac{1}{h}\frac{\partial}{\partial y}\left[h\overline{u_s v_p}\right] \\
&+\overline{\frac{\partial}{\partial x}\left(\nu_t\frac{\partial u_p}{\partial x}\right)} + \overline{\frac{\partial}{\partial y}\left(\nu_t\frac{\partial u_p}{\partial y}\right)} + \overline{\frac{\partial}{\partial x}\left(\nu_t\frac{\partial u_s}{\partial x}\right)} + \overline{\frac{\partial}{\partial y}\left(\nu_t\frac{\partial u_s}{\partial y}\right)} \\
&-\frac{\tau_{bpx}}{\rho h} - \frac{\tau_{bsx}}{\rho h} - \frac{1}{\rho h}\left(\frac{\partial S_{xx}}{\partial x} + \frac{\partial S_{xy}}{\partial y}\right) + \frac{W_x}{\rho h} = \\
&\frac{\partial}{\partial x}\left(\nu_t\frac{\partial u_p}{\partial x}\right) + \frac{\partial}{\partial y}\left(\nu_t\frac{\partial u_p}{\partial y}\right) + \frac{\partial}{\partial z}\left(\nu_t\frac{\partial u_p}{\partial z}\right) \\
&+\frac{\partial}{\partial x}\left(\nu_t\frac{\partial u_s}{\partial x}\right) + \frac{\partial}{\partial y}\left(\nu_t\frac{\partial u_s}{\partial y}\right) + \frac{\partial}{\partial z}\left(\nu_t\frac{\partial u_s}{\partial z}\right) \\
&-\frac{\partial}{\partial x}\left(\left\langle\tilde{u}^2\right\rangle - \left\langle\tilde{w}^2\right\rangle\right) - \frac{\partial}{\partial y}\left(\left\langle\tilde{u}\tilde{v}\right\rangle\right)
\end{aligned} \tag{E.4}$$

Different terms can be distinguished e.g.

- advective terms
- viscous (diffusive) terms
- coriolis
- bed shear stress
- radiation stress
- wind

viscous (diffusive) terms

$$\text{Diffusive terms} = \frac{\partial}{\partial z}\left(\nu_t \frac{\partial u_p}{\partial z}\right) + \frac{\partial}{\partial z}\left(\nu_t \frac{\partial u_s}{\partial z}\right) + other \tag{E.5}$$

with the horizontal diffusion terms neglected:

$$\begin{aligned} other = {} & \frac{\partial}{\partial x}\left(\nu_t \frac{\partial u_p}{\partial x}\right) + \frac{\partial}{\partial y}\left(\nu_t \frac{\partial u_p}{\partial y}\right) + \frac{\partial}{\partial x}\left(\nu_t \frac{\partial u_s}{\partial x}\right) + \frac{\partial}{\partial y}\left(\nu_t \frac{\partial u_s}{\partial y}\right) \\ & - \overline{\frac{\partial}{\partial x}\left(\nu_t \frac{\partial u_p}{\partial x}\right)} - \overline{\frac{\partial}{\partial y}\left(\nu_t \frac{\partial u_p}{\partial y}\right)} + \overline{\frac{\partial}{\partial x}\left(\nu_t \frac{\partial u_s}{\partial x}\right)} - \overline{\frac{\partial}{\partial y}\left(\nu_t \frac{\partial u_s}{\partial y}\right)} \end{aligned} \tag{E.6}$$

Coriolis

Taking all the Coriolis terms together yields:

$$-f_c v_p - f_c v_s = -f_c \overline{v} \tag{E.7}$$

with the condition:

$$u_p = f_p \overline{u} \;,\; v_p = f_p \overline{v} \tag{E.8}$$

the Coriolis terms can be rewritten into:

$$f_c \overline{v}\left(1 - f_p\right) - f_c v_s = 0 \tag{E.9}$$

Advective Terms

$$\begin{aligned}
&\frac{\partial u_p}{\partial t}+u_p\frac{\partial u_p}{\partial x}+v_p\frac{\partial u_p}{\partial y}+w_p\frac{\partial u_p}{\partial z}+\frac{\partial u_s}{\partial t}+u_s\frac{\partial u_s}{\partial x}+v_s\frac{\partial u_s}{\partial y}+w_s\frac{\partial u_s}{\partial z}+\\
&u_s\frac{\partial u_p}{\partial x}+v_s\frac{\partial u_p}{\partial y}+w_s\frac{\partial u_p}{\partial z}+u_p\frac{\partial u_s}{\partial x}+v_p\frac{\partial u_s}{\partial y}+w_p\frac{\partial u_s}{\partial z}=\\
&\frac{\partial \overline{u}}{\partial t}+\overline{f}_p^2\left(\overline{u}\frac{\partial \overline{u}}{\partial x}+\overline{v}\frac{\partial \overline{u}}{\partial y}\right)\\
&+\frac{1}{h}\left[\frac{\partial}{\partial x}\right]\left(h\overline{u}_s^2\right)+\frac{1}{h}\frac{\partial}{\partial y}\left[h\overline{u_s v_s}\right]+\frac{1}{h}\left[\frac{\partial}{\partial x}\right]\left(h\overline{u_p u_s}\right)+\\
&\frac{1}{h}\frac{\partial}{\partial y}\left[h\overline{u_p v_s}\right]+\frac{1}{h}\left[\frac{\partial}{\partial x}\right]\left(h\overline{u_s u_p}\right)+\frac{1}{h}\frac{\partial}{\partial y}\left[h\overline{u_s v_p}\right]
\end{aligned} \tag{E.10}$$

With the condition (E.8) a part of the equation can be rewritten into:

$$\frac{\partial u_p}{\partial t}+u_p\frac{\partial u_p}{\partial x}+v_p\frac{\partial u_p}{\partial y}+w_p\frac{\partial u_p}{\partial z}=f_p\frac{\partial \overline{u}}{\partial t}+f_p^2\overline{u}\frac{\partial \overline{u}}{\partial x}+f_p^2\overline{v}\frac{\partial \overline{u}}{\partial y}+w_p\frac{\partial u_p}{\partial z} \tag{E.11}$$

and the cross-terms :

$$\begin{aligned}
&u_s\frac{\partial u_s}{\partial x}+v_s\frac{\partial u_s}{\partial y}-\frac{1}{h}\left[\frac{\partial}{\partial x}\right]\left(h\overline{u}_s^2\right)-\frac{1}{h}\frac{\partial}{\partial y}\left[h\overline{u_s v_s}\right]=0\\
&u_s\frac{\partial u_p}{\partial x}+v_s\frac{\partial u_p}{\partial y}-\frac{1}{h}\left[\frac{\partial}{\partial x}\right]\left(h\overline{u_p u_s}\right)-\frac{1}{h}\frac{\partial}{\partial y}\left[h\overline{u_p v_s}\right]=0\\
&u_p\frac{\partial u_s}{\partial x}+v_p\frac{\partial u_s}{\partial y}-\frac{1}{h}\left[\frac{\partial}{\partial x}\right]\left(h\overline{u_s u_p}\right)-\frac{1}{h}\frac{\partial}{\partial y}\left[h\overline{u_s v_p}\right]=0
\end{aligned} \tag{E.12}$$

the other terms concern the vertical non-uniformity of the advection of secondary flow momentum by the primary and secondary currents and the advection of primary flow momentum by the secondary current are neglected:

$$others(advective)=\frac{\partial u_s}{\partial t}+w_p\frac{\partial u_p}{\partial z}+w_s\frac{\partial u_s}{\partial z}+w_s\frac{\partial u_p}{\partial z}+w_p\frac{\partial u_s}{\partial z} \tag{E.13}$$

Substitution of (E.11), (E.12) and (E.13) into equation (E.10) results in the following expression for the advective terms:

$$f_p\frac{\partial \overline{u}}{\partial t}+f_p^2\overline{u}\frac{\partial \overline{u}}{\partial x}+f_p^2\overline{v}\frac{\partial \overline{u}}{\partial y}+other(advective) \tag{E.14}$$

Substitution of(E.5), (E.9) and (E.14) into equation (E.4) leads to:

$$
\begin{aligned}
& f_p \frac{\partial \overline{u}}{\partial t} + f_p^2 \overline{u} \frac{\partial \overline{u}}{\partial x} + f_p^2 \overline{v} \frac{\partial \overline{u}}{\partial y} + other(advective) \\
& - \overline{f}_p^2 \left(\overline{u} \frac{\partial \overline{u}}{\partial x} + \overline{v} \frac{\partial \overline{u}}{\partial y} \right) + f_c \overline{v} \left(1 - f_p \right) - f_c v_s \\
& - \frac{\tau_{bpx}}{\rho h} - \frac{\tau_{bsx}}{\rho h} \\
& - \frac{1}{\rho h} \left(\frac{\partial S_{xx}}{\partial x} + \frac{\partial S_{xy}}{\partial y} \right) + \frac{W_x}{\rho h} = \\
& \frac{\partial}{\partial z} \left(\nu_t \frac{\partial u_p}{\partial z} \right) + \frac{\partial}{\partial z} \left(\nu_t \frac{\partial u_s}{\partial z} \right) + other(diffusive) \\
& - \frac{\partial}{\partial x} \left(\left\langle \tilde{u}^2 \right\rangle - \left\langle \tilde{w}^2 \right\rangle \right) - \frac{\partial}{\partial y} \left(\left\langle \tilde{u} \tilde{v} \right\rangle \right)
\end{aligned}
\tag{E.15}
$$

After elaboration this yields

$$
\begin{aligned}
& \frac{\partial}{\partial z} \left(\nu_t \frac{\partial u_p}{\partial z} \right) + \frac{\tau_{bpx}}{\rho h} + \frac{\partial}{\partial z} \left(\nu_t \frac{\partial u_s}{\partial z} \right) + \frac{\tau_{bsx}}{\rho h} + f_c v_s = \\
& \frac{W_x}{\rho h} + \frac{\partial}{\partial x} \left(\left\langle \tilde{u}^2 \right\rangle - \left\langle \tilde{w}^2 \right\rangle \right) - \frac{1}{\rho h} \frac{\partial S_{xx}}{\partial x} + \frac{\partial}{\partial y} \left(\left\langle \tilde{u} \tilde{v} \right\rangle \right) - \frac{1}{\rho h} \frac{\partial S_{xy}}{\partial y} \\
& + \left(f_p - 1 \right) \left(\frac{\partial \overline{u}}{\partial t} - f_c \overline{v} \right) + \left(f_p^2 - \overline{f}_p^2 \right) \left(\overline{u} \frac{\partial \overline{u}}{\partial x} + \overline{v} \frac{\partial \overline{u}}{\partial y} \right) + other\ terms
\end{aligned}
\tag{E.16}
$$

in which the *other terms* are the concern the advective and diffusive other terms.

F Figures

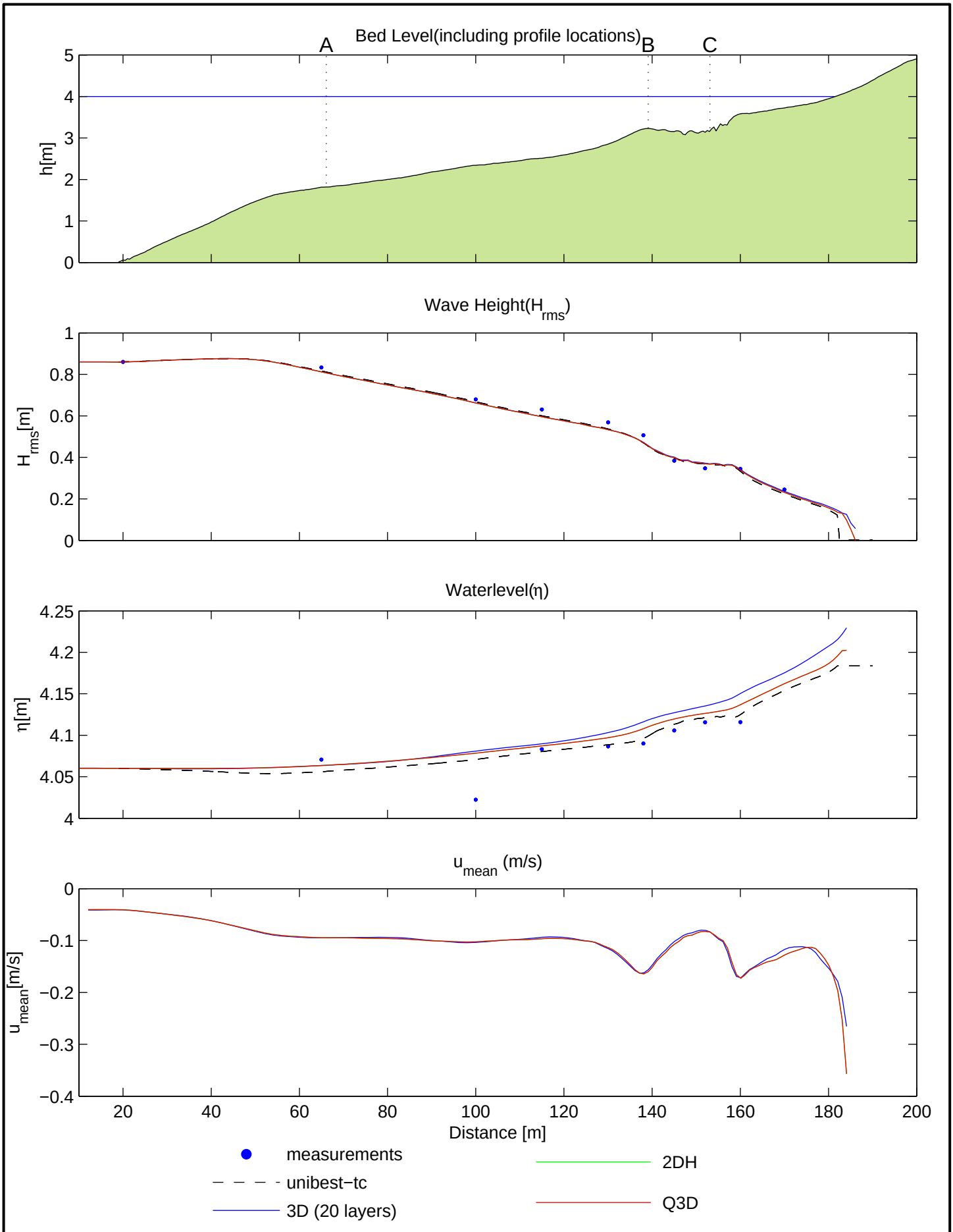

Model results LIP11D−1b experiment Cross−shore distribution Wave height, Water level, Depth−averaged velocity	Compare	LIP
	Delft3D	
Deltares		F3.3.1

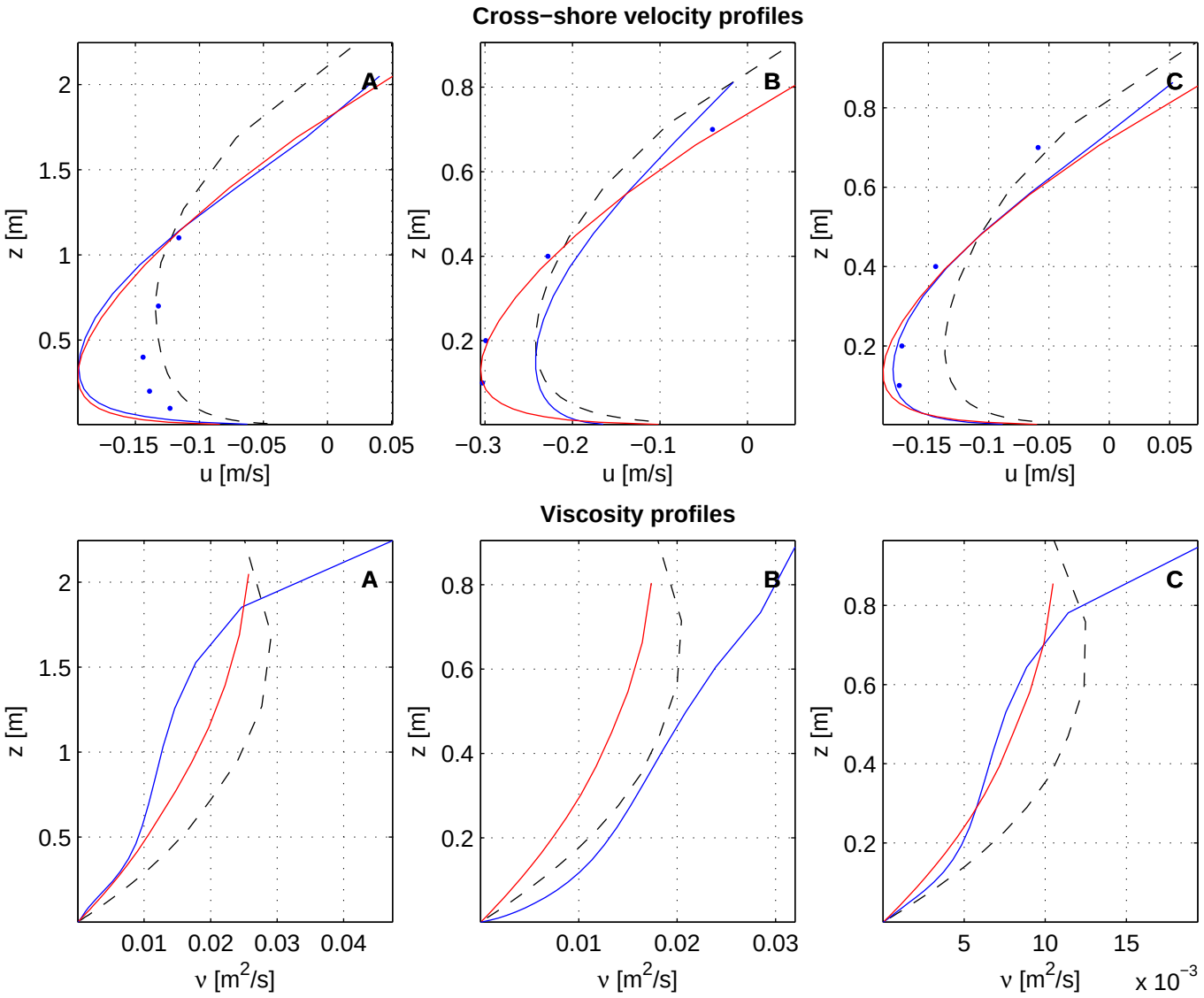

Model results LIP11D−1b experiment Vertical Profiles at location A, B and C Cross−shore velocity, viscosity	Compare	LIP
	Delft3D	
Deltares		F3.3.2

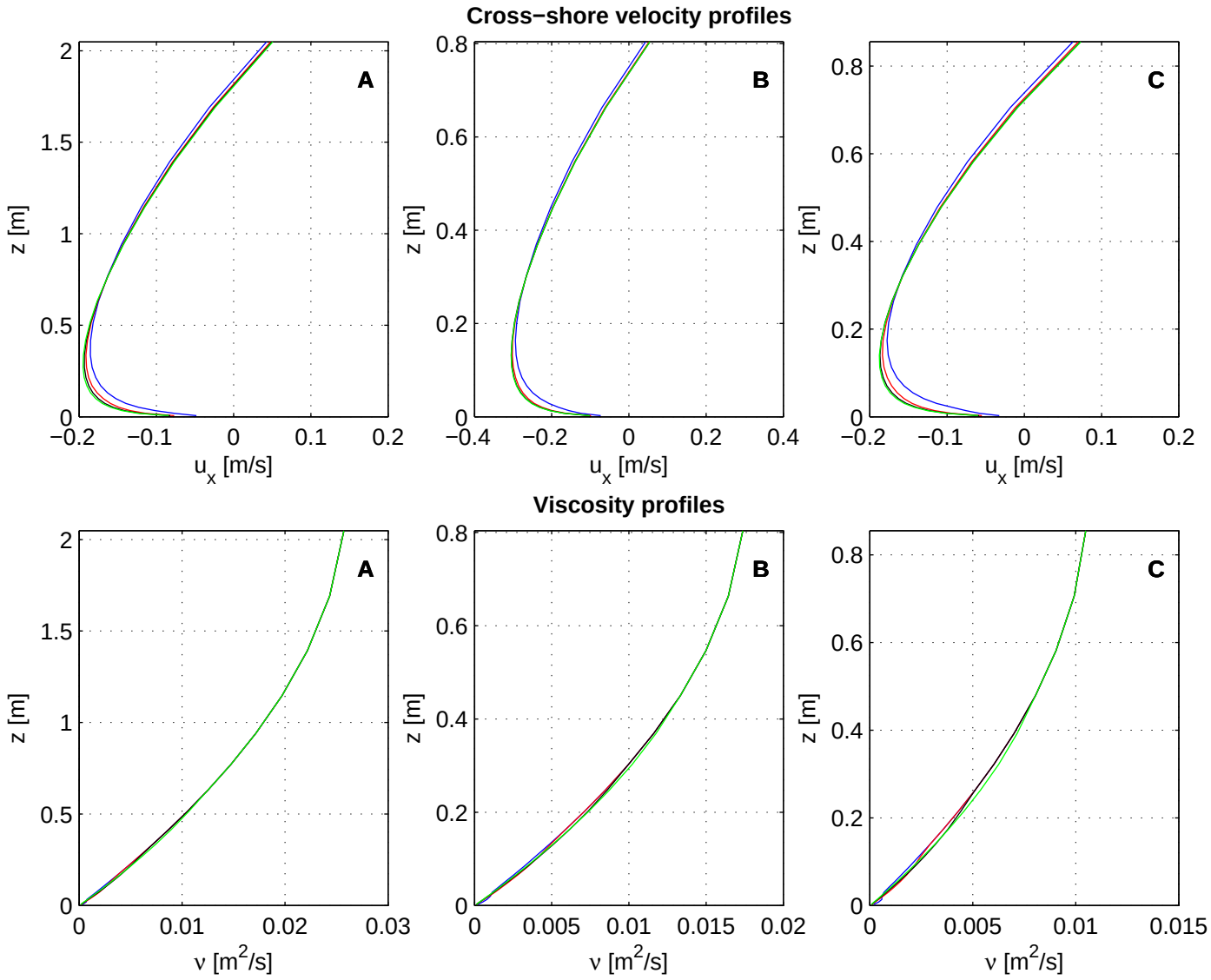

facdel = 1
facdel = 5
facdel = 10
facdel = 20

Model results LIP11D−1b experiment Parameter sensitivity multiplication factor bottom boundary layer thickness[facdel] Cross−shore velocity, viscosity	Q3D	LIP
	Delft3D	
Deltares	facdel	F3.3.3

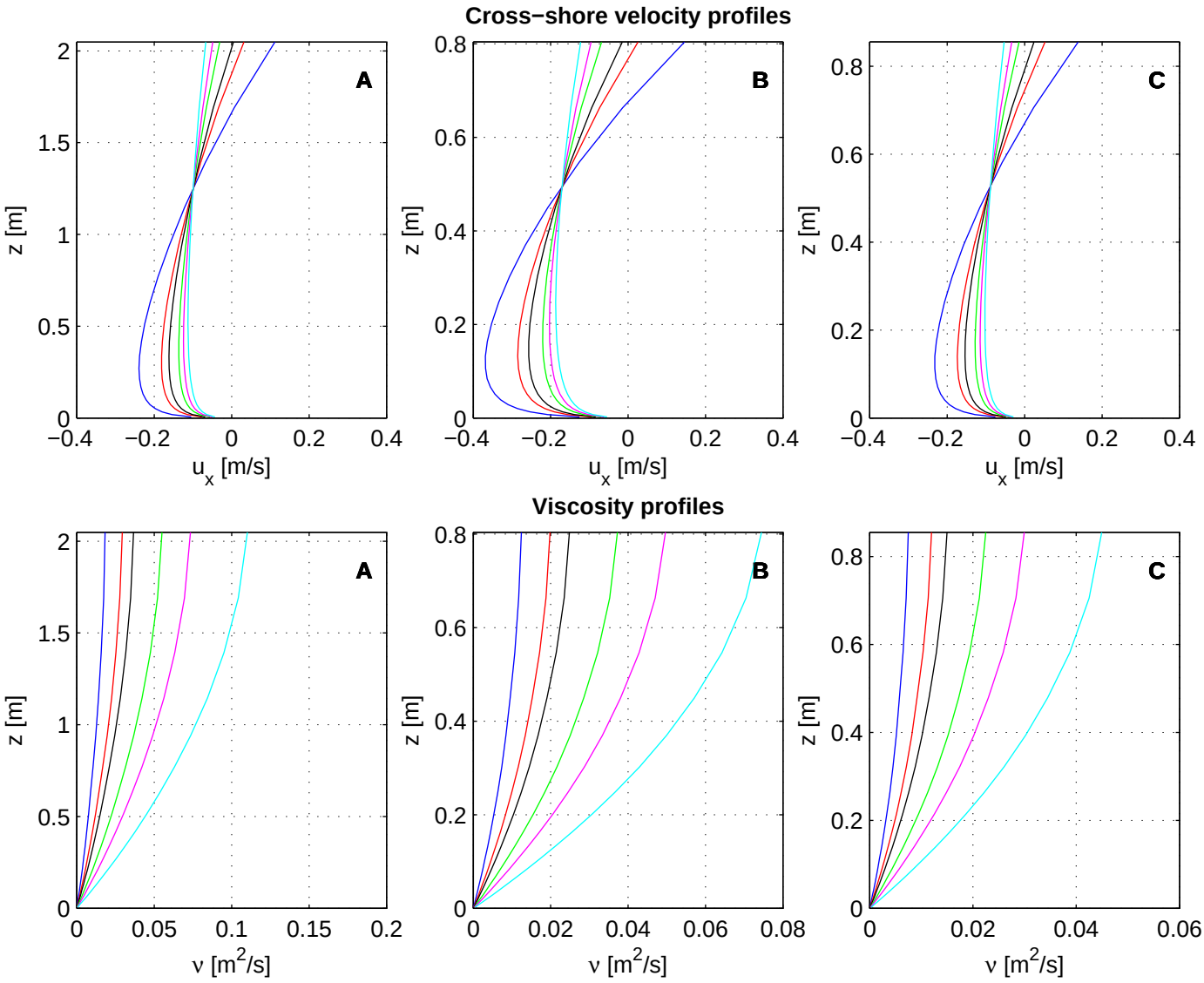

fcvisc = 0.05
fcvisc = 0.08
fcvisc = 0.1
fcvisc = 0.15
fcvisc = 0.2
fcvisc = 0.3

Model results LIP11D−1b experiment Parameter sensitivity multiplication factor wave−induced viscosity[fcvisc] Cross−shore velocity, viscosity	Q3D	LIP
	Delft3D	
Deltares	fcvisc	F3.3.4

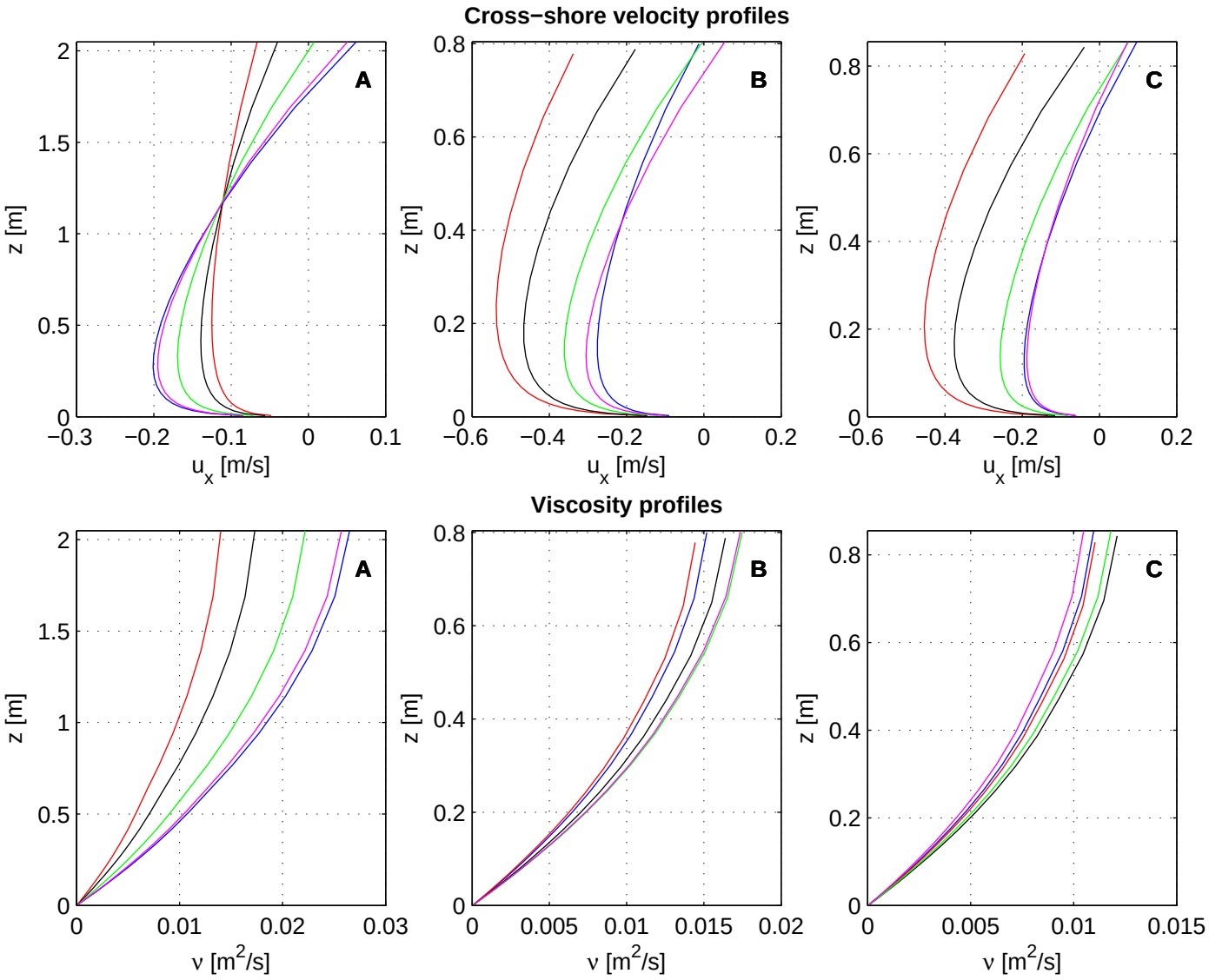

Model results LIP11D−1b experiment Parameter sensitivity angle of wave front [betaro] Cross−shore velocity, viscosity	Q3D	LIP
	Delft3D	
Deltares	betaro	F3.3.5

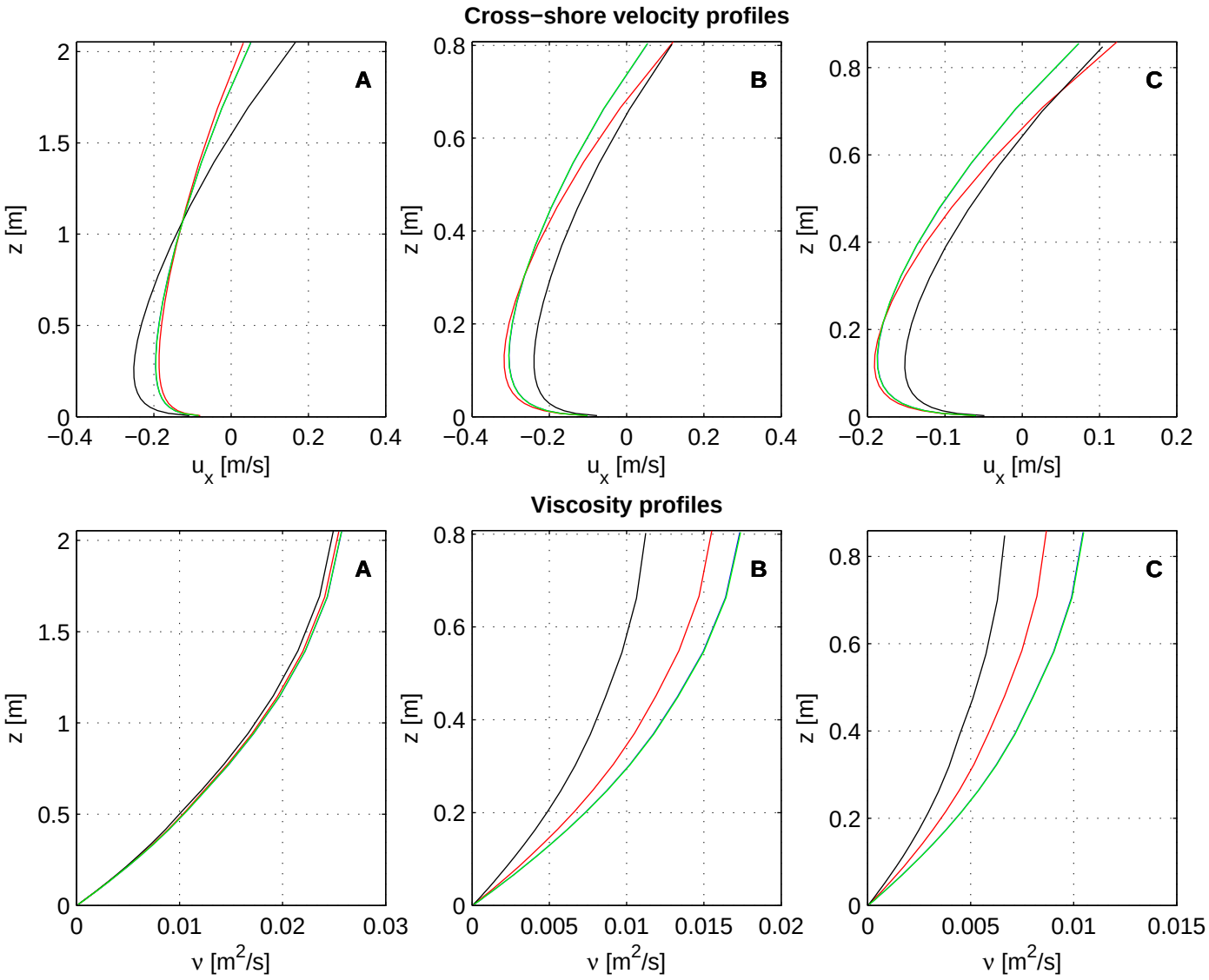

Model results LIP11D−1b experiment Parameter sensitivity breaker parameter [gamdis] Cross−shore velocity, viscosity	Q3D	LIP
	Delft3D	
Deltares	gamdis	F3.3.6

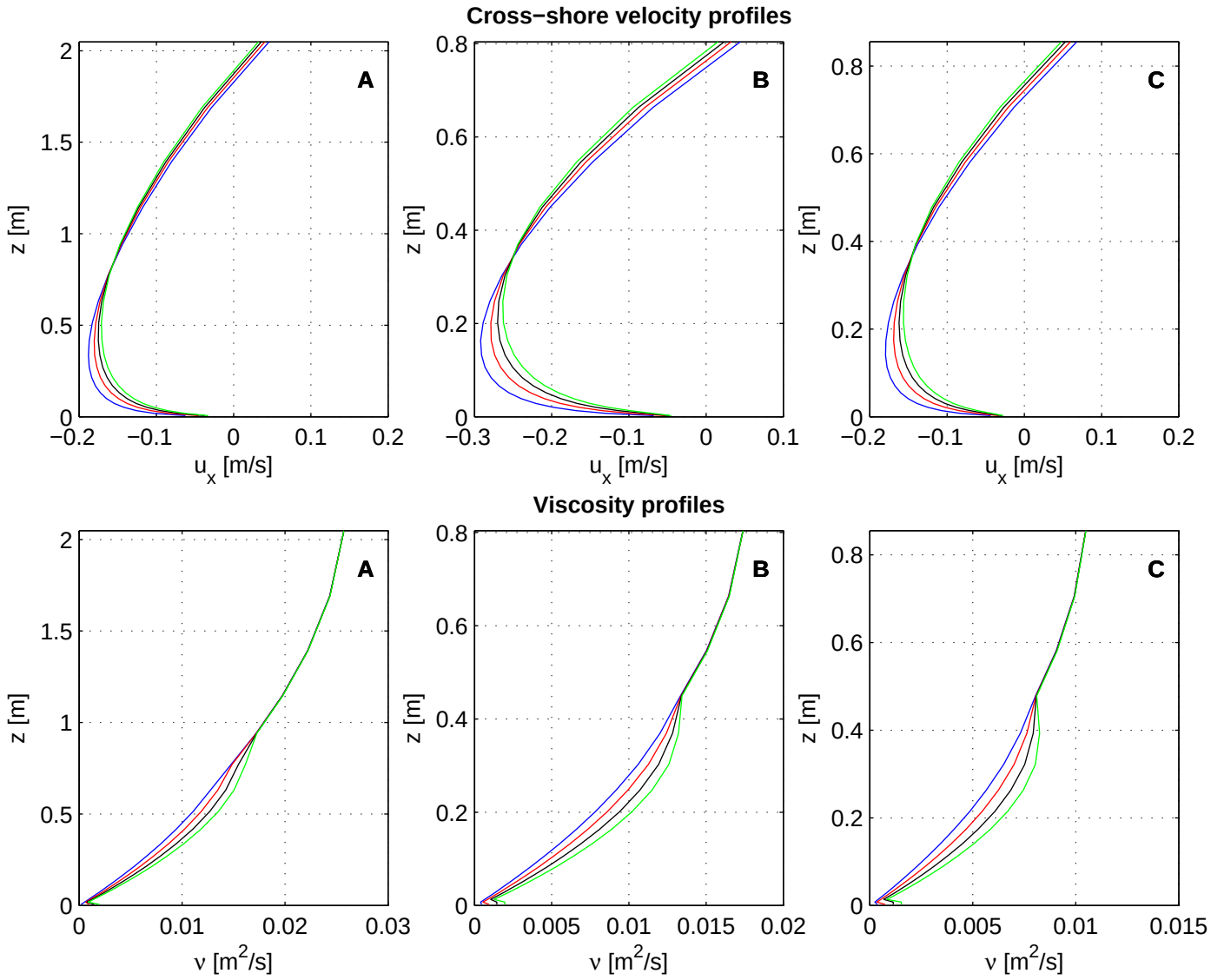

Model results LIP11D−1b experiment Parameter sensitivity roughness height [ks] Cross−shore velocity, viscosity	Q3D	LIP
	Delft3D	
Deltares	ks	F3.3.7

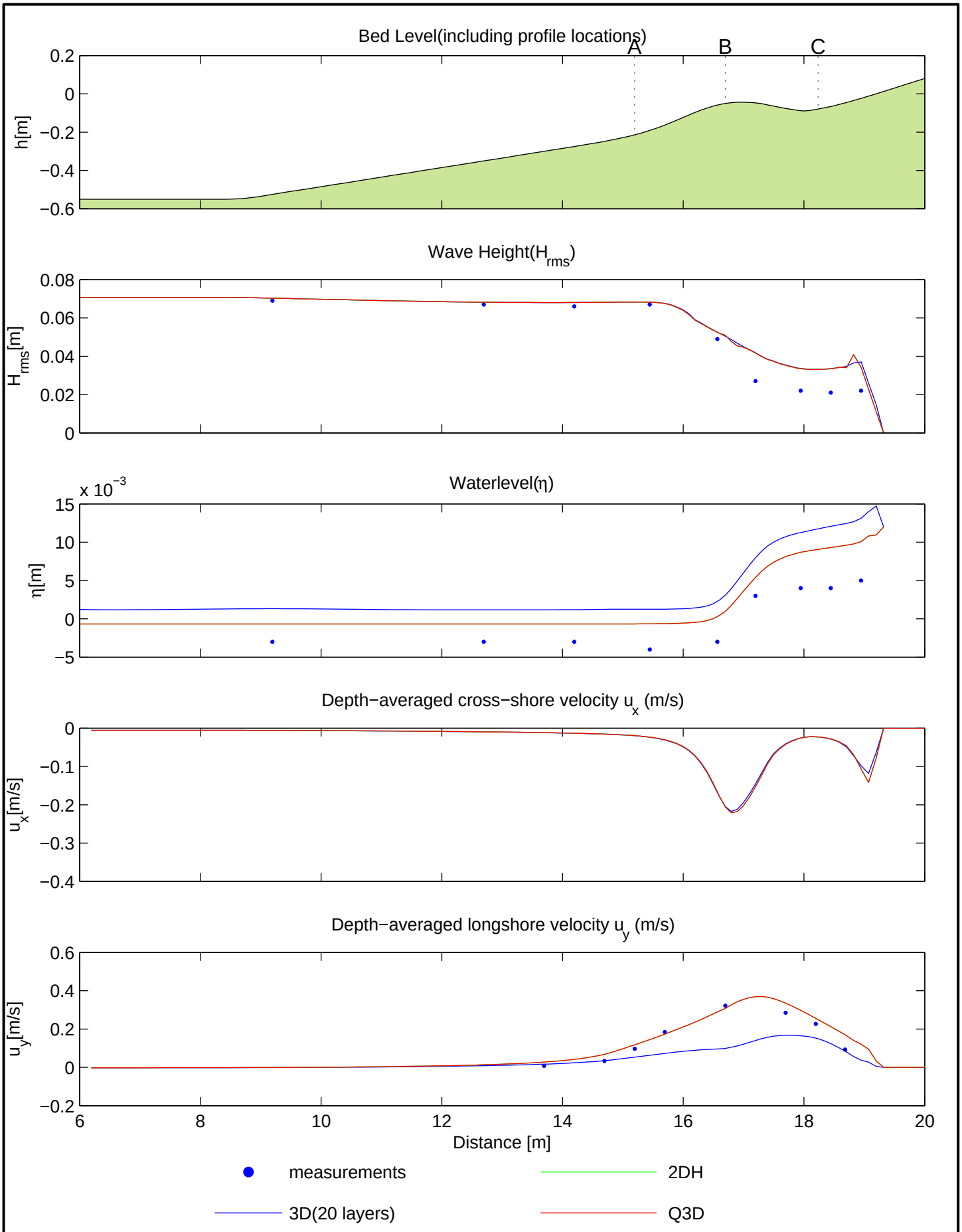

Model results Reniers−SO014 experiment Cross−shore distribution Wave Height, Water Level, Depth Averaged Velocities (u and v)	Compare	Reniers
	Delft3D	
Deltares		F3.3.8

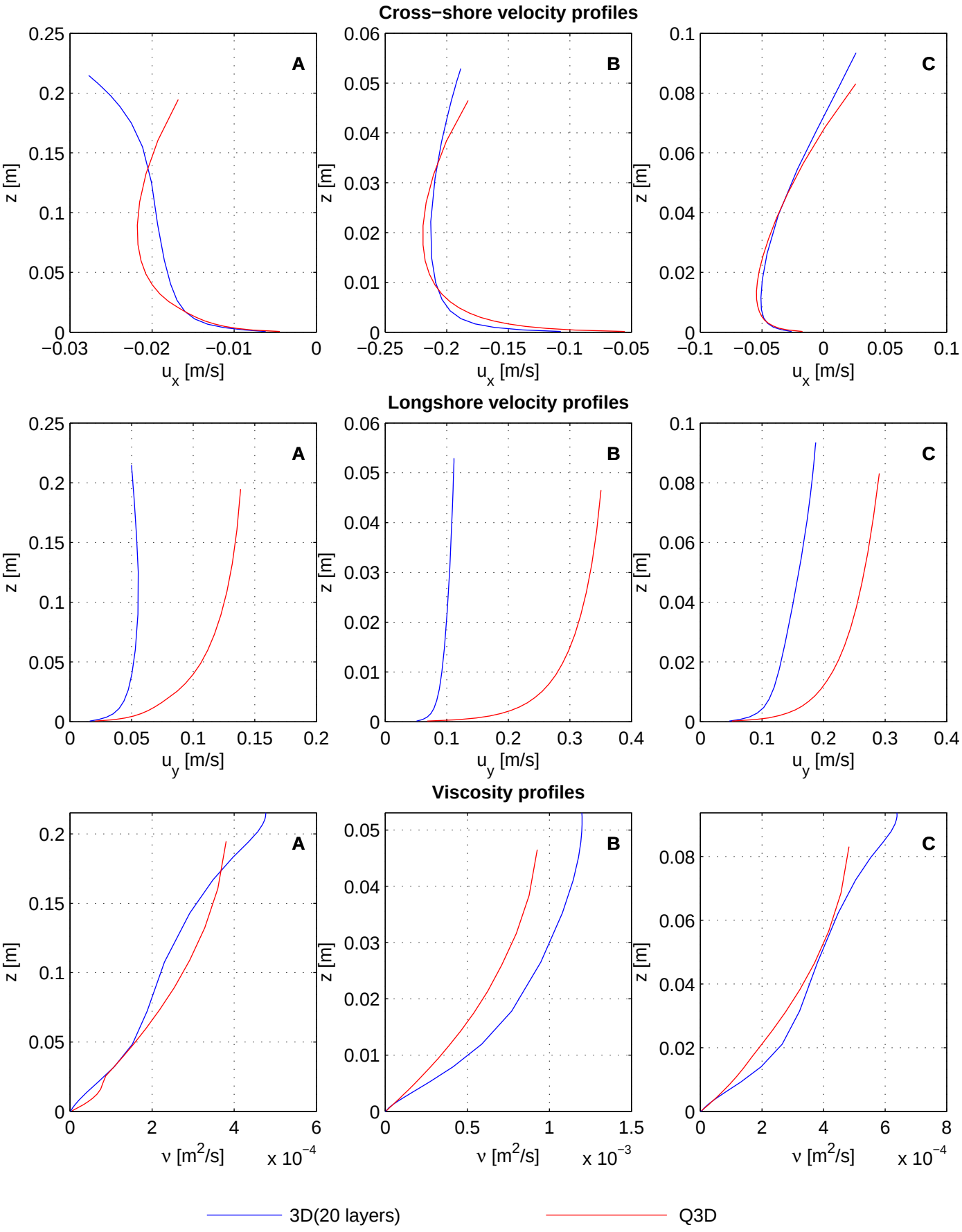

Model results Reniers−SO014 experiment Vertical Profiles at location A, B and C Cross−shore velocity, Longshore velocity and Viscosity profiles	Compare	Reniers
	Delft3D	
Deltares		F3.3.9

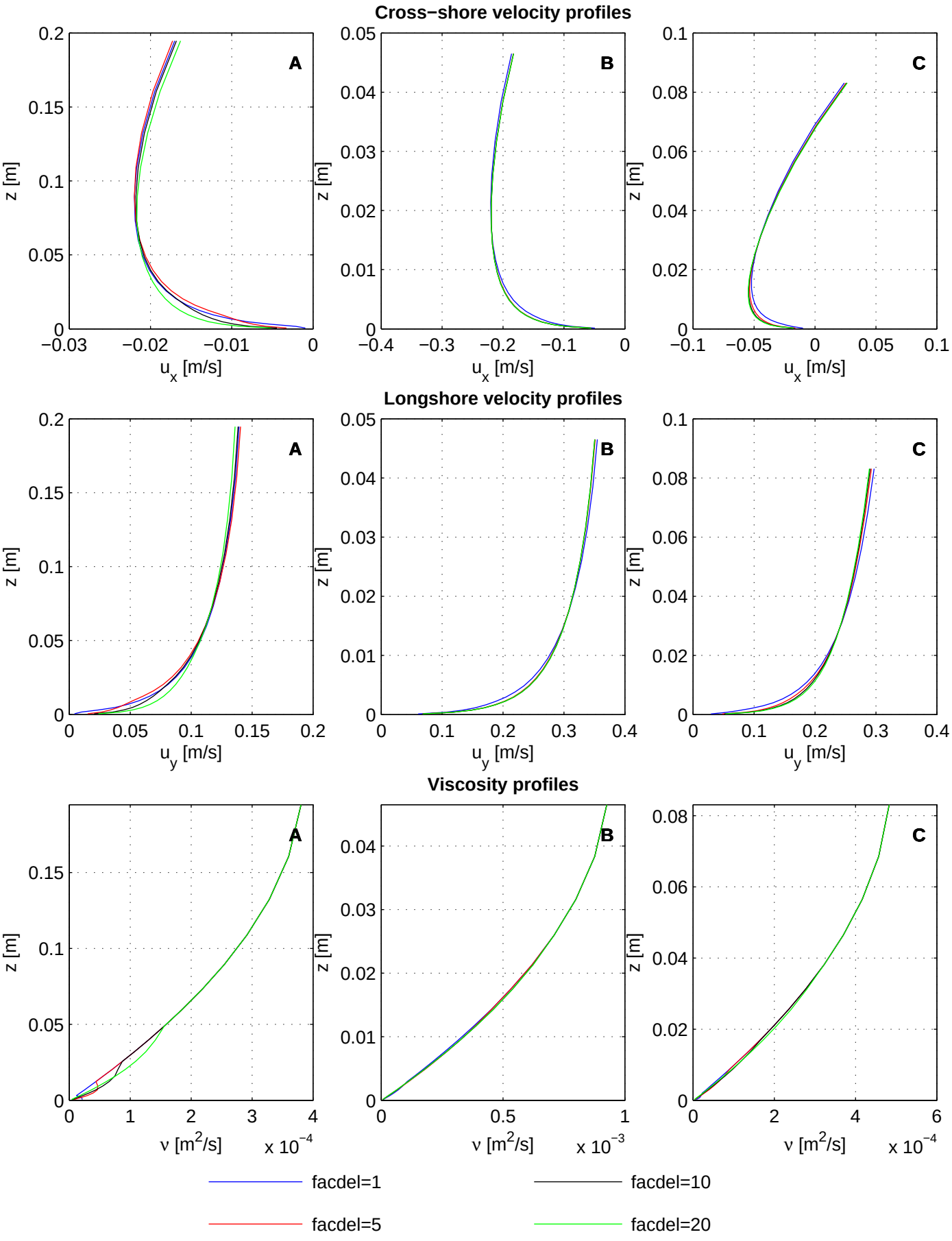

Model results Reniers−SO014 experiment Parameter sensitivity multiplication factor bottom boundary layer thickness[facdel] Cross−shore velocity, Longshore velocity and Viscosity profiles	Q3D	Reniers
	Delft3D	
Deltares	facdel	F3.3.10

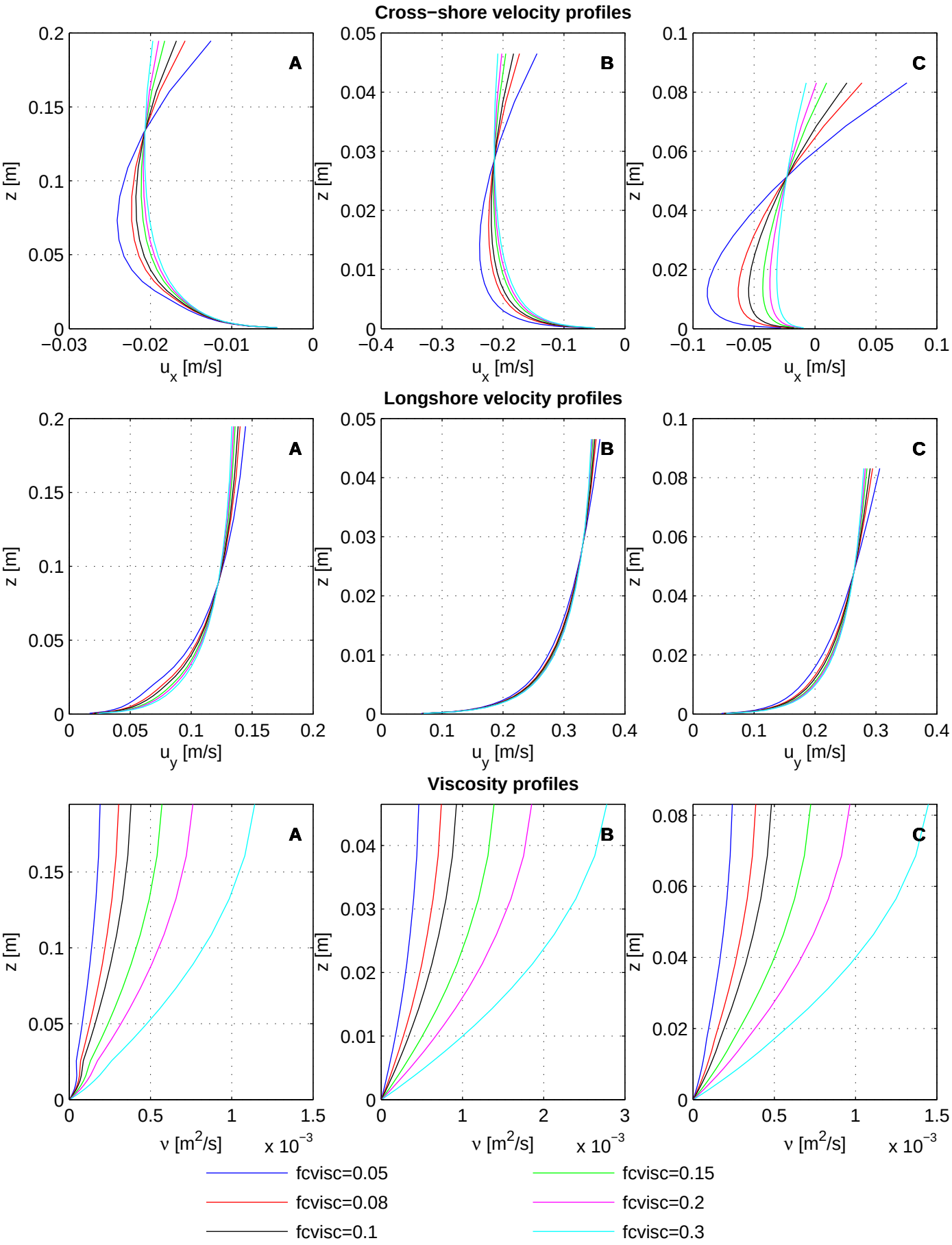

Model results Reniers−SO014 experiment Parameter sensitivity multiplication factor wave−induced viscosity[fcvisc] Cross−shore velocity, Longshore velocity and Viscosity profiles	Q3D	Reniers
	Delft3D	
Deltares	fcvisc	F3.3.11

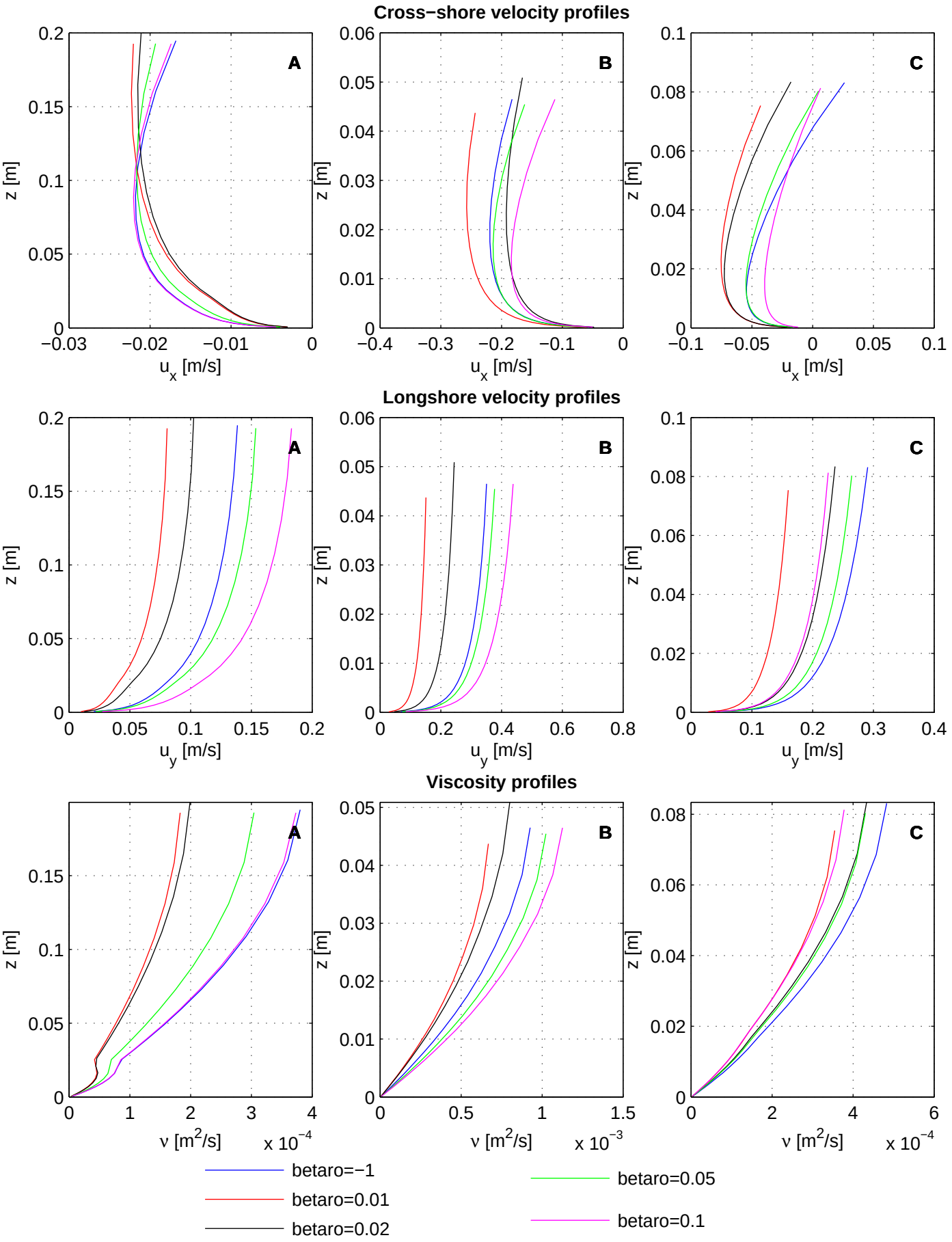

Model results Reniers−SO014 experiment Parameter sensitivity angle of wave front [betaro] Cross−shore velocity, Longshore velocity and Viscosity profiles	Q3D	Reniers
	Delft3D	
Deltares	betaro	F3.3.12

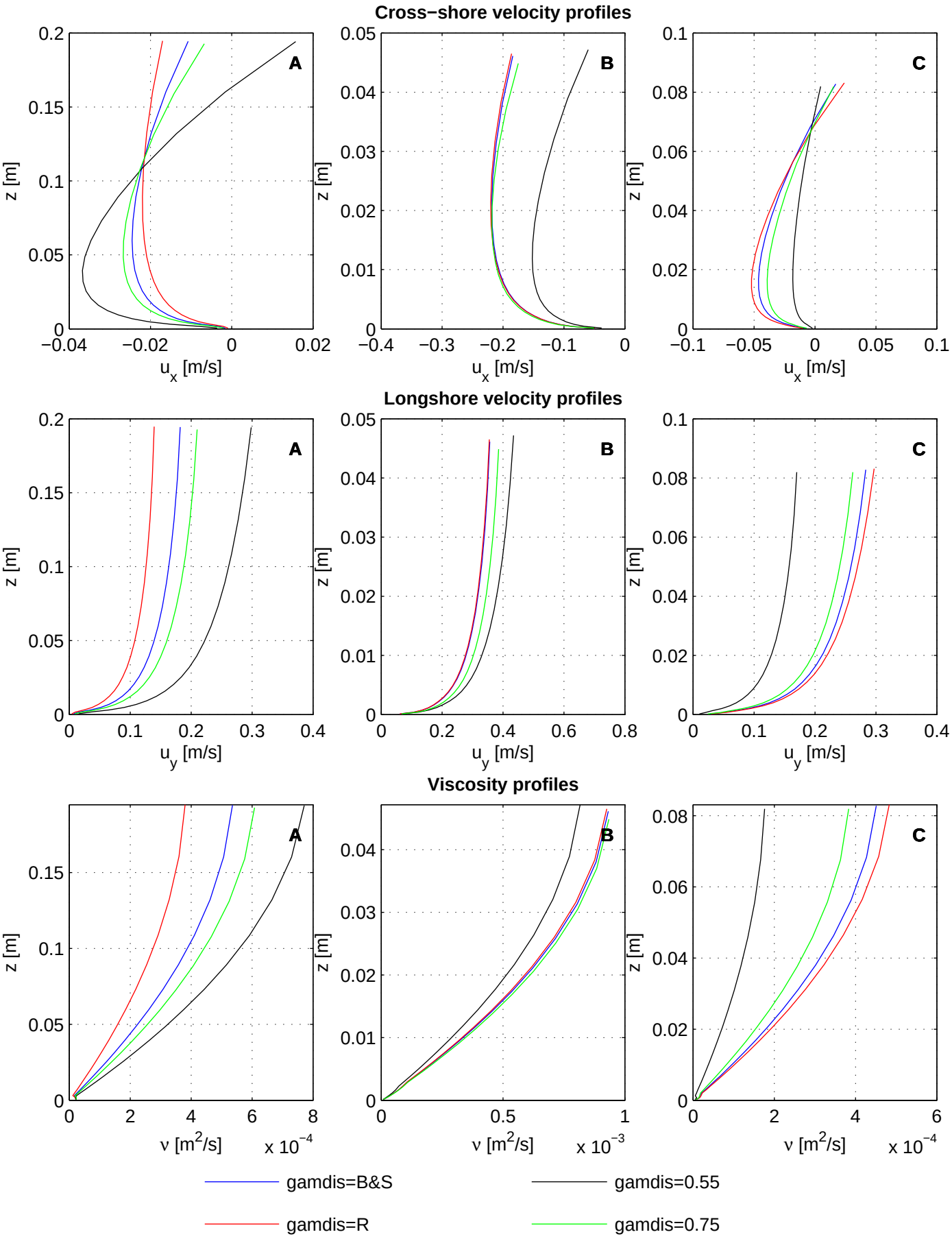

Model results Reniers−SO014 experiment Parameter sensitivity breaker parameter [gamdis] Cross−shore velocity, Longshore velocity and Viscosity profiles	Q3D	Reniers
	Delft3D	
Deltares	gamdis	F3.3.13

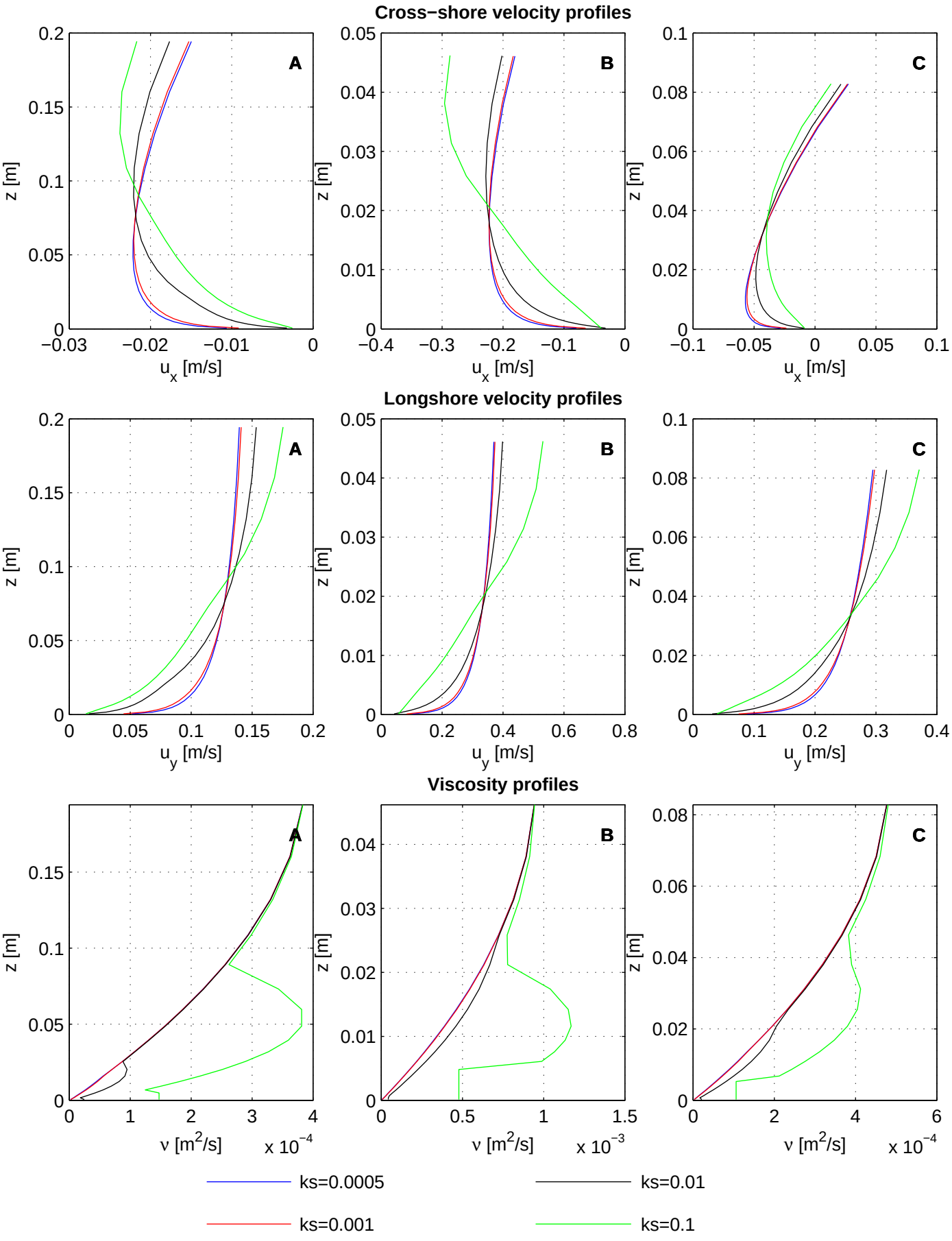

Model results Reniers−SO014 experiment Parameter sensitivity roughness height [ks] Cross−shore velocity, Longshore velocity and Viscosity profiles	Q3D	Reniers
	Delft3D	
Deltares	ks	F3.3.14

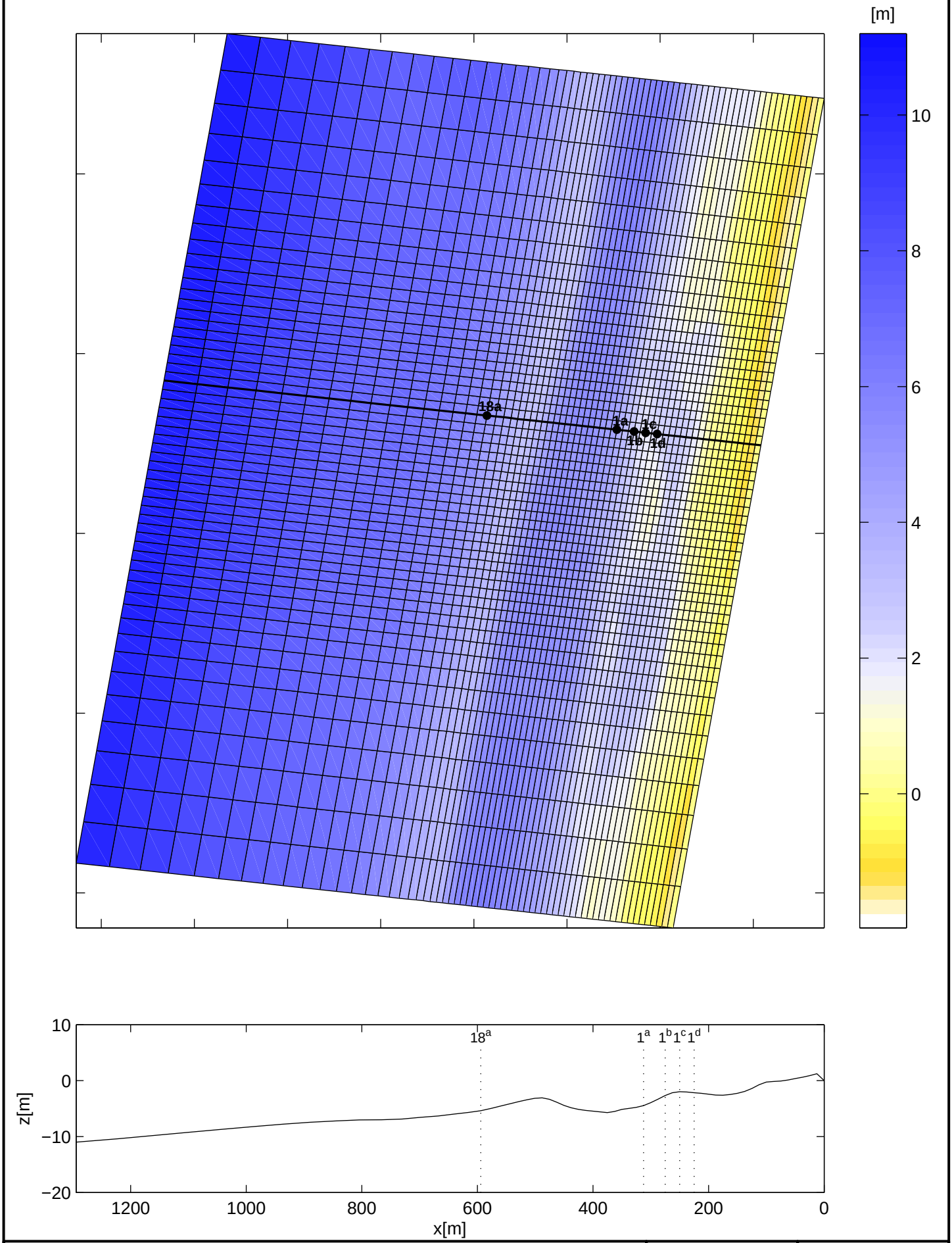

Model results Egmond field case Depth including observation points 18A 1A−D bed level cross−section	Compare	Egmond
	Delft3D	
Deltares	t=18	F3.3.15

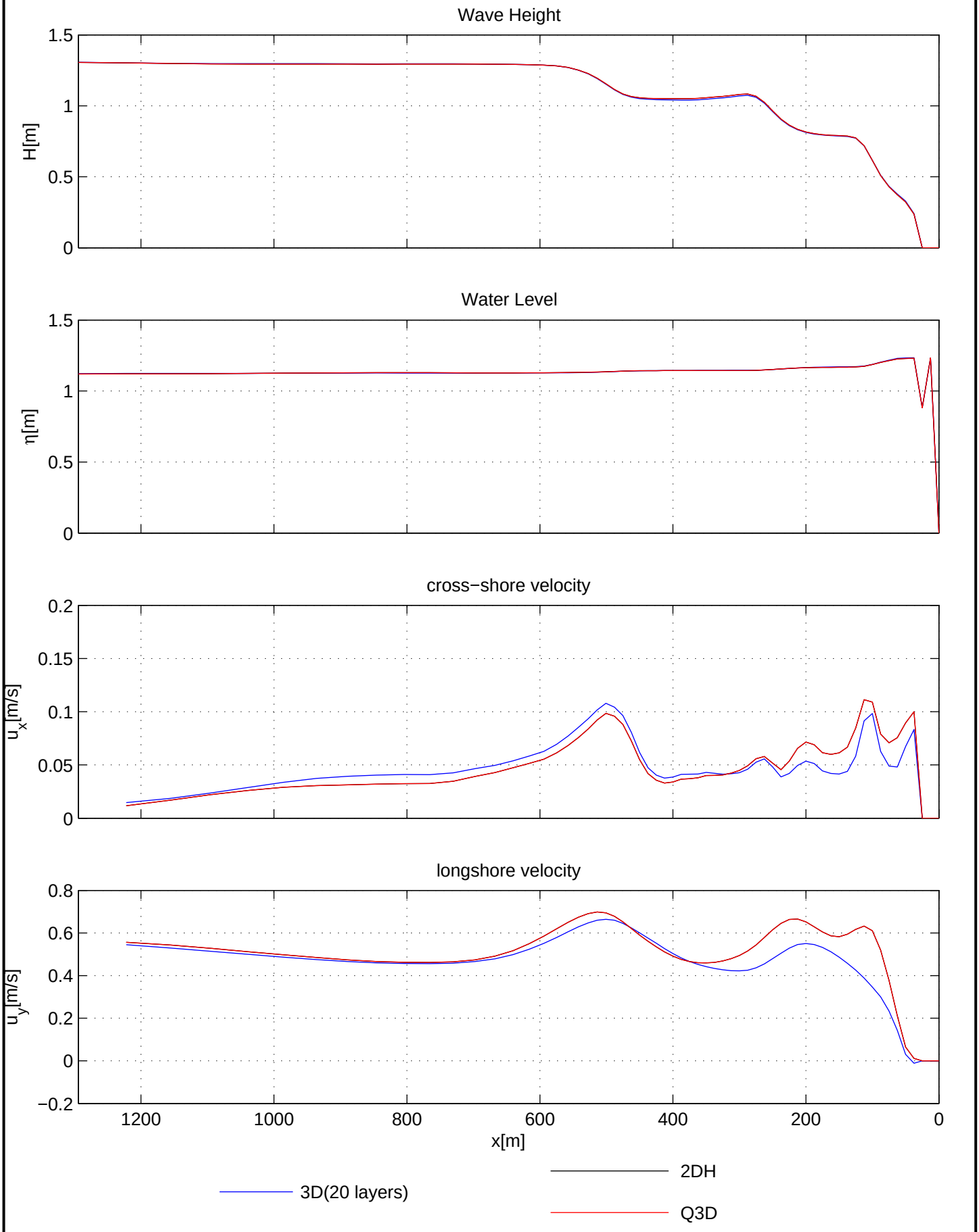

Model results Egmond field case Cross−shore distribution high tide Wave height, Water level, cross−shore velocity, longshore velocity	Compare	Egmond
	Delft3D	
Deltares	t=18	F3.3.16

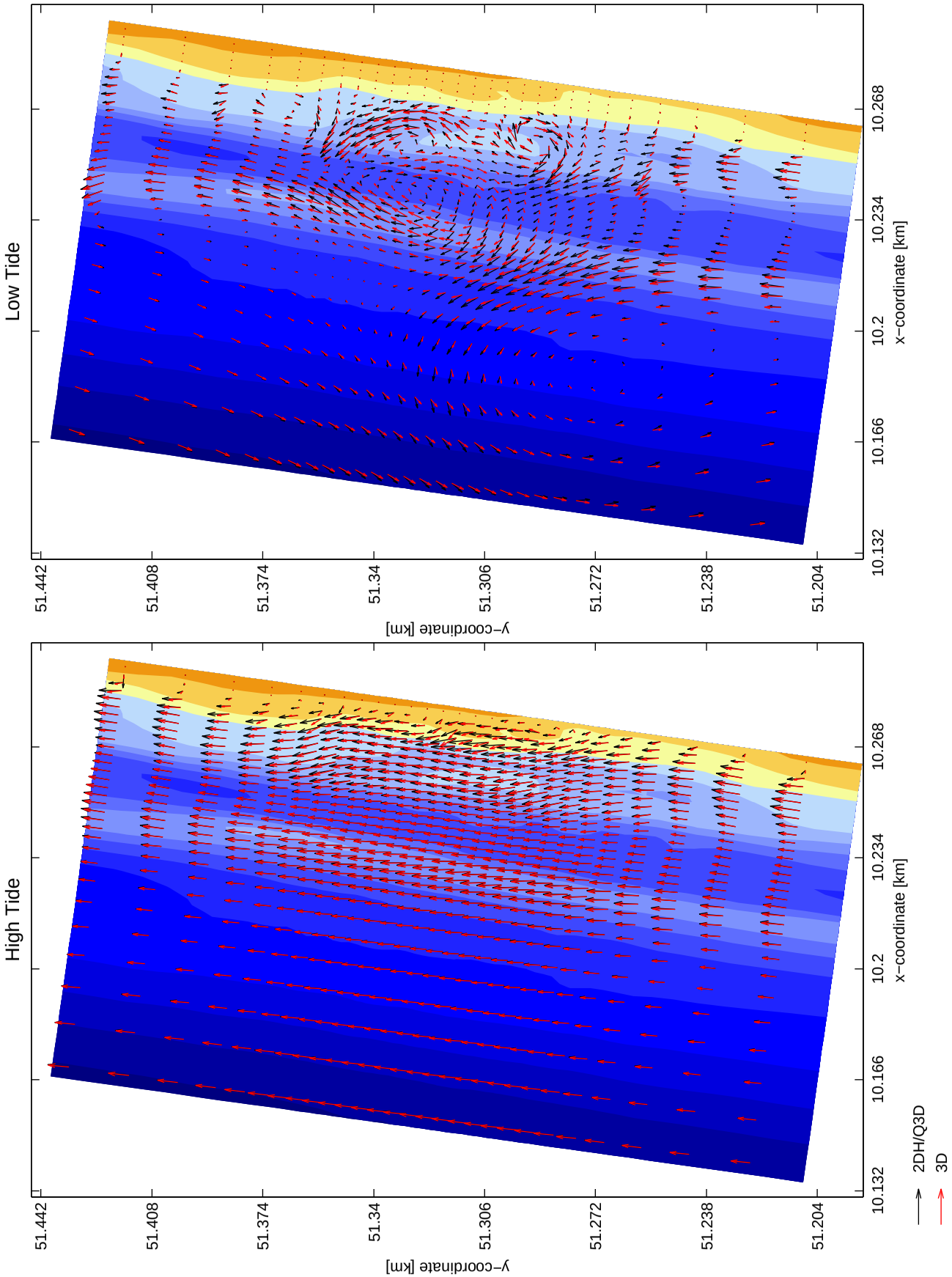

Model results Egmond field model Flow patterns 3D (red) and 2DH/Q3D (black) High tide and low tide	Compare	Egmond
	Delft3D	
Deltares		F3.3.17

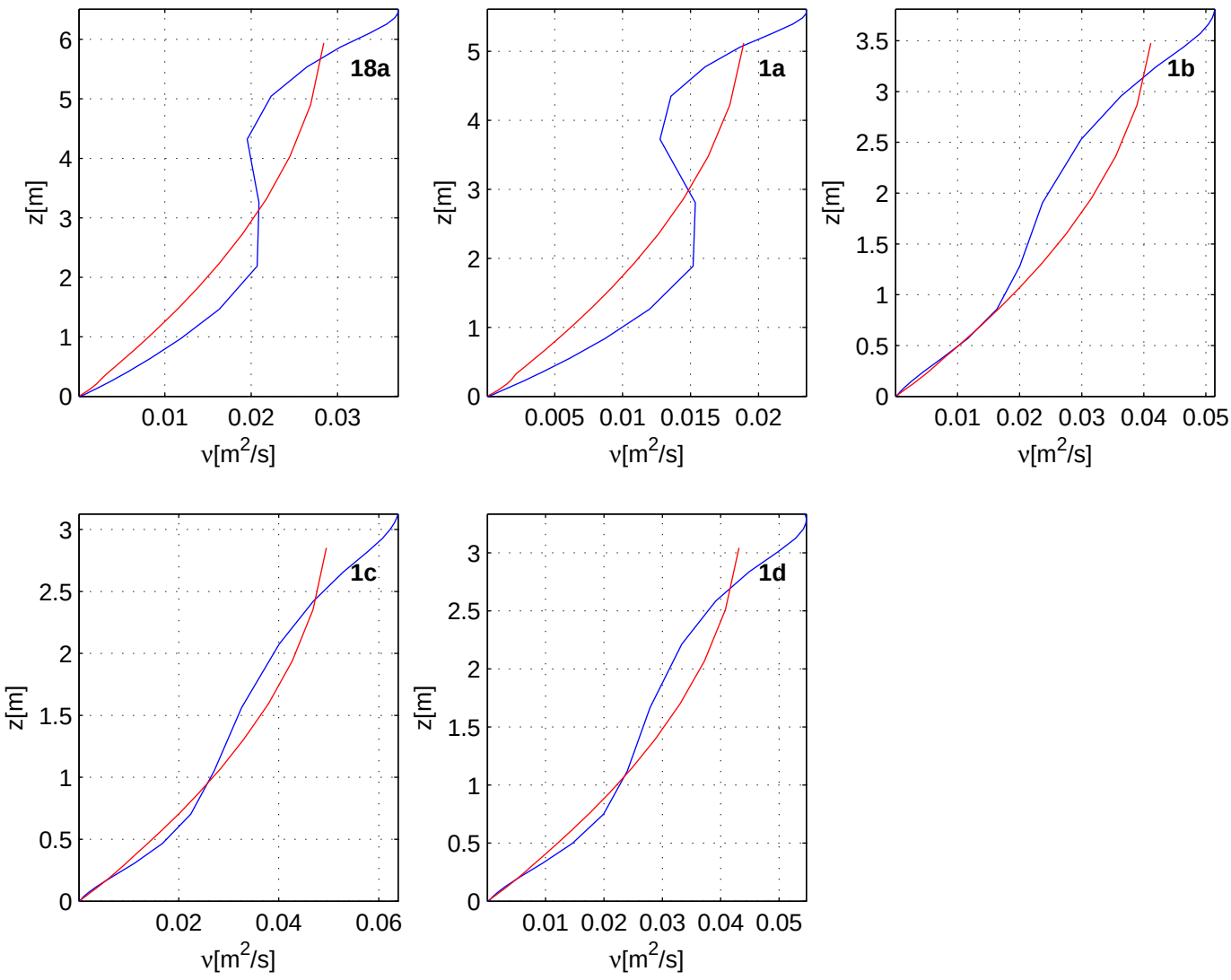

Model results Egmond field case Viscosity Profiles high tide Observation point 18A, 1A−1D	Compare	Egmond
	Delft3D	
Deltares	t=18	F3.3.18

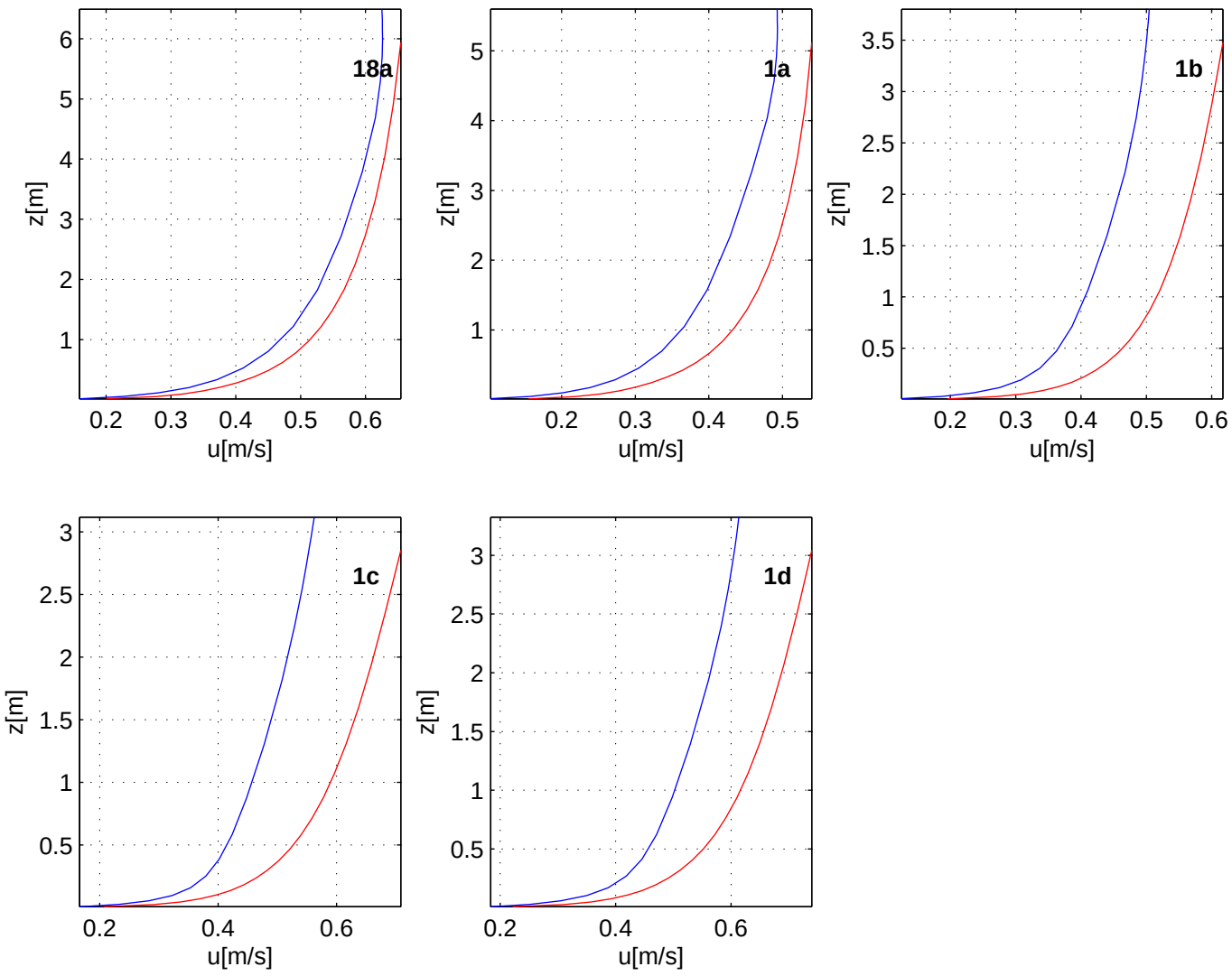

Model results Egmond field case Longshore velocity profiles high tide Observation point 18A, 1A−1D	Compare	Egmond
	Delft3D	
Deltares	t=18	F3.3.19

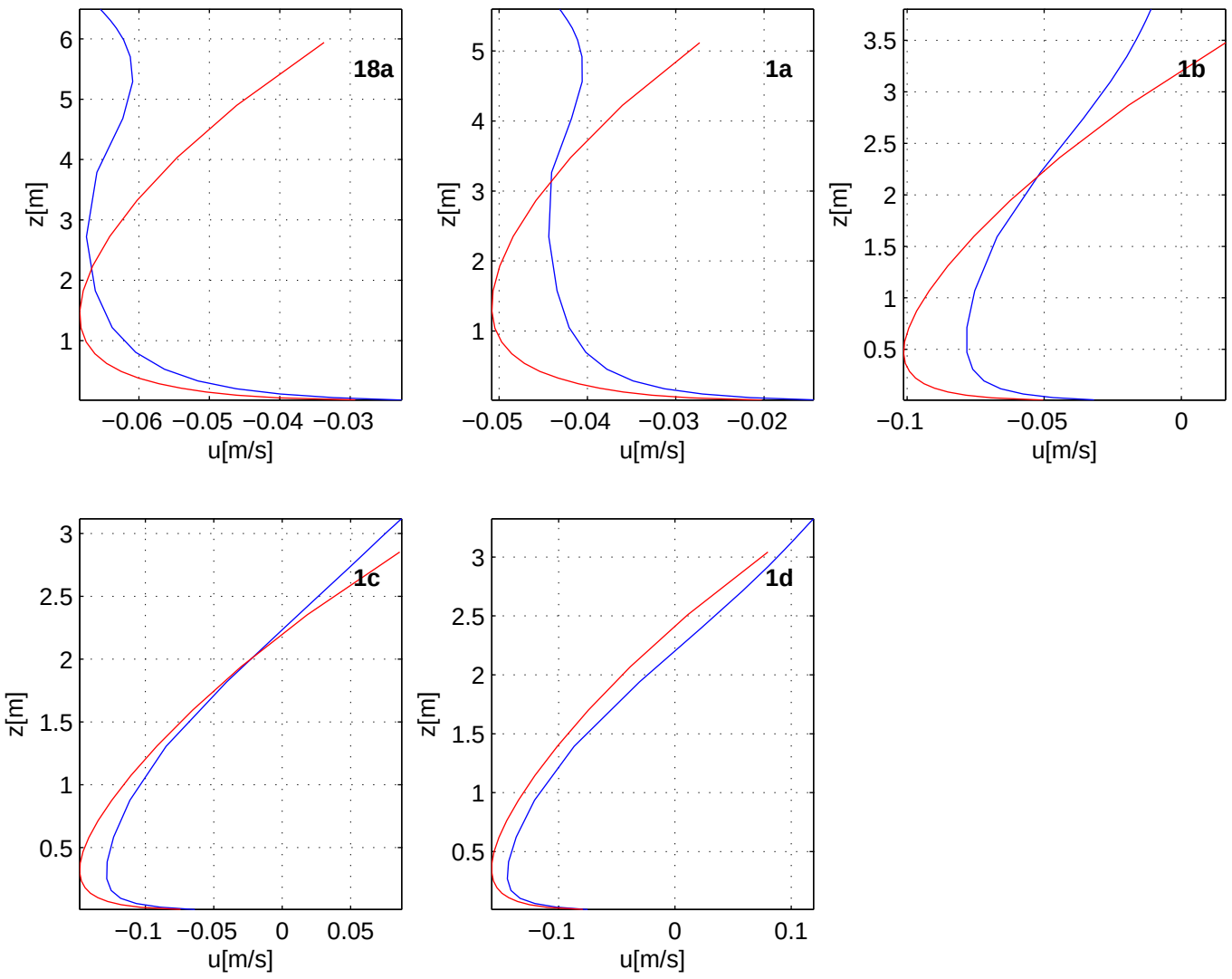

Model results Egmond field case Cross−shore velocity profiles high tide Observation point 18A, 1A−1D	Compare	Egmond
	Delft3D	
Deltares	t=18	F3.3.20

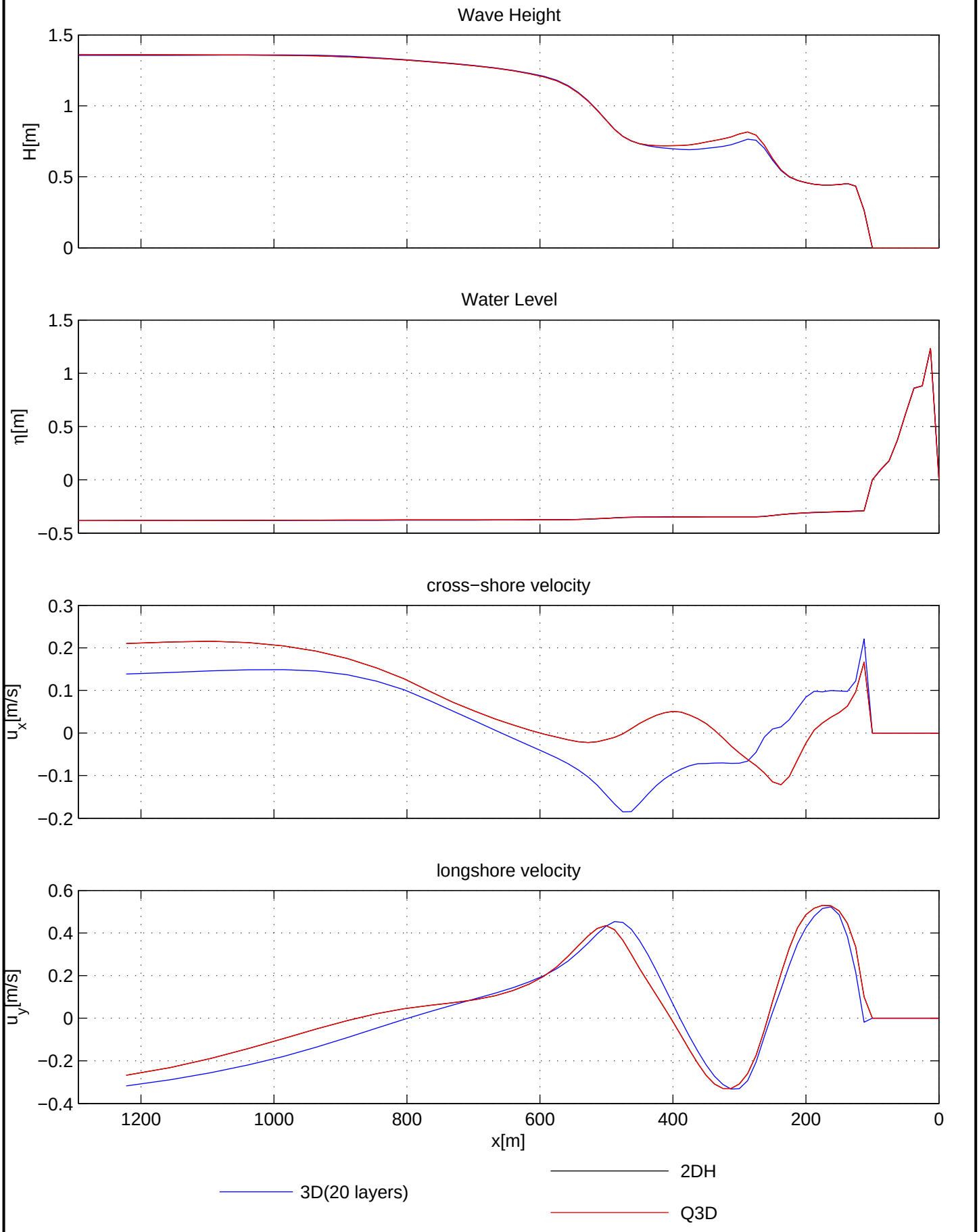

Model results Egmond field case Cross−shore distribution low tide Wave height, Water level, cross−shore velocity, longshore velocity	Compare	Egmond
	Delft3D	
Deltares	t=36	F3.3.21

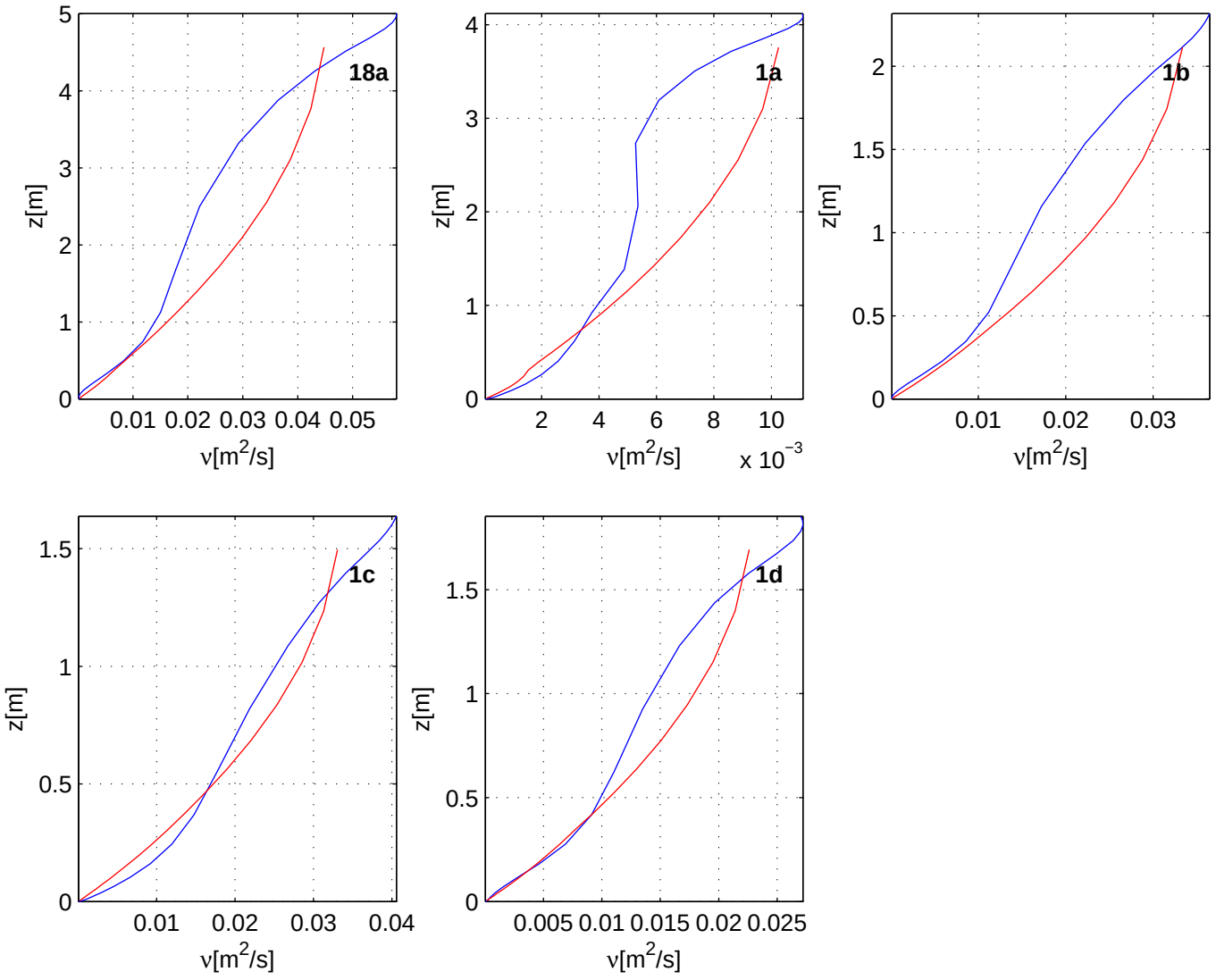

Model results Egmond field case Viscosity Profiles low tide Observation point 18A, 1A−1D	Compare	Egmond
	Delft3D	
Deltares	t=36	F3.3.22

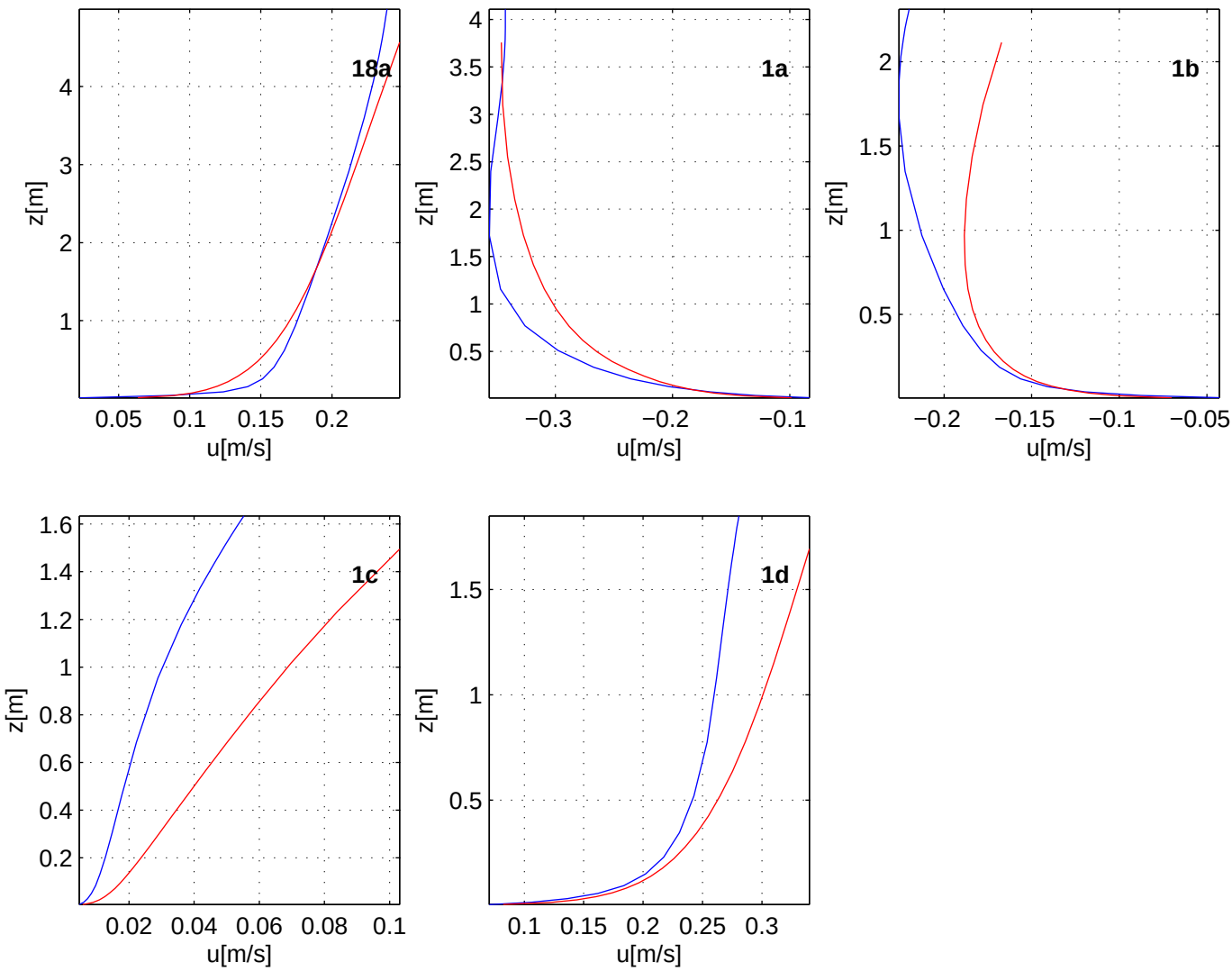

Model results Egmond field case Longshore velocity profiles low tide Observation point 18A, 1A−1D	Compare	Egmond
	Delft3D	
Deltares	t=36	F3.3.23

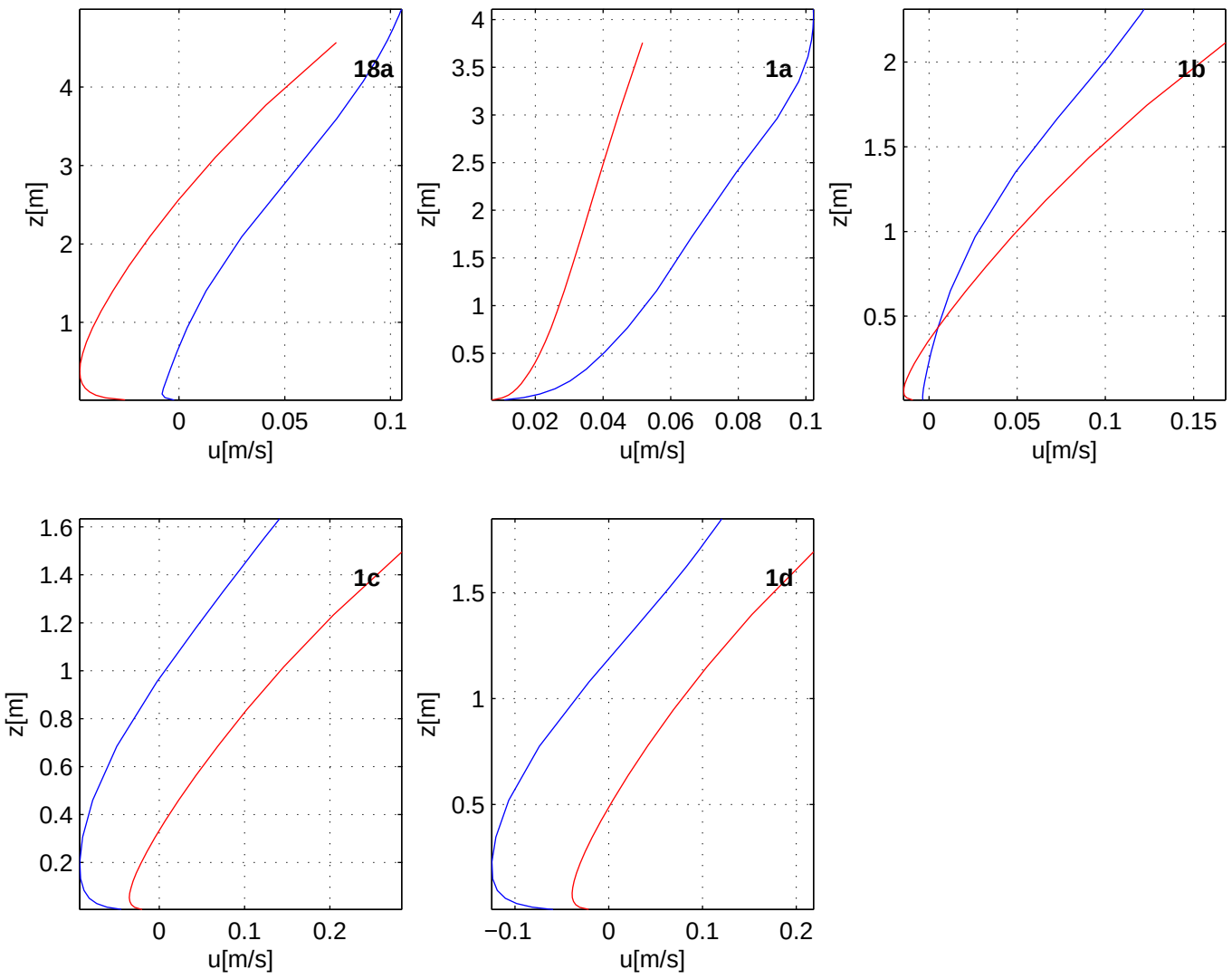

Model results Egmond field case Cross−shore velocity profiles low tide Observation point 18A, 1A−1D	Compare	Egmond
	Delft3D	
Deltares	t=36	F3.3.24

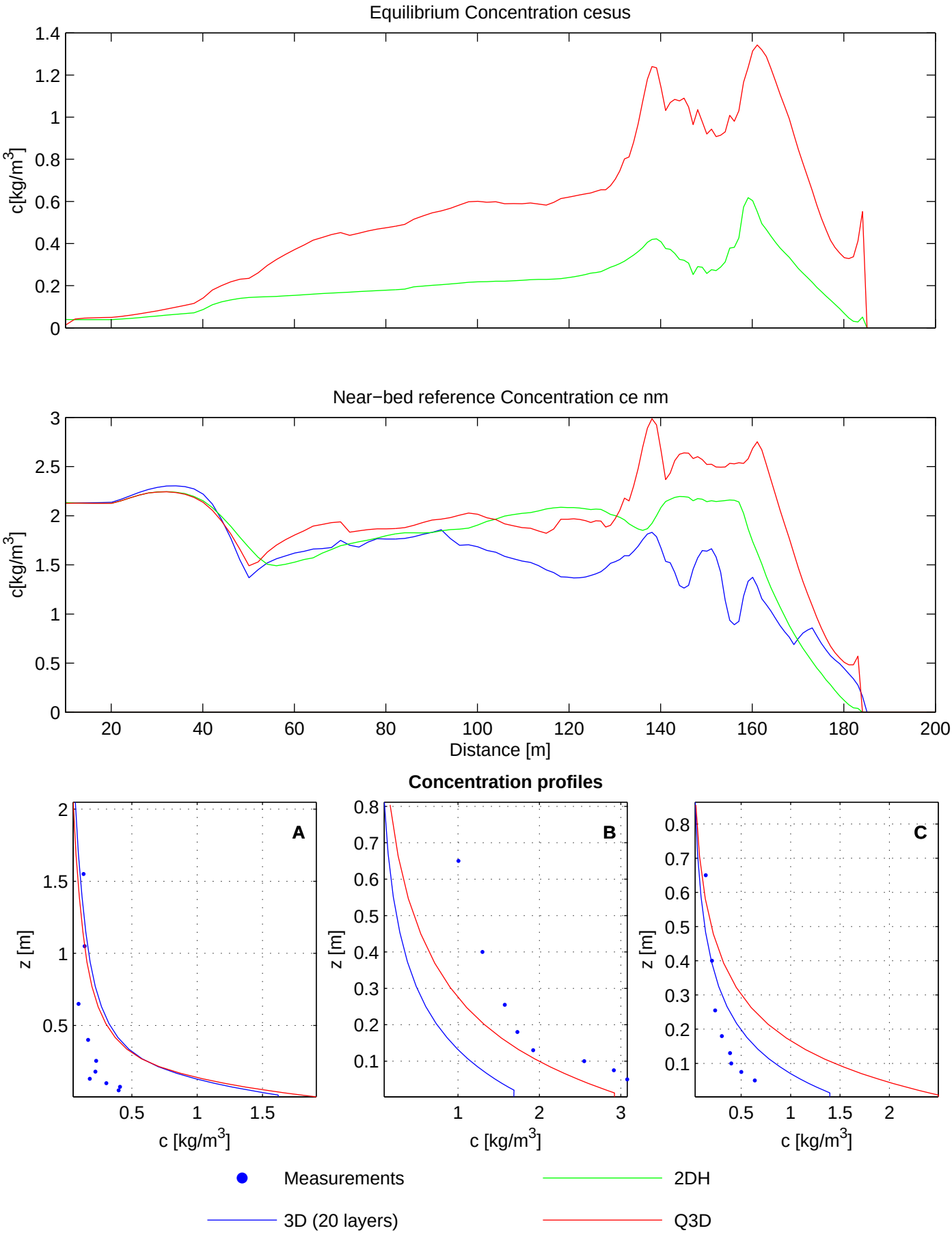

Model results LIP11D−1b experiment Near−bed reference concentration, Equilibrium concentration, Concentration profiles	Compare	LIP
	Delft3D	
Deltares		F3.4.1a

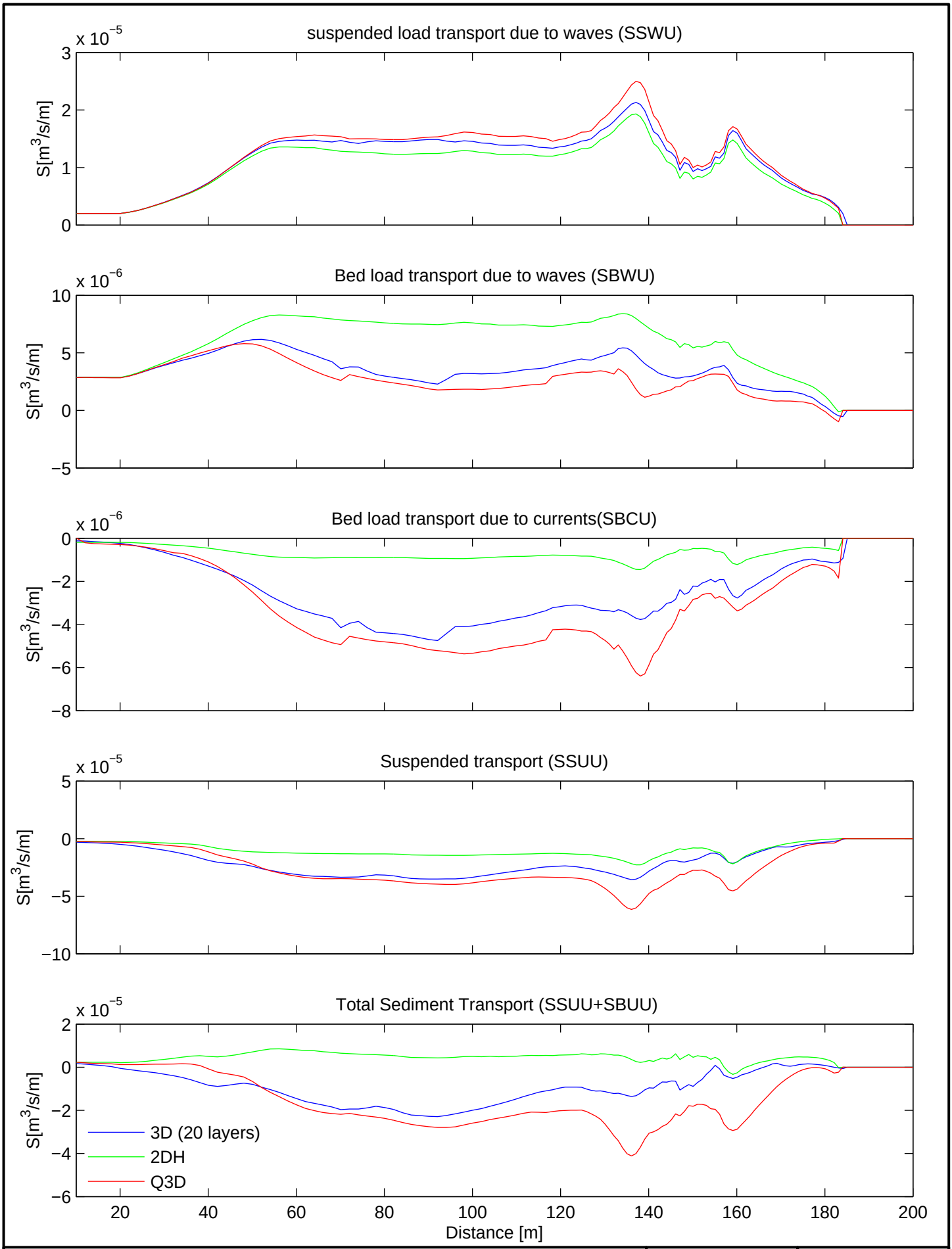

Model results LIP11D−1b experiment Sediment Transport Bed load components, Suspended Load and Total Sediment transport	Compare	LIP
	Delft3D	
Deltares		F3.4.1b

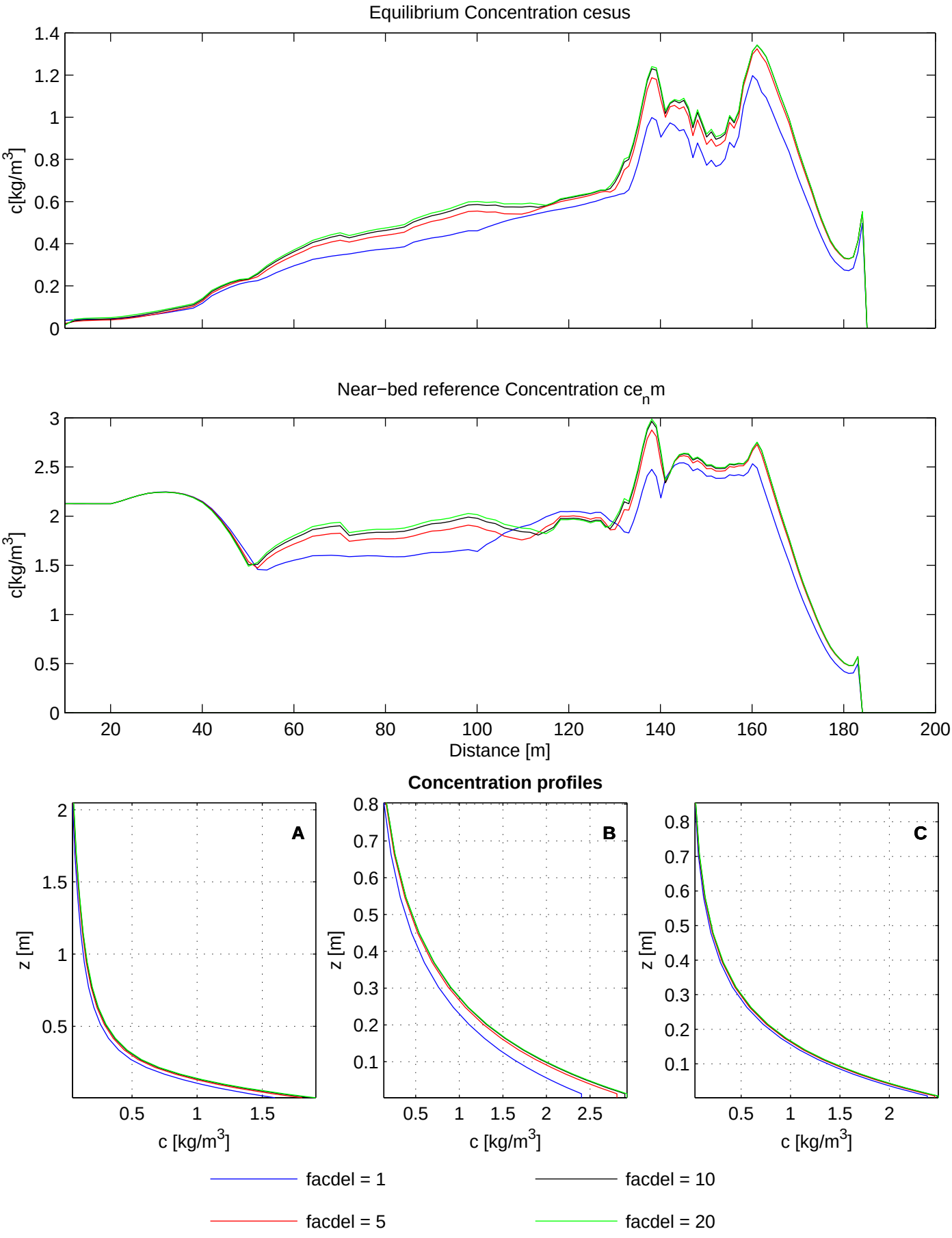

Model results LIP11D−1b experiment Parameter sensitivity multiplication factor bottom boundary layer thickness[facdel] Bed load components, Suspended Load and Total Sediment transport	Q3D	LIP
	Delft3D	
Deltares	facdel	F3.4.2a

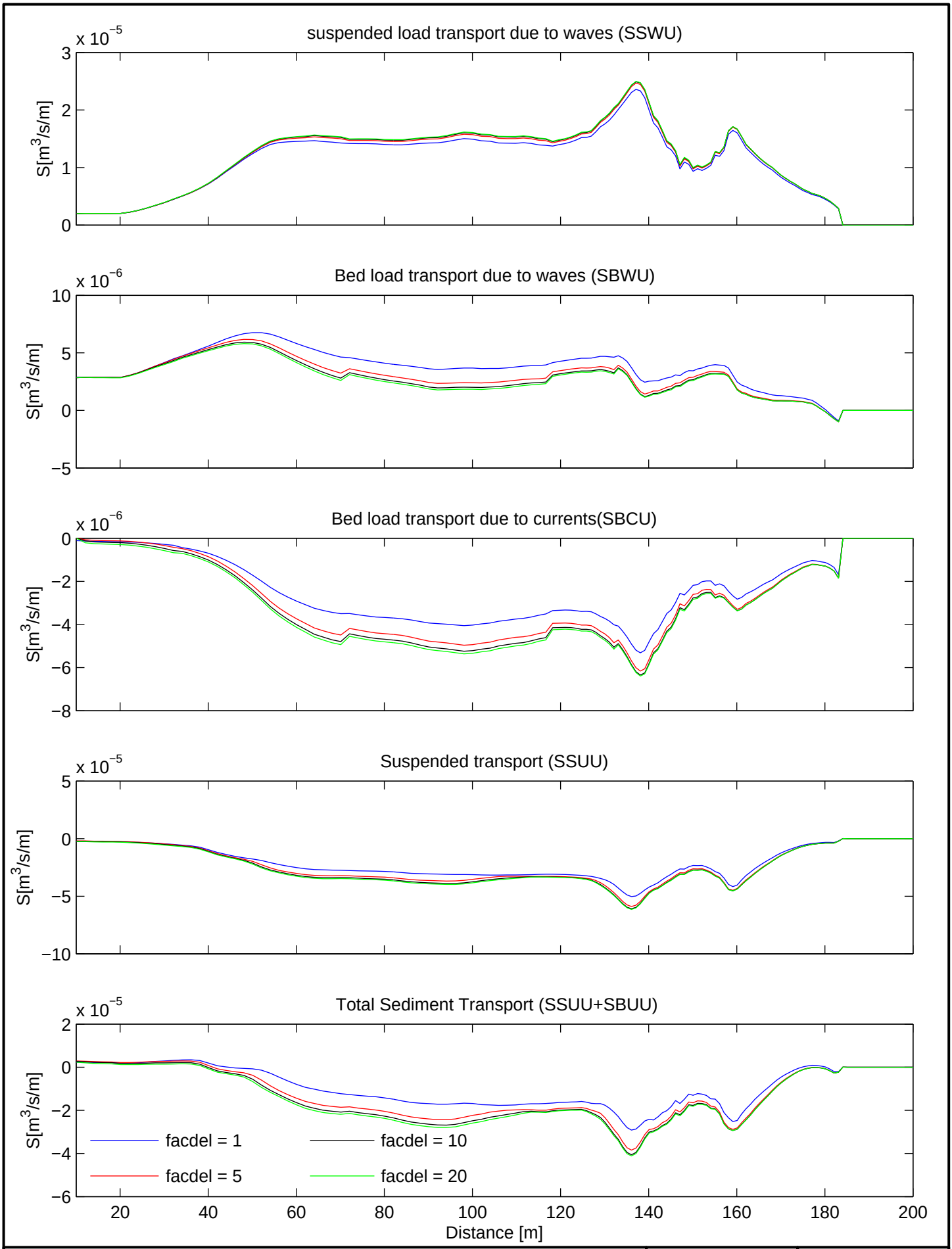

Model results LIP11D−1b experiment Parameter sensitivity multiplication factor bottom boundary layer thickness[facdel] Bed load components, Suspended Load and Total Sediment transport	Q3D	LIP
	Delft3D	
Deltares	facdel	F3.4.2b

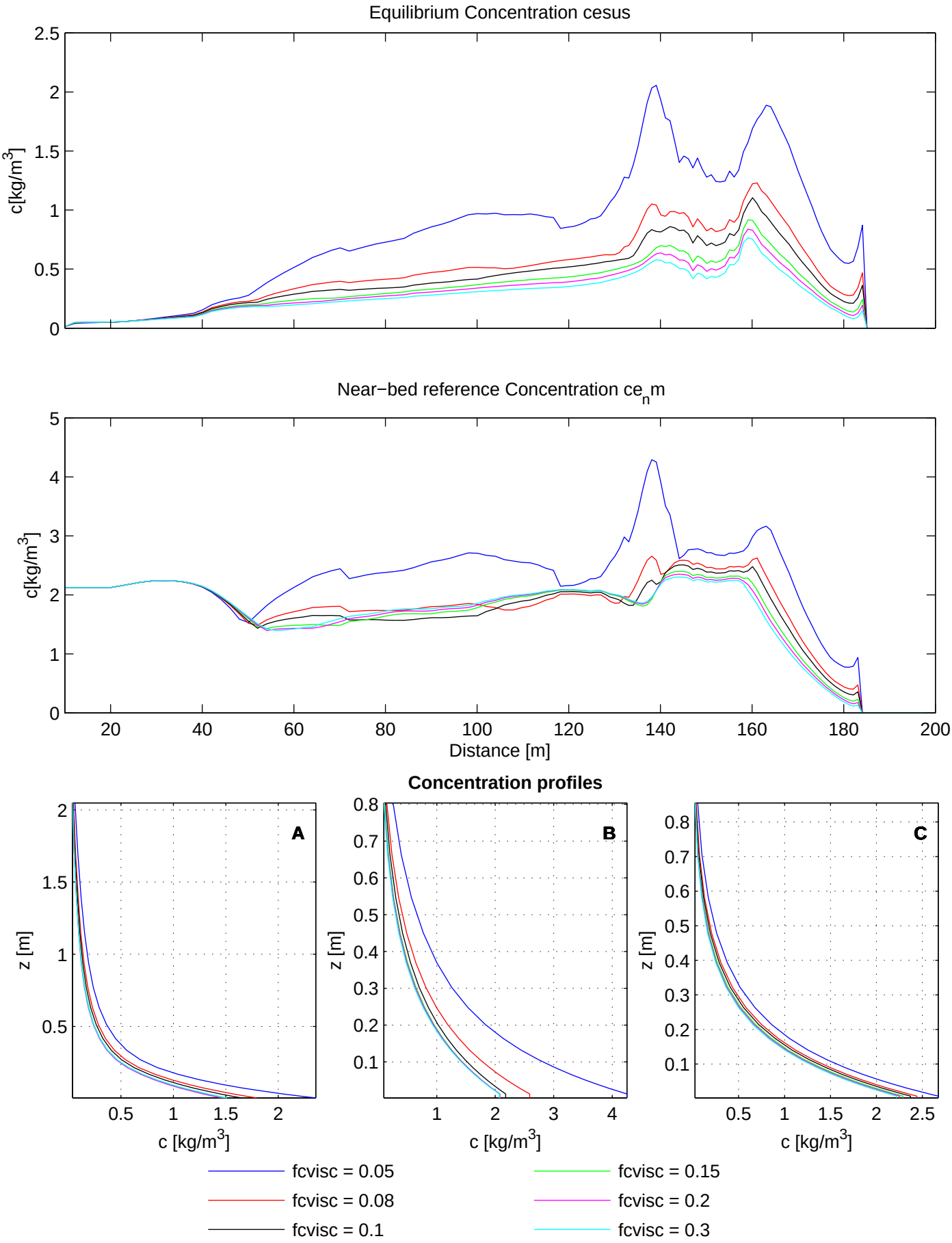

Model results LIP11D−1b experiment Parameter sensitivity multiplication factor wave−induced viscosity[fcvisc] Bed load components, Suspended Load and Total Sediment transport	Q3D	LIP
	Delft3D	
Deltares	fcvisc	F3.4.3a

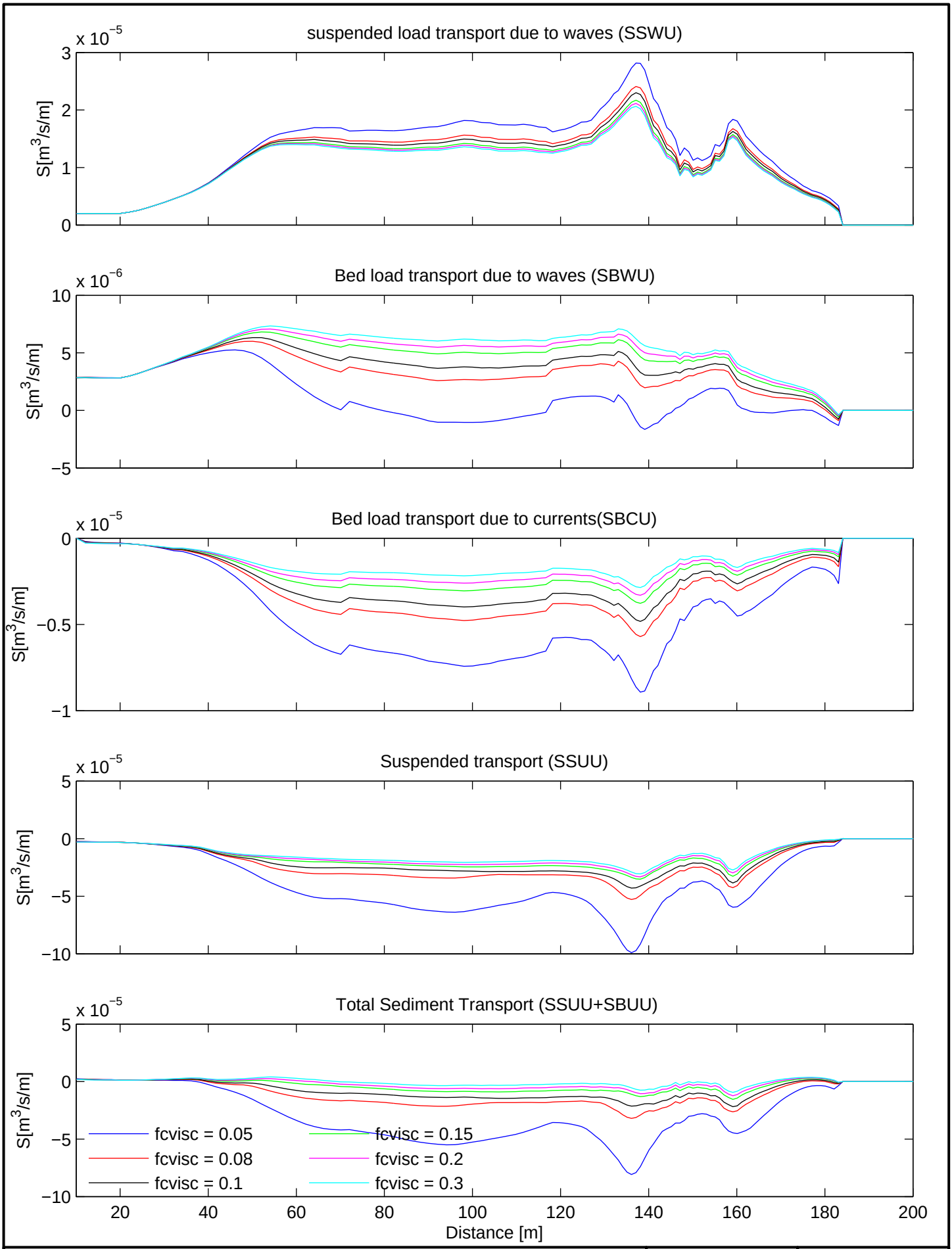

Model results LIP11D−1b experiment Parameter sensitivity multiplication factor wave−induced viscosity[fcvisc] Bed load components, Suspended Load and Total Sediment transport	Q3D	LIP
	Delft3D	
Deltares	fcvisc	F3.4.3b

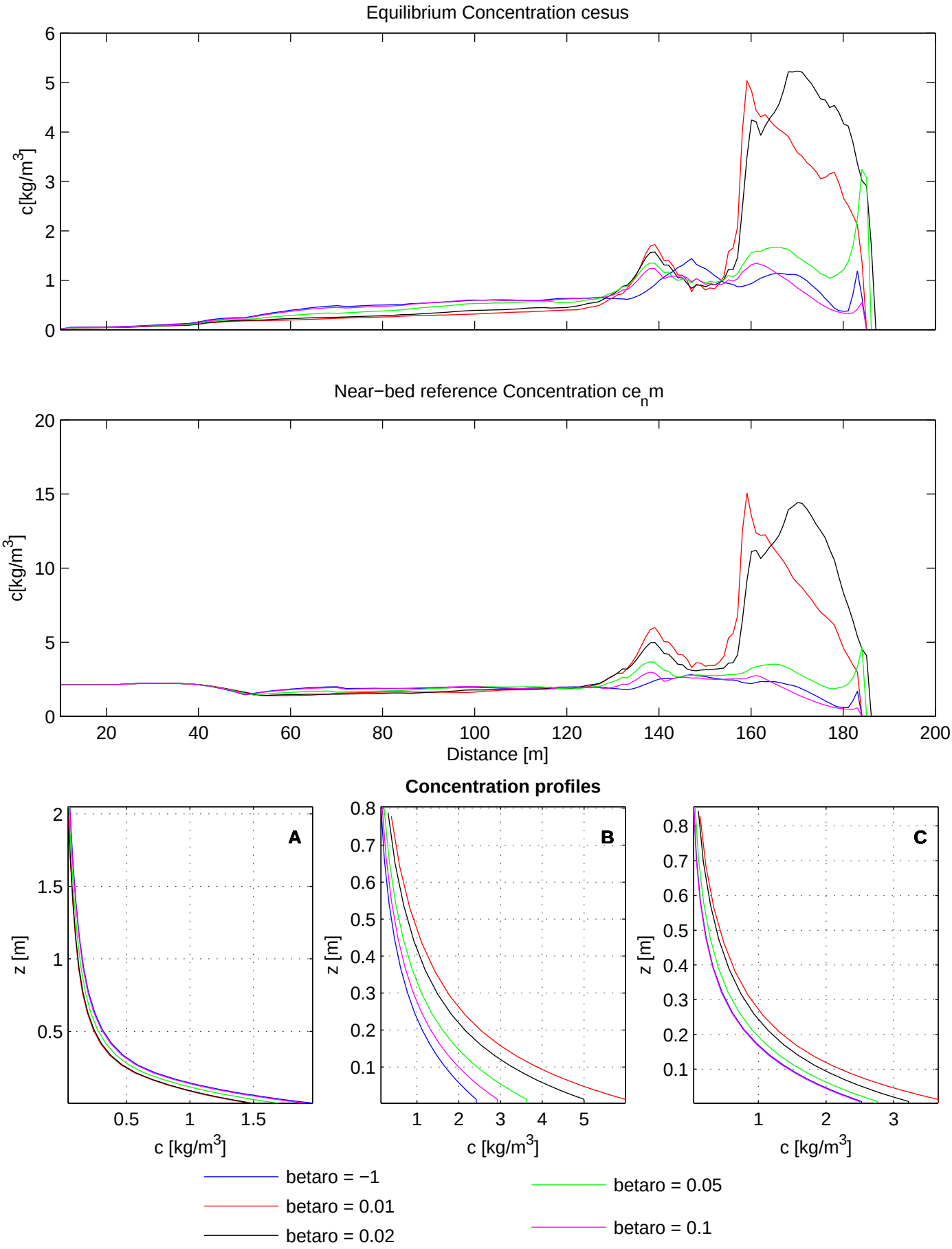

Model results LIP11D−1b experiment Parameter sensitivity angle of wave front [betaro] Bed load components, Suspended Load and Total Sediment transport	Q3D	LIP
	Delft3D	
Deltares	betaro	F3.4.4a

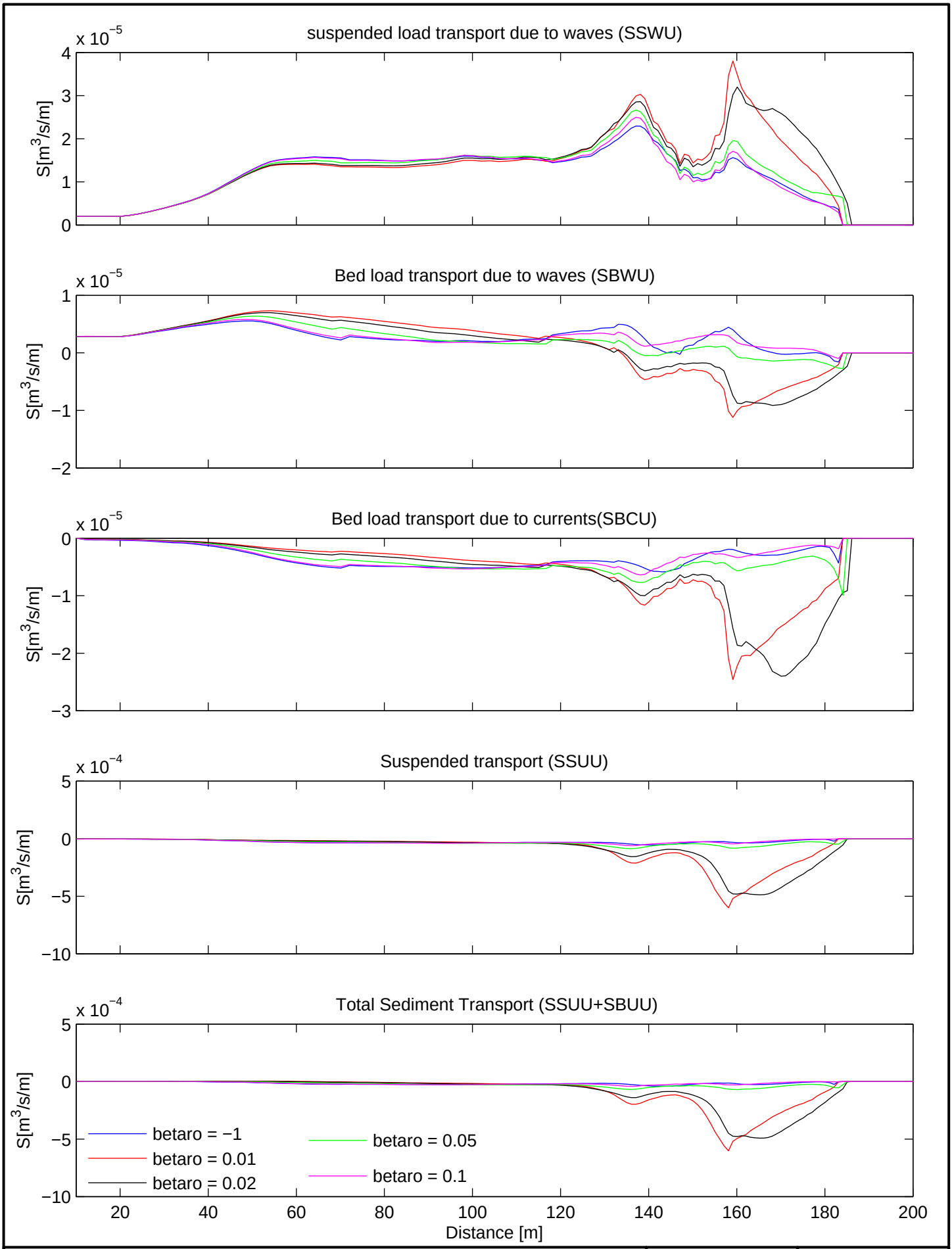

Model results LIP11D−1b experiment Parameter sensitivity angle of wave front [betaro] Bed load components, Suspended Load and Total Sediment transport	Q3D	LIP
	Delft3D	
Deltares	betaro	F3.4.4b

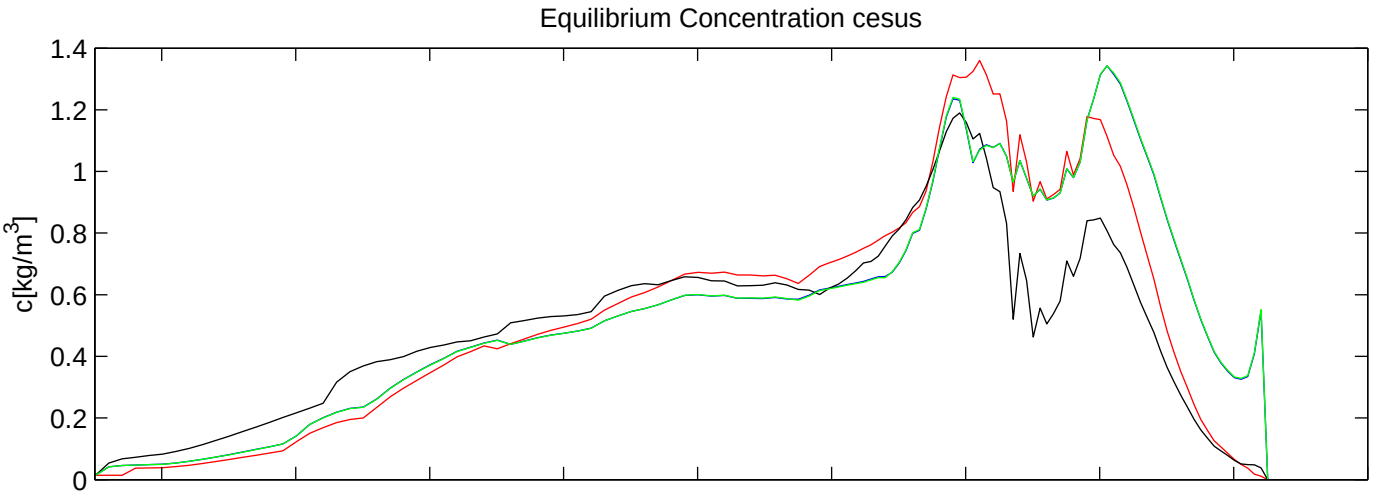

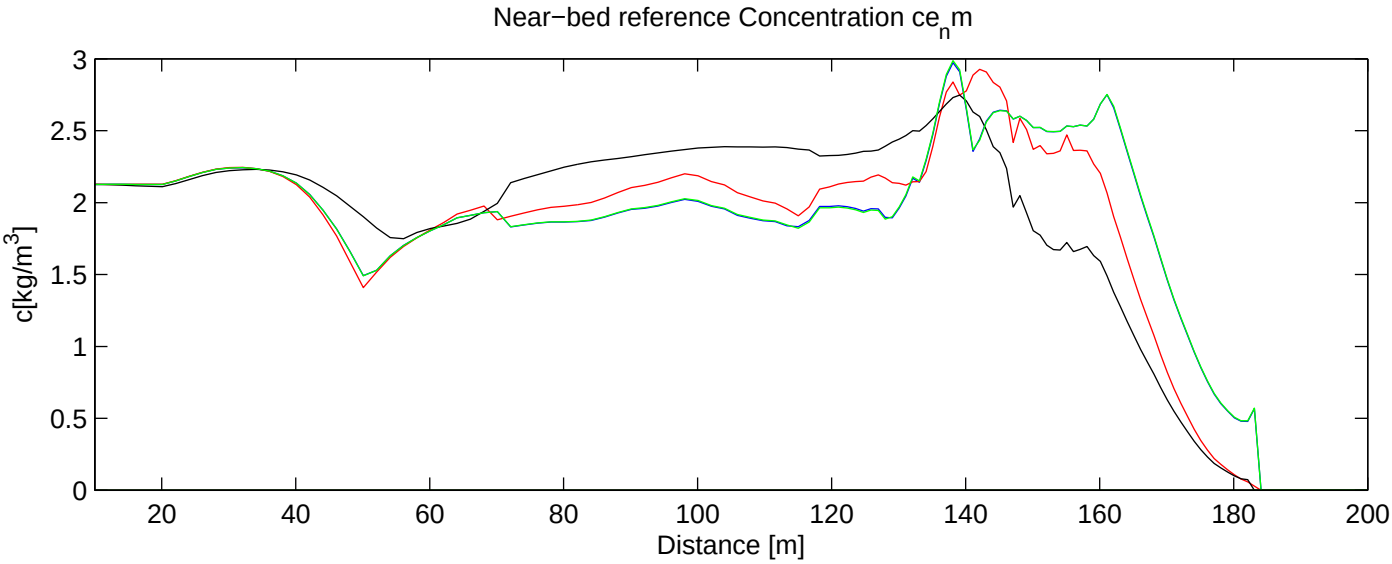

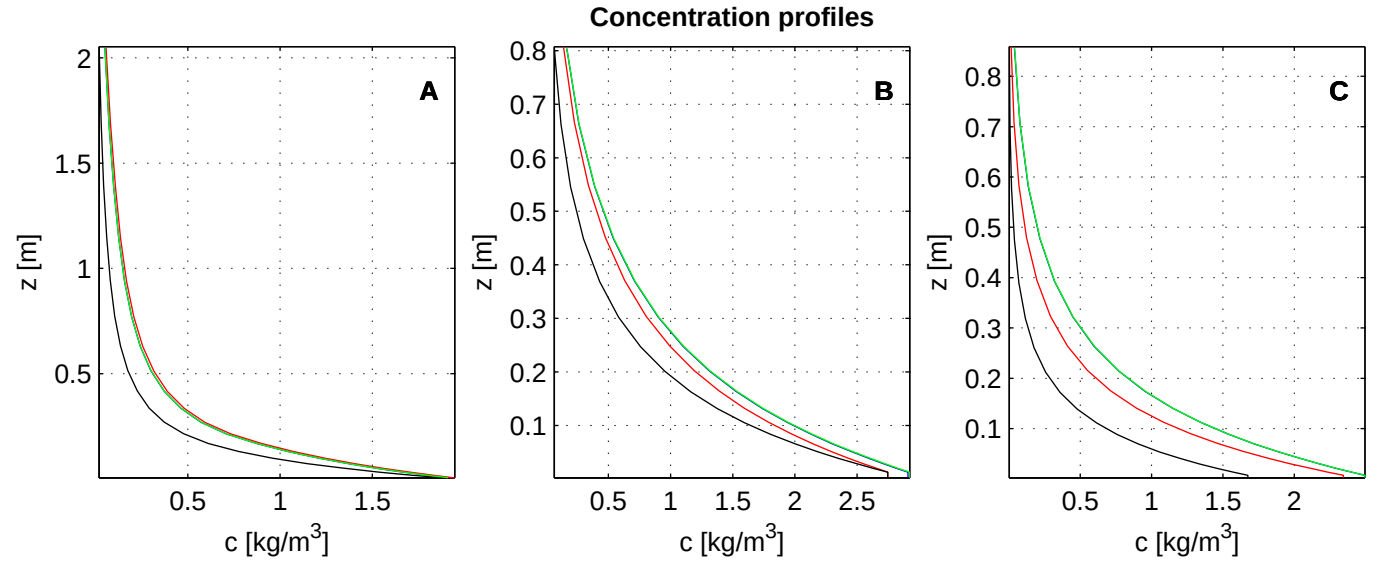

Model results LIP11D−1b experiment Parameter sensitivity breaker parameter [gamdis] Bed load components, Suspended Load and Total Sediment transport	Q3D	LIP
	Delft3D	
Deltares	gamdis	F3.4.5a

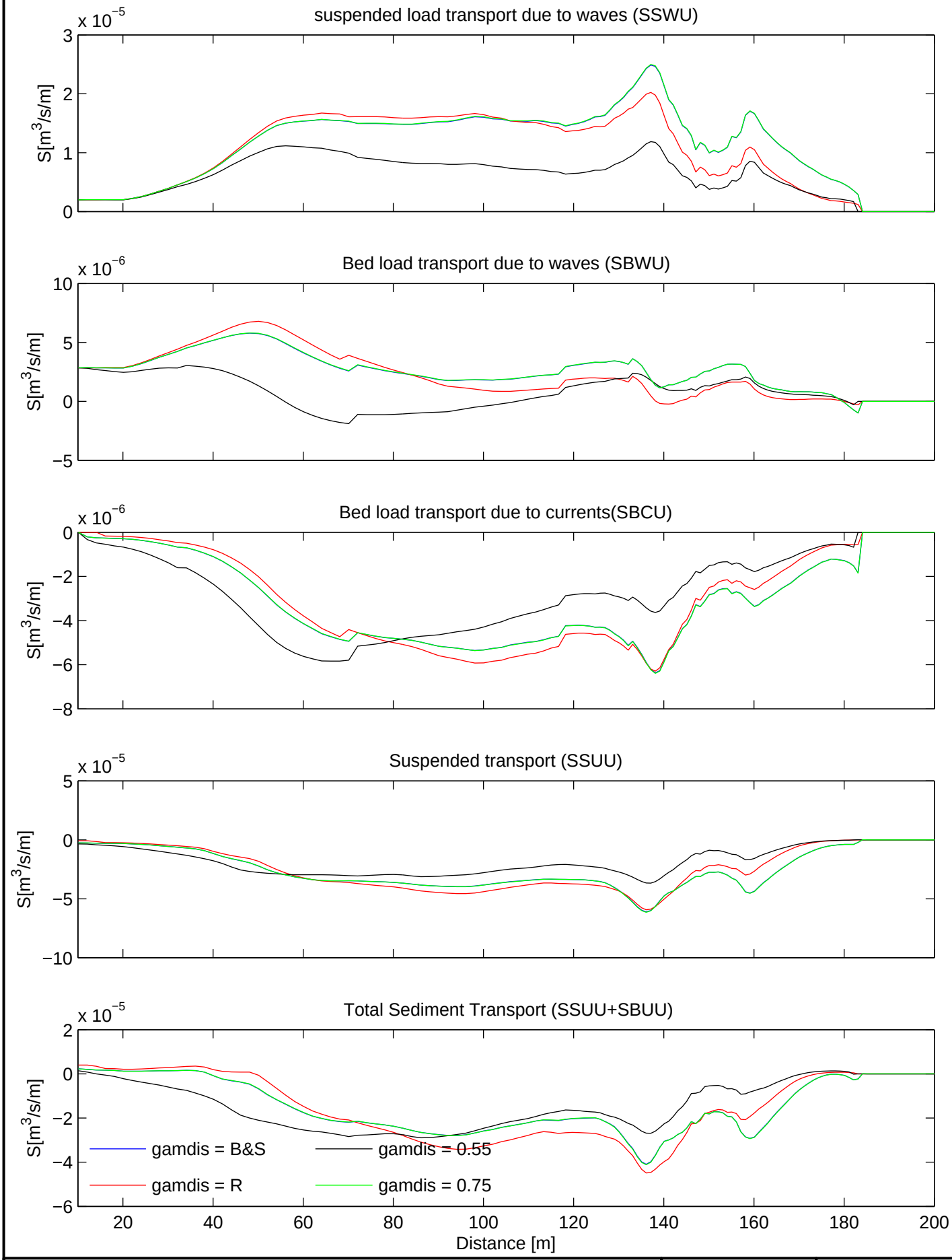

Model results LIP11D−1b experiment Parameter sensitivity breaker parameter [gamdis] Bed load components, Suspended Load and Total Sediment transport	Q3D	LIP
	Delft3D	
Deltares	gamdis	F3.4.5b

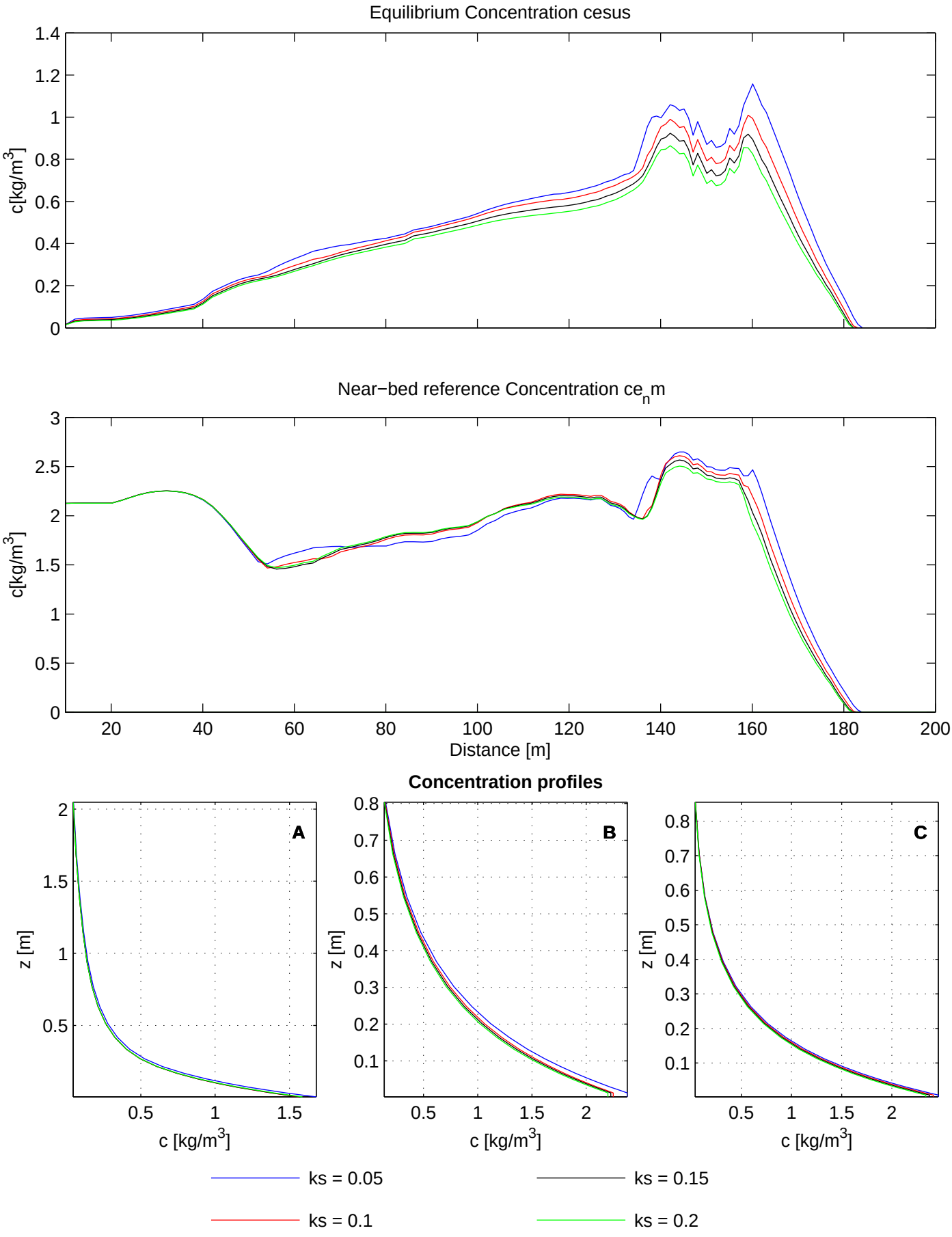

Model results LIP11D−1b experiment Parameter sensitivity roughness height [ks] Bed load components, Suspended Load and Total Sediment transport	Q3D	LIP
	Delft3D	
Deltares	ks	F3.4.6a

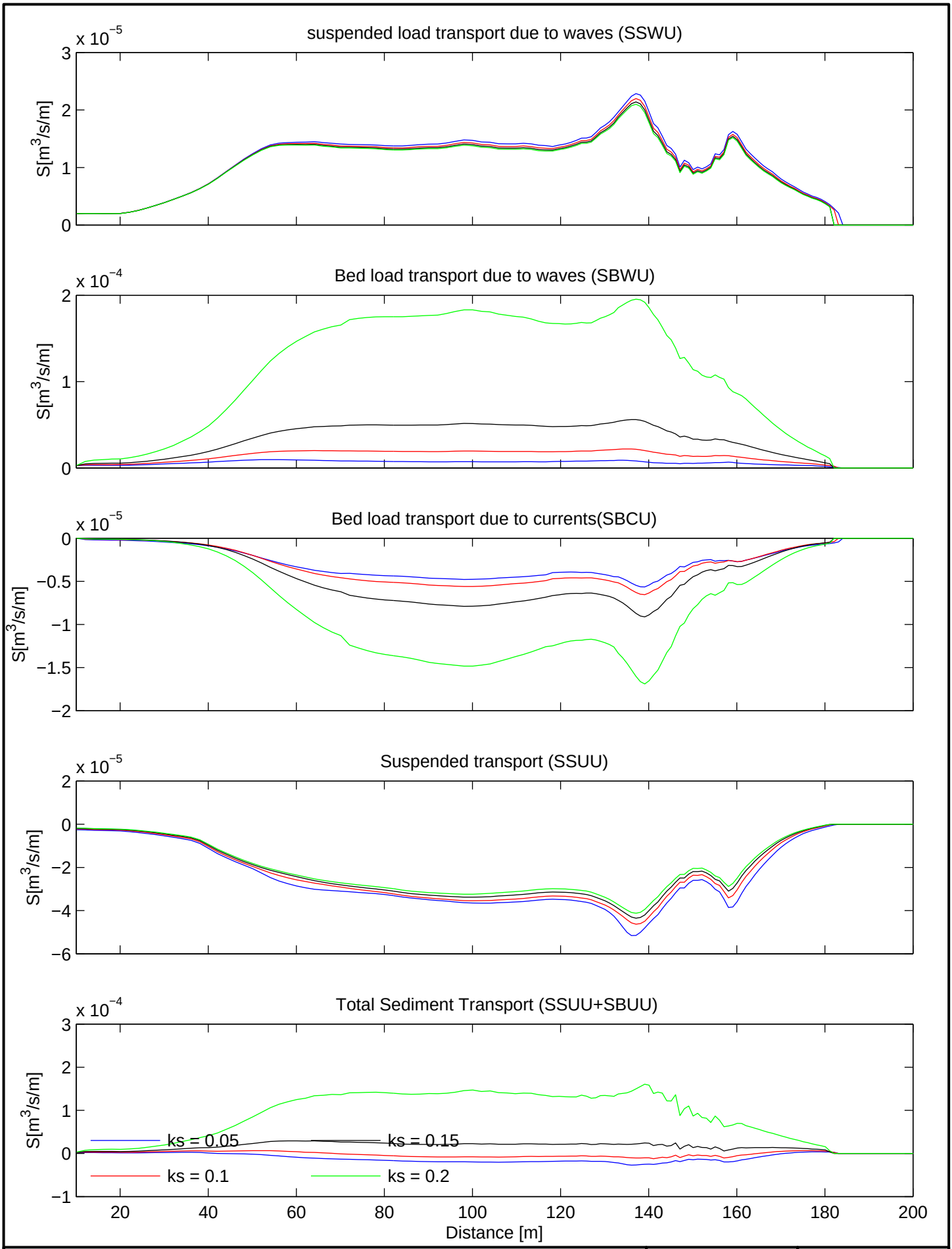

Model results LIP11D−1b experiment Parameter sensitivity roughness height [ks] Bed load components, Suspended Load and Total Sediment transport	Q3D	LIP
	Delft3D	
Deltares	ks	F3.4.6b

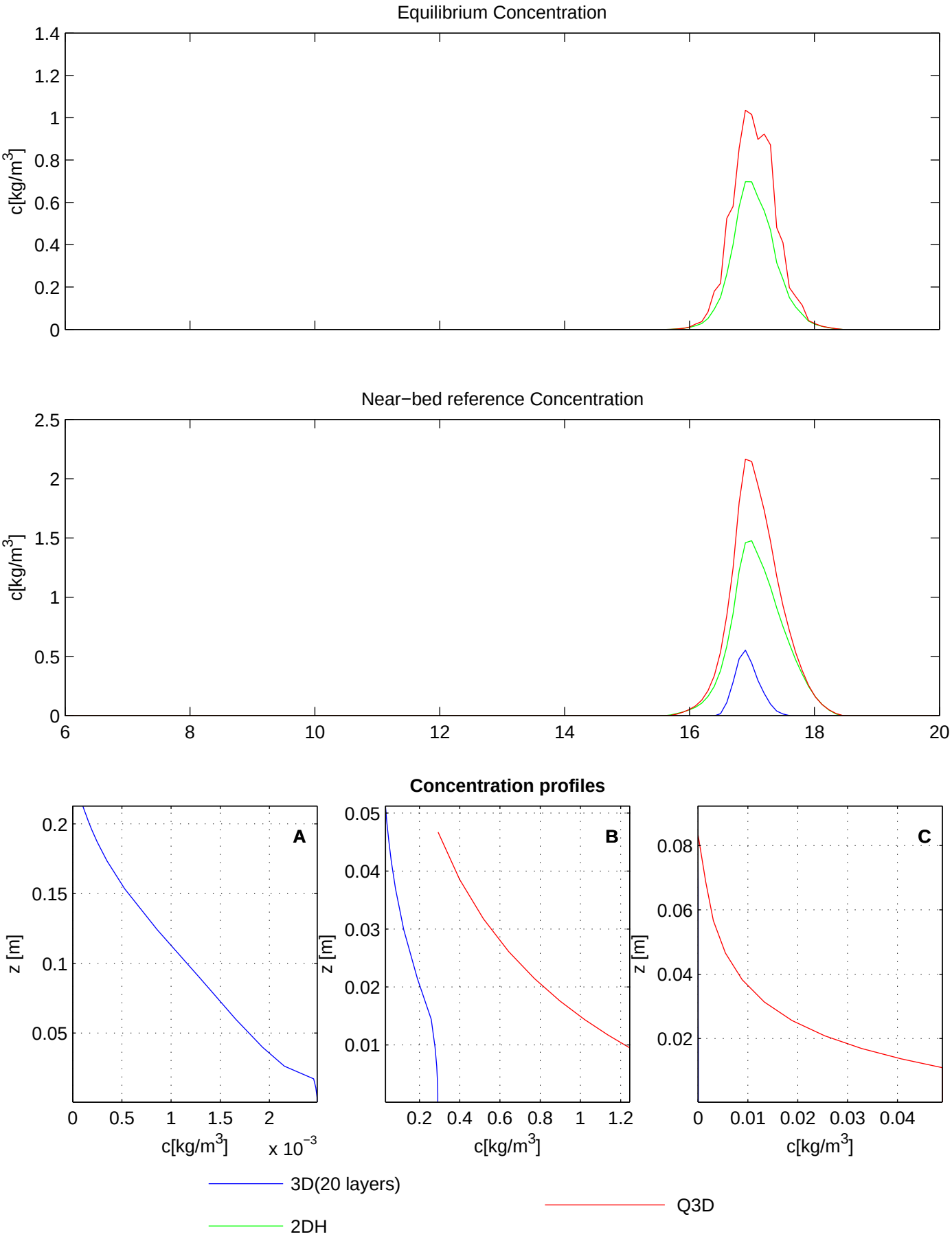

Model results Reniers−SO014 experiment Near−bed reference concentration, Equilibrium concentration, Concentration profiles	Compare	Reniers
	Delft3D	
Deltares		F3.4.7a

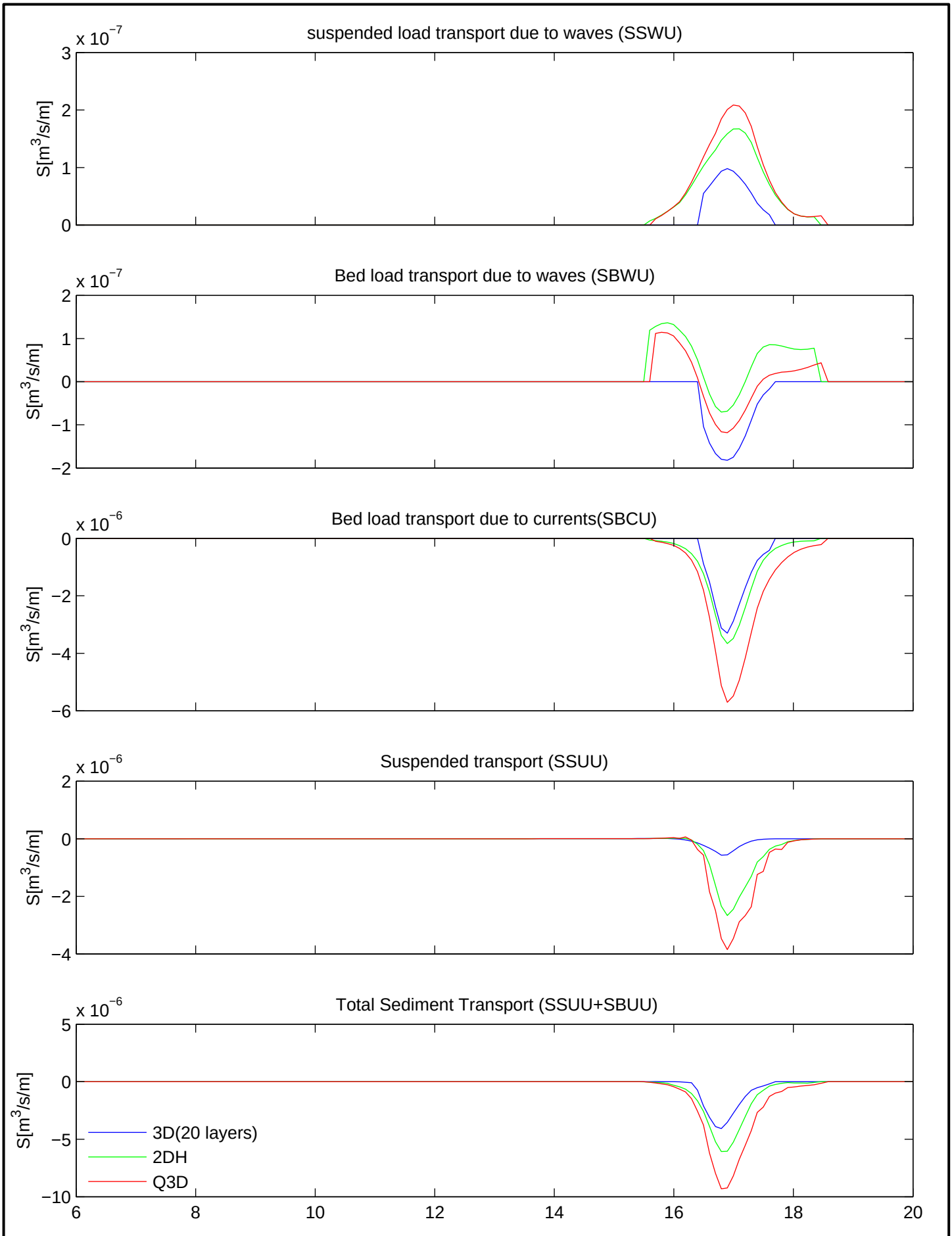

Model results Reniers−SO014 experiment Cross−shore Sediment Transport Bed load components, Suspended Load and Total Sediment transport	Compare	Reniers
	Delft3D	
Deltares		F3.4.7b

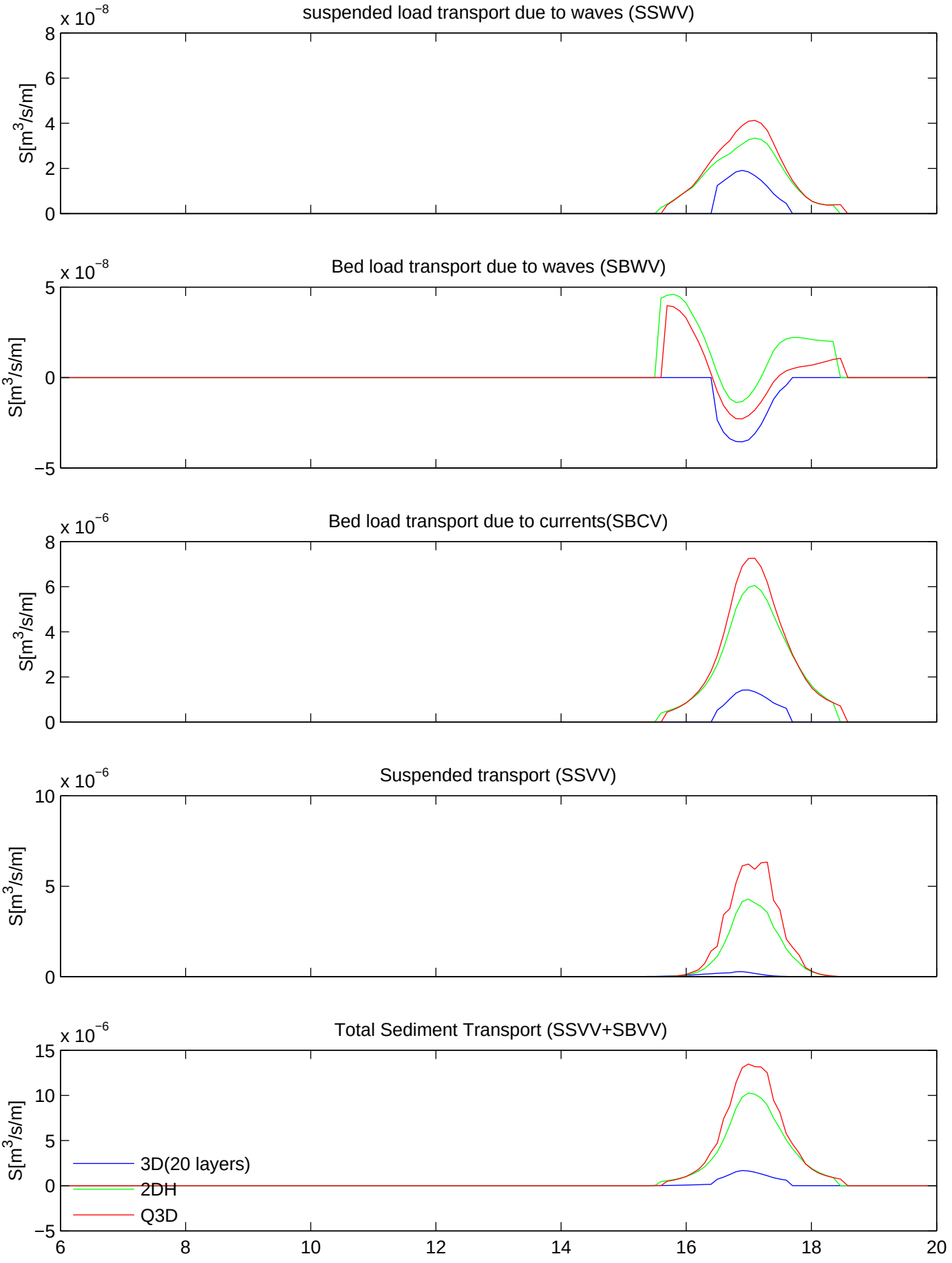

Model results Reniers−SO014 experiment Longshore Sediment Transport Bed load components, Suspended Load and Total Sediment transport	Compare	Reniers
	Delft3D	
Deltares		F3.4.7c

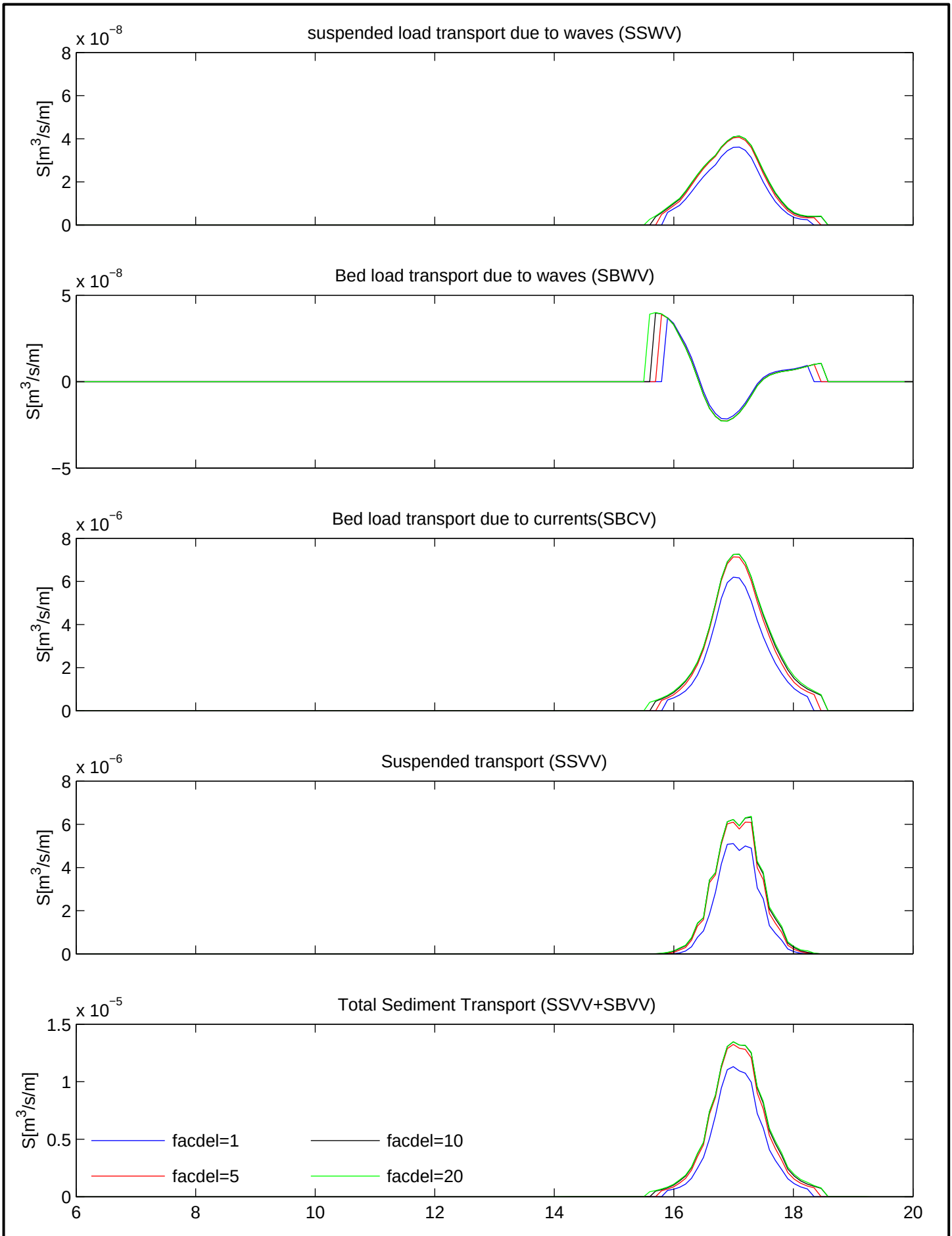

Model results Reniers−SO014 experiment Longshore Parameter sensitivity multiplication factor bottom boundary layer thickness[facdel] Bed load components, Suspended Load and Total Sediment transport	Q3D	Reniers
	Delft3D	
Deltares	facdel	F3.4.8

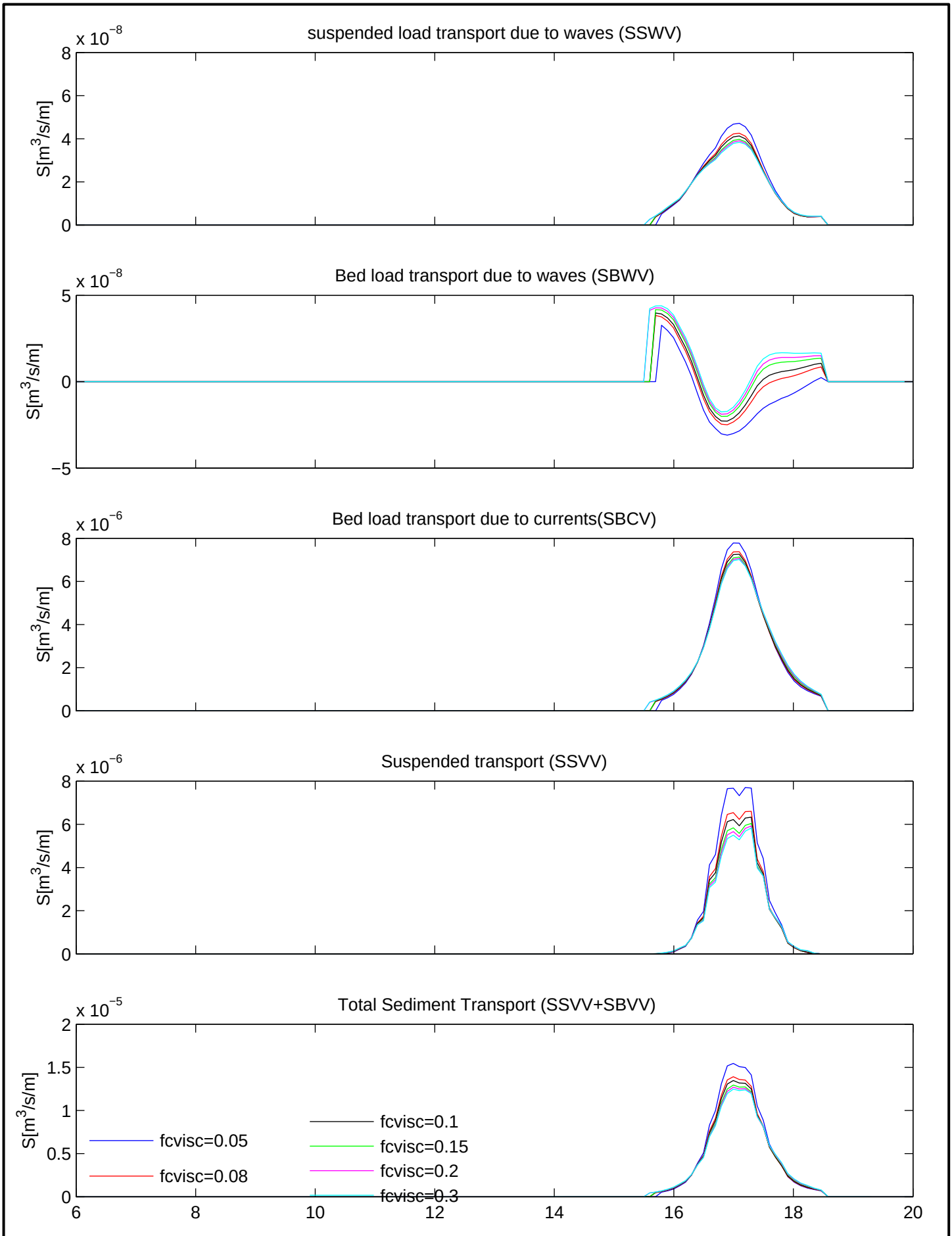

Model results Reniers−SO014 experiment Longshore Parameter sensitivity multiplication factor wave−induced viscosity[fcvisc] Bed load components, Suspended Load and Total Sediment transport	Q3D	Reniers
	Delft3D	
Deltares	fcvisc	F3.4.9

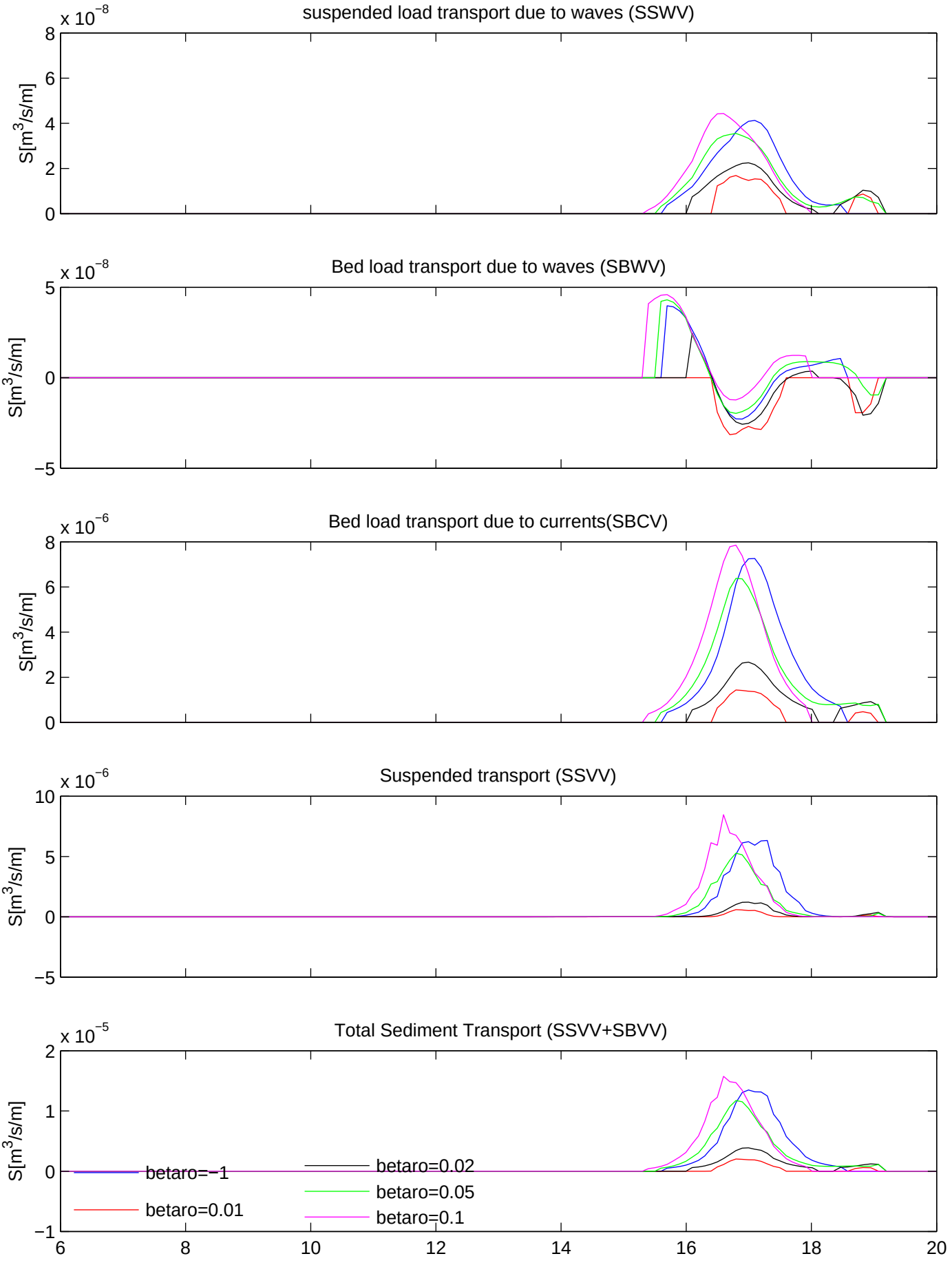

Model results Reniers−SO014 experiment Longshore Parameter sensitivity angle of wave front [betaro] Bed load components, Suspended Load and Total Sediment transport	Q3D	Reniers
	Delft3D	
Deltares	betaro	F3.4.10

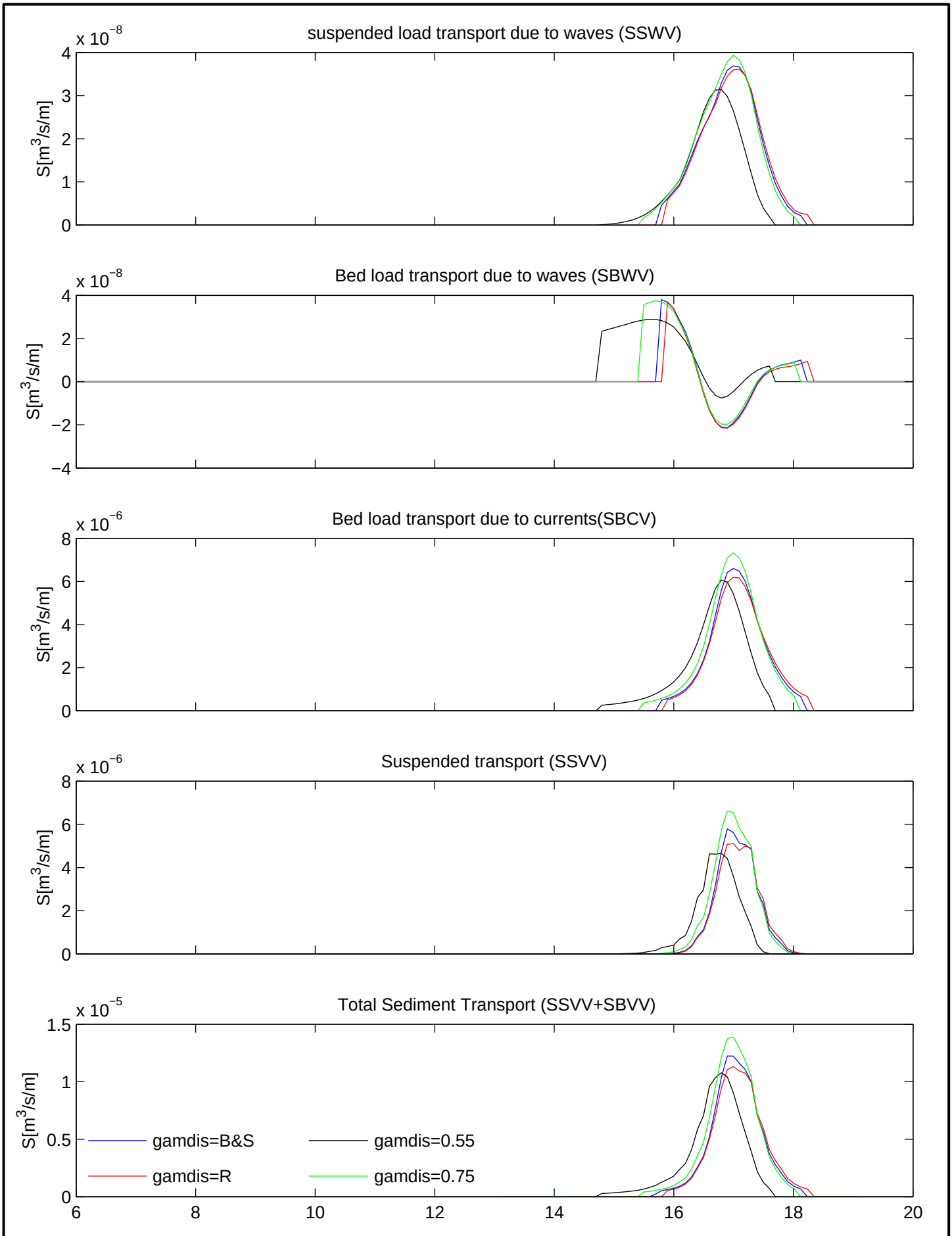

Model results Reniers−SO014 experiment Longshore Parameter sensitivity breaker parameter [gamdis] Bed load components, Suspended Load and Total Sediment transport	Q3D	Reniers
	Delft3D	
Deltares	gamdis	F3.4.11

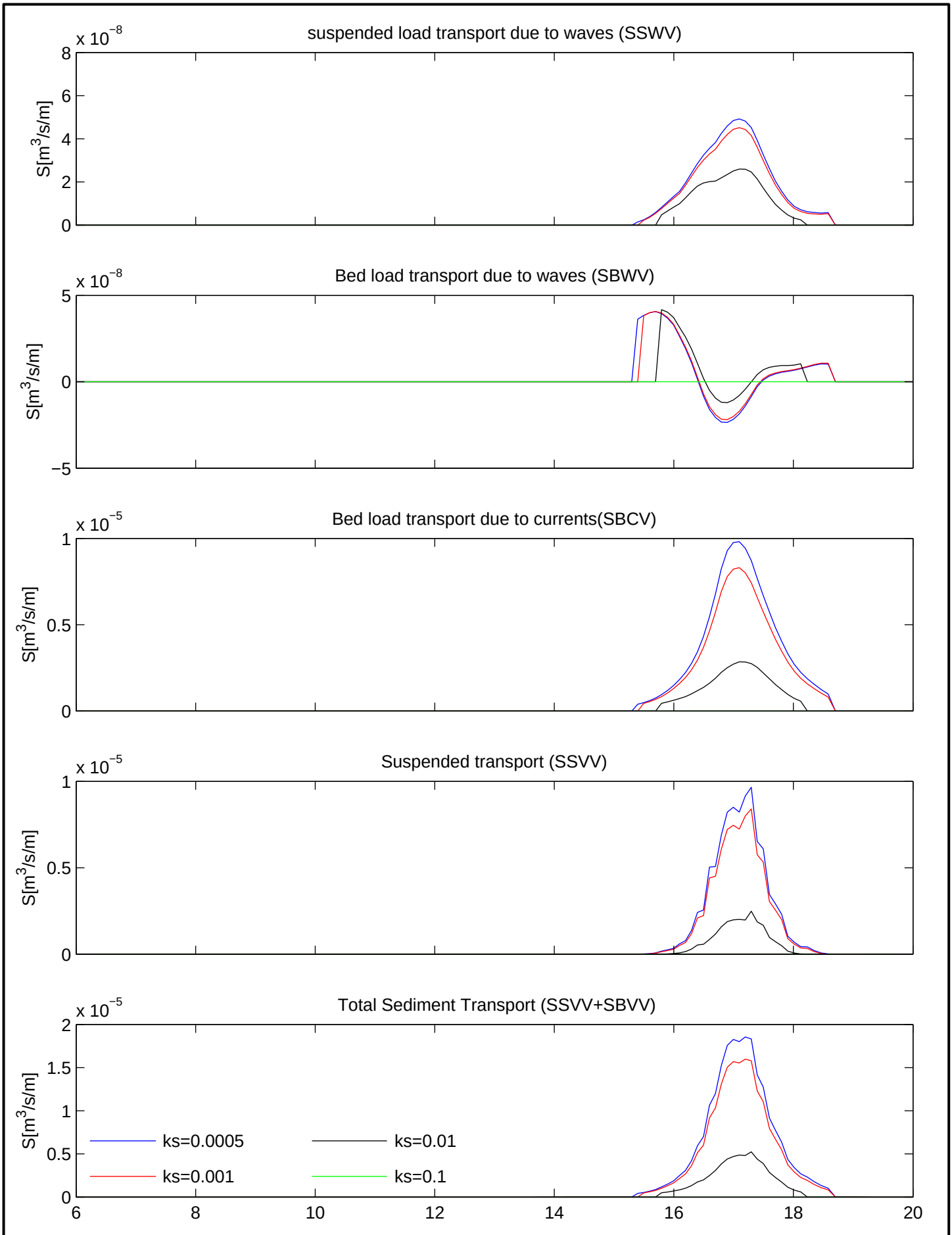

Model results Reniers−SO014 experiment Longshore Parameter sensitivity roughness height [ks] Bed load components, Suspended Load and Total Sediment transport	Q3D	Reniers
	Delft3D	
Deltares	ks	F3.4.12

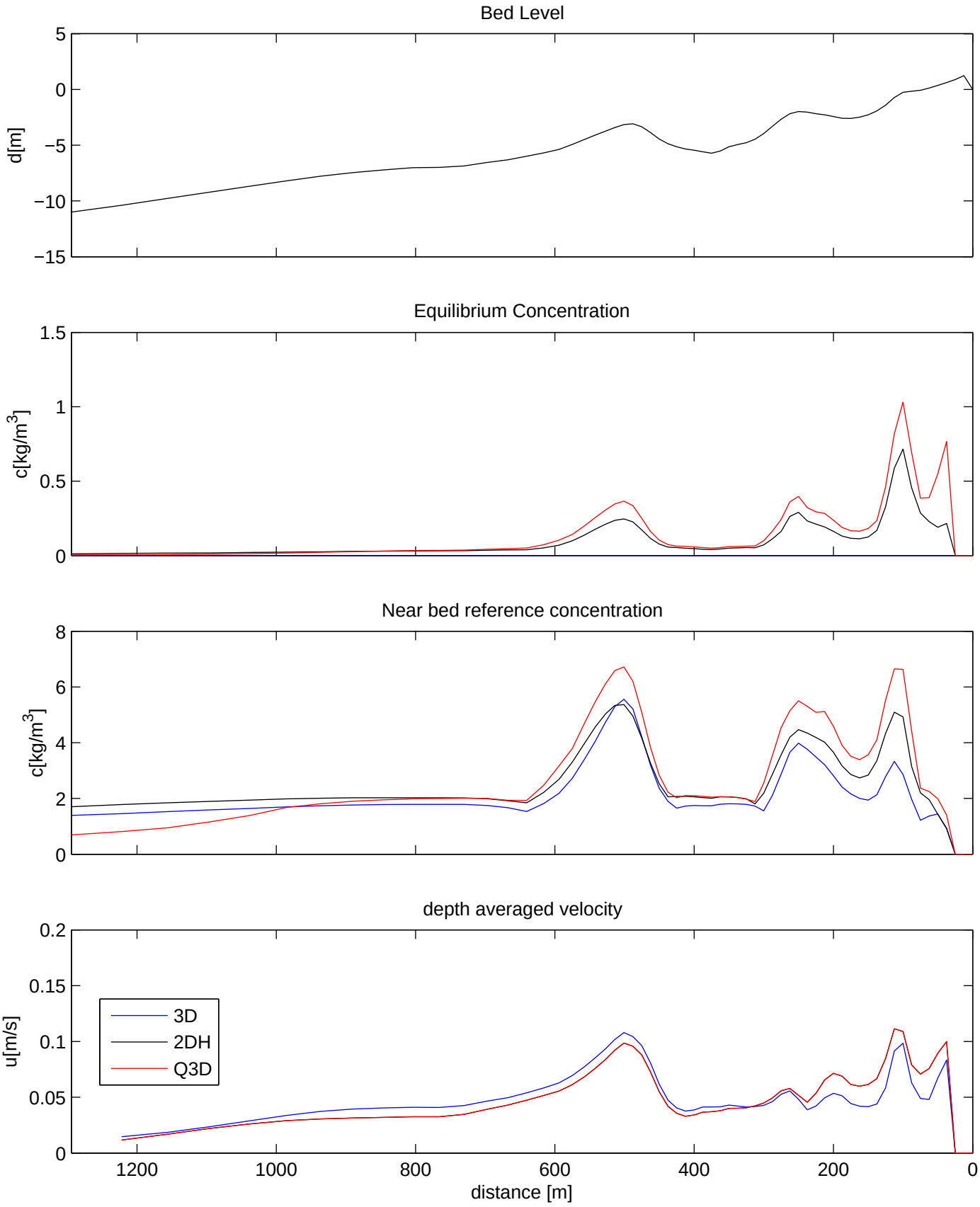

Model results Egmond field case Concentration values (high tide)	Compare	Egmond
	Delft3D	
Deltares	t=18	F3.4.13

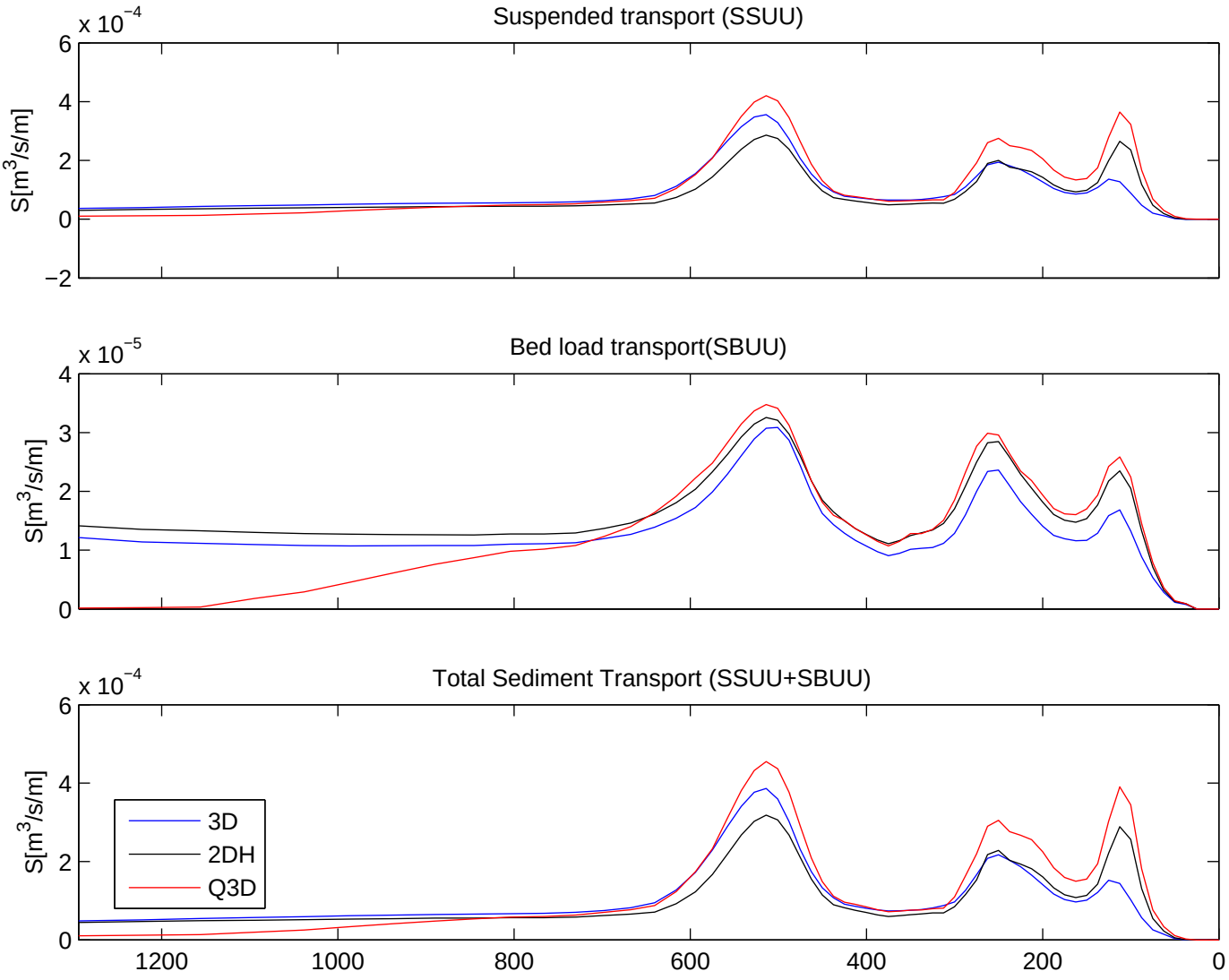

Model results Egmond field case Bed−load and suspended load transport rates (high tide) Longshore sediment transport	Compare	Egmond
	Delft3D	
Deltares	t=18	F3.4.14

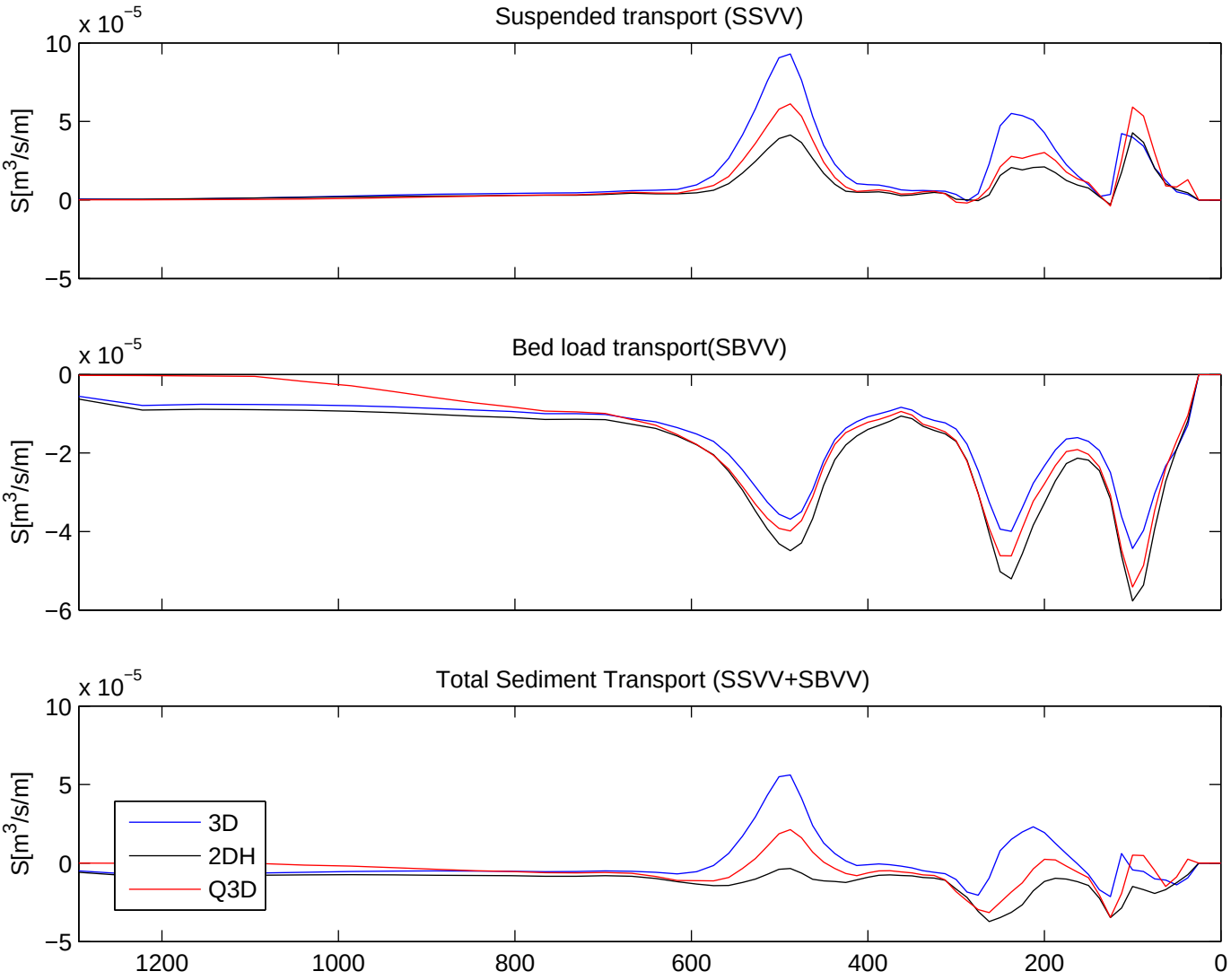

Model results Egmond field case Bed−load and suspended load transport rates (high tide) Cross−shore Sediment transport	Compare	Egmond
	Delft3D	
Deltares	t=18	F3.4.15

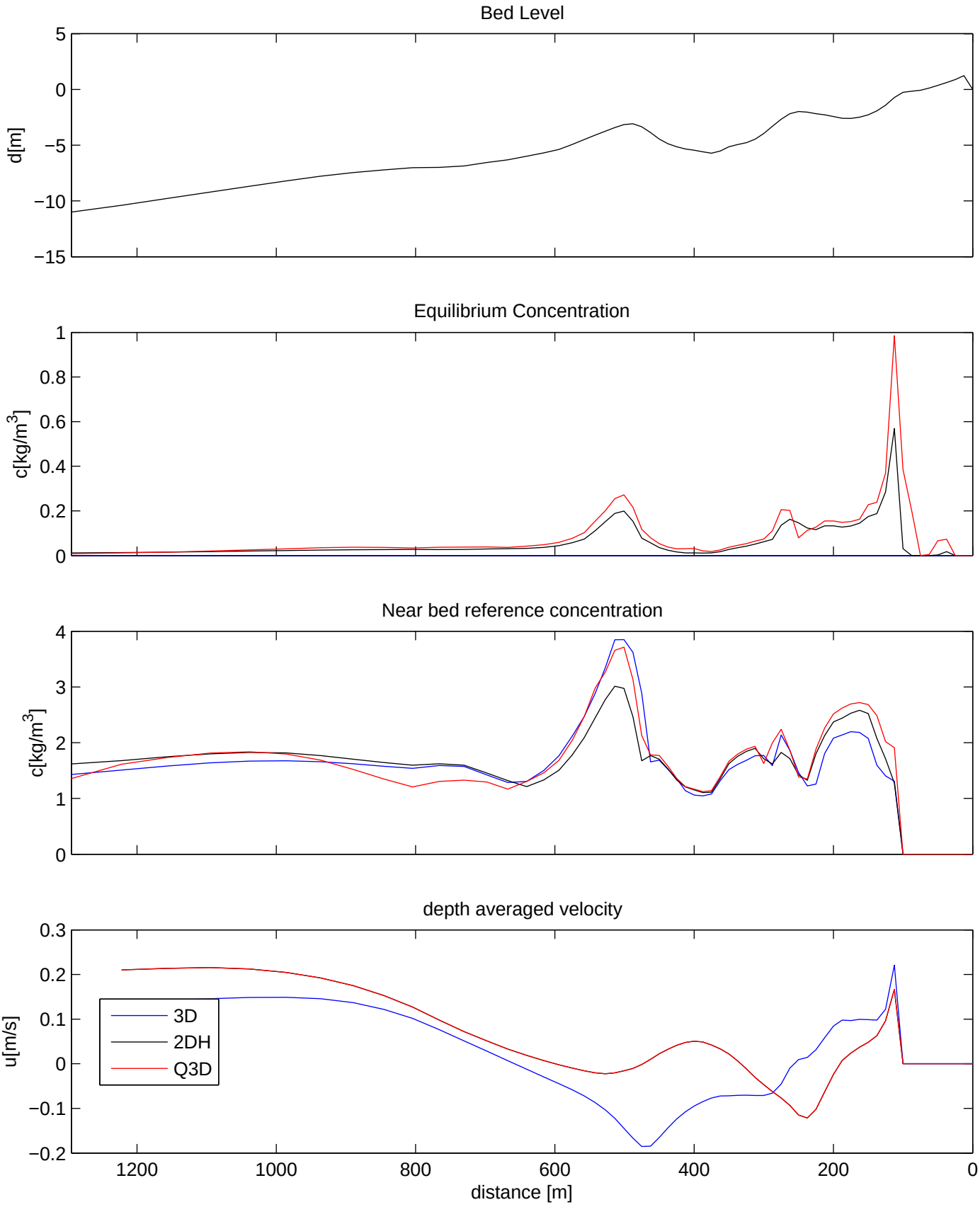

Model results Egmond field case Concentration values (low tide)	Compare	Egmond
	Delft3D	
Deltares	t=36	F3.4.16

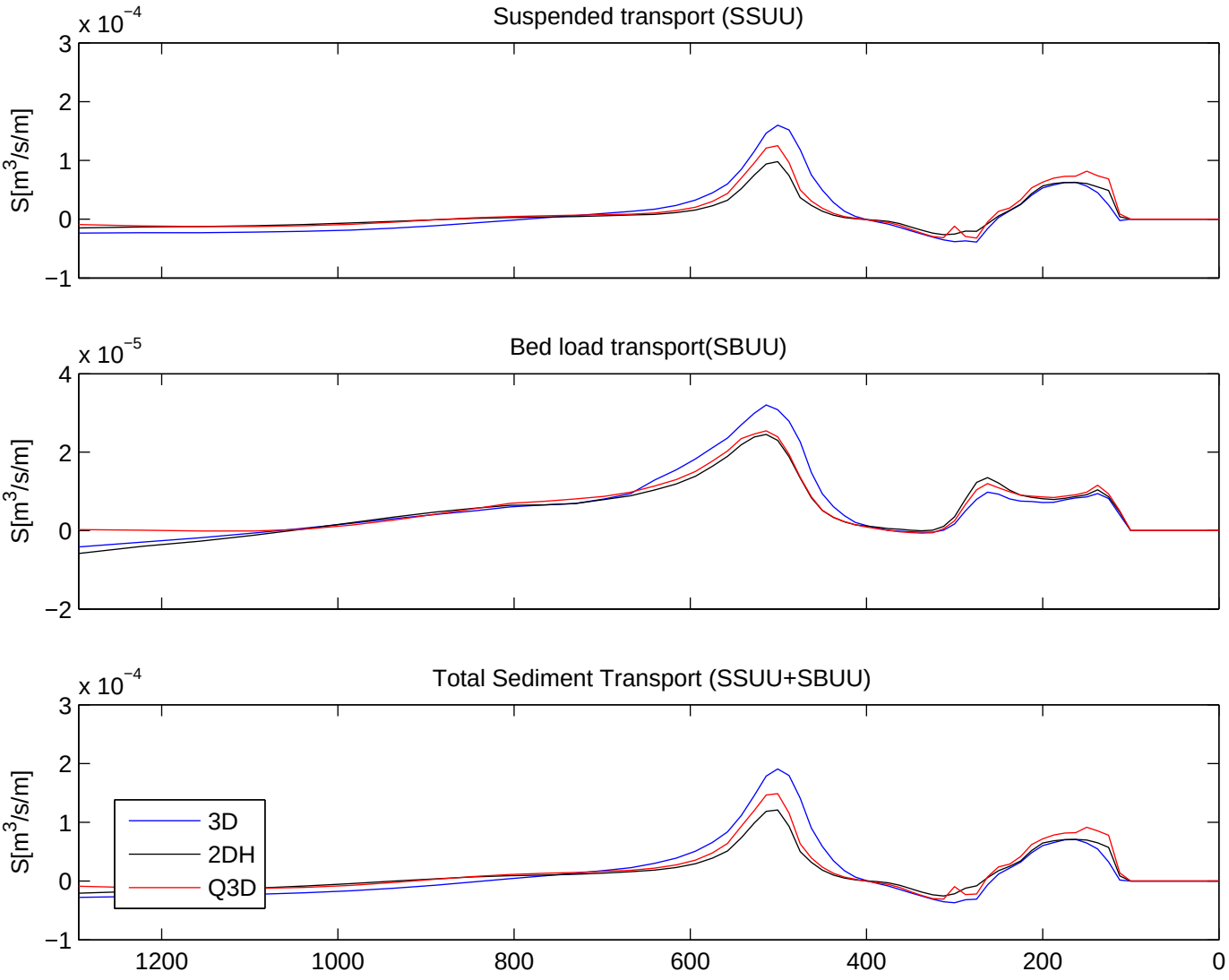

Model results Egmond field case Bed−load and suspended load transport rates (low tide) Longshore sediment transport	Compare	Egmond
	Delft3D	
Deltares	t=36	F3.4.17

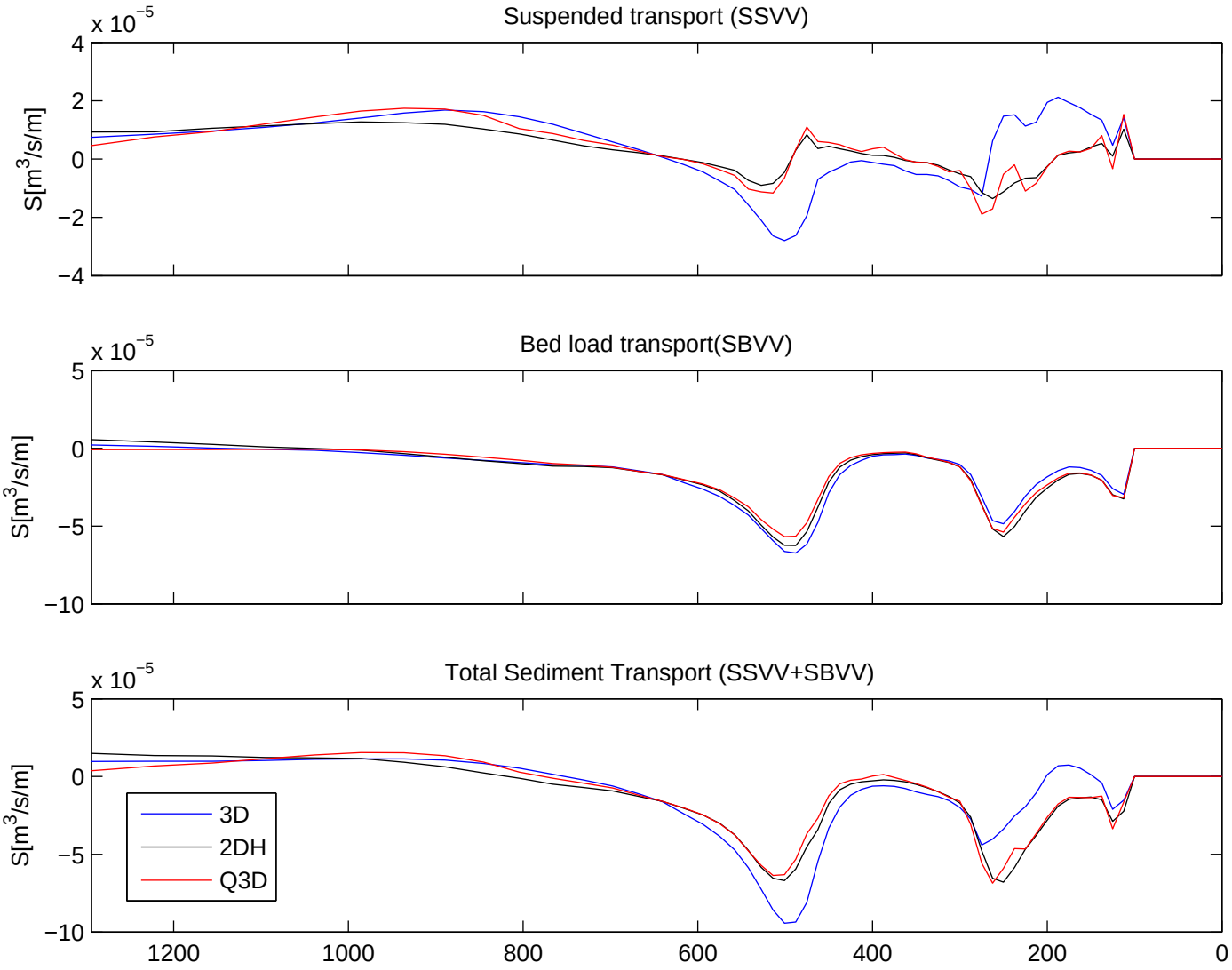

Model results Egmond field case Bed−load and suspended load transport rates (low tide) Cross−shore Sediment transport	Compare	Egmond
	Delft3D	
Deltares	t=36	F3.4.18

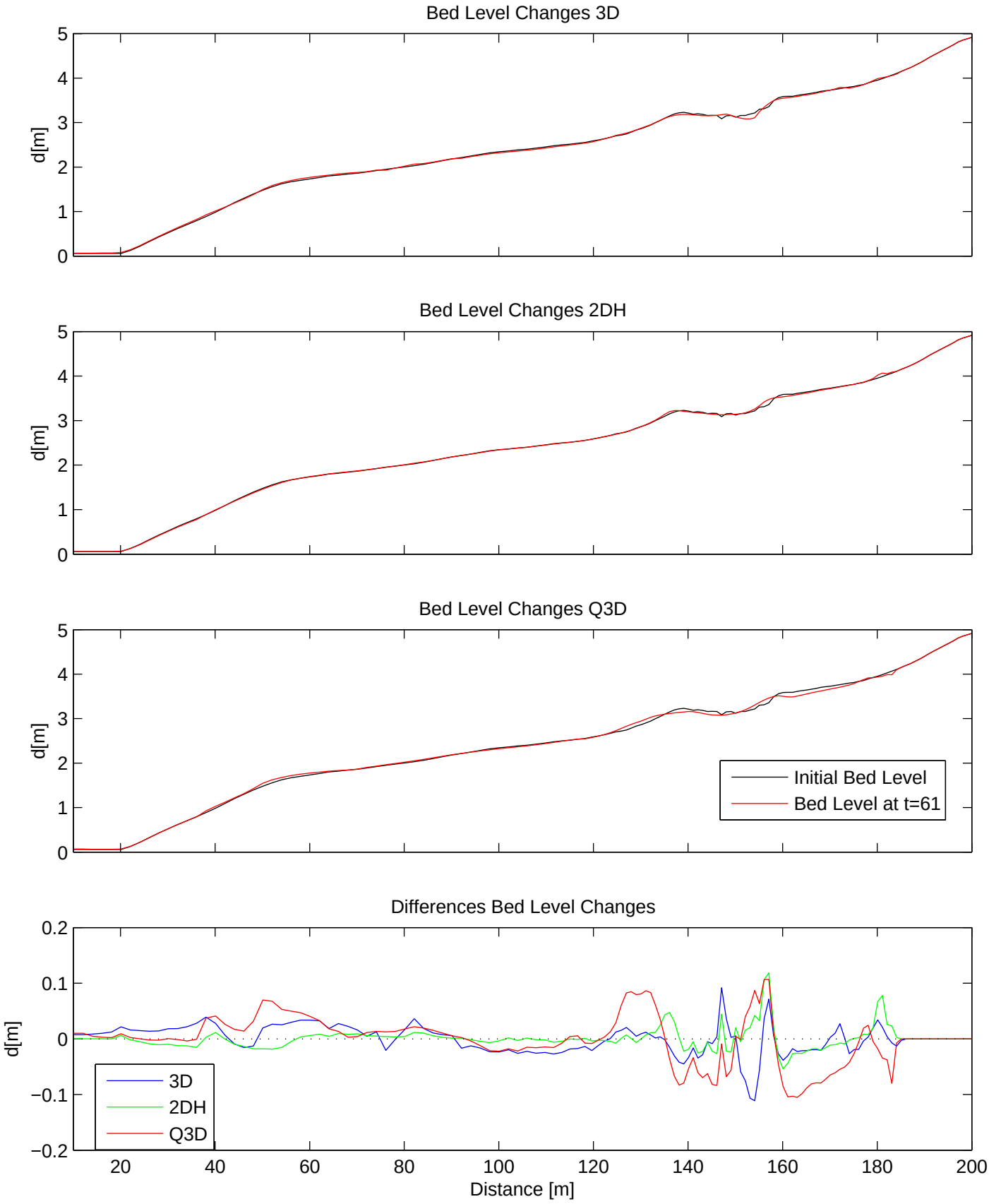

Model results LIP11D−1b experiment Bed Level changes for 3D, 2DH and Q3D model results Differences in bed level changes	Compare	LIP
	Delft3D	
Deltares		F3.5.1

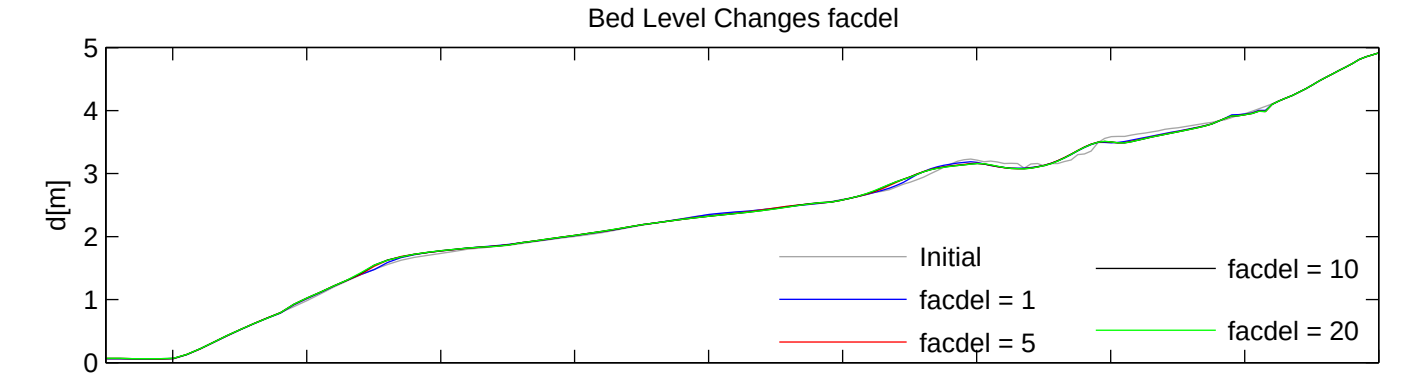

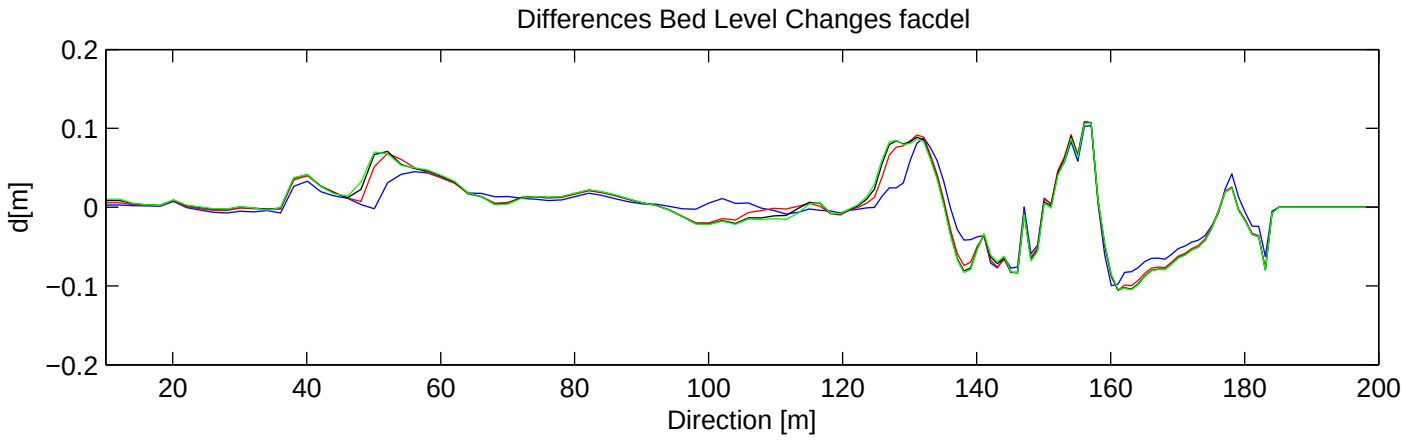

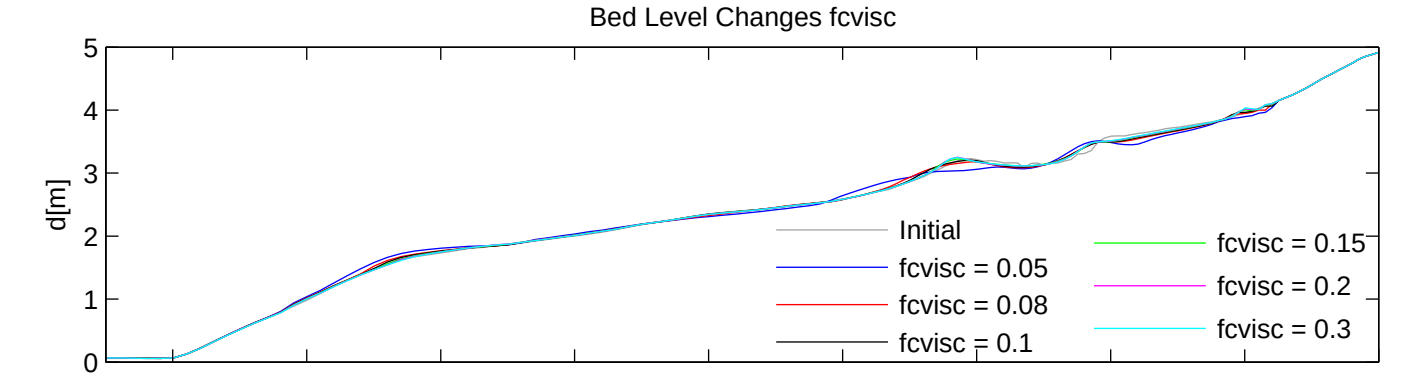

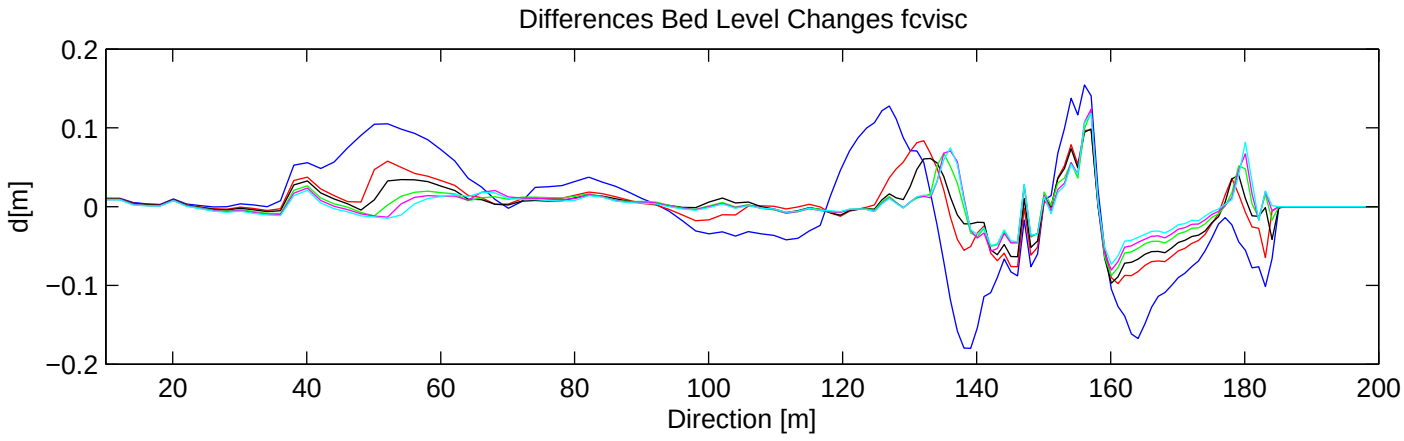

Model results LIP11D−1b experiment Parameter sensitivity multiplication factor bottom boundary layer thickness[facdel] Parameter sensitivity multiplication factor wave−induced viscosity[fcvisc]	Q3D	LIP
	Delft3D	
Deltares	facdel/fcvisc	F3.5.2

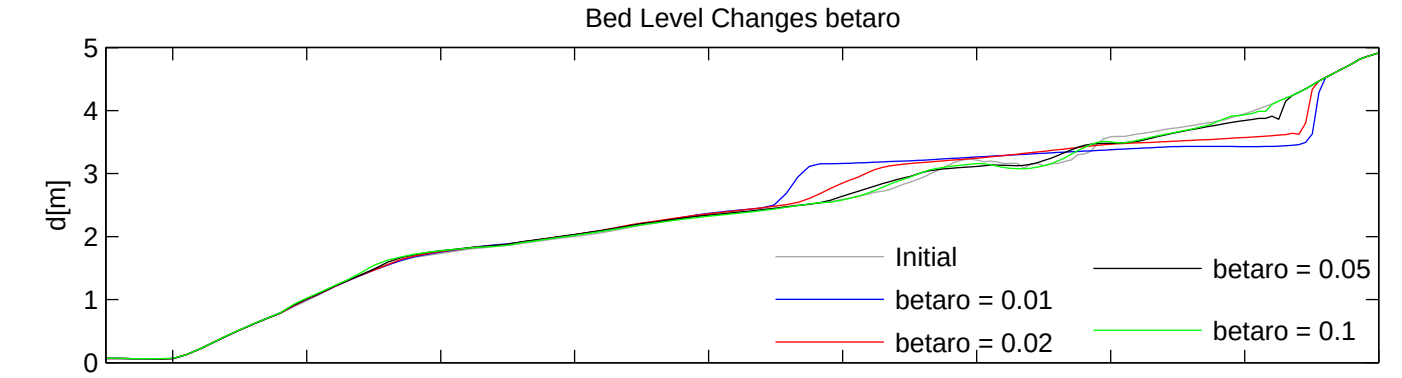

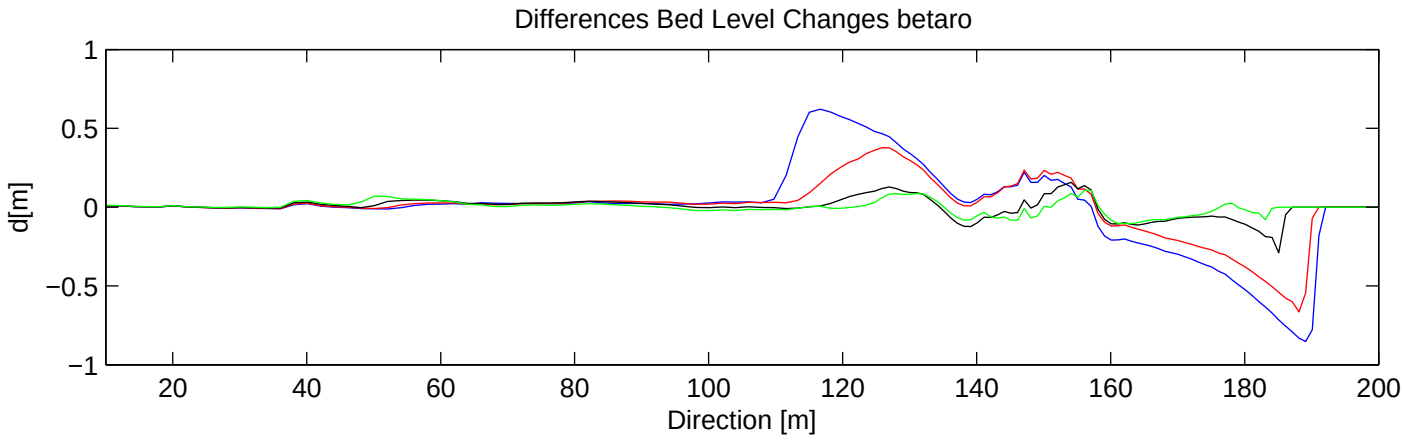

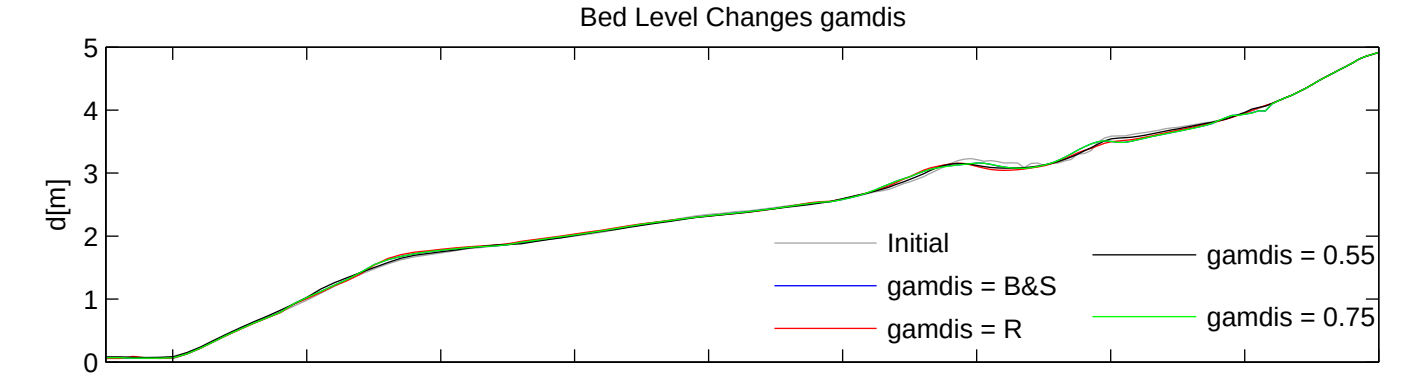

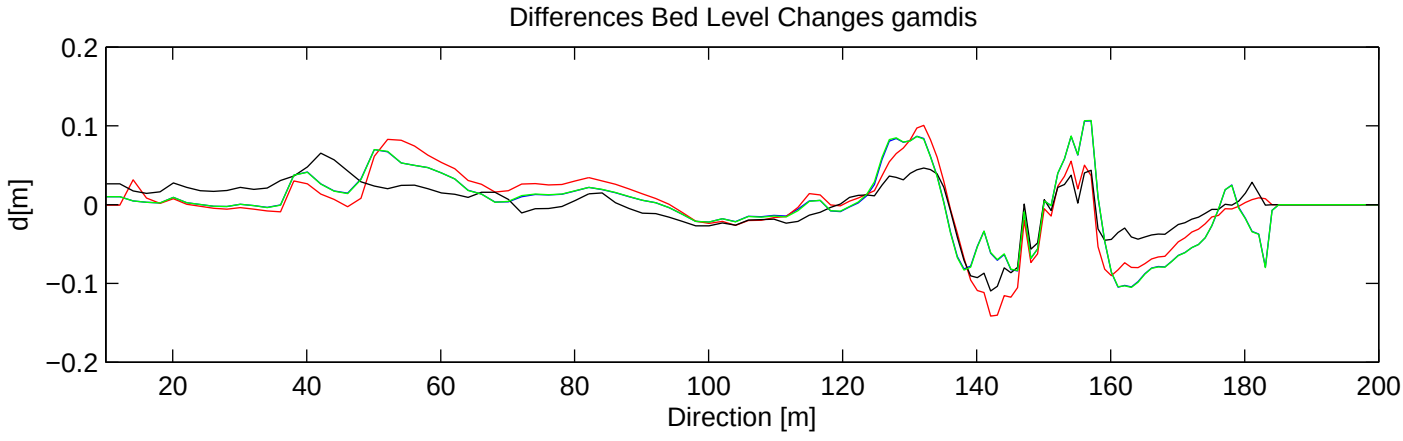

Model results LIP11D−1b experiment Parameter sensitivity angle of wave front [betaro] Parameter sensitivity breaker parameter [gamdis]	Q3D	LIP
	Delft3D	
Deltares	betaro/gamdis	F3.5.3

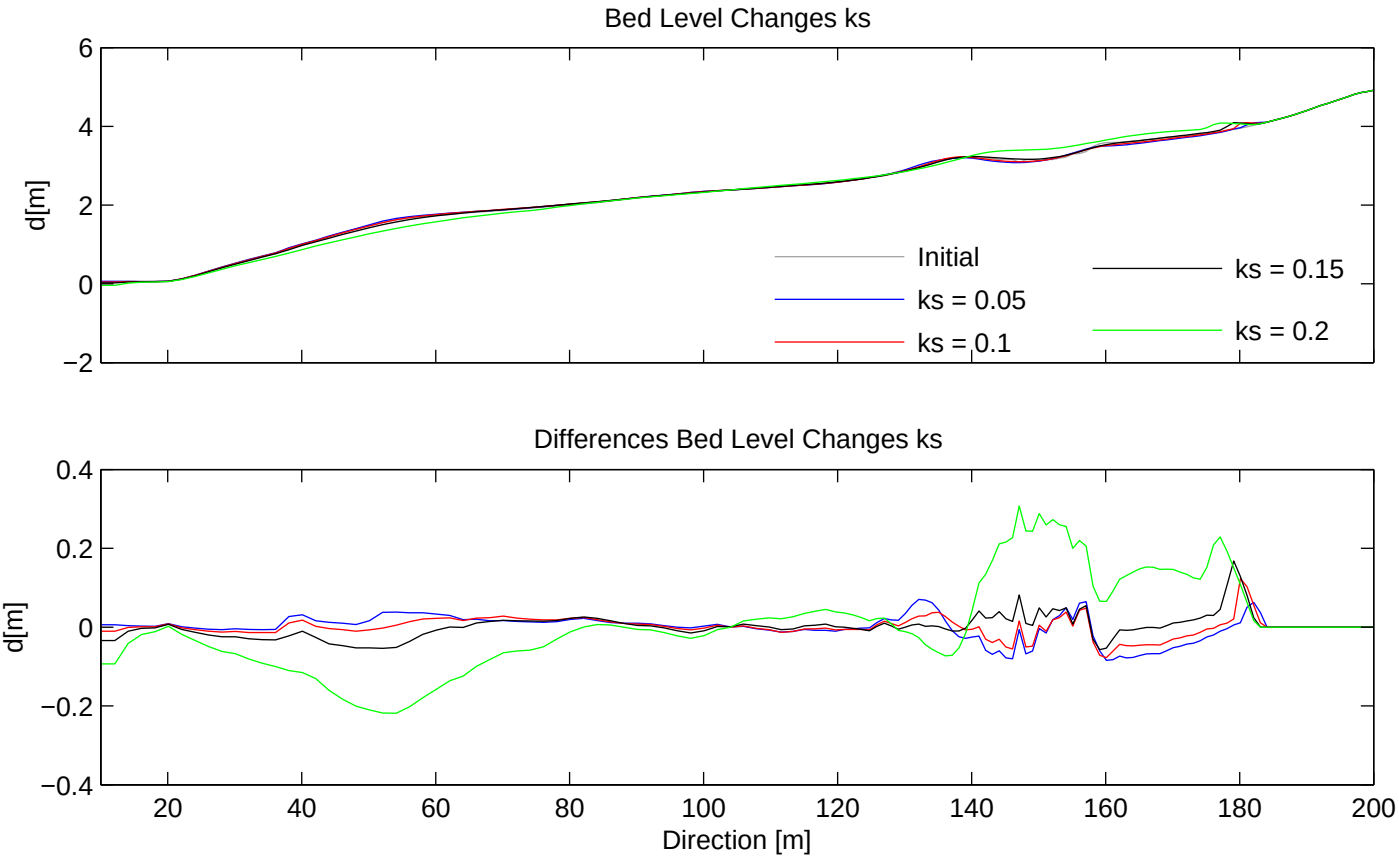

Model results LIP11D−1b experiment Parameter sensitivity roughness height [ks]	Q3D	LIP
	Delft3D	
Deltares	ks	F3.5.4

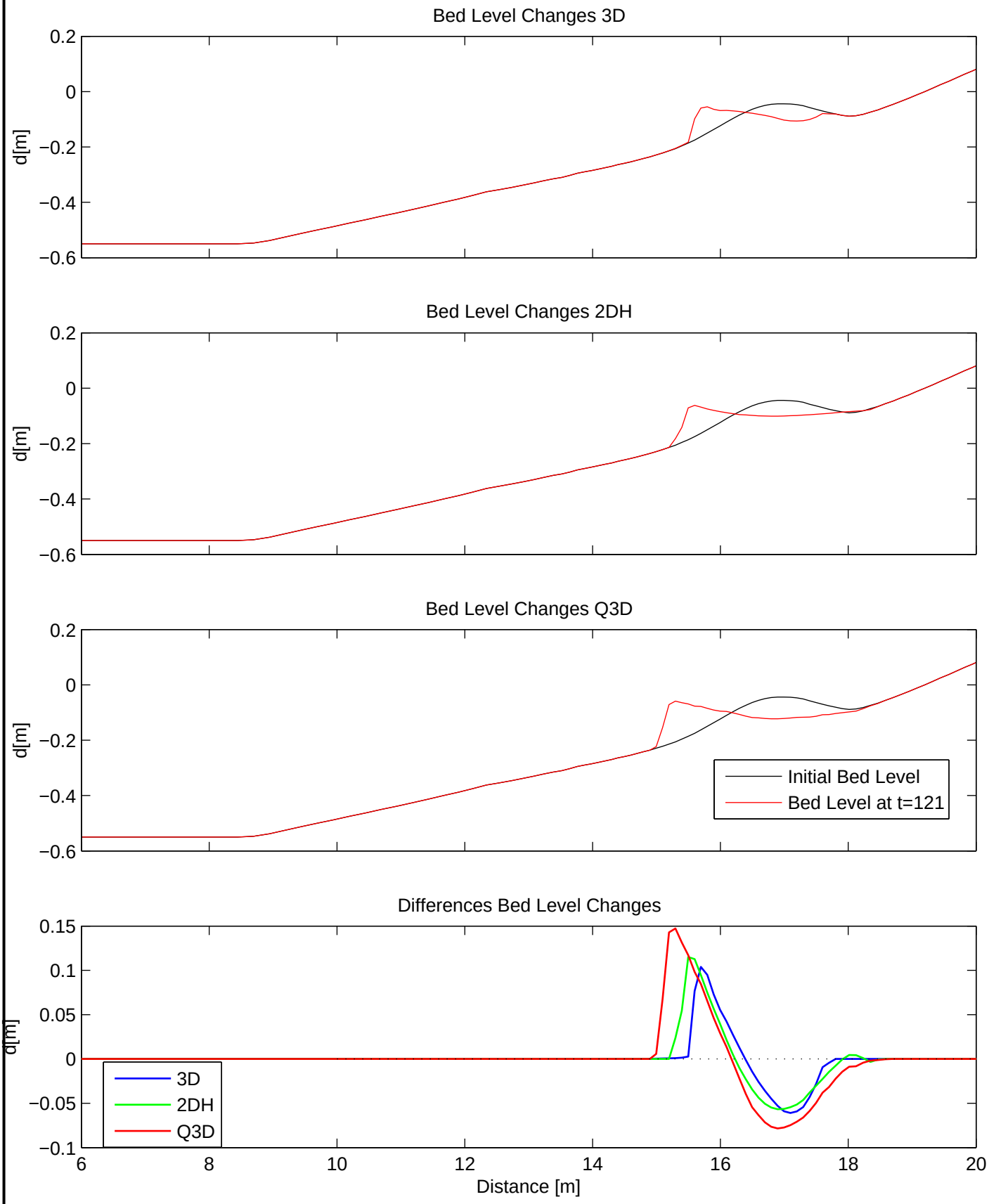

Model results Reniers−SO014 experiment Bed Level changes for 3D, 2DH and Q3D model results Differences in bed level changes	Compare	Reniers
	Delft3D	
Deltares		F3.5.5

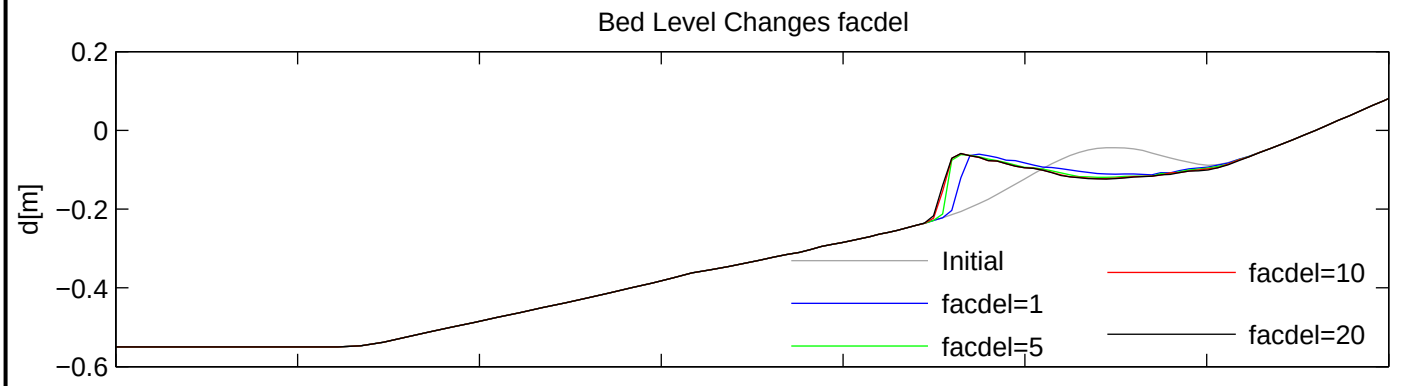

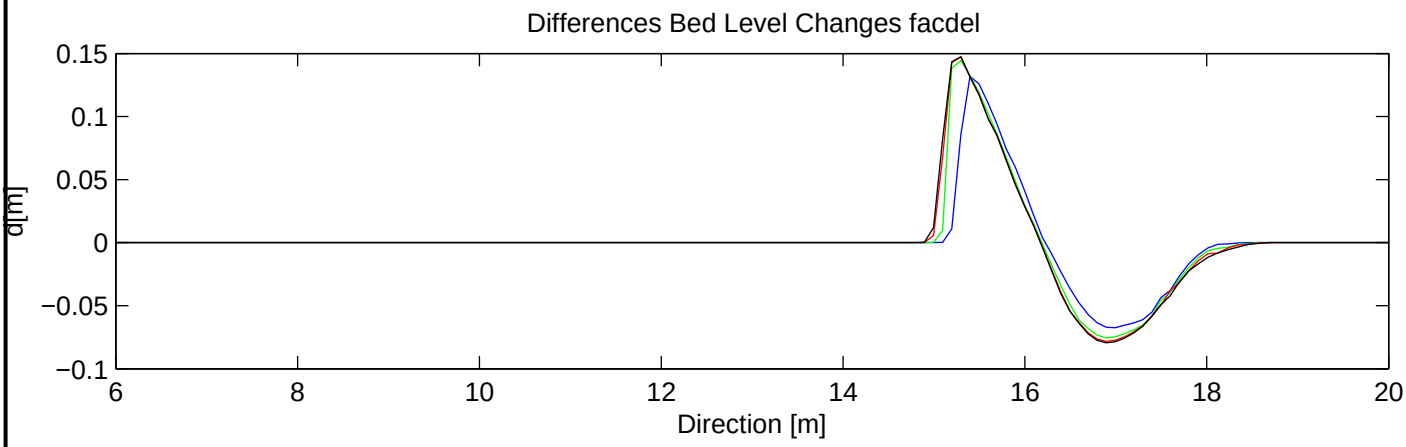

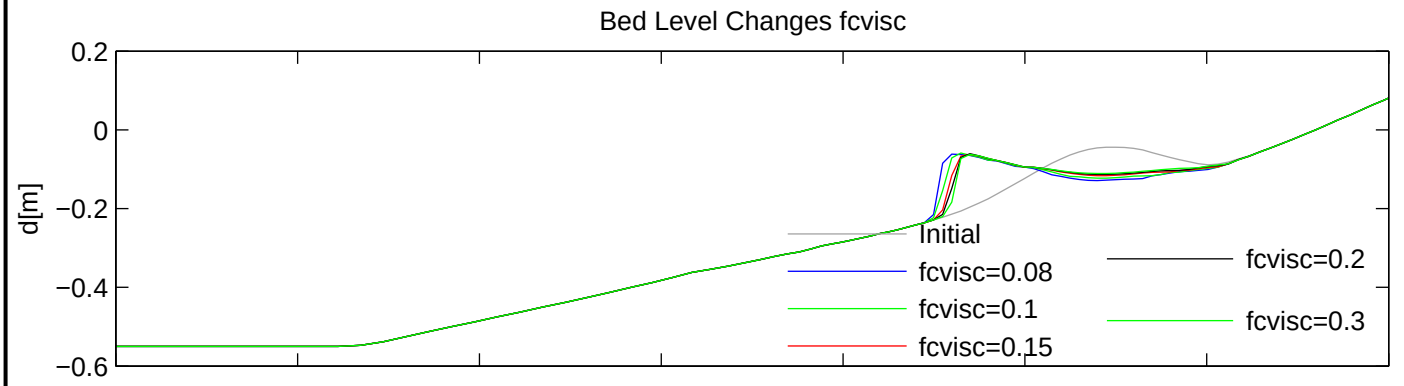

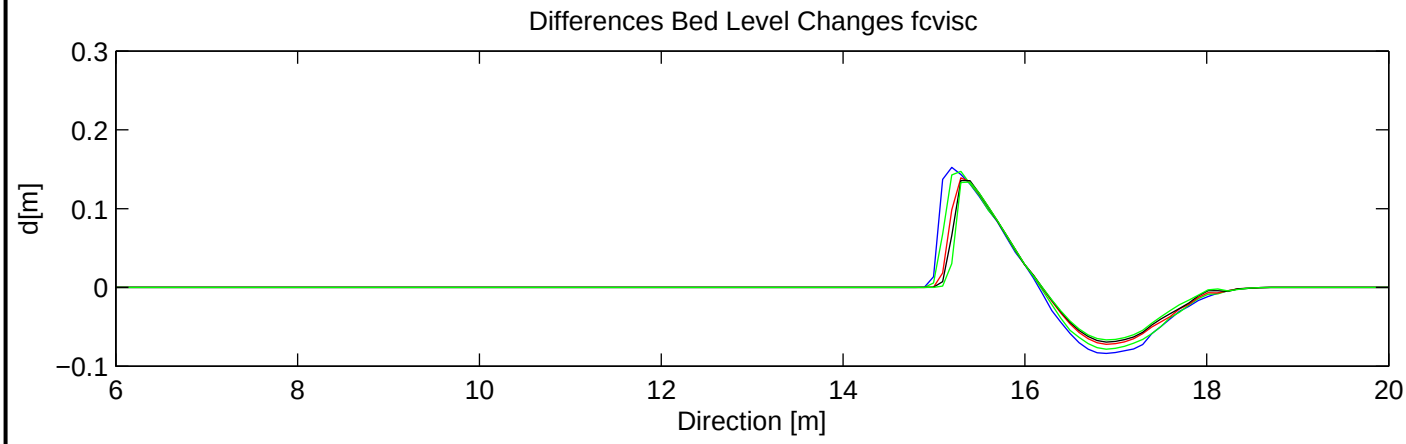

Model results Reniers−SO014 experiment Parameter sensitivity multiplication factor wave−induced viscosity[fcvisc] Differences in bed level changes	Q3D	Reniers
	Delft3D	
Deltares	facdel/fcvisc	F3.5.6

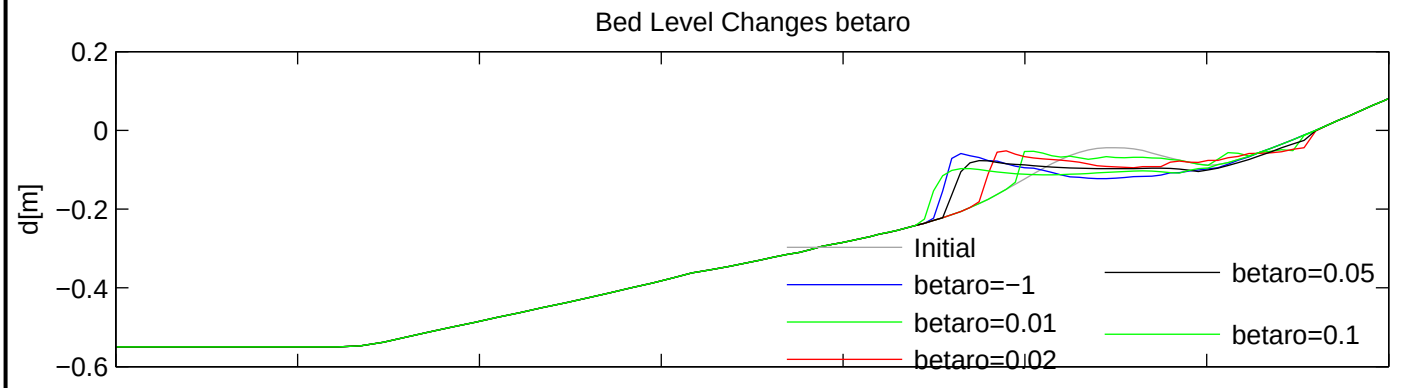

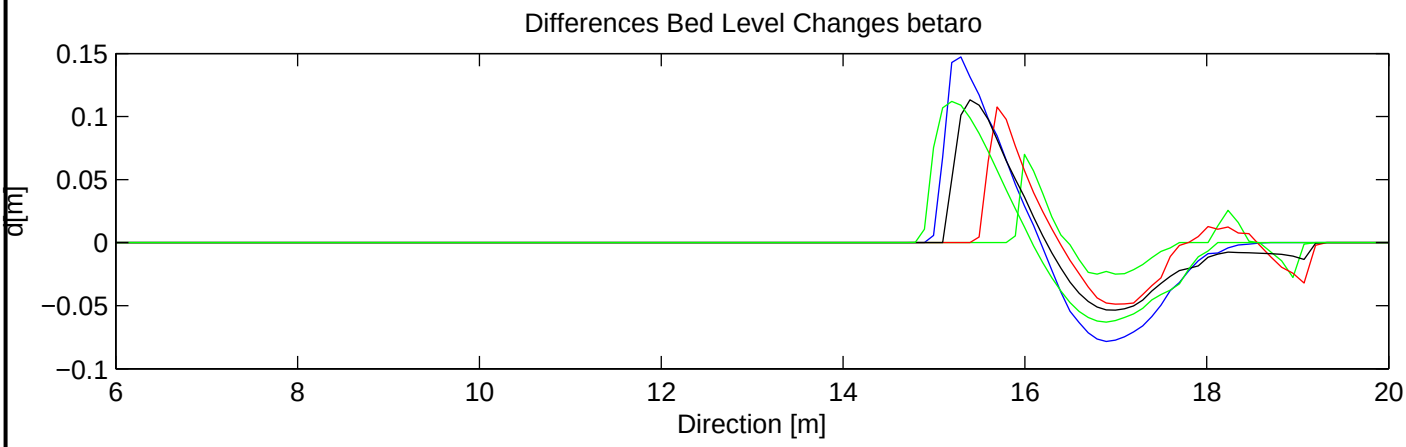

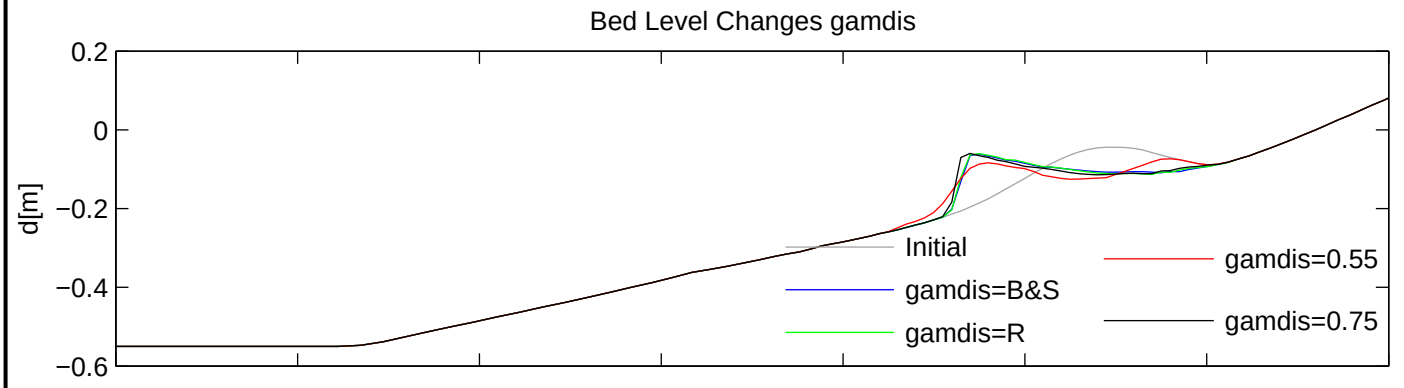

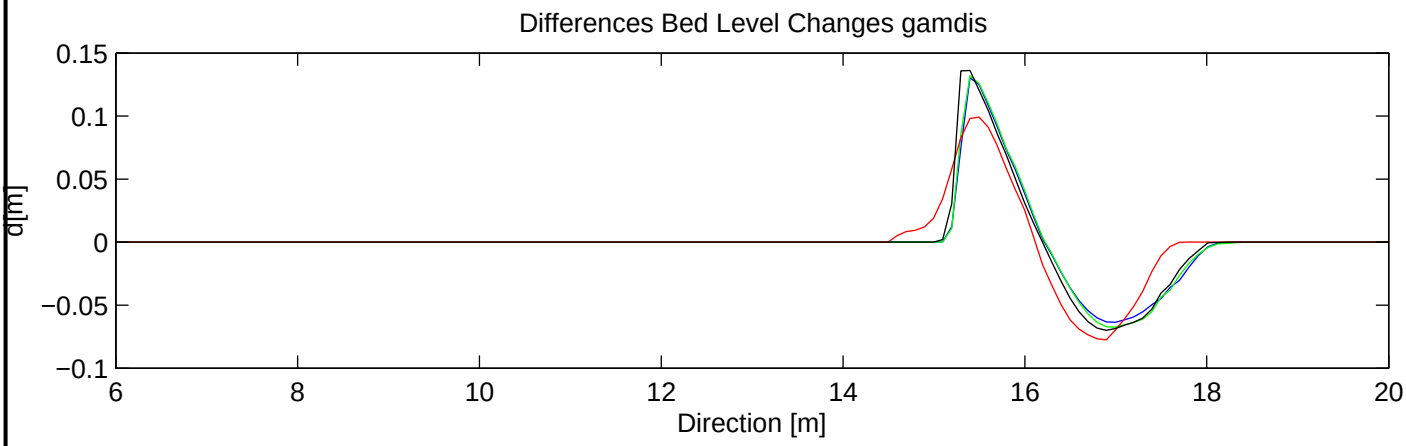

Model results Reniers−SO014 experiment Parameter sensitivity breaker parameter [gamdis] Differences in bed level changes	Q3D	Reniers
	Delft3D	
Deltares	betaro/gamdis	F3.5.7

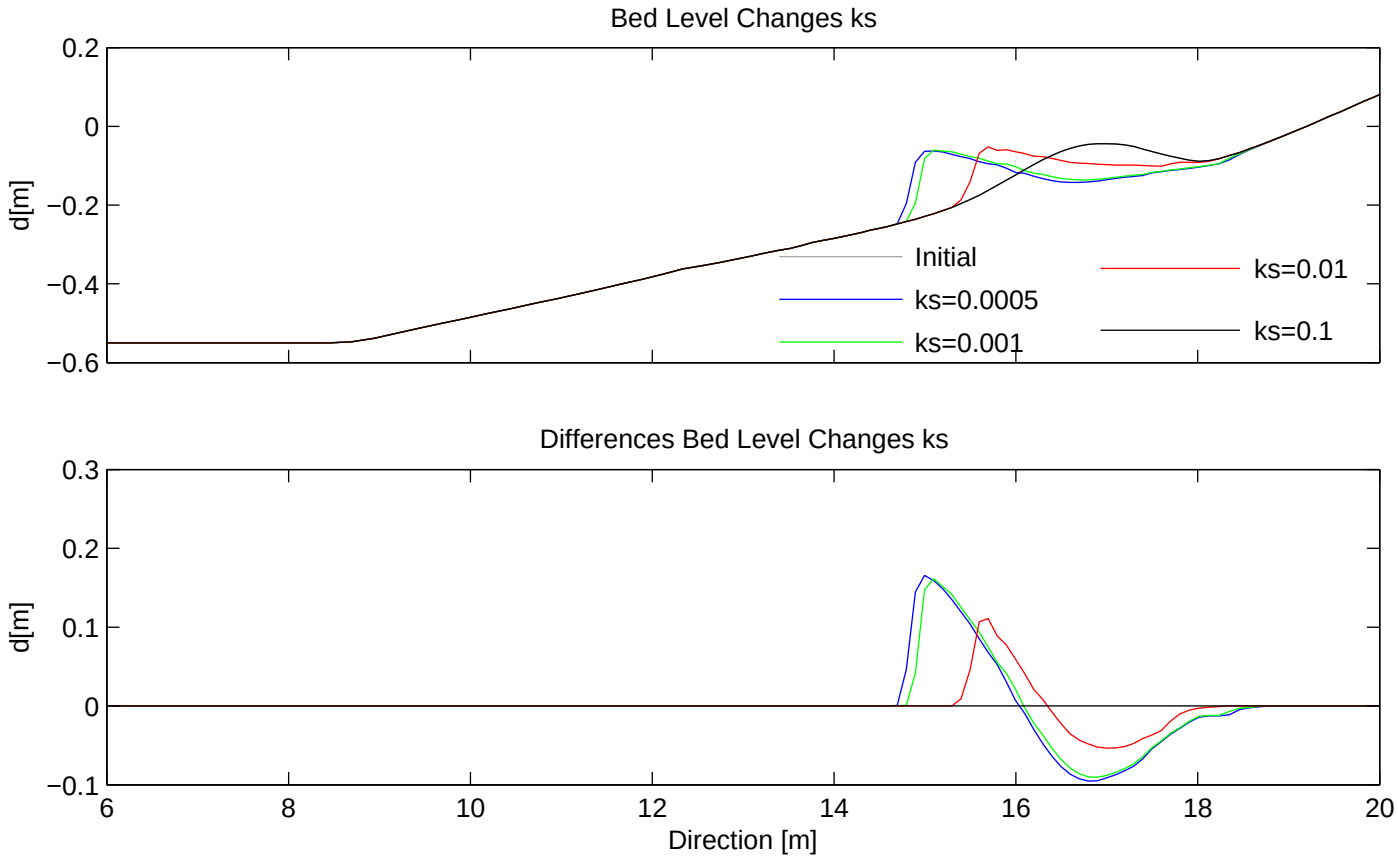

Model results Reniers−SO014 experiment Parameter sensitivity roughness height [ks] Differences in bed level changes	Q3D	Reniers
	Delft3D	
Deltares	ks	F3.5.8

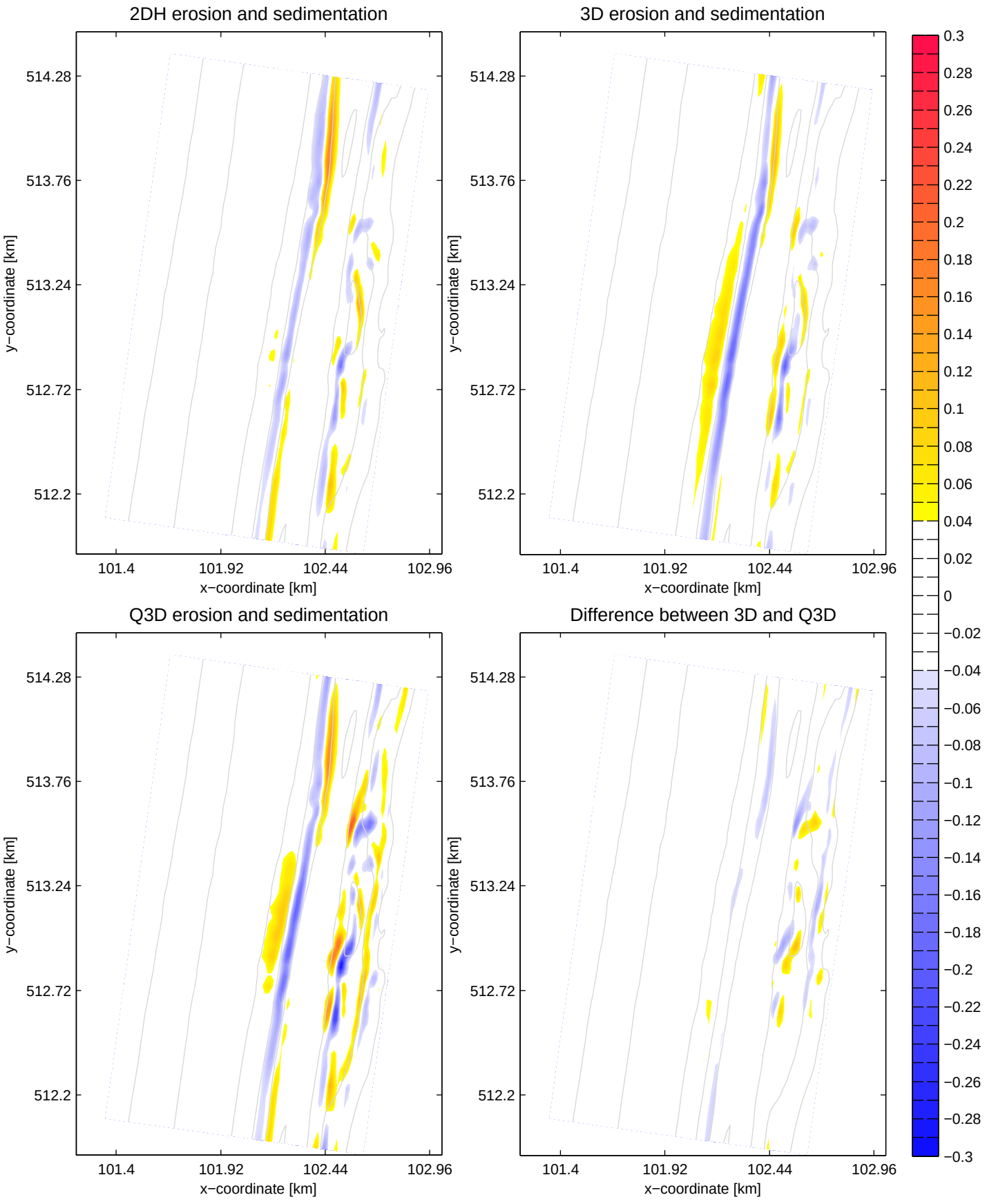

Model results Egmond field case Erosion and sedimentation 2DH, 3D and Q3D Differences between 3D and Q3D	Compare	Egmond
Deltares	Delft3D	F3.5.9

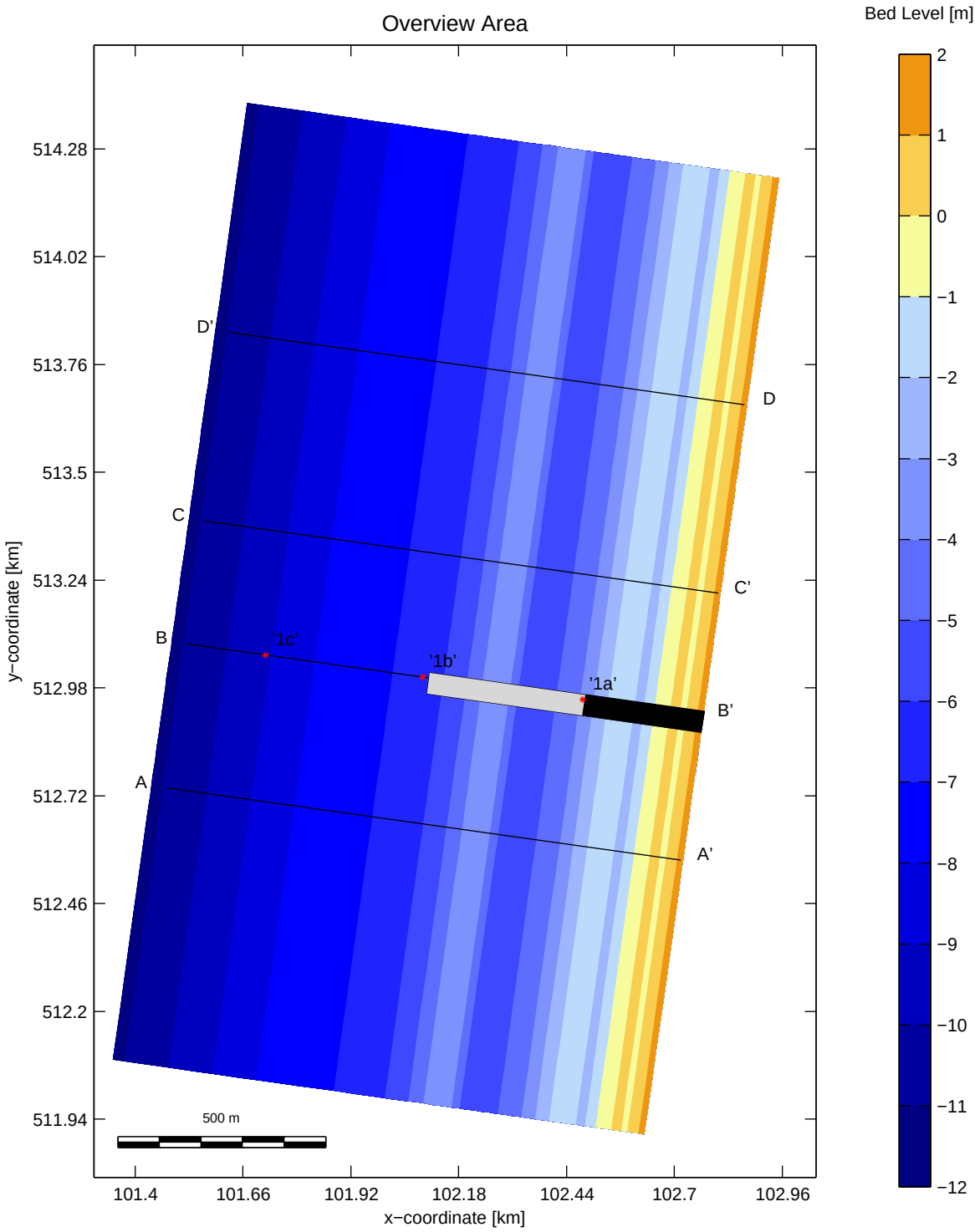

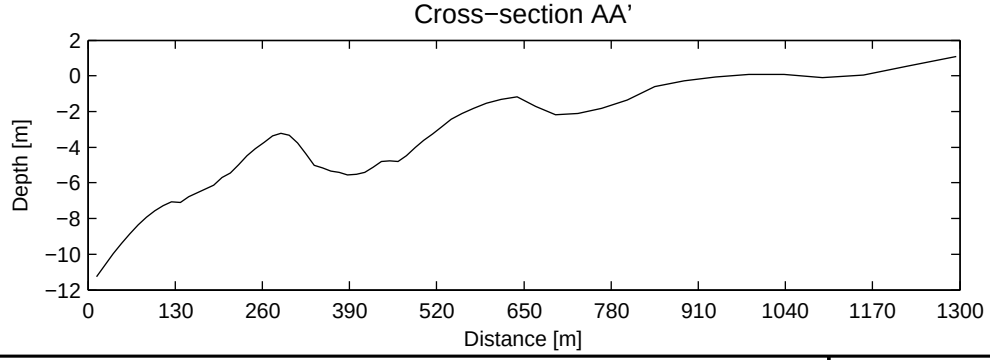

Overview area uniform coast incl. short and long groyne	Overview	V04,V05,V06
	uniform coast	
Deltares	Delft3D	F4.1.1

Deltares

Model results uniform coast, no obstacles
Depth−averaged velocity 2DH and 3D
Differences depth averaged velocity between 2DH and 3D

Delft3D | uniform coast | Compare | V04 | F4.2.1

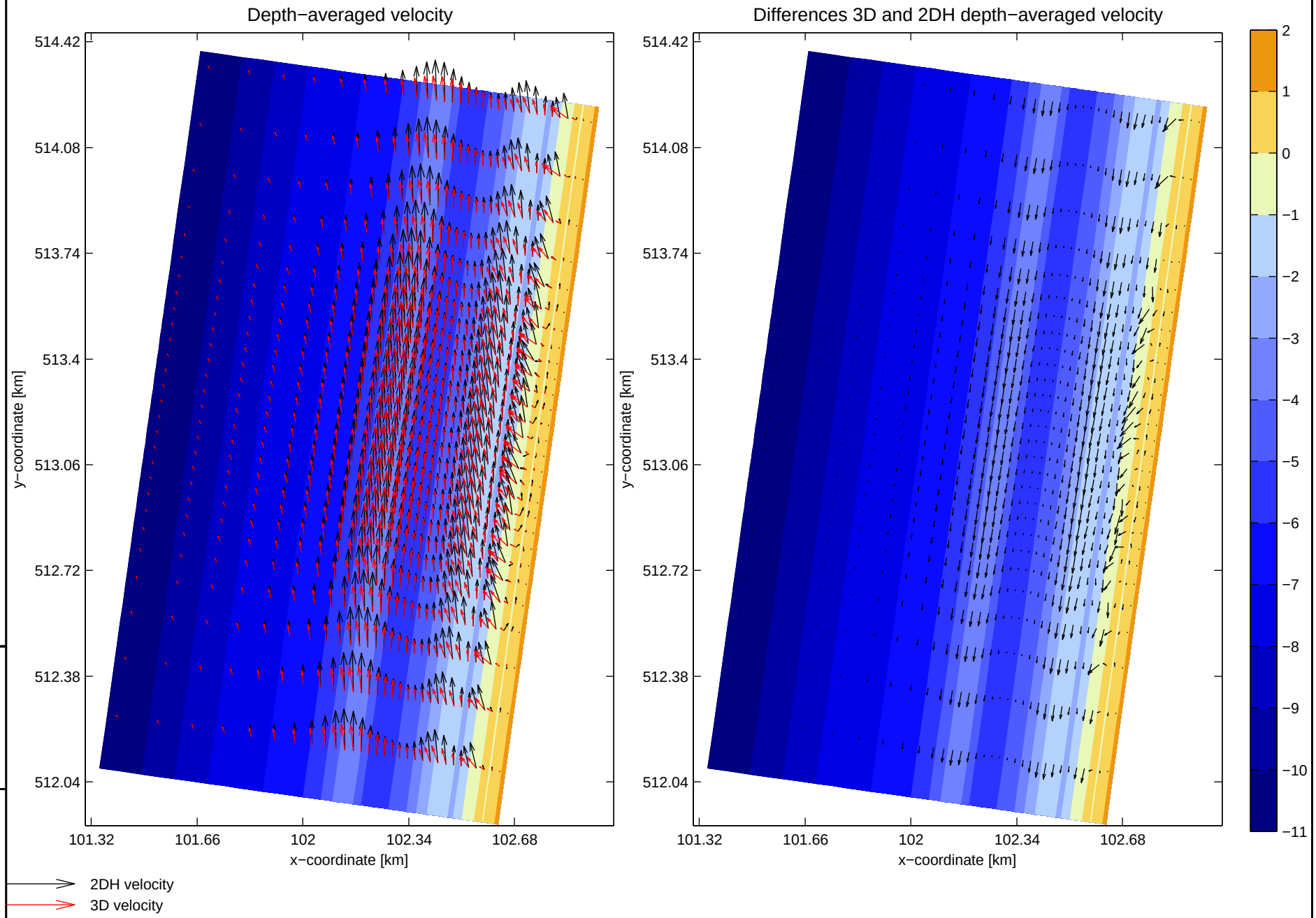

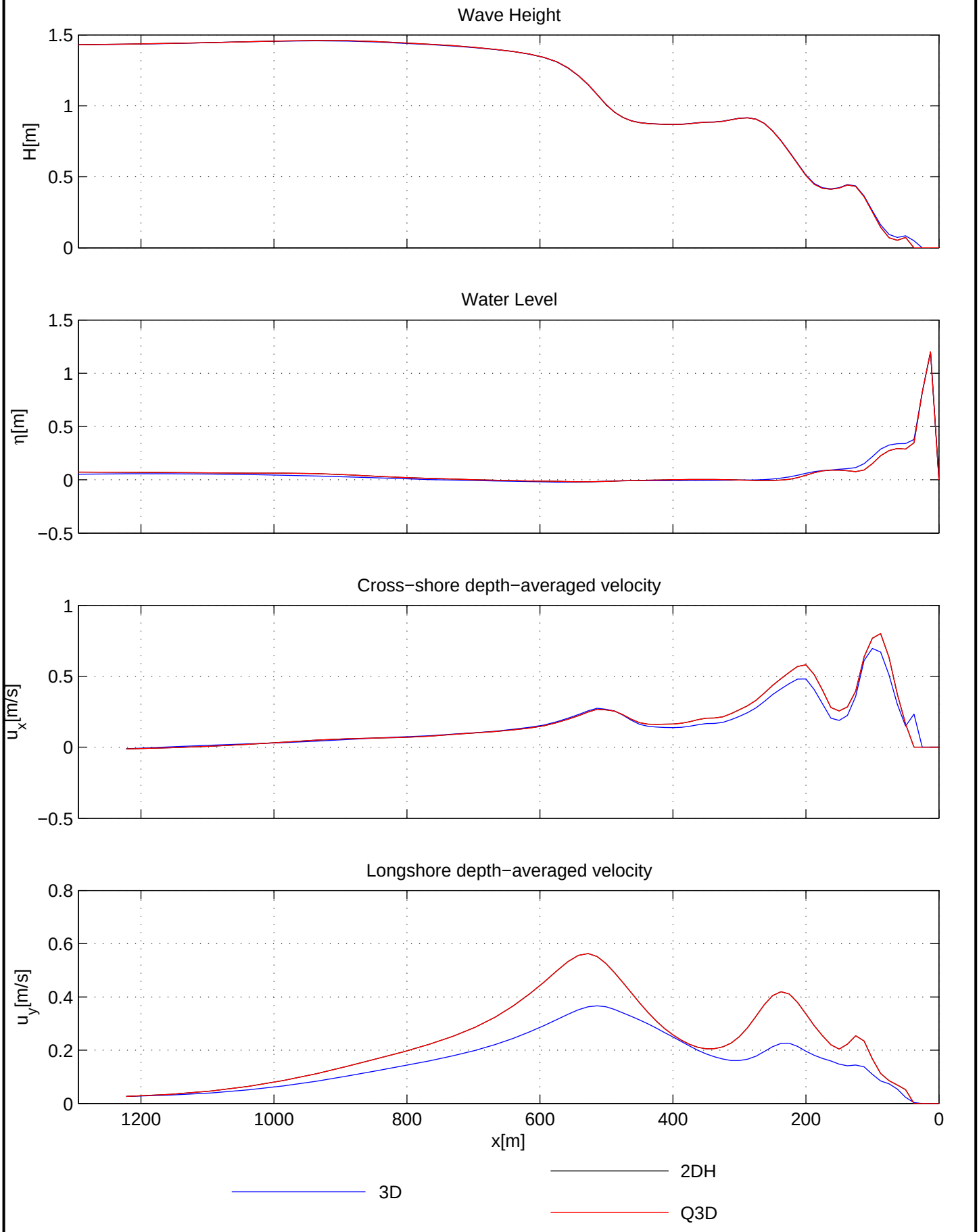

Model results uniform coast, no obstacles Wave height [m], water level [m] and longshore and cross−shore depth−averaged velocity [m/s]	Compare	V04
	Uniform coast	
Deltares	Delft3D	F4.2.2

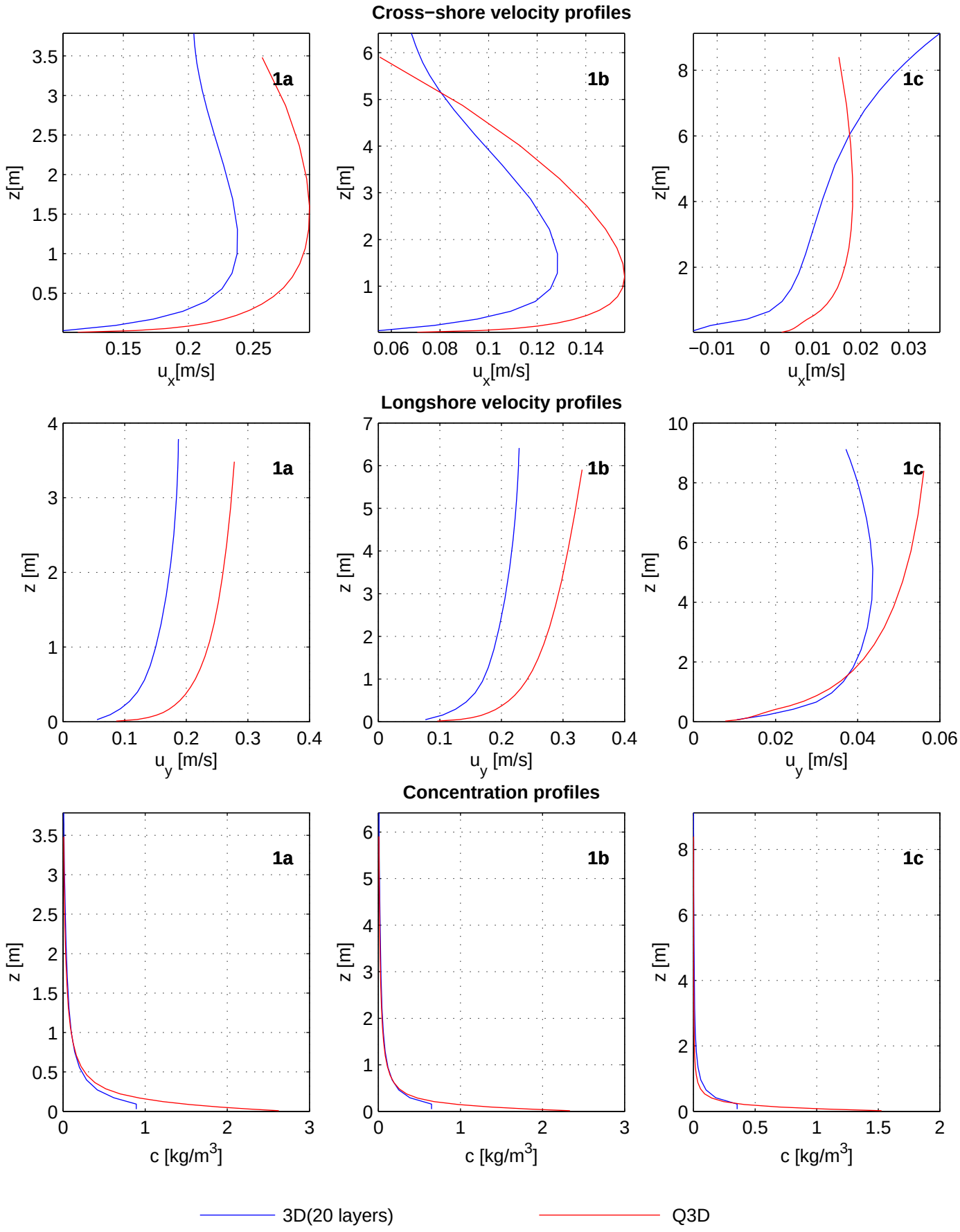

Model results uniform coast, no obstacles Cross−shore velocity, longshore velocity and concentration profiles Cross−section BB, profiles 1,2 and 3	Compare	V04
	Uniform coast	
Deltares	Delft3D	F4.2.3

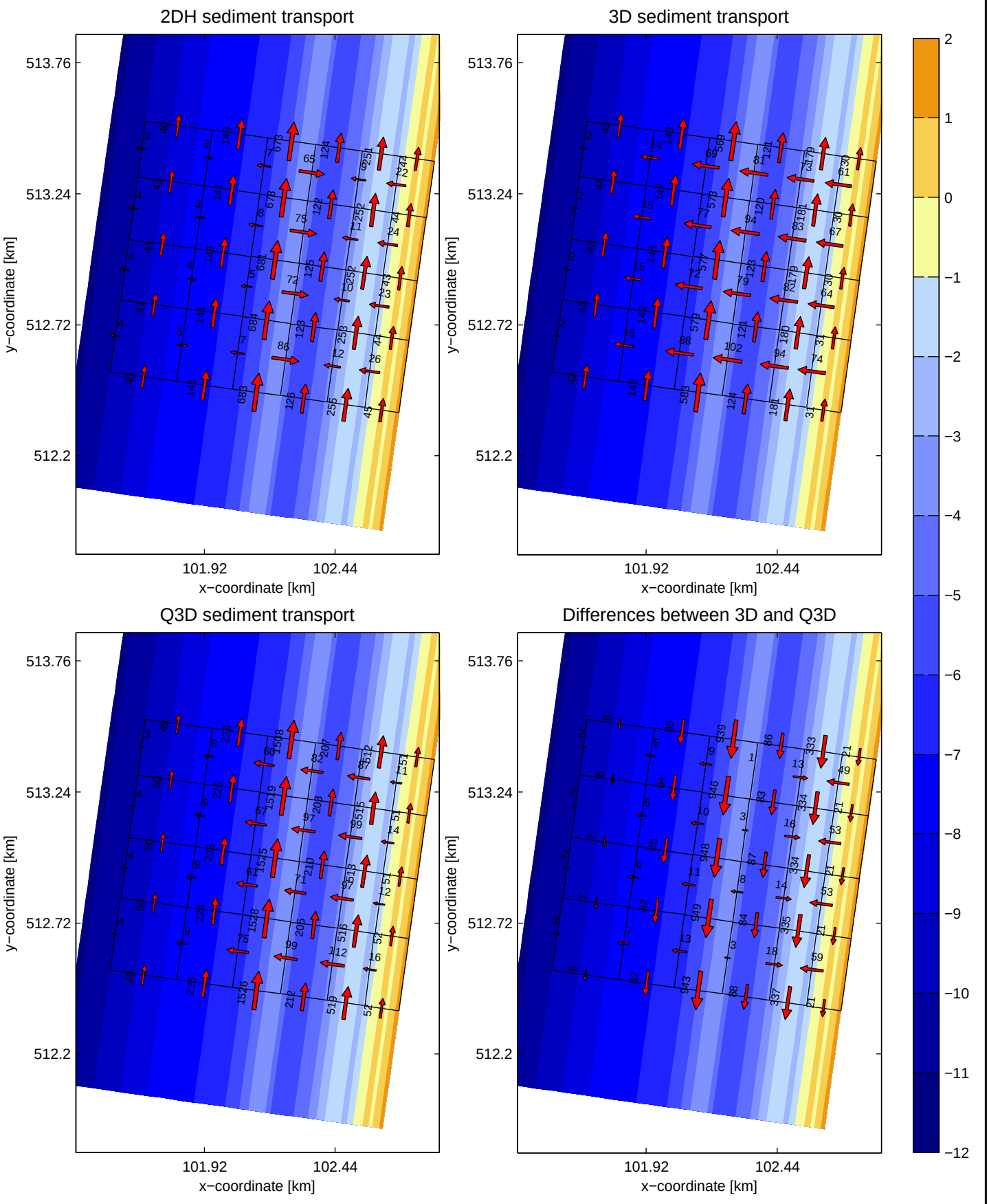

Model results uniform coast, no obstacles Total sediment transport through transects [10^3 m^3/year] 2DH, 3D, Q3D and differences between 3D and Q3D	Compare	V04
	uniform coast	
Deltares	Delft3D	F4.2.4

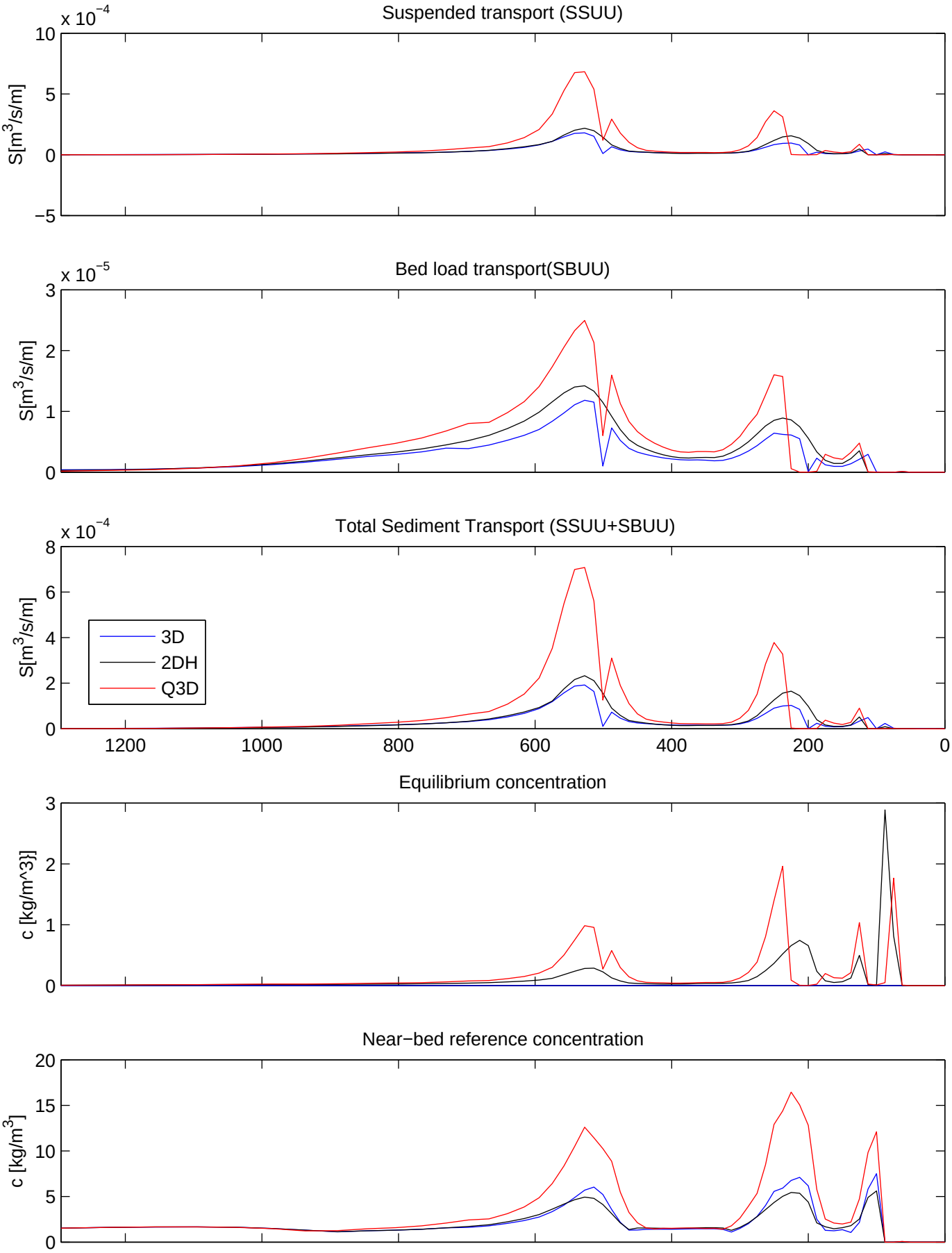

Model results uniform coast, no obstacles Bed−load and suspended load longshore sediment transport rates Cross−section BB	Compare	V04
	Uniform coast	
Deltares	Delft3D	F4.2.5

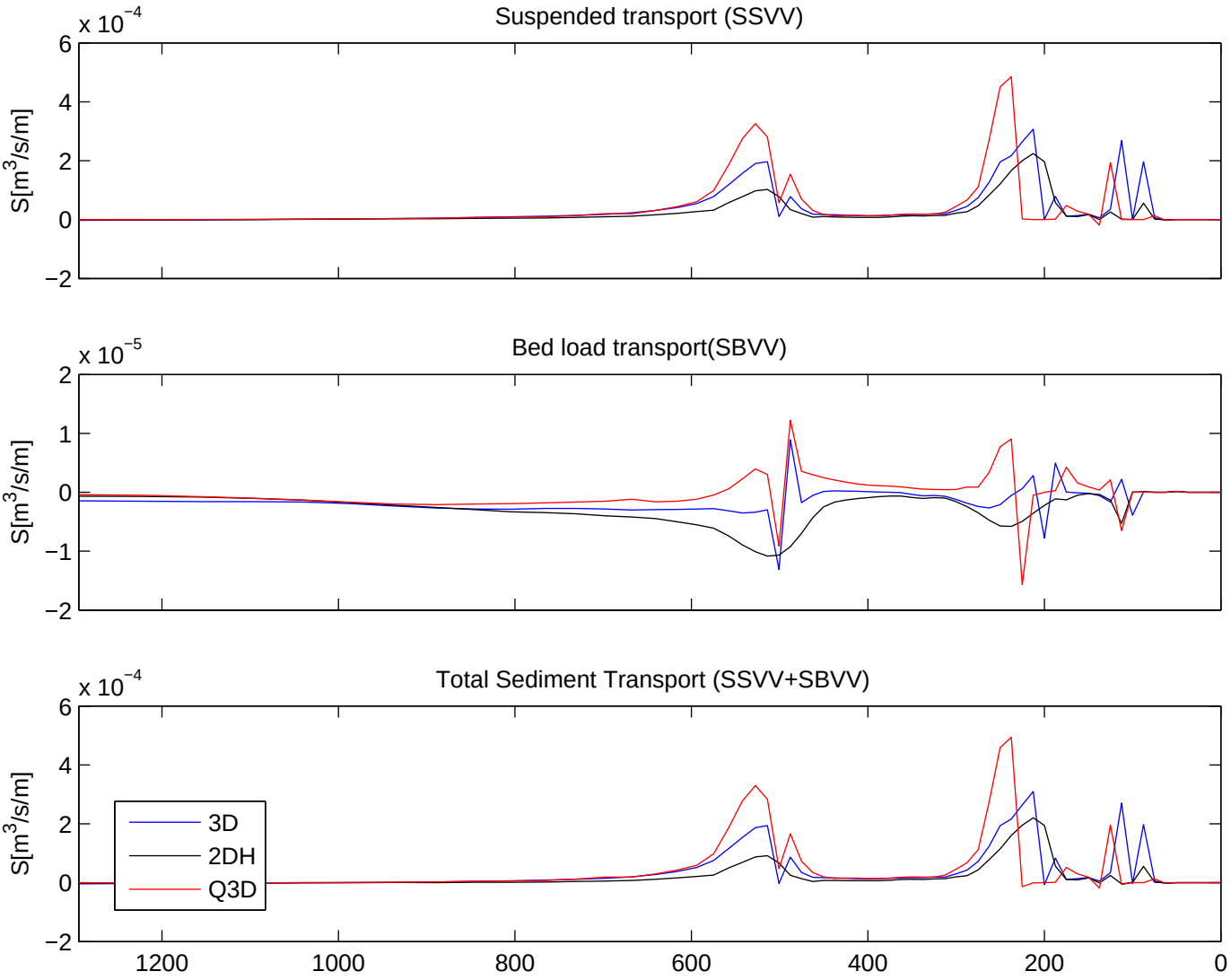

Model results uniform coast, no obstacles Bed−load and suspended load cross−shore sediment transport rates Cross−section BB	Compare	V04
	Uniform coast	
Deltares	Delft3D	F4.2.6

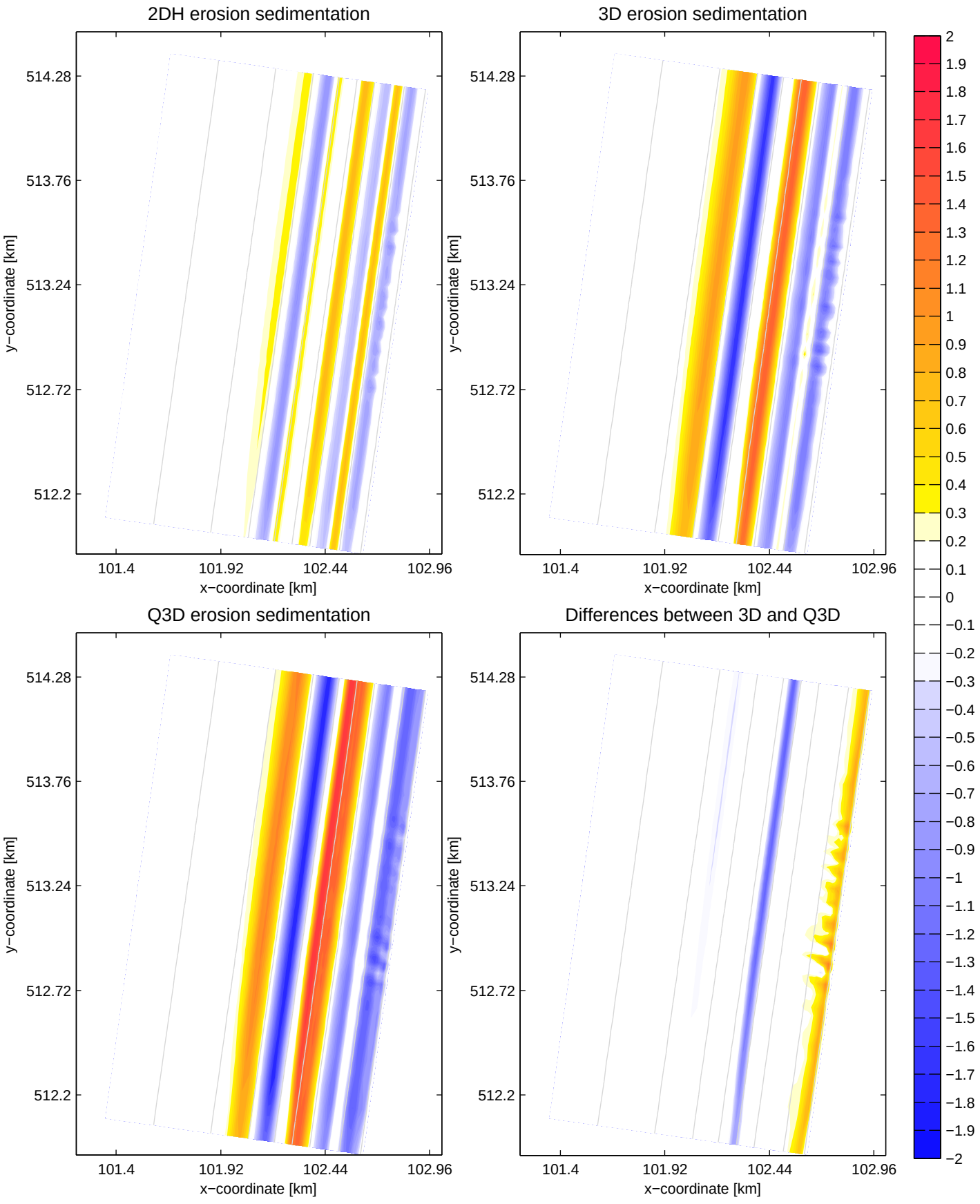

Model results uniform coast, no obstacles Erosion / sedimentation 2DH, 3D and Q3D model Differences erosion/sedimentation between 3D and Q3D	Compare	V04
	uniform coast	
Deltares	Delft3D	F4.2.7

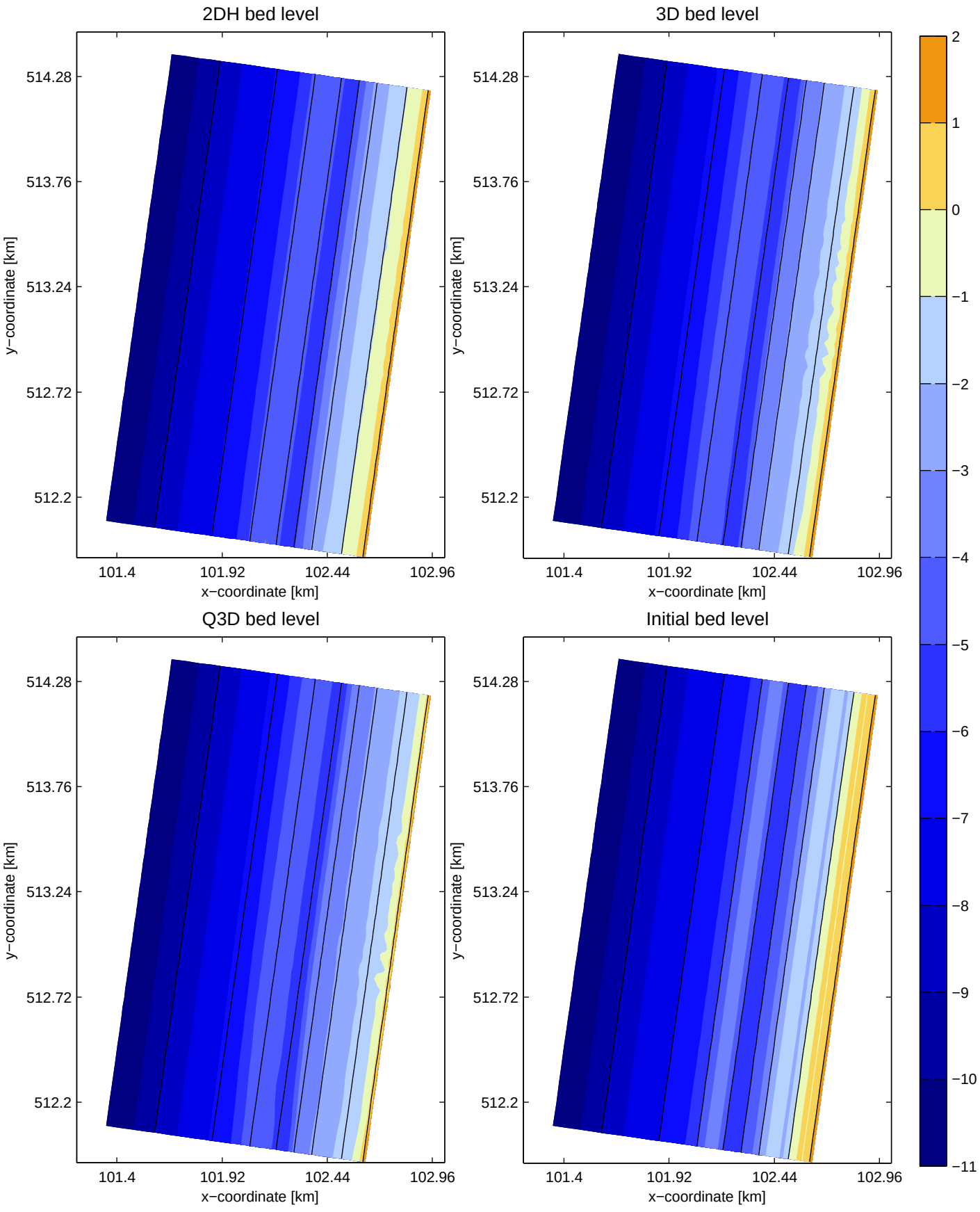

Uniform coast, no obstacles Bed level 2DH, 3D, Q3D and initial	Compare	V04
	uniform coast	
Deltares	Delft3D	F4.2.8

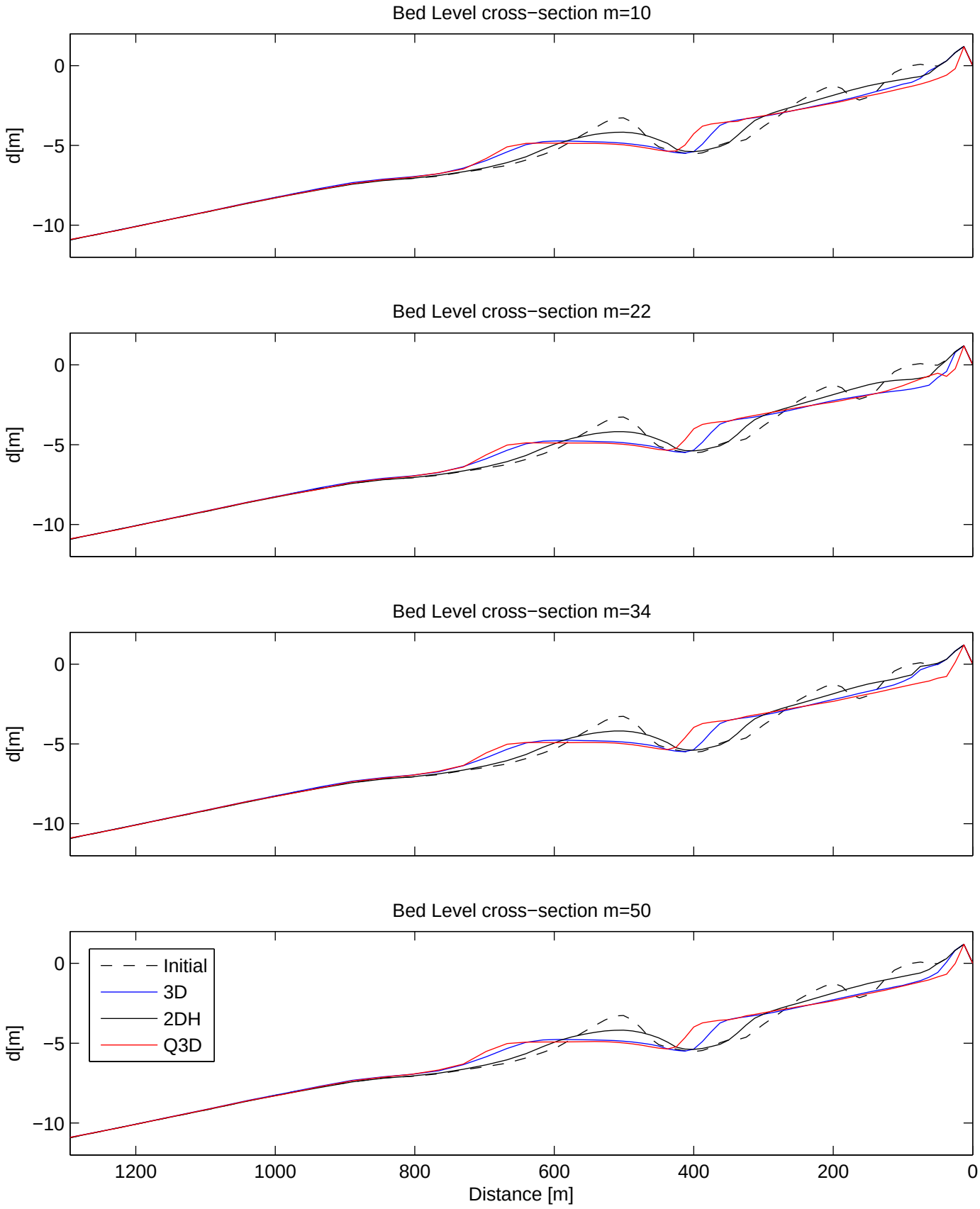

Model results uniform coast, no obstacles bed level intial, 2DH, 3D and Q3D Cross−section m=10, 20 , 34 and 50	Compare	V04
	Uniform coast	
Deltares	Delft3D	F4.2.9

Deltares

Model results uniform coast, including long groyne

Depth−averaged velocity2DH and 3D

Differences depth−averaged velocity between 3D and 2DH

Compare

long groyne

V05

Delft3D

F4.3.1

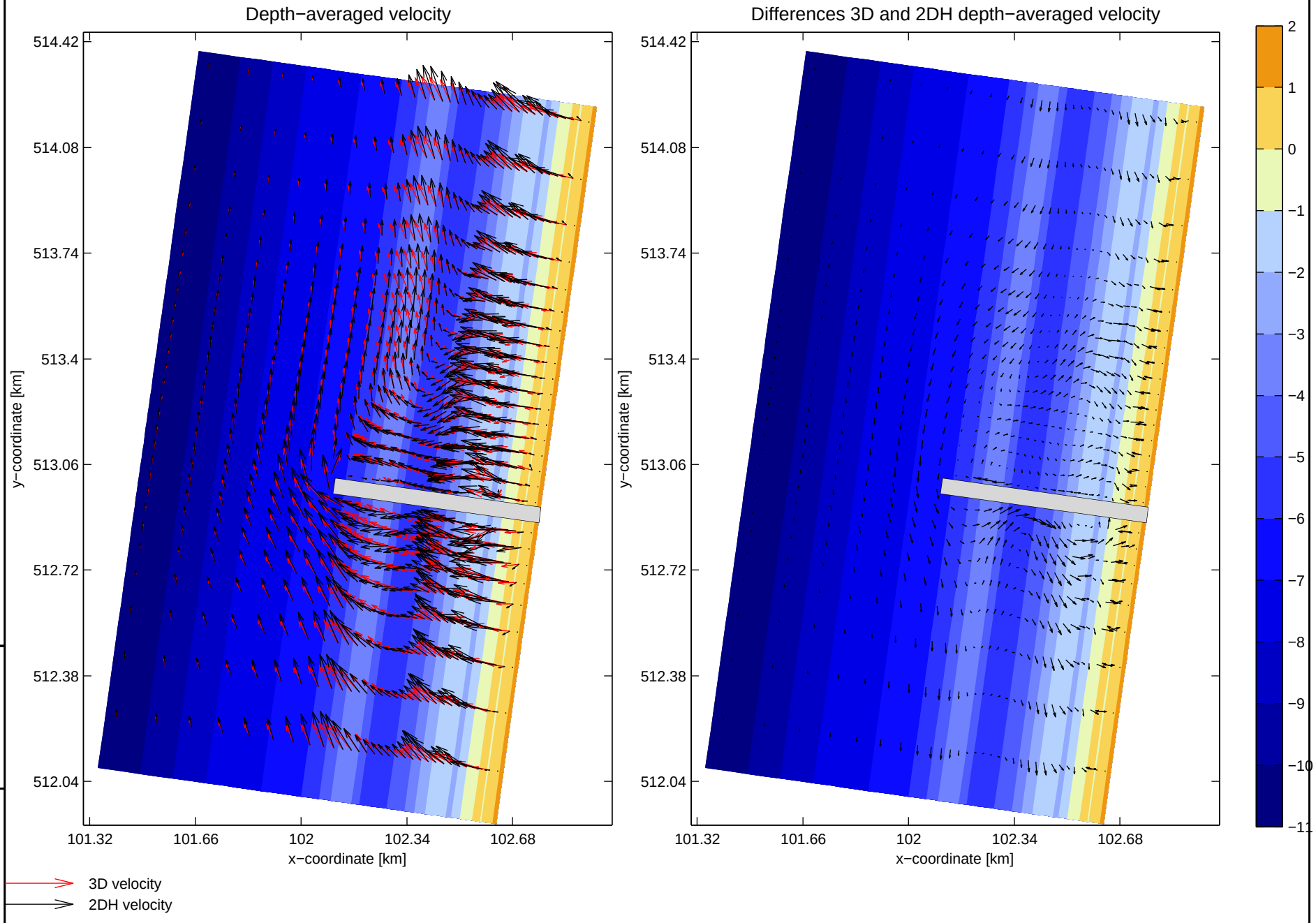

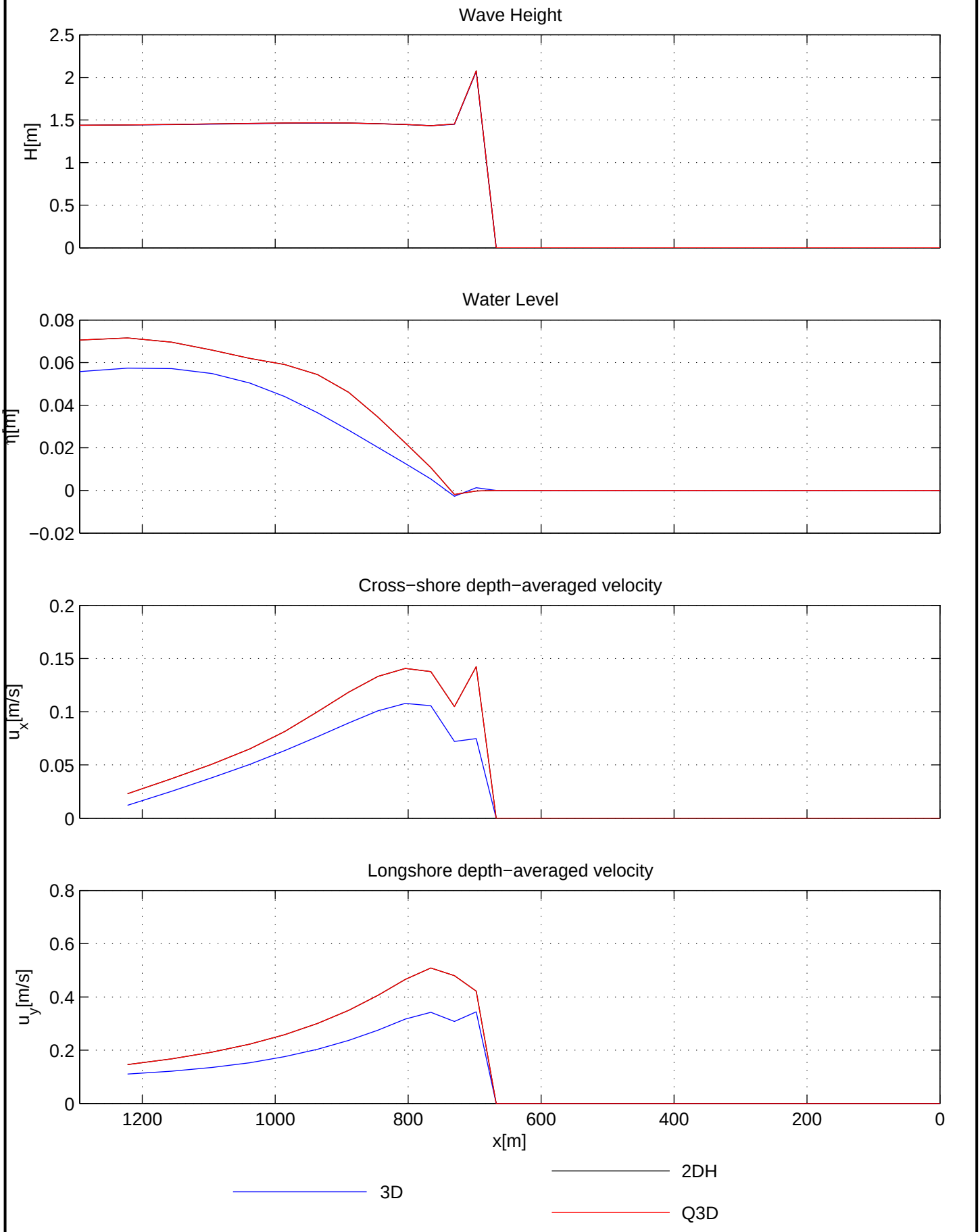

Model results uniform coast, including long groyne Wave height [m], water level [m] and longshore and cross−shore depth−averaged velocity [m/s]	Compare	V05
	long groyne	
Deltares	Delft3D	F4.3.2

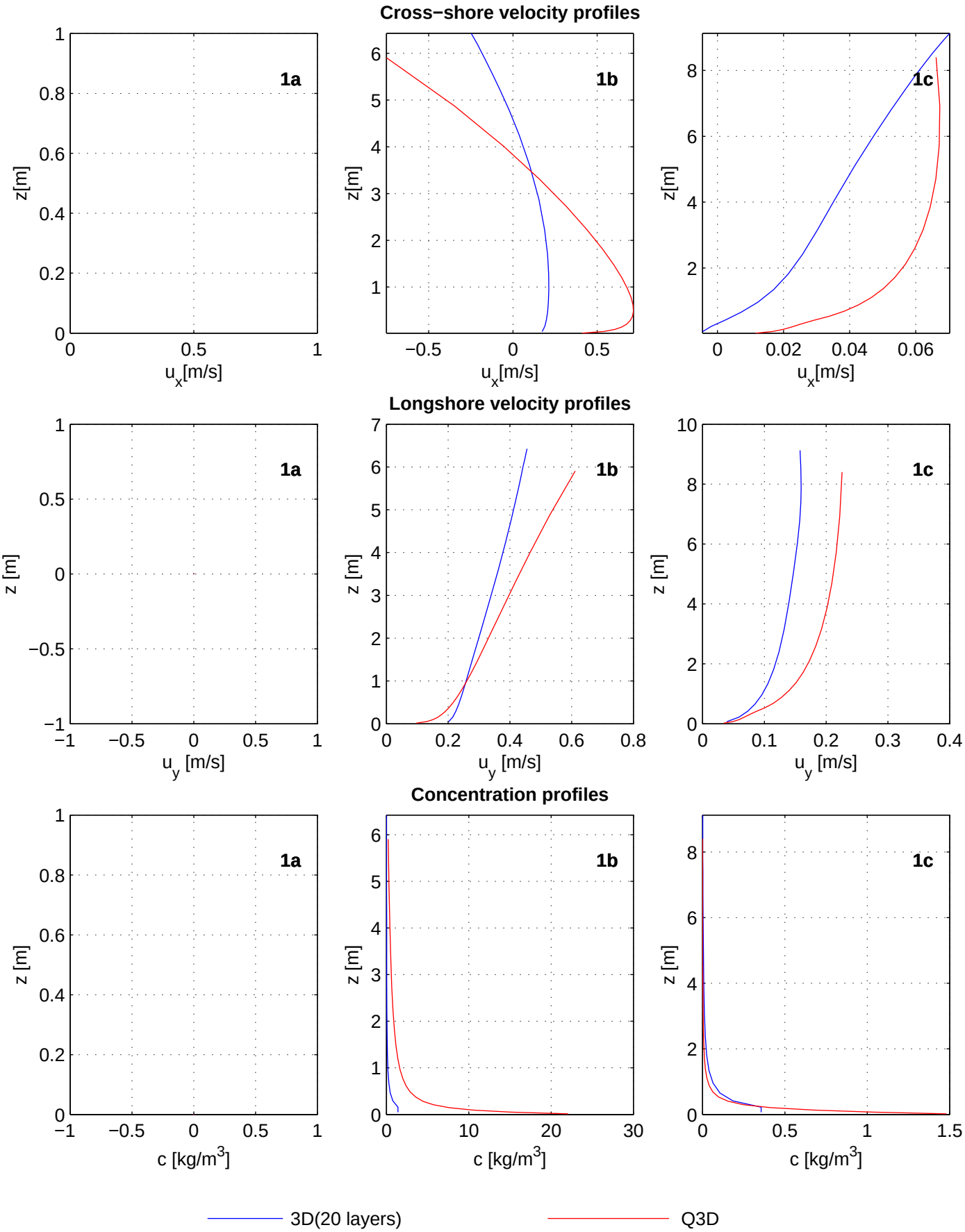

Model results uniform coast, including long groyne Cross−shore velocity, longshore velocity and concentration profiles Cross−section BB, profiles 1,2 and 3	Compare	V05
	long groyne	
Deltares	Delft3D	F4.3.3

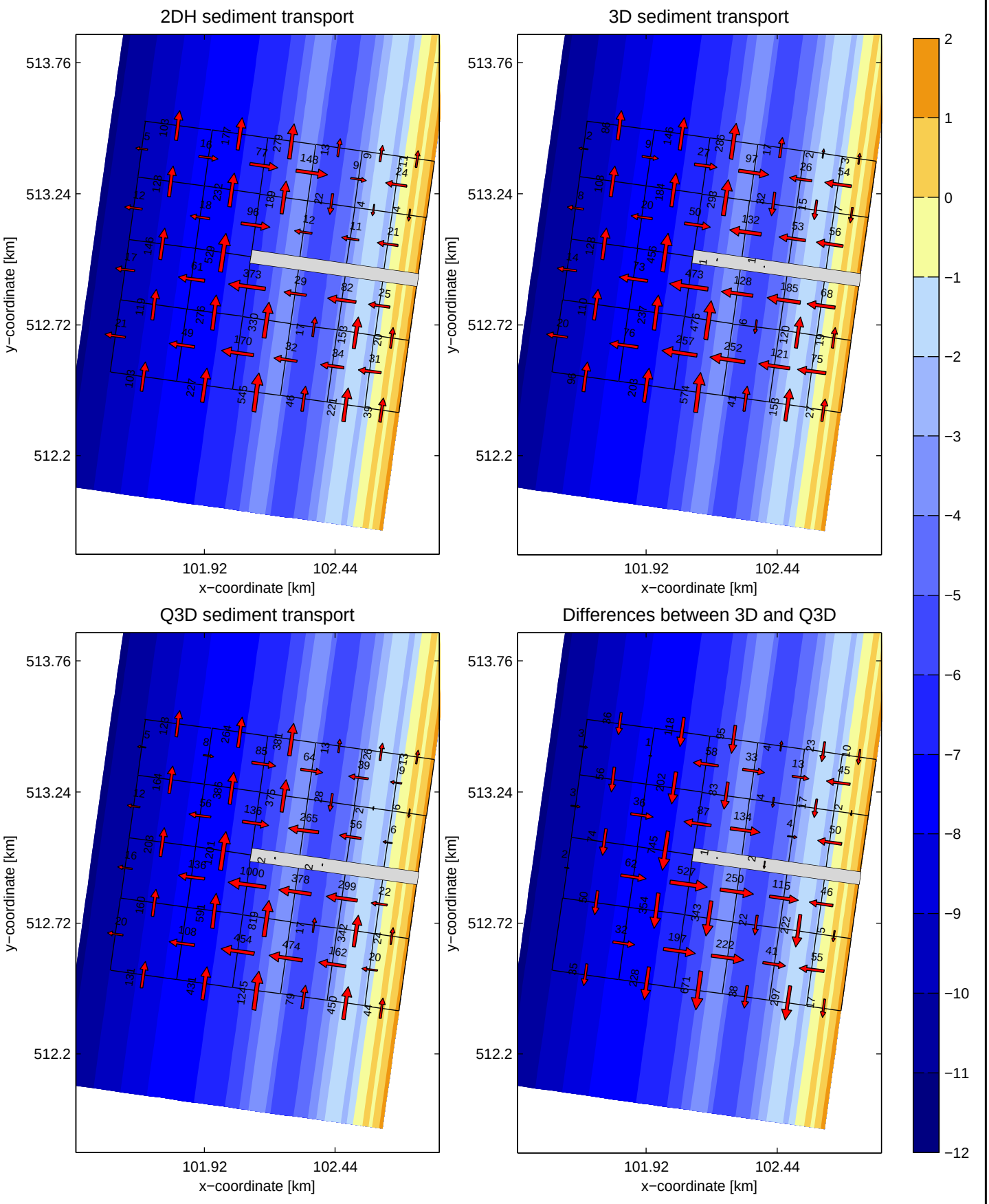

Model results uniform coast, inlcuding long groyne Total sediment transport through transects [10^3 m^3/year] 2DH, 3D, Q3D and differences between 3D and Q3D	Compare	V05
	uniform coast	
Deltares	Delft3D	F4.3.4

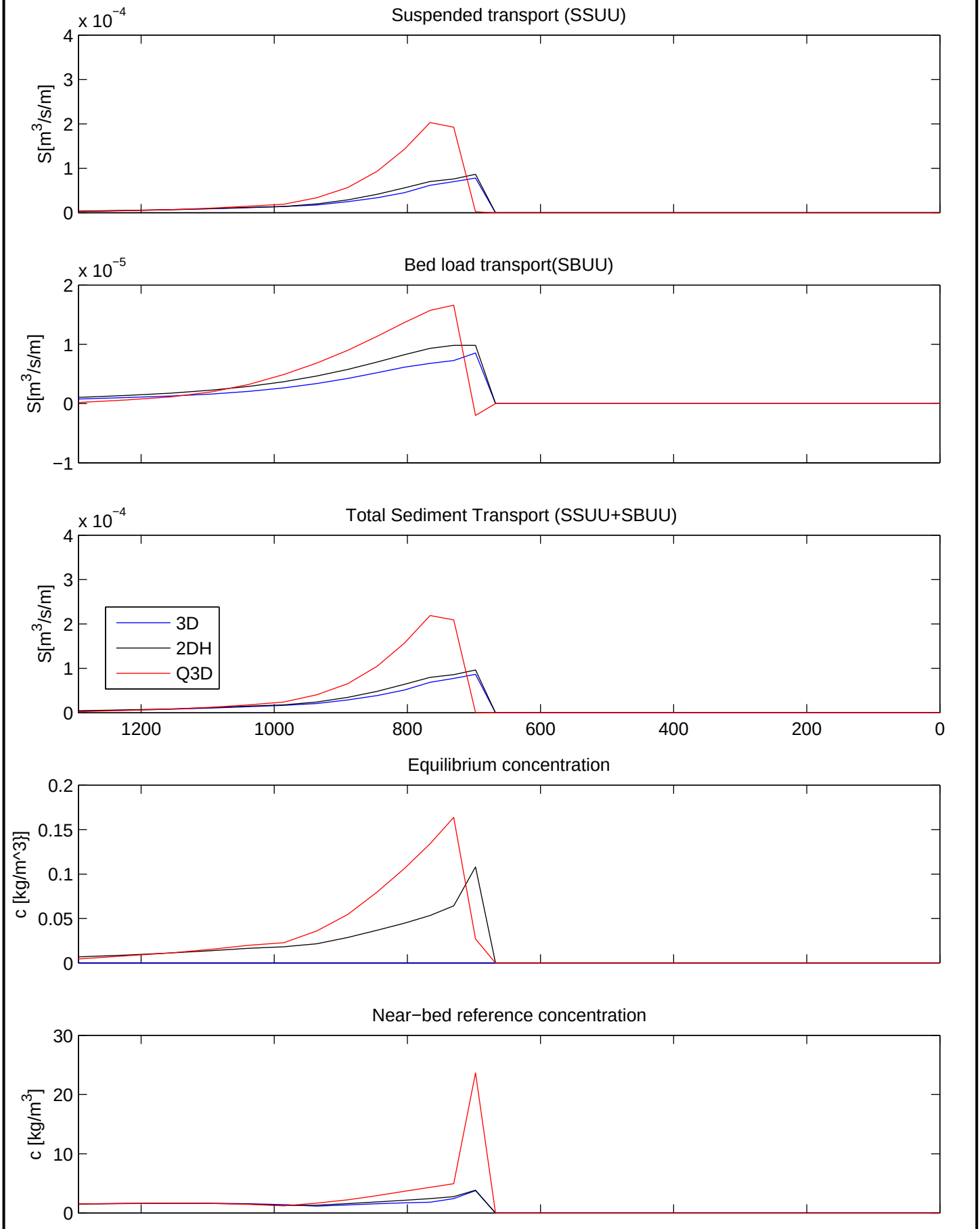

Model results uniform coast, including long groyne Bed−load and suspended load longshore sediment transport rates Cross−section BB	Compare	V05
	long groyne	
Deltares	Delft3D	F4.3.5

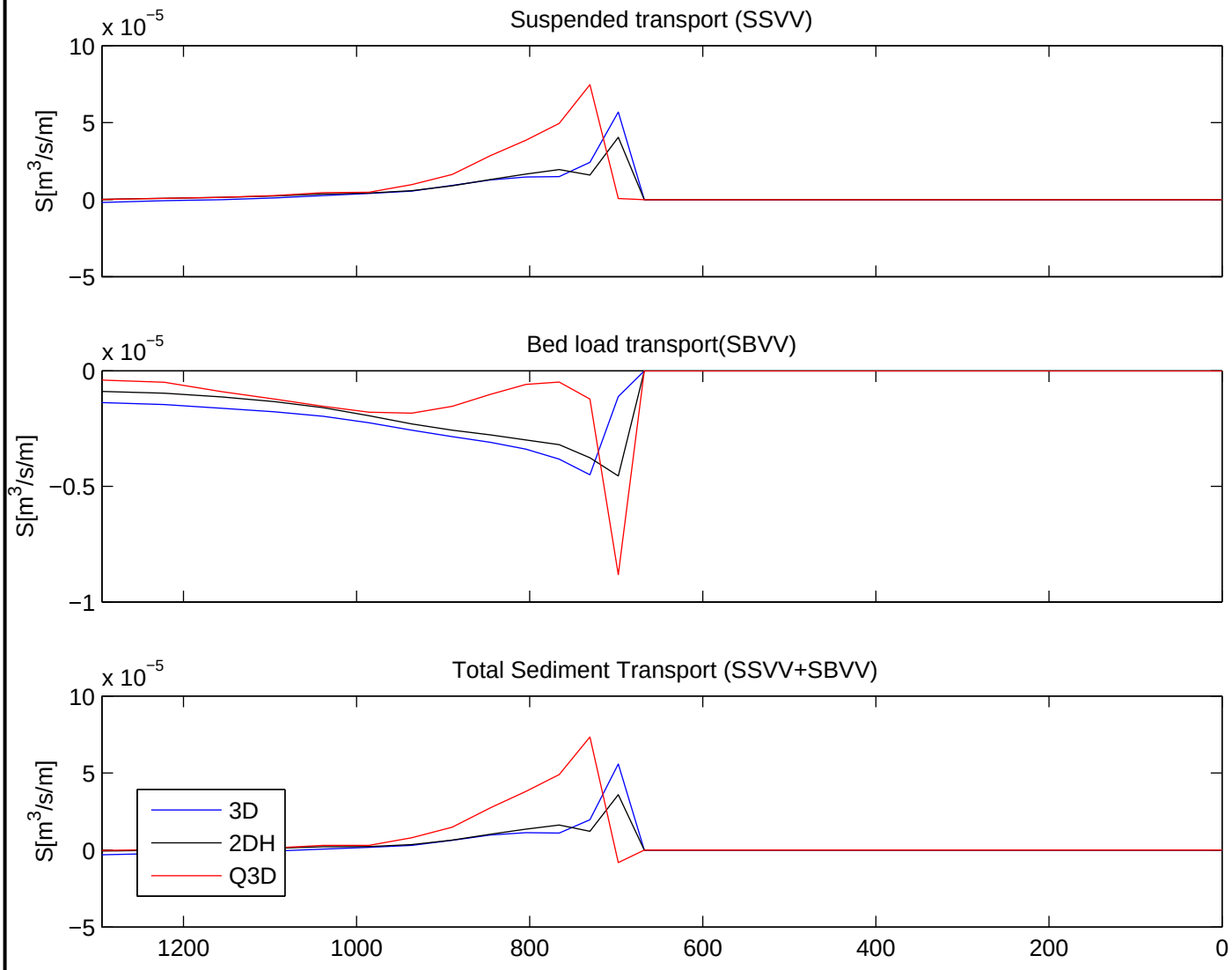

Model results uniform coast, including long groyne Bed−load and suspended load cross−shore sediment transport rates Cross−section BB	Compare	V05
	long groyne	
Deltares	Delft3D	F4.3.6

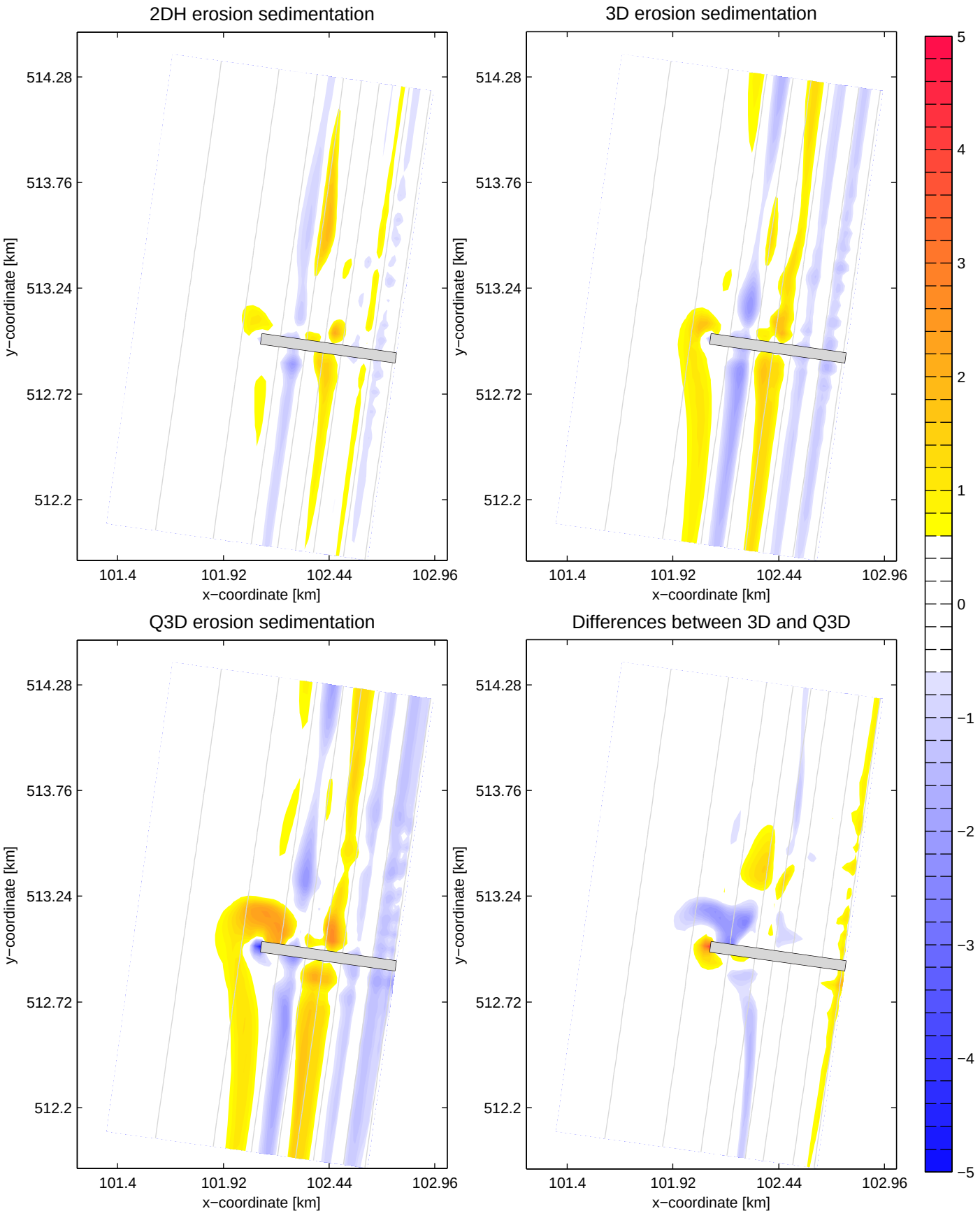

Model results uniform coast, including long groyne Erosion / sedimentation 2DH, 3D and Q3D model Differences erosion/sedimentation between 3D and Q3D	Compare	V05
	long groyne	
Deltares	Delft3D	F4.3.7

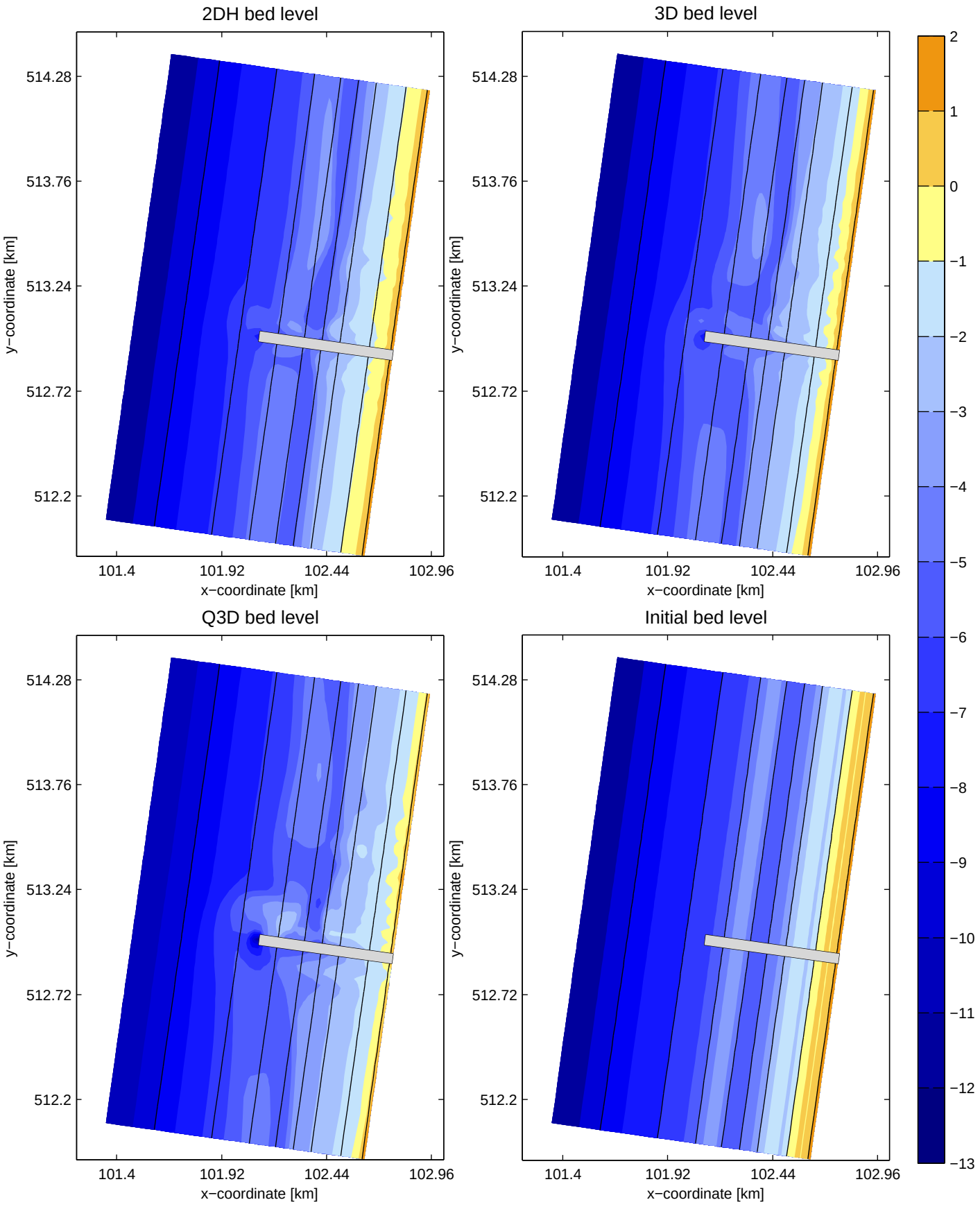

Uniform coast, including long groyne Bed Level 2DH, 3D, Q3D and initial	Compare	V05
	long groyne	
Deltares	Delft3D	F4.3.8

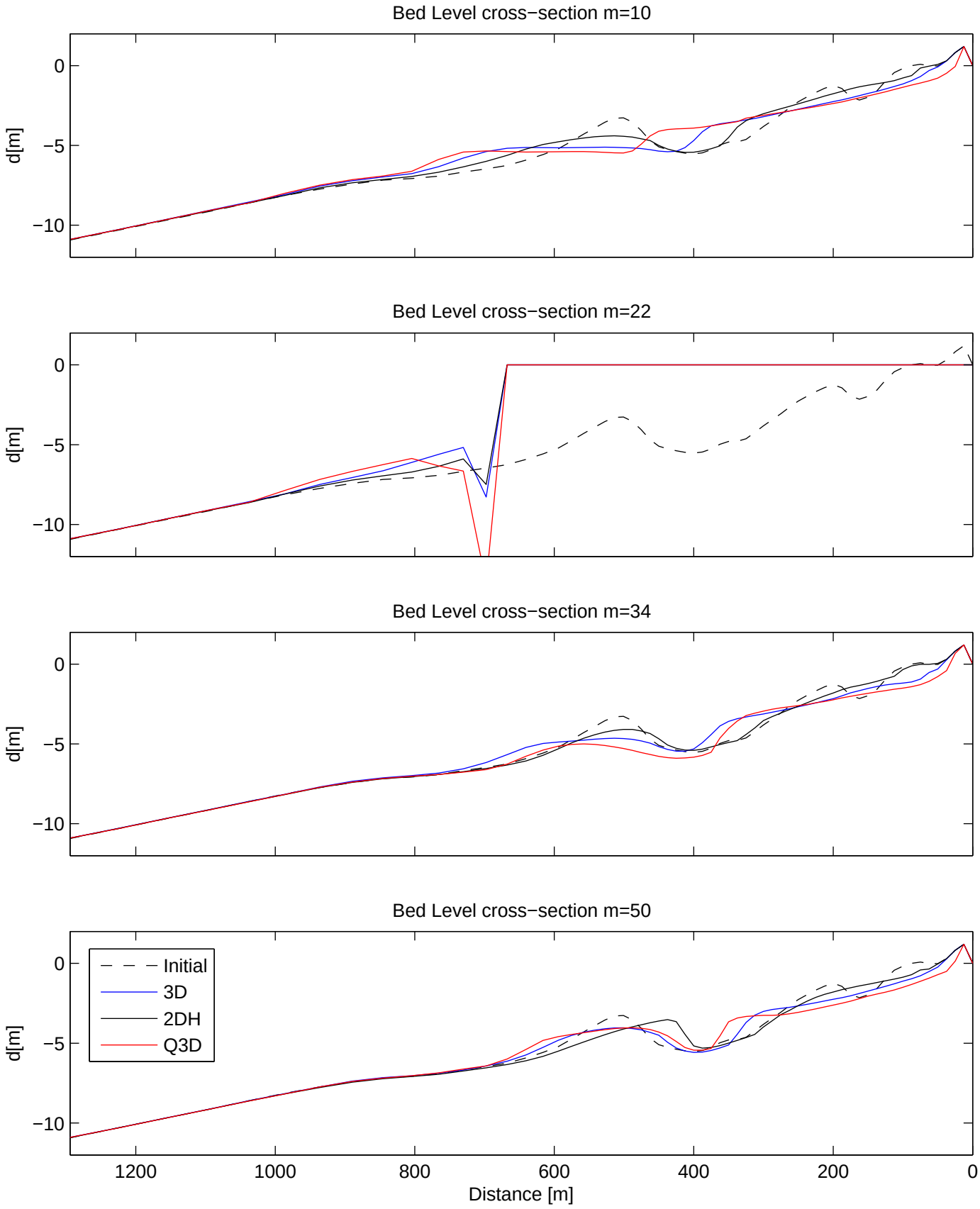

Model results uniform coast, including long groyne bed level intial, 2DH, 3D and Q3D Cross−section m=10, 20 , 34 and 50	Compare	V05
	Uniform coast	
Deltares	Delft3D	F4.3.9

Deltares

Model results uniform coast, including short groyne

Depth−averaged velocity 2DH and 3D

Differences depth−averaged velocity between 3D and 2DH

Delft3D

short groyne

Compare

F4.4.1

V06

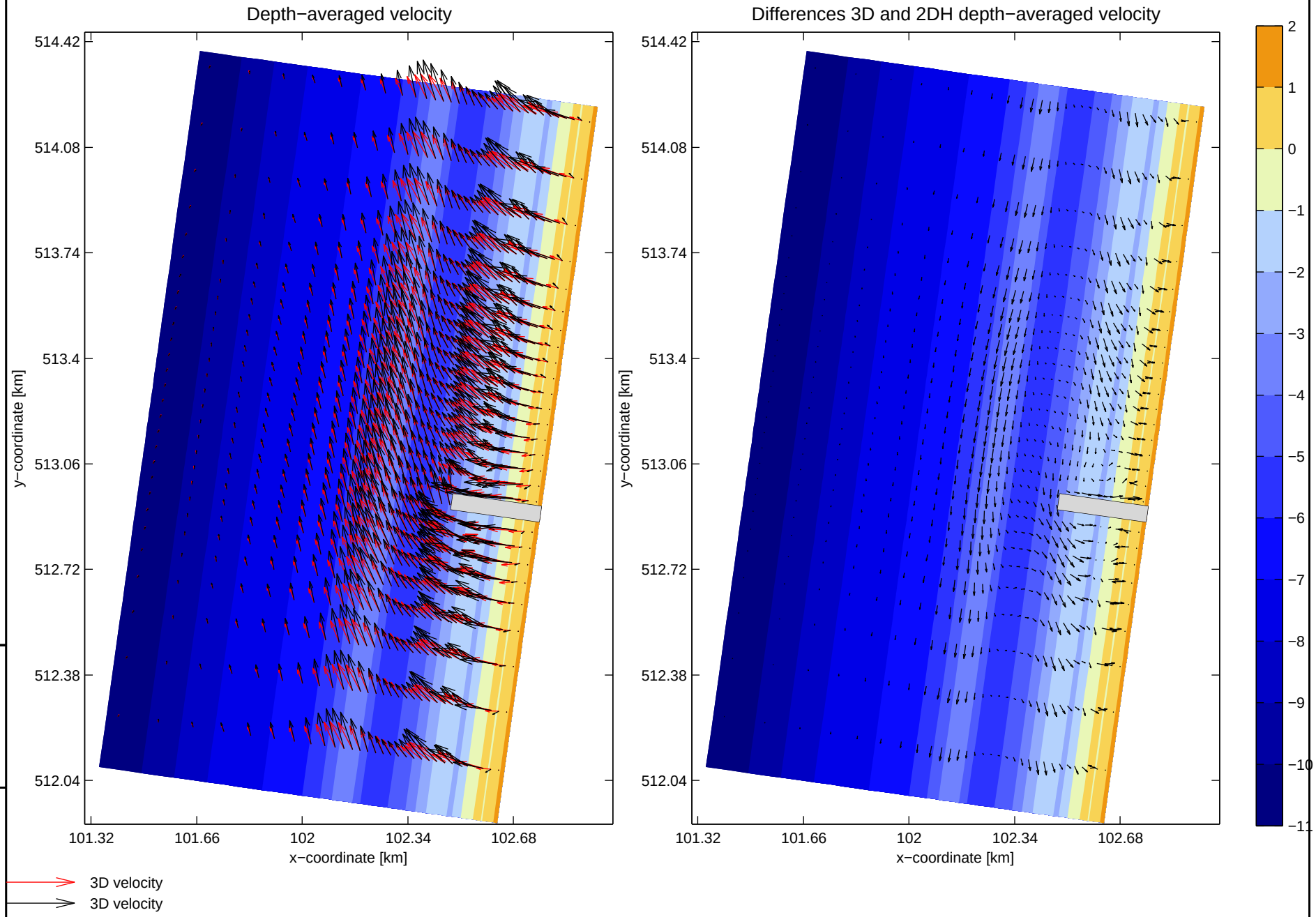

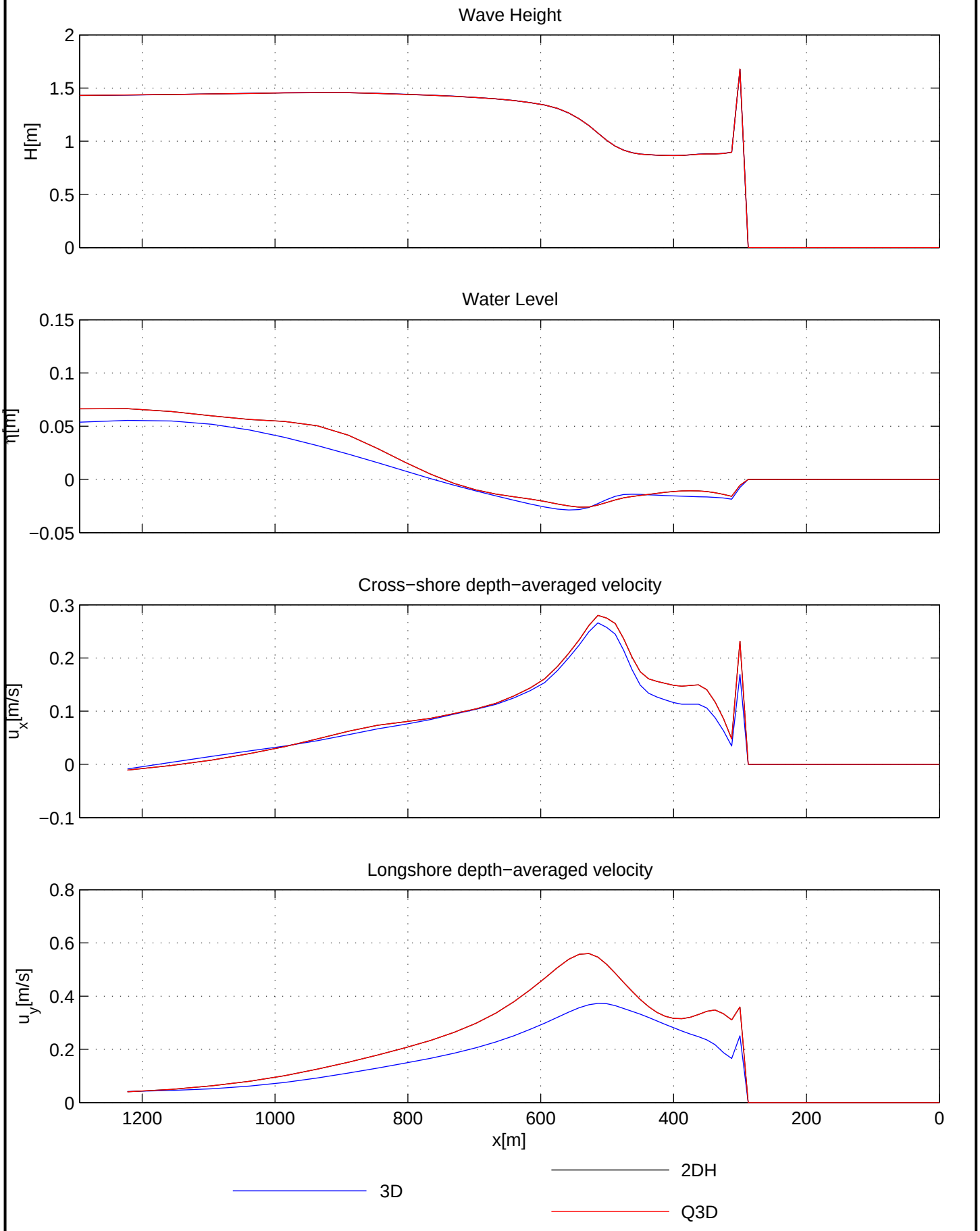

Model results uniform coast, including short groyne Wave height [m], water level [m] and longshore and cross−shore depth−averaged velocity [m/s]	Compare	V06
	short groyne	
Deltares	Delft3D	F4.4.2

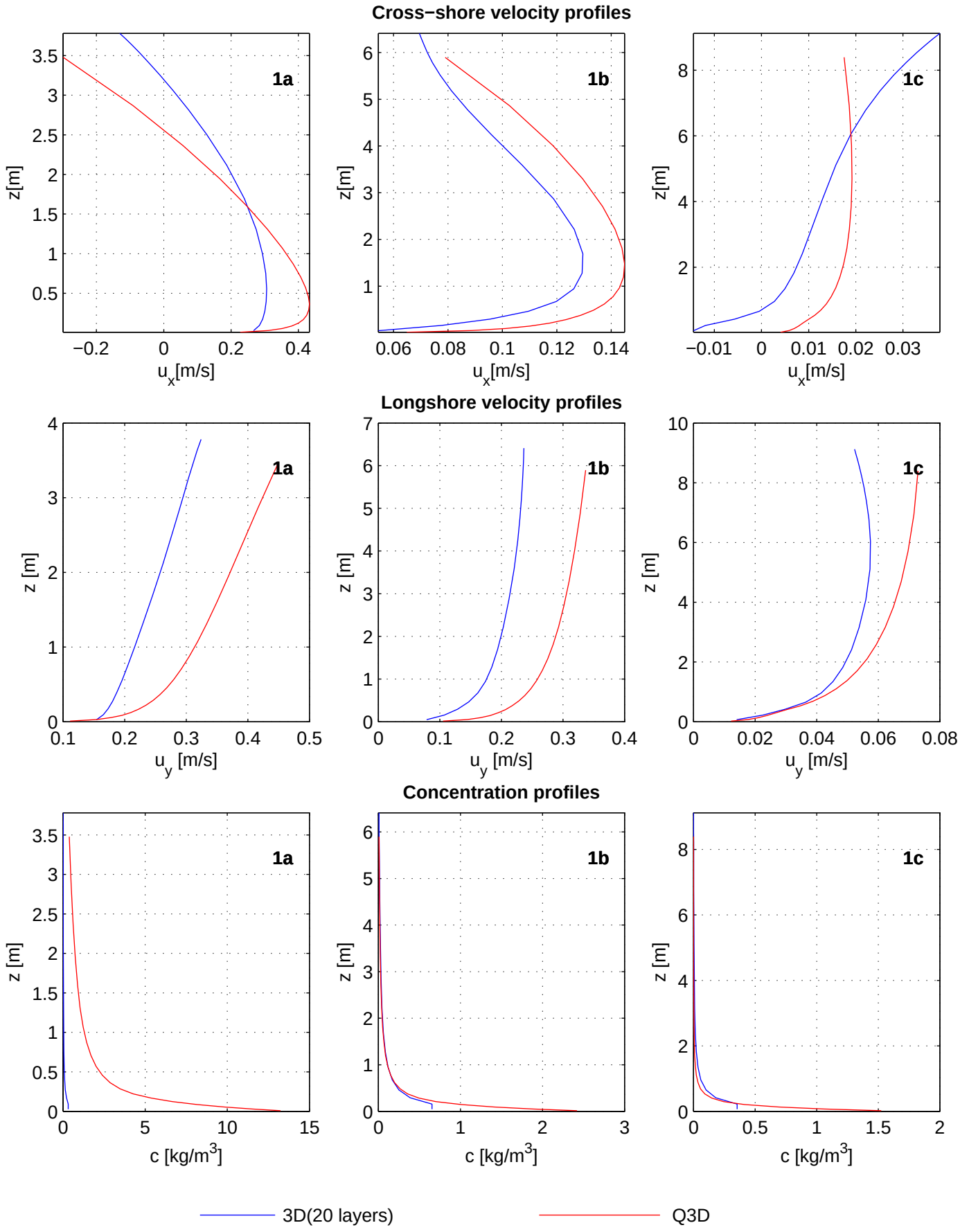

Model results uniform coast, including short groyne Cross−shore velocity, longshore velocity and concentration profiles Cross−section BB, profiles 1,2 and 3	Compare	V06
	short groyne	
Deltares	Delft3D	F4.4.3

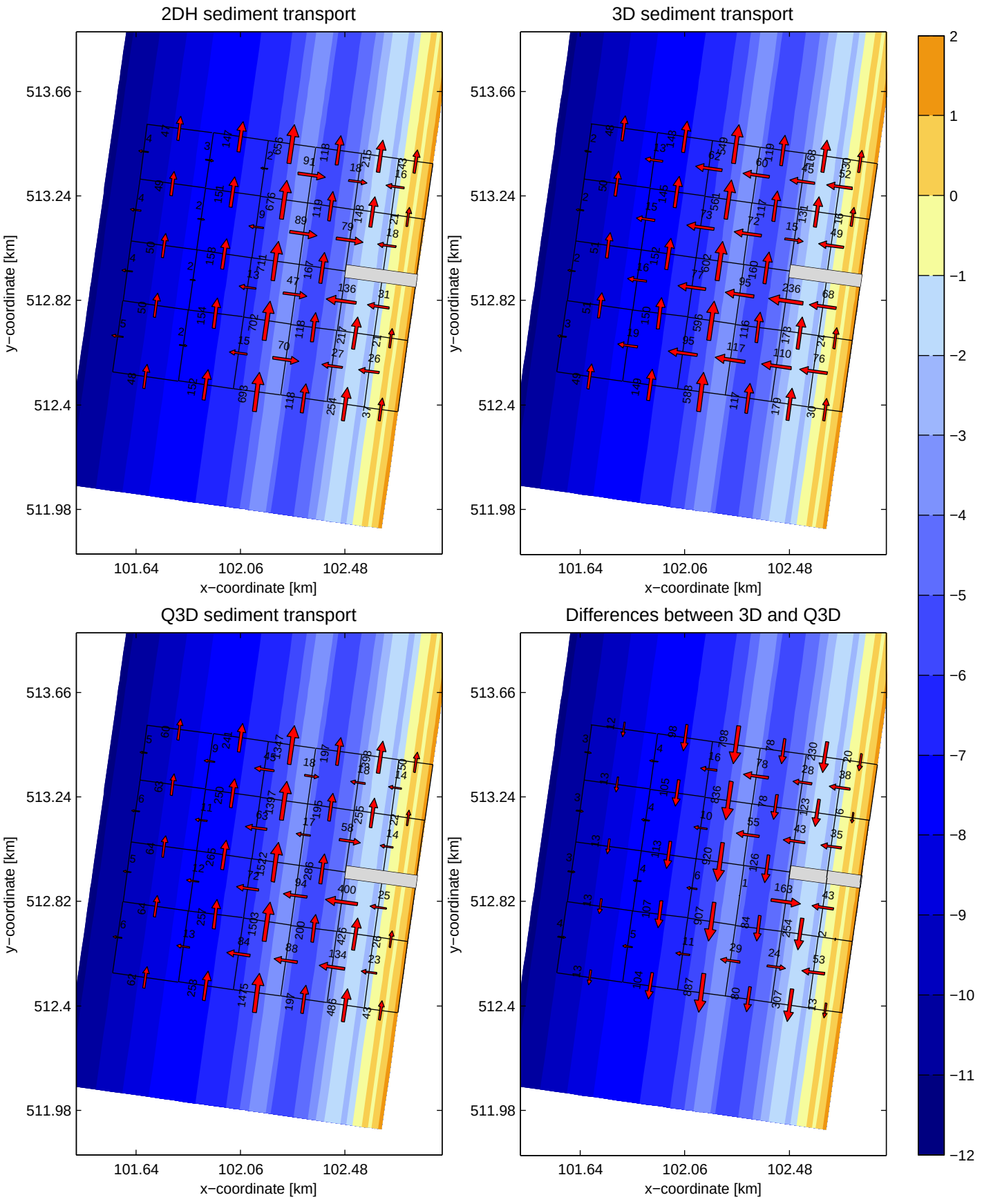

Model results uniform coast, including short groyne Total sediment transport through transects [10^3 m^3/year] 2DH, 3D, Q3D and differences between 3D and Q3D	Compare	V06
	short groyne	
Deltares	Delft3D	F4.4.4

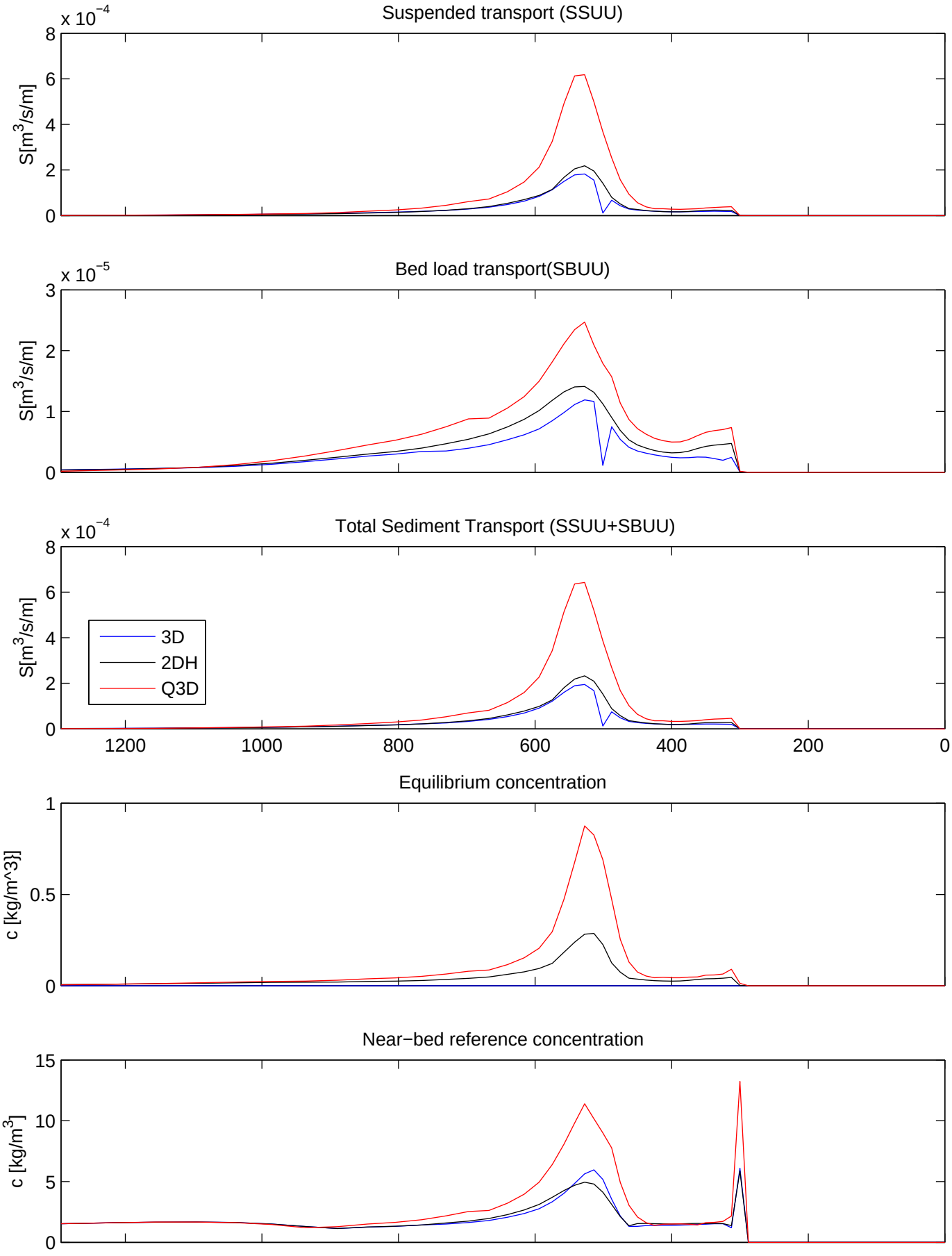

Model results uniform coast, including short groyne Bed−load and suspended load longshore sediment transport rates Cross−section BB	Compare	V06
	short groyne	
Deltares	Delft3D	F4.4.5

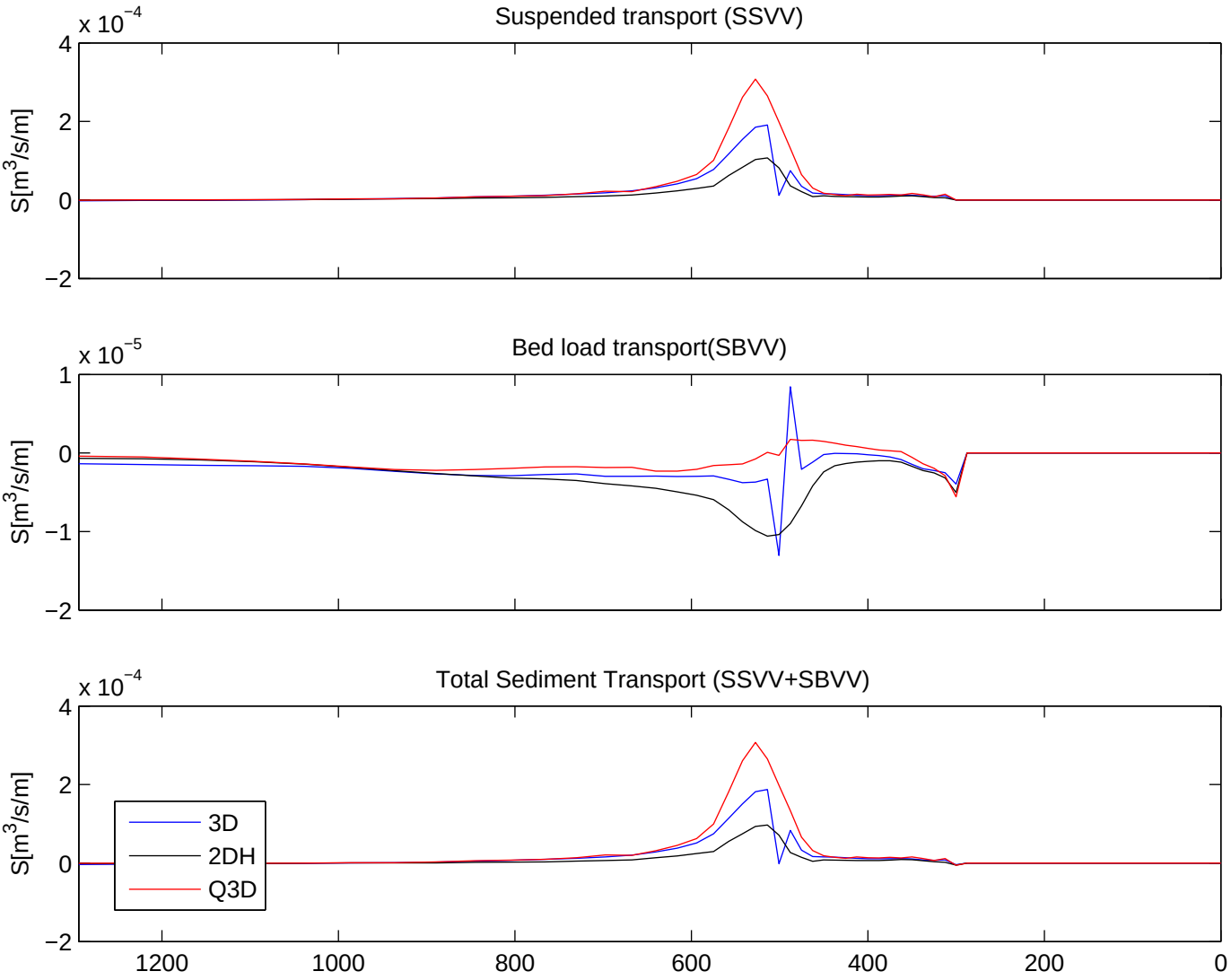

Model results uniform coast, including short groyne Bed−load and suspended load cross−shore sediment transport rates Cross−section BB	Compare	V06
	short groyne	
Deltares	Delft3D	F4.4.6

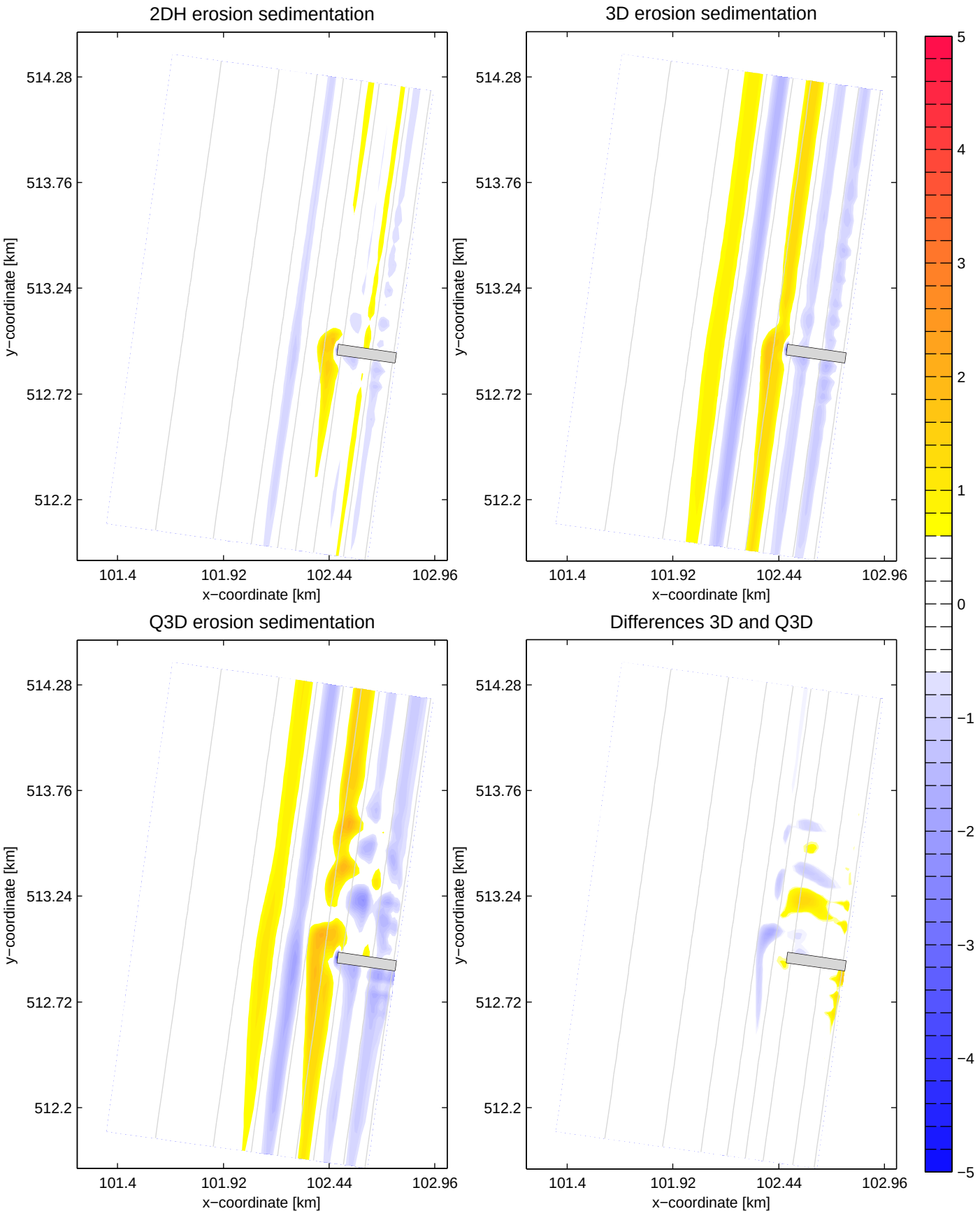

Model results uniform coast, including short groyne Erosion / sedimentation 2DH, 3D and Q3D model Differences erosion/sedimentation between 3D and Q3D	Compare	V06
	short groyne	
Deltares	Delft3D	F4.4.7

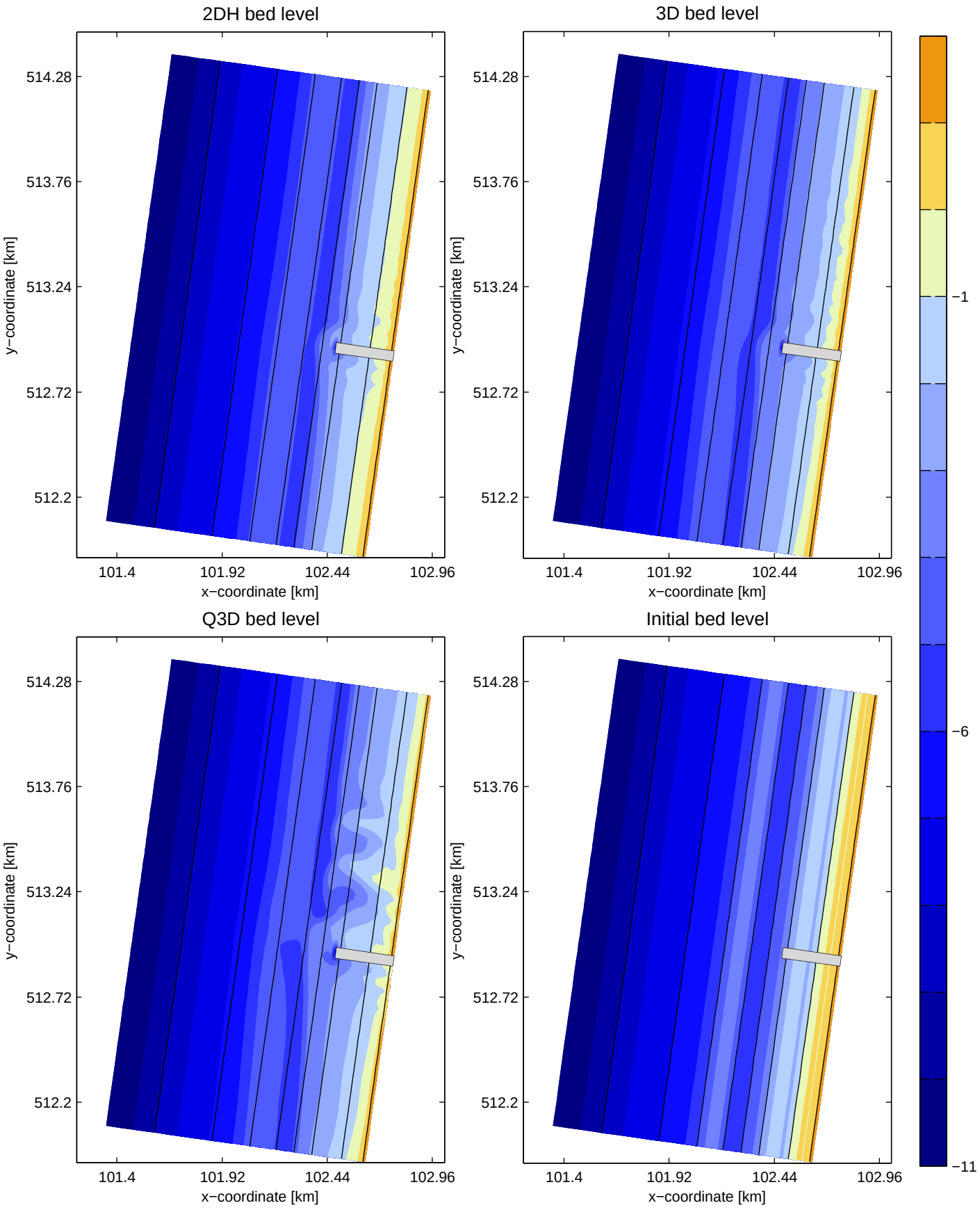

Model results uniform coast, including short groyne Bed Level 2DH, 3D, Q3D and initial	Compare	V06
	short groyne	
Deltares	Delft3D	F4.4.8

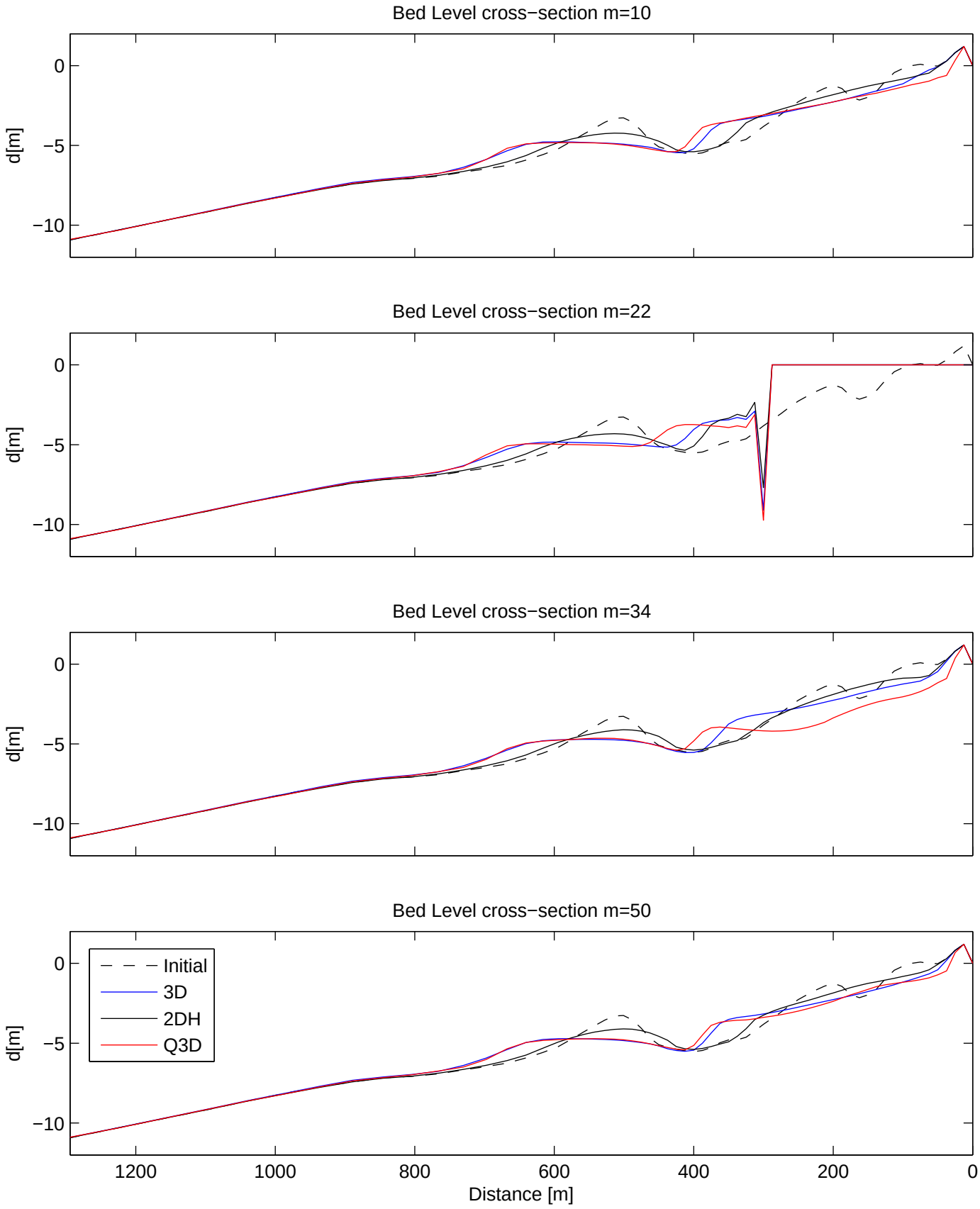

Model results uniform coast, including short groyne bed level intial, 2DH, 3D and Q3D Cross−section m=10, 20 , 34 and 50	Compare	V06
	Uniform coast	
Deltares	Delft3D	F4.4.9

Deltares

Pocket beach including submerged breakwater

Overview area

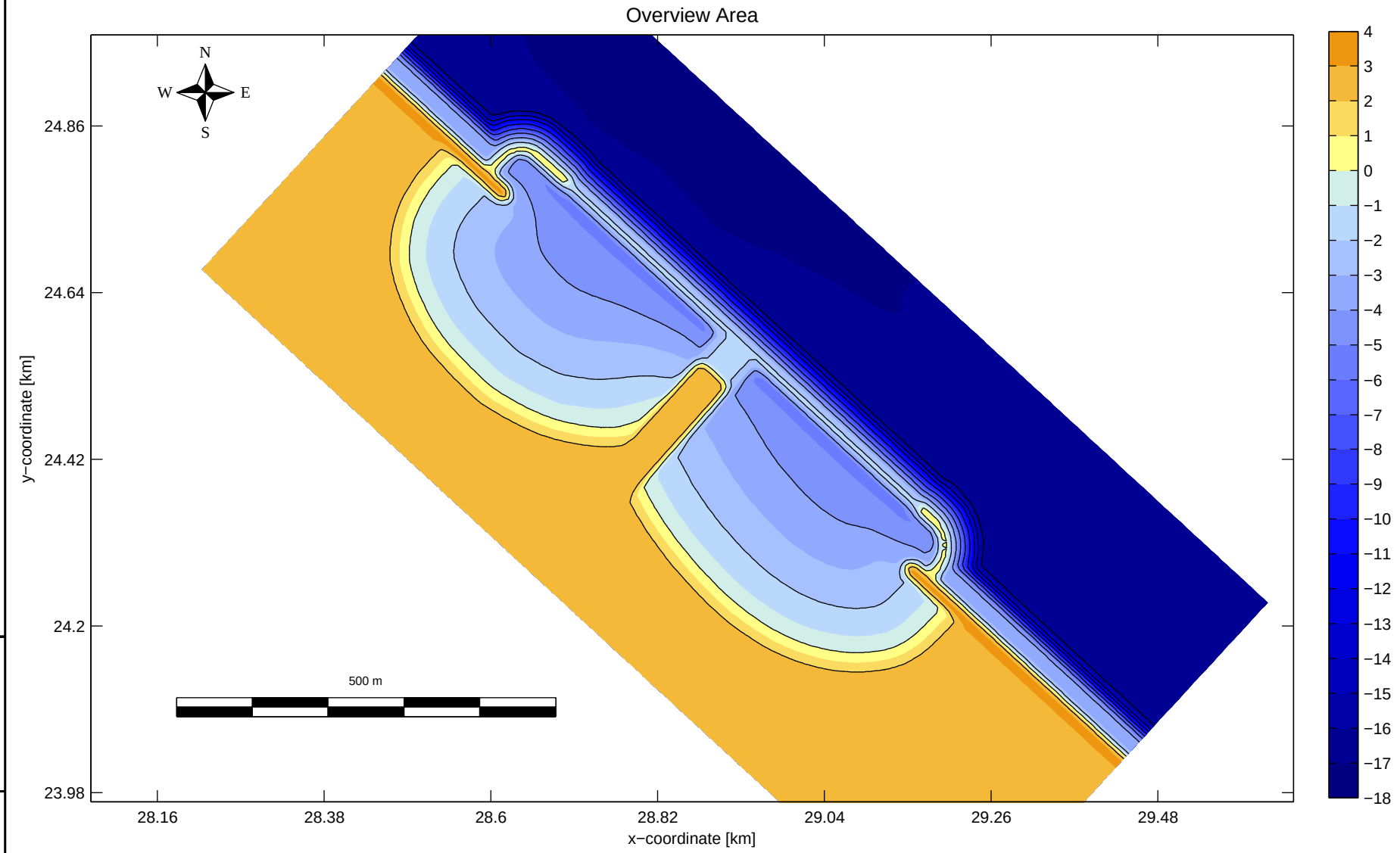

Delft3D

Overview

F4.5.1

Pocket beach

Deltares

Pocket beacg including submerged breakwater model results

Depth−averaged velocity 2DH and 3D

Differences between 2DH and 3D

Compare

Pocket Beach

Submerged breakwater

Delft3D

F4.5.2

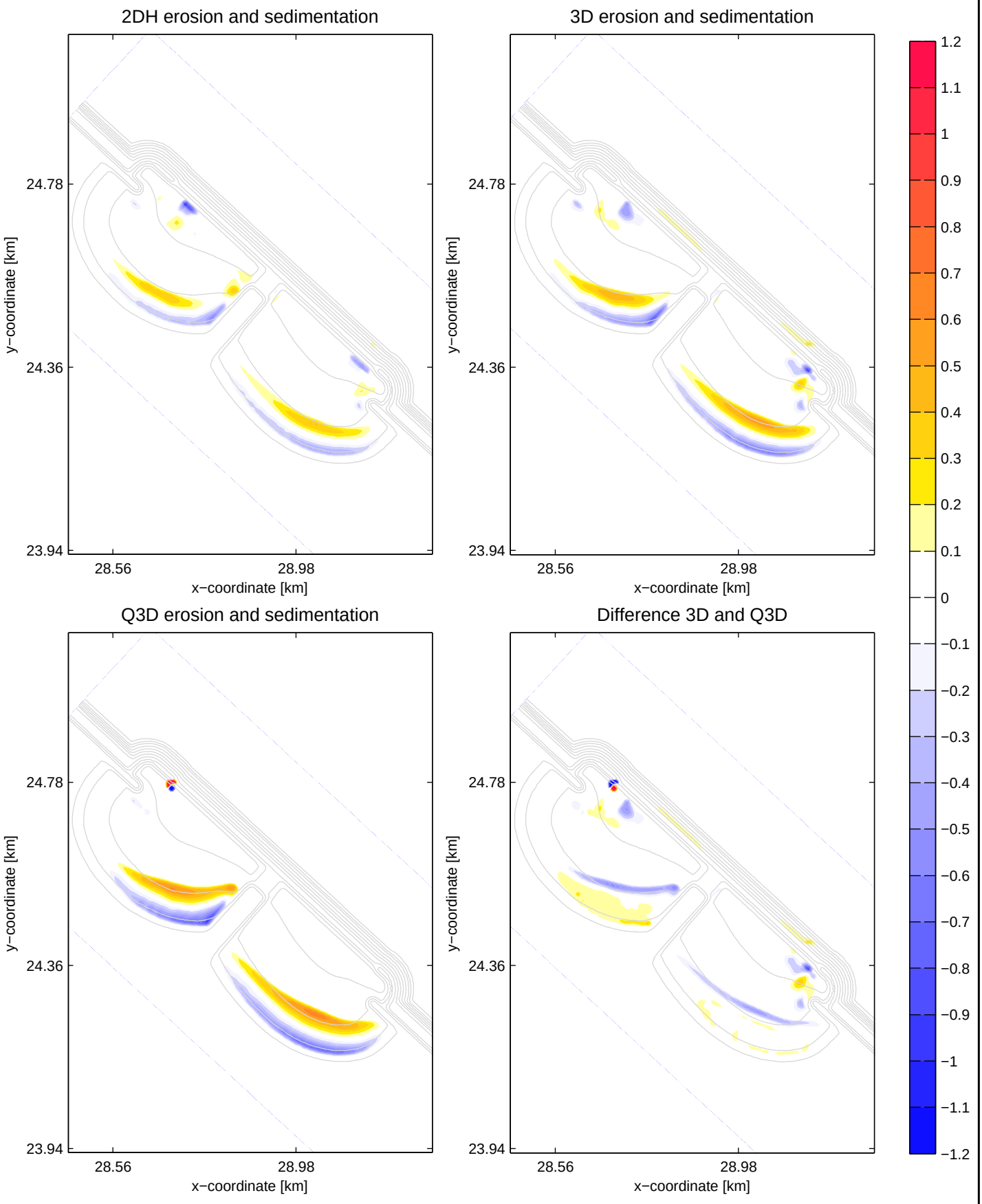

Pocket beach including submerged breakwater model results Erosion and Sedimentation 2DH, 3D, Q3D and differences between 3D and Q3D	Compare	Pocket beach
		including submerged breakwater
Deltares	Delft3D	F4.5.3

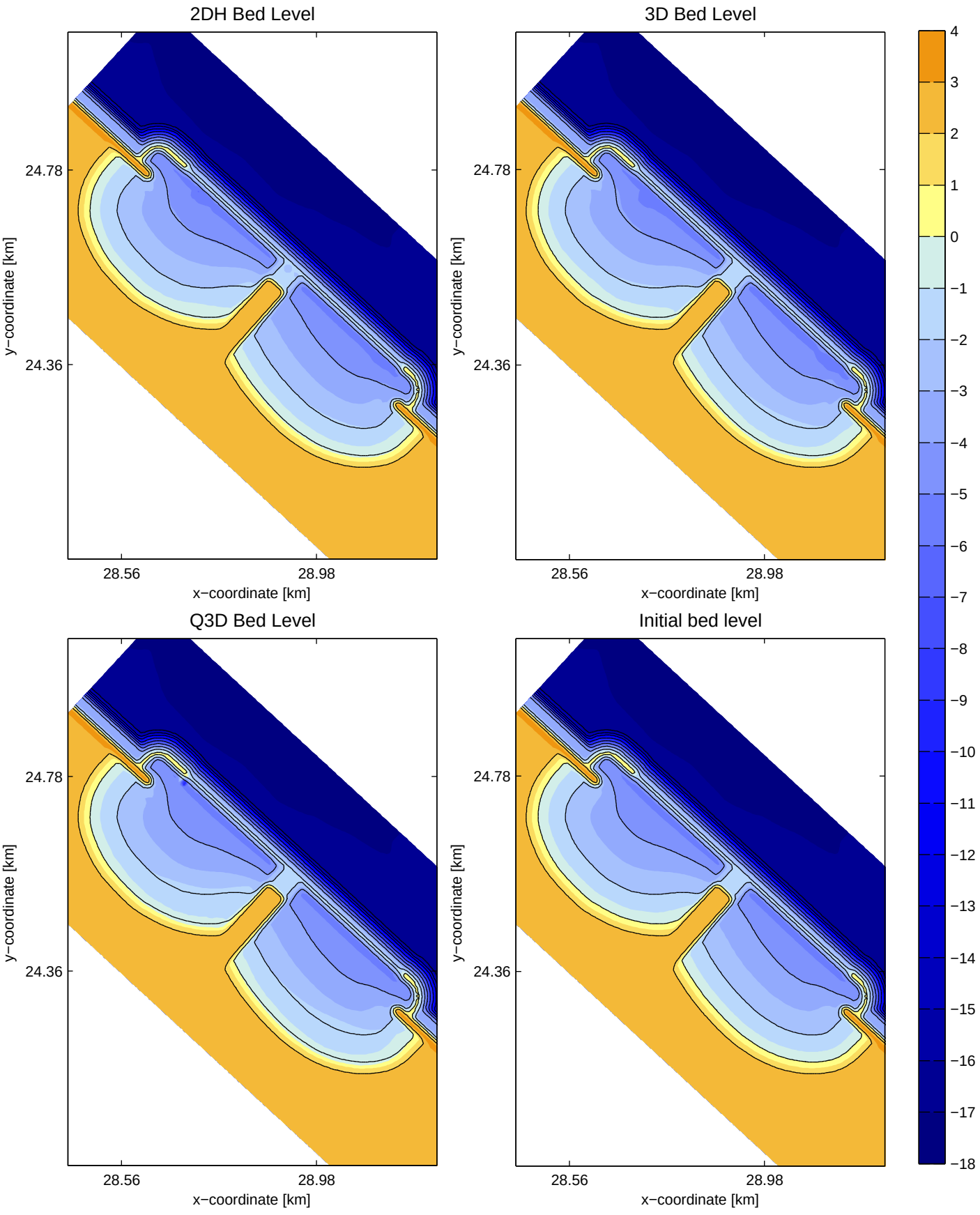

Pocket beach including breakwater model results Bed Level 2DH, 3D, Q3D and initial bed level	Compare	Pocket beach
	including submerged breakwater	
Deltares	Delft3D	F4.5.4

G Description of Unibest-TC

This chapter describes the UNIBEST TC model, based on Bosboom et al. [1997]. Uniform Beach Sediment Transport – Time dependent Cross-shore is a process-based model that incorporates models for hydronamic processes.

G.1 Schematic representation of UNIBEST TC model

The model can be divided into five sub models. The scheme in Figure G.1 shows how these sub models interact with each other. In one time step UNIBEST TC computes first the local wave height according to wave height decay model ENDEC (Battjes and Janssen, 1978). From the local wave height, the orbital velocity and mean current are computed. Subsequently separate transport formulations are used for bed load transport and suspended transport. Finally, bottom changes are computed using a sediment mass balance equation, resulting in a new profile, which is used in the next time step.

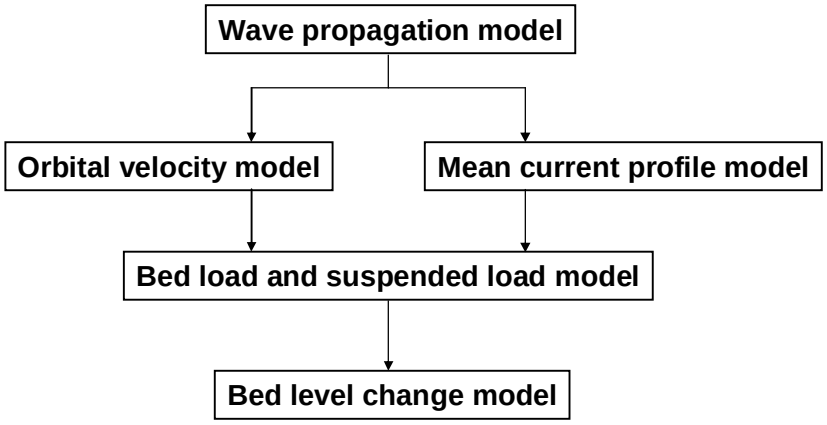

Figure G.1 Set-up of model Unibest-TC

The model requires an initial profile, grain sizes and offshore boundary conditions. In the subsequent Sections the sub-models are described.

The models are briefly described in the following sections, which are partly derived from Den Heijer (2005).

G.1.1 Wave propagation model

The wave propagation model solves three first-order differential equations by numerical integration. The equations describe the wave energy balance (Battjes and Janssen, 1978), the energy contained in surface rollers in breaking waves (Nairn et al., 1990) and the horizontal momentum balance.

The energy balance equation yields:

$$\frac{\partial}{\partial x}\left(Ec_g \cos\theta\right) = -D_w - D_f \qquad \text{(G.1)}$$

in which, E is the wave energy, c_g is the wave group velocity, θ the angle of incidence of the wave field, D_w the dissipation of wave energy due to breaking and D_f dissipation due to bottom friction.

For the dissipation of wave energy due to breaking an expression by Battjes and Janssen is used:

$$D_w = \frac{1}{4}\frac{\rho g \alpha}{T_p} H_{\max}^2 Q_b \qquad \text{(G.2)}$$

Where Q_b is the fraction of breaking waves computed from $H_{rms} / H_{\max}$, T_p the wave period and α and γ are dissipation coefficients.

The model applies a Rayleigh distribution for the non-breaking waves, assuming that waves smaller than Hmax are not breaking. Hmax is defined according to:

$$H_{\max} = \frac{0.88}{k}\tanh\left(\frac{\gamma k h_r}{0.88}\right) \qquad \text{(G.3)}$$

For the dissipation of energy due to bottom friction, D_f, the following expression is implemented.

$$D_f = \frac{f_w \rho}{\sqrt{\pi}} u_{orb}^3 \qquad \text{(G.4)}$$

Where: f_w is a user defined friction factor, u_{orb} is the amplitude of the orbital velocity at the bottom, according to linear wave theory and root mean square wave height.

The second equation used for the energy contained in surface rollers in breaking waves was modelled by Nairn:

$$\frac{\partial}{\partial x}\left(2E_r C \cos\theta\right) = D_w - Diss \qquad \text{(G.5)}$$

in which the roller energy E_r represents the amount of kinetic energy in a roller with area A and length L:

$$E_r = \frac{1}{2}\rho c^2 \frac{A}{L} \qquad \text{(G.6)}$$

The dissipation of roller energy is modelled according to:

$$Diss = \beta \rho g c \frac{A}{L} \qquad \text{(G.7)}$$

Where β is the slope of the face of the wave.

A delay for the breaking of waves was applied, as waves require a certain distance over critically shallow water before breaking occurs. The third differential equation represents the set-up equation:

$$\frac{\partial \overline{\eta}}{\partial x} = -\frac{1}{\rho g h}\frac{\partial S_{xx}}{\partial x} \tag{G.8}$$

in which: η is the mean wave set-up S_{xx} the radiation stress in and h the water depth.

G.1.2 Mean current profile Model

In UNIBEST TC the modelling of the mean current profile is done according to Roelvink and Reniers (1994), using a quasi-3D model in which effects of wind stress, breaking-induced forcing, surface slope and wave boundary layer are taken into account. The model is derived from a model according to De Vriend and Stive (1987), who identified three layers.

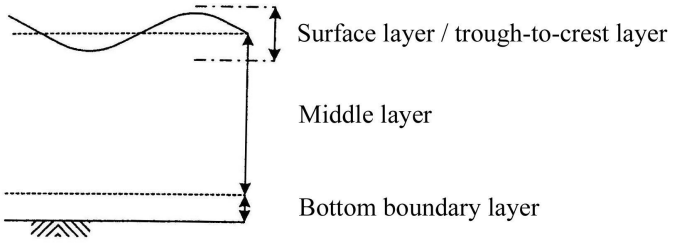

Figure G.2 Three layers, according De Vriend and Stive (1987)

In this model, the surface layer is replaced by a shear stress ($\tau_{s,wave}$) induced by wind and surface rollers and a mass flux (m) for calculation of the net mean flow below trough level.

$$\tau_{s,wave} = \frac{Diss}{c} \tag{G.9}$$

$$m = \frac{E + 2E_r}{c} \tag{G.10}$$

For the two other layers, the shear stress over the water height caused by the forcing on the surface is calculated from which a velocity gradient over the depth can be calculated after the eddy viscosity is established. This velocity gradient is then integrated, resulting in a velocity profile over the depth.

G.1.3 Wave orbital velocity model

The model of the time-variation of the near-bed velocity is based on a concept by Roelvink and Stive (1989). The model consists of two parts:

- A contribution due to wave asymmetry, computed according to the Rienecker and Fenton method.

- A contribution due to long waves, occurring due to grouping of short waves in a random wave field.

The two contributions are implemented separately, and added. The first step is a time series of the near-bed velocity U1 in case of regular waves, taking into account the wave symmetry contribution:

$$U_1(t) = \sum_{j=1}^{n} B_j \cos(j\omega t) \tag{G.11}$$

Subsequently a second velocity time series, which is slightly out of phase with U1, is added.

$$U_2(t) = \sum_{j=1}^{n} \cos(j\omega t)\left[\frac{1}{2}\left(1+\cos(\Delta\omega t)\right)\right]^j \tag{G.12}$$

The magnitude of U2 is corrected to U'_2 in such a way, that the third moment of U'_2 equals the third moment of U1.

$$U'_2(t) = \left(\frac{\frac{1}{T}\int_0^T U_1^3 dt}{\frac{1}{mT}\int_0^{mT} U_2^3 dt}\right) U_2(t) \tag{G.13}$$

Secondly, in case of a random wave field the grouping of the short waves will generate bound long waves. Modelling of a bound long wave is done according to Roelvink and Stive (1989). It is assumed that wave-group related features of a random wave field may be represented by a bichromatic wave train with equal amplitudes a_m and a_n and an accompanying bound long wave with amplitude ξ_a.
In order to find values for $a_m = a_n$ and ξ_a, the wave train is required to have the same total surface variance.

$$m_0 \cong \frac{1}{8}H_{rms}^2 = \frac{1}{2}a_n^2 + \frac{1}{2}a_m^2 + \frac{1}{2}\xi_n^2 \tag{G.14}$$

The long wave amplitude resulting from two waves with equal amplitudes and different frequencies is given by Sands (1982),

$$\xi_a = -G_{nm}\frac{a_n a_m}{d} \tag{G.15}$$

in which Gnm is a transfer function. The long wave velocity U_3 is represented by:

$$U_3(t) = \xi_a \frac{\sqrt{gd}}{d}\cos\left(\frac{\omega}{m}t + \varphi\right) \tag{G.16}$$

The phase shift φ is calculated according to an empirical relationship found by Roelvink and Stive (1989).

$$\cos(\varphi) = C_r \left[1 - 2 \left(\frac{H_{rms}}{H_{rms,0}} \right)^2 \right] \tag{G.17}$$

in which, C_r is the correlation coefficient between the wave envelope and long wave surface variation $H_{rms,0}$ is the incoming wave height at the seaward boundary of the model.

Finally, addition of the effects due to short-wave envelope and the bound long wave results in the total orbital velocity:

$$U_4(t) = U_2'(t) + U_3(t) \tag{G.18}$$

G.1.4 Bed load and suspended load transport model

Bed load and suspended load are modelled separately by UNIBEST-TC and added. Bed load is transport of sediment due to grains rolling or jumping over the bed, suspended load is caused by a part of the grains suspended in the water, moving along with the movement of the water.

Bed load transport

For calculation of the bed load transport, UNIBEST-TC applies a non-dimensional bed-load transport vector Φ_{bd} according to Ribberink:

$$\Phi_{bd}(t) = \frac{q_b(t)}{\sqrt{\Delta g D_{50}^3}} = 9.1 \frac{\beta_s}{(1-p)} \left\{ \left| \theta'(t) \right| - \theta_{cr} \right\}^{1.8} \frac{\theta'(t)}{\left| \theta'(t) \right|} \tag{G.19}$$

which implies the ratio of bed load-transport rate q_b and the square root of a parameter representing the specific under water weight of sand grains. The difference between the dimensionless effective shear stress (θ') and the critical shear stress (θ) determines the transport. The critical shear stress is the shear stress for which the grains on the bed just start to move.

θ', the effective shear stress due to current and waves represents the sediment forcing as a ratio of the flow drag-force on the grains and the under water weight of grains:

$$\theta'(t) = \frac{\tau_b'(t)}{(\rho_s - \rho) g d_{50}} \tag{G.20}$$

in which:

$$\tau_b' = \frac{\frac{1}{2} \rho f_{cw}' \left| u_b(t) \right| u_b(t)}{(\rho_s - \rho) g d_{50}} \tag{G.21}$$

where, f'_{cw} is the weighted friction factor and u_b is the near bottom velocity at top of the bottom layer.

In the transport formulation the Bagnold parameter β_s is included, taking into account the bottom slope. Grains moved uphill by water movement will cause a smaller transport than grains moved downhill by water movement. This factor therefore decreases uphill transport and increases downhill transport. The magnitude of the factor depends on the difference between the actual bottom slope and the angle of repose. The factor, and therefore the bottom transport, can become infinitely big when these two approach each other. The actual bottom slope is in any case not allowed to exceed the angle of repose.

$$\beta_s = \frac{\tan\varphi}{\tan\varphi + \frac{dz_b}{ds}} \tag{G.22}$$

in which $\frac{dz_b}{ds}$ represent the bottom slope and φ the angle of repose.

Suspended load transport

The suspended transport rate q_s can be computed from the vertical distribution of fluid velocities and sediment concentrations:

$$q_s = \int_a^{h+\eta} VCdz \tag{G.23}$$

in which velocity V and concentration C can be divided in an averaged and a fluctuating component:

$$V = v + \tilde{v} \tag{G.24}$$

$$C = c + \tilde{c} \tag{G.25}$$

Substituting these components, and subsequently averaging over time and space yields:

$$\overline{q_s} = \int_a^d vcdz + \int_a^d \overline{\tilde{v}\tilde{c}}dz = \overline{q}_{s,c} + \overline{q}_{s,w} \tag{G.26}$$

in which, $q_{s,c}$ is the current related suspended sediment transport and $q_{s,w}$ is the wave related suspended sediment transport.

For the suspended load, the wave-related suspended transport is assumed to be small compared to the current related suspended transport. Therefore, the mean current velocity is used and the suspended load transport in volume per unit time and width inclusive pores is computed as:

$$q_{s,c} = \frac{\int_a^h vcdz}{(1-p)\rho_s} \tag{G.27}$$

The concentration is derived by establishing a gradient in concentration over the depth through calculation of sediment stirring up and falling of sediment. A concentration near the bottom is then established, after which this concentration gradient profile can be integrated into a concentration profile over the depth. The convection diffusion equation yields:

$$w_{s,m}c + \varphi_d \varepsilon_{s,cw} \frac{dc}{dz} = 0 \tag{G.28}$$

in which, $w_{s,m}$ is the fall velocity of suspended sediment in a fluid sediment mixture
φ_d is the damping factor dependent on the concentration
$\varepsilon_{s,cw}$ is the sediment mixing coefficient for combined current and waves, that can be modelled as:

$$\varepsilon_{s,cw} = \sqrt{\left(\varepsilon_{s,w}\right)^2 + \left(\varepsilon_{s,c}\right)^2} \tag{G.29}$$

where, $\varepsilon_{s,c}$ symbolizes the current related mixing coefficient and $\varepsilon_{s,w}$ is the wave related mixing coefficient.

The convection diffusion equation is solved by numerical integration from a near bed reference level a to the water surface. The reference concentration c_a is given by:

$$c_a = 0.015\rho_s \frac{D_{50}}{a} \frac{T^{1.5}}{D_*^{0.3}} \tag{G.30}$$

in which, T is the dimensionless bed shear stress parameter and D_* is the dimensionless particle diameter.

G.1.5 Bed level change model

After the computation of the transport rates along the profile, the bed level changes are computed from the depth integrated mass balance:

$$\frac{\delta z}{\delta t} + \frac{\delta q_{bot+sus}}{\delta x} = 0 \tag{G.31}$$

in which $q_{bot+sus}$ is the combined bed load and suspended transport rate including pores

$$q_s = \int_a^{h+\eta} VCdz \tag{G.32}$$